Nematic Liquid Crystals in Confinement - Multistability and Defects

Joseph Harris

Department of Mathematical Sciences

University of Strathclyde

A Thesis presented for the degree of
Doctor of Philosophy

January 2022

Declaration

This thesis is the result of the author's original research. It has been composed by the author and has not been previously submitted for examination which has led to the award of a degree.

Chapters 3 and 4 of the thesis contain material published in an article, reference [1]; the results contained therein are the result of the author's original research in collaboration with the article's co-authors, Apala Majumdar, Giacomo Canevari and Yiwei Wang.

Chapter 5 of the thesis contains material posted to arXiv, reference [2]; the results contained therein are the result of the author's original research in collaboration with the article's co-authors, Apala Majumdar, Yucen Han and Lei Zhang.

Chapter 6 of the thesis contains material published in an article, reference [3]; the results contained therein are the result of the author's original research in collaboration with the article's co-authors, Apala Majumdar, Yucen Han and Joshua Walton.

Signed:

Date:

Acknowledgements

I would like to thank my supervisor Prof. Apala Majumdar for her endless support, scientific guidance, advice and friendship. From our beginnings in Bath, to our new home in Glasgow, to our virtual collaborations in lockdown, I am immensely grateful to have been her student over the last four years.

I also thank my other collaborators - Yucen Han for her limitless guidance and friendship, Giacomo Canevari and Yiwei Wang who have been constantly supportive and generous, Lei Zhang who hosted my visit to Beijing and made me feel most welcome, Josh Walton who has been a true friend and source of inspiration during my time at Strathclyde, and Angela Mihai and Thomas Woolley for their kind yet brief tutelage. I would like to thank my examiners Giampaolo D'Alessandro and Mikhail Osipov for their helpful comments on this thesis and I gratefully acknowledge financial support from the University of Strathclyde and an EPSRC studentship.

Numerous relocation has led to a long list of friends who I have to thank - Raj, Aidan, Joseph, Russell, Craig, Alistair, Alge, Sam, Will, Marie, Richard, Abi, Libby, Ioana, Hannah, Ewan, James, Ruma, Sourav, Lidong and the boys from home.

A massive thanks goes to my Mum, Dad and Sister for putting up with me all these years and at least pretending to have an interest in my research. And to Emma for her unyielding support and optimism, without whom I could not have done it.

Abstract

We model nematic liquid crystals using the Landau-de Gennes continuum theory, where equilibrium configurations are solutions of complex boundary-value problems of systems of coupled nonlinear partial differential equations. We analyse and present the exotic defect structures in model geometries with different boundary conditions and material properties. We study three-dimensional wells with tangent boundary conditions on the lateral surfaces, and two physically relevant boundary conditions on the top and bottom surfaces, and prove the existence of the globally minimizing Well Order Reconstruction Solution for small geometries. This work is corroborated by an exhaustive numerical study of three-dimensional wells with square and rectangular cross-sections, where we have looked at the effects of geometrical anisotropy and anchoring. We then consider a two-term elastic energy density in the Landau-de Gennes free energy to investigate the role of elastic anisotropy in different asymptotic limits, focusing on two-dimensional square wells with tangent boundary conditions. We then model ferronematics in two-dimensional polygonal wells, tailoring multistability of the equilibrium profiles, and presenting new exotic states with interior domain walls and nematic point defects. Lastly, we study the nematic-isotropic phase transition for a fourth-order thermotropic bulk potential in a stochastic setting, where certain material-dependent parameters are assumed to follow a non-Gaussian probability distribution.

List of Figures

1.1 Thin-film liquid crystal samples under a polarising microscope. Courtesy: Oleg Lavrentovich, Liquid Crystal Institute, Kent State University, National Science Foundation (www.nsf.gov). 3

1.2 A schematic representation of the uniaxial nematic liquid crystal phase for increasing temperature, T. The ellipsoidal shapes represent calamatic molecules, whose average direction of molecular alignment is given by the unit vector $\mathbf{n}$, called the director. . . 5

1.3 A schematic representation of the cholesteric liquid crystal phase, with cross-sections normal to the helical axis. Here, the director, represented by black arrows, rotates through a full 360° along a distance given by the pitch P. 6

1.4 A schematic representation of the smectic liquid crystal phases. In the smectic A phase, the prescribed layers of liquid crystal are positioned normal to the director, $\mathbf{n}$. In the smectic C phase, the director aligns at some angle, θ, to the layer normal. 7

1.5 Diagrams of the OFF and ON states in a twisted nematic (TN) liquid crystal device. 9

1.6 Homogeneous, homeotropic and conical anchoring alignments with director given by $\mathbf{n}$. 10

1.7 A diagram of the molecular orientation angles, adapted from [19]. The blue arrow represents the molecular orientation of a single molecule, and the average orientation of molecules in the region $\mathcal{B}$ is given by the director $\mathbf{n}$. θ_m is the zenithal angle between the molecule and director, and ϕ_m is the azimuthal angle, where ν is some fixed direction normal to the director. 14

1.8 Illustrations of point defects with topological charge $+1$ (top left), -1 (top right), $+\frac{1}{2}$ (bottom left), and $-\frac{1}{2}$ (bottom right). . . . 16

1.9 The splay, twist and bend curvature strains from the Oseen-Frank elastic energy density (1.3.2). 17

1.10 Plots of the thermotropic bulk energy density, f_b, as a function of the scalar order parameter, s, for various temperature regimes. The red circle represents the isotropic state, $s = 0$. 27

2.1 Side view and perspective view of the planar bistable nematic device. Adapted from [60]. 36

2.2 The director orientation of a diagonal (D) solution, rotated (R) solution and WORS. 37

3.1 The truncated unit square $\Omega \subset \mathbb{R}^2$. 49

3.2 $q_1 \in W^{1,2}(\Omega_+)$ in the admissible space $\mathcal{G}$. 56

4.1 The 3D WORS with $\bar{\lambda}^2 = 5$ and $\epsilon = 4$. 96

4.2 The 3D diagonal solution with $\bar{\lambda}^2 = 100$ and $\epsilon = 4$. 98

4.3 The 3D rotated solution with $\bar{\lambda}^2 = 100$ and $\epsilon = 4$. 98

4.4 A locally stable mixed diagonal solution for $\bar{\lambda}^2 = 100$ and $\epsilon = 4$ with 2D cross-sections (from left to right) at $z = \epsilon$, $z = \frac{9\epsilon}{16}$, $z = \frac{\epsilon}{2}$, $z = \frac{7\epsilon}{16}$ and $z = 0$, respectively. 100

4.5 A mixed diagonal solution for $\bar{\lambda}^2 = 10$ and $\epsilon = 4$. Colours given by the biaxiality parameter and the director orientation is given by white lines. Cross-sectional heights as in Figure 4.4. 101

4.6 A locally stable solution with $\bar{\lambda}^2 = 5$ and $\epsilon = 0.2$ and $W = 2 \times 10^{-3}\text{Jm}^{-2}$ in (4.1.4). 103

4.7 A locally stable solution with $\bar{\lambda}^2 = 5$ and $\epsilon = 0.2$ and $W = 10^{-3}\text{Jm}^{-2}$ in (4.1.4). 103

4.8 A locally stable solution with $\bar{\lambda}^2 = 5$ and $\epsilon = 0.2$ and $W = 10^{-4}\text{Jm}^{-2}$ in (4.1.4). 103

4.9 An unstable numerical solution with $\bar{\lambda}^2 = 5$ and $\epsilon = 0.2$ and $W = 10^{-4}\text{Jm}^{-2}$ given an isotropic initial guess ($\mathbf{Q} = 0$). 104

4.10 An unstable numerical solution with $\bar{\lambda}^2 = 5$ and $\epsilon = 0.2$ and $W = 8 \times 10^{-4}\text{Jm}^{-2}$ given a uniform horizontal initial guess. . . 104

4.11 Bifurcation points $\bar{\lambda}^*$, such that the WORS is the unique solution for $\bar{\lambda}^2 < \bar{\lambda}^2_*$, as a function of anchoring strength W. The blue dashed line indicates the bifurcation point of the WORS for Dirichlet boundary condition in a 2D square domain ($\bar{\lambda}^2 \approx 6.4$). . 105

4.12 The stable WORS-like solution with $\bar{\lambda}^2 = 5$, $\epsilon = 0.2$ and $\alpha = \gamma = 1$ in (4.3.2). 107

4.13 A locally stable numerical solution with $\bar{\lambda}^2 = 5$, $\epsilon = 0.2$ and $\alpha = 0.1$, $\gamma = 1$ in (4.3.2). 107

4.14 A locally stable numerical solution with $\bar{\lambda}^2 = 5$, $\epsilon = 0.2$ and $\alpha = 1$, $\gamma = 0.2$ in (4.3.2). 107

4.15 A locally stable numerical solution with $\bar{\lambda}^2 = 5$, $\epsilon = 0.2$ and $\alpha = 1$, $\gamma = 0.1$ in (4.3.2). 107

4.16 Escaped configuration with -1-disclination line in the center of the well where $\bar{\lambda}^2 = 100$, $\epsilon = 4$ and $W_z = 10^{-5}\mathrm{Jm}^{-2}$ in (4.1.5). . . . 109

4.17 Escaped configuration with $+1$-disclination line in the center of the well where $\bar{\lambda}^2 = 100$, $\epsilon = 4$ and $W_z = 10^{-5}\mathrm{Jm}^{-2}$ in (4.1.5). . . . 110

4.18 Critical anchoring strength W_z, in (4.1.5), for which the escaped configurations lose stability as a function of ϵ. 110

4.19 Director orientations for the D, R and U states in a rectangular domain. 113

4.20 A 3D diagonal (D) solution in a rectangle with $\delta = 1.45$, $\bar{\lambda}^2 = 100$ and $\epsilon = 4$. 114

4.21 A 3D lower energy rotated (R) solution in a rectangle with $\delta = 1.45$, $\bar{\lambda}^2 = 100$ and $\epsilon = 4$. 115

4.22 A 3D higher energy rotated (U) state in a rectangle with $\delta = 1.45$, $\bar{\lambda}^2 = 100$ and $\epsilon = 4$. 115

4.23 The 3D sBD2 state with $\delta = 1.45$, $\bar{\lambda}^2 = 5$ and $\epsilon = 4$. 116

4.24 Bifurcation points $\bar{\lambda}_c^2$, such that the sBD2 is the unique solution for $\bar{\lambda}^2 < \bar{\lambda}_c^2$, as a function of δ. 117

4.25 Bifurcation points $\bar{\lambda}_c^2$, such that the rotated states lose their stability for $\bar{\lambda}^2 < \bar{\lambda}_c^2$, as a function of geometric anisotropy δ. Blue markers for the R states and green markers for the U states. For $\delta > 1.5$ we cannot obtain the U rotated states in our numerical simulations. We include the bifurcation points from Figure 4.24, shown by the red markers. 118

4.26 A locally stable mixed 3D diagonal solution in a rectangle with $\bar{\lambda}^2 = 100$, $\epsilon = 4$ and $\delta = 1.45$. Cross-sectional heights as in Figure 4.4. 120

4.27 A locally stable mixed 3D rotated (R_1 and R_2) solution in a rectangle with $\bar{\lambda}^2 = 100$, $\epsilon = 4$ and $\delta = 1.45$. Cross-sectional heights as in Figure 4.4. 121

4.28 A mixed 3D diagonal (D) and rotated (R) solution in a rectangle with $\bar{\lambda}^2 = 100$, $\epsilon = 4$ and $\delta = 2.1$. 2D cross-sections (from left to right) at $z = 4, 1.8, 1.53, 1.26, 0$. 123

4.29 Bifurcation points ϵ_*, such that the mixed solutions lose their stability for $\epsilon < \epsilon_*$, as a function of δ. The red markers indicate the critical well heights for the mixed diagonal solutions, the blue markers for the mixed rotated solutions, and the green markers for the mixed diagonal and rotated solutions. 124

5.1 The truncated unit square, $\Omega \subset \mathbb{R}^2$. 132

5.2 The reflected solution $q_1^s(x, y)$. 143

5.3 The unique stable solution of the Euler-Lagrange equations (5.1.8)–(5.1.10) with $\bar{\lambda}^2 = 5$, and (from the first to fourth row) $L_2 = -0.5$, 0, 1 and 10, respectively. We plot s^2, q_1, q_2 and q_3, in the first to fourth columns, respectively. 151

5.4 Solutions of (5.1.8)–(5.1.10) with $\bar{\lambda}^2 = 500$, and (on the first, second and third row) $L_2 = -0.5$, 0, 1 and 10, respectively. We plot s^2, q_1, q_2 and q_3, in the first to fourth columns, respectively. . 152

5.5 Error of the $\mathcal{O}(L_2)$ small λ approximations. Plots (from left to right) of $q_1 - q_0$, q_2, and $q_3 + \frac{s_+}{6} - L_2 h_0$, respectively, with $\bar{\lambda}^2 = 0.01$, $L_2 = 0.1$. 156

5.6 Solutions, ρ, σ, τ, of the leading order Euler-Lagrange system (5.4.12)–(5.4.14) in the $L_2 \to \infty$ limit. Plots of (from left to right) ρ, σ, τ, and (x, y, τ). Taken from [2]. 160

5.7 The D and R solutions with $L_2 = 3.5$ and $\bar{\lambda}^2 = 1000$. 165

5.8 The D solution with $\bar{\lambda}^2 = 1000$, and $L_2 = 0, 10, 30$, and 45, respectively. 166

5.9 The $\mathcal{O}(L_2^2)$ contribution of q_2, γ, with $\bar{\lambda}^2 = 5$, 100 and 500, respectively. 167

5.10 The pWORS with $L_2 = 3.5$ and $\bar{\lambda}^2 = 350, 1000$ (top and bottom, respectively). We plot (from left to right), s^2, q_1, q_2, and q_3, respectively. 168

5.11 Energy of the WORS, Ring$^+$ and Constant solutions verses L_2 when $\bar{\lambda}^2 = 100$ and 200, respectively. 169

5.12 Bifurcation diagram as a function of $\bar{\lambda}^2$, and corresponding energy $(J - \int_\Omega \min f_b \, \mathrm{dA})$ plot, for the LdG model in square domain with $L_2 = 0$. 171

5.13 Bifurcation diagram and energy plot for $L_2 = 1$. 173

5.14 Bifurcation diagram and energy plot for $L_2 = 2.6$. 174

5.15 Bifurcation diagram and energy plot for $L_2 = 3$. 175

5.16 Bifurcation diagram and energy plot for $L_2 = 10$. 176

6.1 Director orientation at a *splay* and *bend* vertex. 193

6.2 The plots of two D and four R solutions with $\ell = 10^{-3}$ and $c = 0.25$. 195

6.3 The two Peppa solutions with $\ell = 10^{-3}$ and $c = 0.25$. 196

6.4 The Ring solution for $c = 0.25$ and $\ell = 0.05$. 197

6.5 Bifurcation diagram for (6.1.1) as a function of ℓ on a square domain with $c = 0.25$. 198

6.6 The plots of four D and eight R solutions with $\ell = 10^{-3}$ and $c = -0.25$. 200

6.7 Plots of the two Peppa$_{in}$ and two Peppa$_{out}$ solutions with $\ell = 10^{-3}$ and $c = -0.25$. 201

6.8 The Ring solution for $c = -0.25$ and $\ell = 0.05$. 202

6.9 Bifurcation diagram for (6.1.1) as a function of ℓ on a square domain with $c = -0.25$. 203

6.10 The Ring solution with $c = 0.25$. Plots in the first row from left to right are: $\mathbf{Q}_1$; the Q_{11} and Q_{12} components; and the difference $S_1 S_{100} \sin(2\theta_{100} - 2\theta_1)$. The second row from left to right shows: the corresponding $\mathbf{M_1}$; the M_1 and M_2 profile; and the difference $R_1 R_{100} \sin(\phi_{100} - \phi_1)$. 212

6.11 Nematic director orientation for the Para, Meta, and Ortho states in a hexagon. 213

6.12 The nematic $\mathbf{Q}$-profile for $\ell = 10^{-4}$ and (from left to right) $c = 5, 6, 7 \times 10^{-3}$, respectively. 215

6.13 Bifurcation diagram for (6.1.1) as a function of ℓ on a hexagon domain with $c = 0.25$. 216

6.14 Para and Meta solution profiles for $c = 0.02$ and Ortho solution profile for $c = 1$, respectively with $\xi = 0.01$ and $\ell = 5 \times 10^{-4}$. . . . 218

6.15 Peppa$_{in}$ and Peppa$_{out}$ solution profiles (from left to right) for $c = -0.1$, with $\xi = 1$, and $\ell = 5 \times 10^{-4}$. 219

6.16 Bifurcation diagram for (6.1.1) on a hexagon domain as a function of ℓ with $c = -0.25$. 221

6.17 Nematic director orientation for the Meta, and Ortho states in a pentagon. 223

6.18 Meta and Ortho solutions in a pentagon for $c = 0.05$, $\ell = 5 \times 10^{-4}$. 224

6.19 Bifurcation diagram for (6.1.1) as a function of ℓ on a pentagon domain with $c = 0.25$. 225

6.20 Bifurcation diagram (6.1.1) as a function of ℓ on a pentagon domain with $c = -0.25$. 226

7.1 Probability distributions (7.1.3) and (7.1.4) given by the blue and red solid lines, respectively. Simulated data is given by the yellow and purple lines. The vertical dashed line represents the (deterministic) nematic super-heating temperature, $A = \frac{\bar{B}^2}{24C}$. 236

7.2 Completed probability distribution of the order parameter, s, as a function of temperature, A, when B follows the Gamma distribution (7.1.2) with $\rho_1 = 40$, $\bar{B} = 0.64 \times 10^4$. $C = 0.35 \times 10^4$. The deterministic values are shown by the black lines (stable is solid and unstable is dashed). We also include a 3D surface plot of the same diagram. 238

Contents

Declaration **ii**

Acknowledgements **iv**

Abstract **vi**

List of Figures **vii**

1 Introduction **1**

1.1 What are liquid crystals? 1

1.1.1 The nematic phase 4

1.1.2 The cholesteric phase 5

1.1.3 The smectic phase 6

1.2 Applications of liquid crystals 7

1.2.1 Liquid crystal displays 8

1.2.2 Liquid crystals in confinement 10

1.2.3 Colloidal particles in a nematic host 11

1.3 Modelling nematic liquid crystals 12

1.3.1 The scalar order parameter 12

1.3.2 Defects 15

1.3.3 The Oseen-Frank theory 16

1.3.4 The Ericksen theory 18

1.4 The Landau-de Gennes theory 19

1.4.1 The de Gennes Q-tensor 19

1.4.2 Thermotropic contributions 23

1.4.3 Elastic contributions 26

1.4.4 The biaxiality parameter 28

1.4.5 Results on minimizers 29

1.5 Thesis outline 31

1.6 Publication and collaboration details 34

2 Literature review **35**

2.1 The planar bistable nematic device 35

2.2 Elastic anisotropy 40

2.3 Ferronematics 41

2.4 Stochastic models for nematic liquid crystals 44

3 Analysis of the well order reconstruction solution in three dimensions 46

3.1 Model formulation 47

3.1.1 The working domain 48

3.1.2 Boundary conditions on the lateral surfaces 49

3.2 The 3D WORS and related results 51

3.2.1 Natural boundary conditions on the top and bottom plates 52

3.2.2 A more general class of critical points 62

3.2.3 Weak anchoring on the top and bottom plates 72

3.3 Summary 81

4 Numerical simulations of three-dimensional nematic equilibria in confinement 83

4.1 The computational model 84

4.2 The numerical methods 87

4.2.1 Limited-memory BFGS 88

4.2.2 Stability of solutions 91

4.2.3 Initial guesses 92

4.3 Numerical results 94

4.3.1 Strong anchoring on the lateral surfaces 95

4.3.2 Weak anchoring on the lateral surfaces 101

4.3.3 Escaped solutions 108

4.3.4 Simulations in a rectangular domain 111

4.4 Summary 125

5 Elastic anisotropy in a 2D square domain 127

5.1 Model formulation 128

5.2 Numerical methods 135

5.3 Qualitative properties of the equilibrium configurations 138

5.4 Asymptotic studies 153

5.4.1 The $L_2 \to 0$ limit for small λ 153

5.4.2 The $L_2 \to \infty$ limit 158

5.4.3 The $\lambda \to \infty$ limit 161

5.4.4 The novel pWORS 165

5.5 Bifurcation diagrams 168

5.6 Summary 179

6 Ferronematic equilibria on 2D polygons 182

6.1 Model formulation 183

6.1.1 The effective ferronematic free energy 184

6.1.2 The working domains and boundary conditions 188

6.1.3 Numerical methods 190

6.2 Solution landscape on a square 192

6.2.1 The $\ell \to 0$ limit 204

6.2.2 The $\ell \to \infty$ limit 210

6.3 Ferronematics on 2D hexagons 212

6.4 Ferronematics on 2D pentagons 222

6.5 Summary 227

7 The nematic-isotropic phase transition for a stochastic bulk potential 231

7.1 Stochastic problem formation 232

7.2 Numerical results 235

8 Conclusions and future work 240

Bibliography 245

Chapter 1

Introduction

1.1 What are liquid crystals?

We are all familiar with the three basic states of matter - solids, liquids and gases. If we heat up an ice cube above $0°C$, it becomes liquid water. This is one of the simplest and most well-known examples of a phase transition where, at certain temperatures or pressures, pure substances change state. Solid crystalline materials consist of highly ordered molecules with a prescribed orientation and position, whereas in a liquid, any sense of molecular order is lost, and the constituent molecules can move freely. The term 'liquid crystal' therefore might seem quite counterintuitive. However, many materials experience a liquid crystalline phase, exhibiting both partial molecular order, and the fluidity of a conventional liquid.

The defining feature of liquid crystals is the constituent molecules are strongly elongated in one or more dimension - usually rod, disc or board-like in shape [4]–[6]. The attractive forces between neighbouring particles are therefore directionally dependent, and so liquid crystals display different material responses in different

directions i.e., they are *anisotropic*. Most notably, the anisotropy of the liquid crystal phase affects the polarisation and transmission of incident light, and the optical response is different in different directions [7]. This can be clearly observed in thin film samples under a polarising microscope, as seen in Figure 1.1. In these figures, the different colours are a result of the changing molecular orientation and some variation in the thickness of the film. In regions where the average molecular orientation is parallel to either polarizer, we see black lines. We also see these lines intersecting each other at junctions, referred to as 'topological defects'. These defects correspond to small regions of the liquid crystal where the average molecular orientation is no longer defined. Depending on their chemical make up, some liquid crystalline materials go through phase transitions due to a change in temperature, for which they are deemed *thermotropic*, and others due to a change in concentration, for which we call them *lyotropic* [8], [9]. In this thesis, we will be focusing purely on thermotropic liquid crystals.

Liquid crystals were first discovered in 1888 by the Austrian botanist and chemist Friederich Reinitzer [10]. Whilst studying the chemicals in plants, Reinitzer heated a sample of cholesteryl benzoate which, at $145°C$, melted into a cloudy fluid, and at $178.5°C$, changed once more into the originally expected clear liquid. We now know the cloudy substance to be a *cholesteric* liquid crystal, and the temperature at which it transitions to a clear liquid to be the *clearing point*. Reinitzer sent two samples of the curious cloudy liquid to the German physicist Otto Lehmann, along with an accompanying letter. It was Lehmann who, upon a systematic study of the cholesteryl benzoate (and other related compounds that presented two melting points), first used the term 'liquid crystals' to describe this phenomenon. This work was expanded on by the German chemist Daniel Vorländer at the beginning of the 20^{th} century and, in 1907, determined that

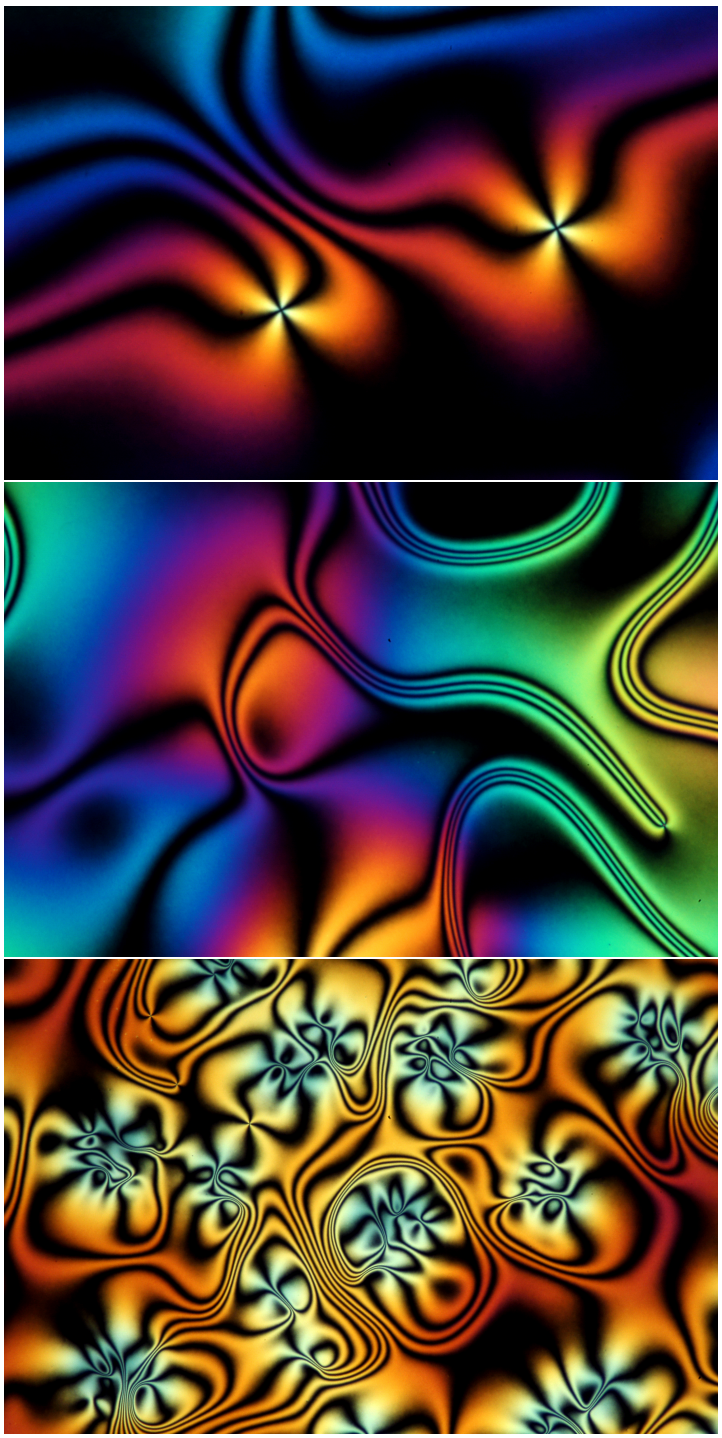

Figure 1.1: Thin-film liquid crystal samples under a polarising microscope. Courtesy: Oleg Lavrentovich, Liquid Crystal Institute, Kent State University, National Science Foundation (www.nsf.gov).

rod-like molecules were essential for the occurrence of two melting points [11].

Most liquid crystals are *mesogenic* i.e., they display a series of intermediate states of matter between the solid and liquid phases called *mesophases*. In 1922, G. Friedel [12] classified these mesophases into three broad categories which are still in use today - the *nematic*, *cholesteric* and *smectic* phases.

1.1.1 The nematic phase

The simplest liquid crystalline phase is the nematic phase. Here, the constituent molecules orient themselves in locally preferred directions, called *directors* in the literature, but they do not display any sense of positional order. The term nematic derives from the Greek $\nu\hat{\eta}\mu\alpha$, meaning 'thread', which stems from the dark lines that are often observed in nematic liquid crystal samples, as in Figure 1.1. In many nematic liquid crystals, the molecules tend to align parallel to a single director, which defines an anisotropic axis, and are hence called *uniaxial* nematics [13]. The molecules in a uniaxial nematic are typically rod-like in shape, or elongated in the direction of the anisotropic axis, for which we call them *calamitic*. Others are disc-like in shape, or shortened in the direction of the anisotropic axis, for which we call them *discotic* [14]. A typical calamitic liquid crystal molecule, such as *p*-azoxyanisole (PAA), has a length of a few nanometers and is fairly rigid for some portion of its length [15]. A schematic of the uniaxial nematic phase for a calamitic liquid crystal is shown in Figure 1.2, which shows approximately how these molecules tend to arrange themselves for very low and high temperatures. When the temperature is low enough, the liquid crystal molecules acquire a degree of positional order, and for high enough temperatures, the molecules lose any sense of molecular order and enter an isotropic fluid phase [16]–[18].

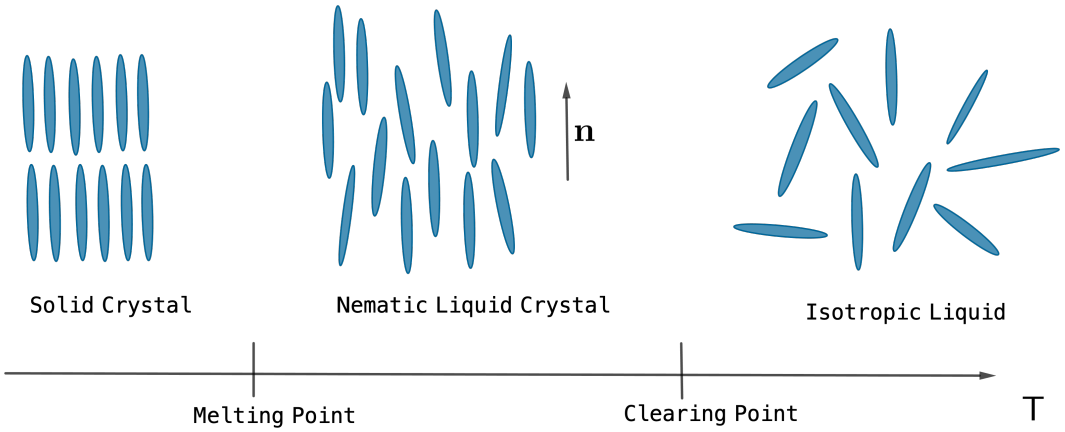

Figure 1.2: A schematic representation of the uniaxial nematic liquid crystal phase for increasing temperature, T. The ellipsoidal shapes represent calamatic molecules, whose average direction of molecular alignment is given by the unit vector $\mathbf{n}$, called the director.

The key feature of nematic liquid crystals is that the axis of uniaxial symmetry has no polarity. This means that if we describe the director by some vector $\mathbf{n}$, as in Figure 1.2, then $\mathbf{n}$ and $-\mathbf{n}$ will be indistinguishable from each other. It is also possible for a nematic liquid crystal to have two locally preferred directions of alignment. We refer to these as *biaxial* nematic liquid crystals [19].

1.1.2 The cholesteric phase

In the *cholesteric* phase, chiral molecules (which have a different left and right-hand orientation) form a helical structure [20]. The helical axis is perpendicular to the local director, as shown in Figure 1.3. The pitch of the cholesteric helix, P, is the distance along the helical axis (typically of the order of microns), over which the local director rotates through 360°. The term cholesteric originates from the word 'cholesterol', a substance for which many of its derivatives exhibit

a cholesteric liquid crystalline phase. This may seem slightly ambiguous since cholesterol itself is not a cholesteric liquid crystal, and so the expression *chiral nematic* is also used to describe this phase [15].

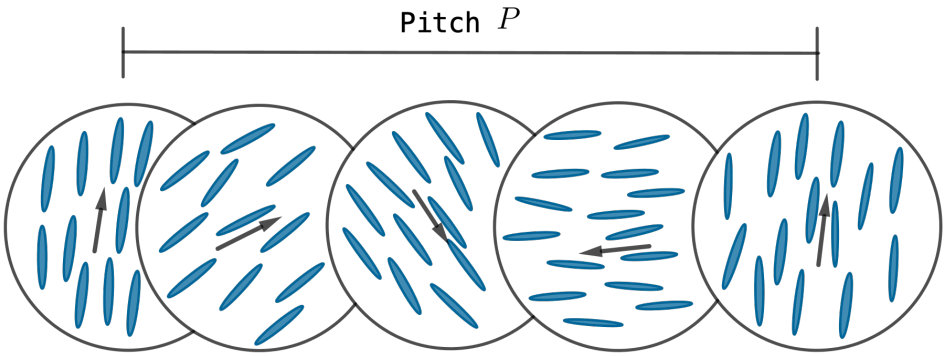

Figure 1.3: A schematic representation of the cholesteric liquid crystal phase, with cross-sections normal to the helical axis. Here, the director, represented by black arrows, rotates through a full 360° along a distance given by the pitch P.

1.1.3 The smectic phase

In a *smectic* liquid crystalline phase, the constituent molecules exhibit some degree of positional order and arrange themselves in layers. These layers typically have a prescribed thickness sometimes called the smectic interlayer distance. Unlike the conventional solid crystal, these layers can still move over each other freely and, within each layer, molecules behave like a nematic with an average orientation given by a director. In Figure 1.4, we show a schematic of two common smectic phases - *smectic A* and *smectic C*. In the smectic A phase, the layers are normal to the director and, in the smectic C phase, the director may orient itself at an angle to the layer normal [5], [9].

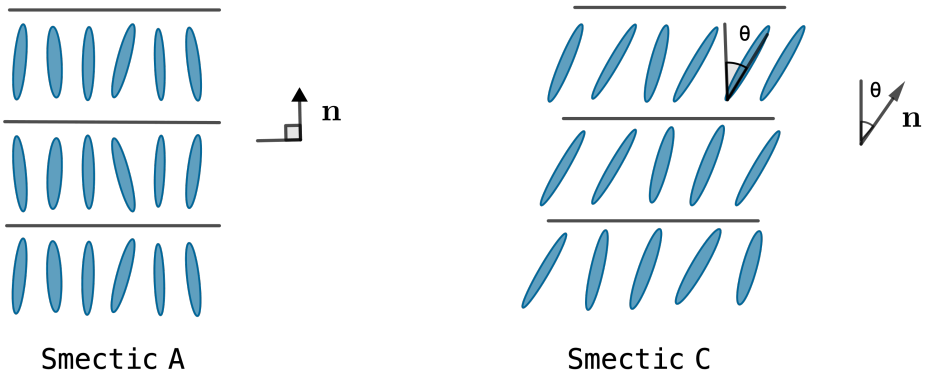

Figure 1.4: A schematic representation of the smectic liquid crystal phases. In the smectic A phase, the prescribed layers of liquid crystal are positioned normal to the director, $\mathbf{n}$. In the smectic C phase, the director aligns at some angle, θ, to the layer normal.

We will focus on nematic liquid crystals for the remainder of this thesis, but for a more in depth mathematical introduction to these phases, the reader is referred to the seminal work by De Gennes and Prost [9].

1.2 Applications of liquid crystals

The special properties of liquid crystals make them excellent working materials in a number of industrial applications [21]. Most notably, the anisotropy of liquid crystals means they are optically birefringent. In general, light entering an isotropic medium will travel at a constant speed, regardless of the material's orientation relative to the direction of incident light. However, the director in a uniaxial nematic defines an optic axis for the material, and the refractive index, $n_{\parallel}$, parallel to the director $\mathbf{n}$, is different from the refractive index perpendicular to the director, $n_{\perp}$. The 'birefringence' of the material is simply defined by $\Delta n = n_{\parallel} - n_{\perp}$

[9]. Furthermore, a nematic liquid crystal's orientational order is highly sensitive to external electromagnetic fields and mechanical stresses [15]. An applied electric field, **E**, for example, will induce a dipole moment per unit volume, **P**, referred to as the polarisation. This quantity is proportional to the field strength and electric susceptibility of the liquid crystal. The electric displacement, **D**, induced by **E** and **P** is given by

$$\mathbf{D} = \epsilon_0 \epsilon_\perp \mathbf{E} + \epsilon_0 \Delta\epsilon (\mathbf{n} \cdot \mathbf{E})\mathbf{n}, \tag{1.2.1}$$

where **n** is the director, ϵ_0 is the dielectric permittivity of free space, and $\Delta\epsilon = \epsilon_\parallel - \epsilon_\perp$ is the *dielectric anisotropy* of the liquid crystal. The unitless dielectric constants, $\epsilon_\parallel$ and $\epsilon_\perp$, are the relative permittivities parallel and perpendicular to the director, respectively [13]. These important characteristics have led to the explosion of interest in nematic liquid crystals and their use in the multibillion-dollar display industry.

1.2.1 Liquid crystal displays

The liquid crystal display (LCD) was invented in 1964 at RCA Laboratories in Princeton [22], [23]. These early designs didn't become commercially viable until the invention of the twisted nematic (TN) mode of operation in 1970 [24]. In a TN device, the orientation of nematic liquid crystal molecules is imposed by two suitably treated substrates where, in the absence of any external electric field (the OFF state), polarized light is allowed to pass through a twisted nematic layer. When an electric field is applied (the ON state), the nematic molecules are oriented in such a way that the incident light cannot pass through. A diagram of the fundamental mechanism in a TN device is shown in Figure 1.5. In this example,

the nematic liquid crystal has positive dielectric anisotropy ($\Delta\epsilon > 0$), and so the director is attracted to be parallel to the applied electric field. The addition of

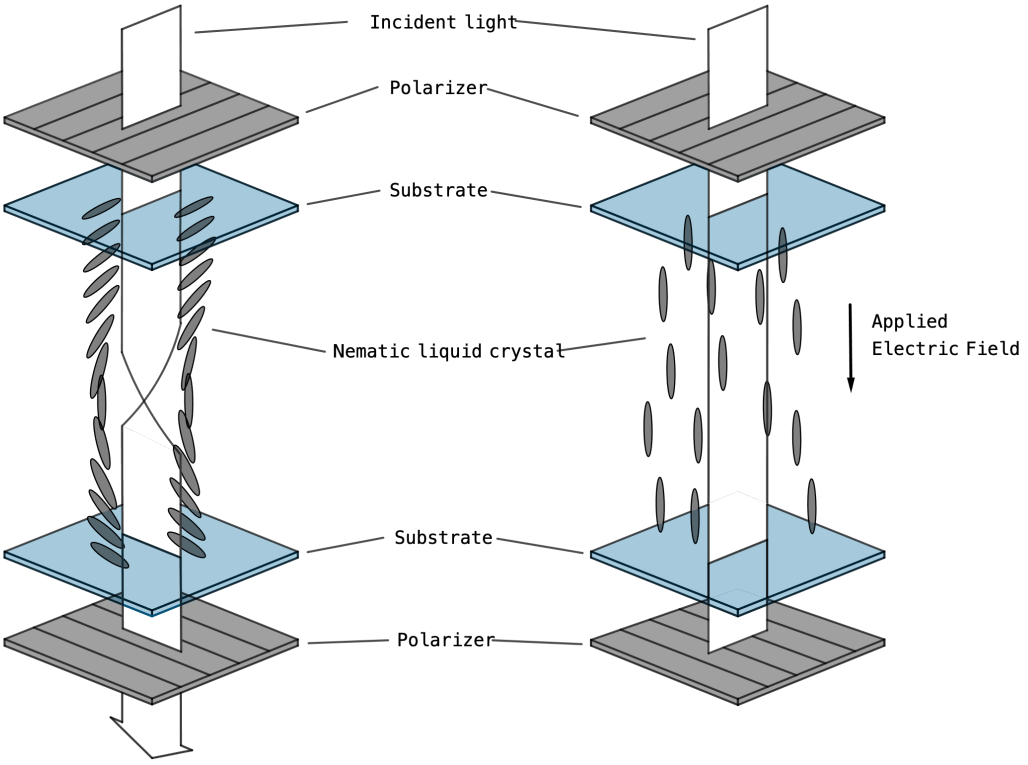

Figure 1.5: Diagrams of the OFF and ON states in a twisted nematic (TN) liquid crystal device.

thin-film transistors (TFTs) to these devices made it possible to construct LCD TV's, and many of the modern displays used today. More complex modes of operation, such as the in-plane switching (IPS) mode, have use in displays with enhanced viewing angles and which can endure additional mechanical stresses such the touch screens on smart phones [22], [25]. More modern inventions, such as the zenithal bistable device (ZBD), utilise particular confining geometries that permit multiple stable orientations for the nematic molecules, improving the display's efficiency [26], [27]. The prescribed molecular orientation on surfaces is an important feature in display devices, and will play a large role in the modelling

aspect of this thesis. For this reason, we briefly describe the types of anchoring that are employed in applications.

1.2.2 Liquid crystals in confinement

The confining geometry of a liquid crystal sample can drastically alter the orientational order in the absence of external fields. Interaction forces between the nematic molecules and the bounding surface can impose variable degrees of orientational order and preferred directions of alignment. The ways in which the director in a nematic liquid crystal is aligned on the bounding surfaces of a container is referred to as *anchoring*. The term *homogeneous* (or planar) alignment refers to anchoring which aligns the director parallel to the bounding surface. This is typically achieved by rubbing the surface in one direction. Other methods that induce anchoring include chemical treatment of the bounding surfaces, which may force the director to be perpendicular to the surface. This is referred to as *homeotropic* anchoring. More generally, we may prescribe *conical* anchoring, where the nematic director at the boundary makes a fixed angle, φ, with the tangent plane of the surface, defining a cone of 'easy directions' for which it may orient itself. In Figure 1.6 we present a simple schematic, which has been adapted from [13], that shows these three anchoring alignments.

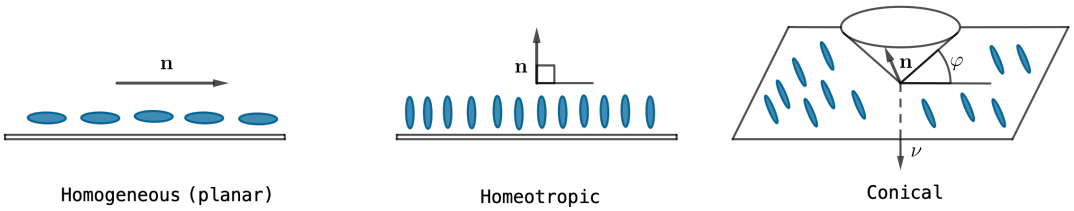

Figure 1.6: Homogeneous, homeotropic and conical anchoring alignments with director given by $\mathbf{n}$.

1.2.3 Colloidal particles in a nematic host

In recent years, there has been substantial interest in liquid crystal nanoscience and nanotechnology [28], [29]. This exciting field of research focuses its attention on controlling and enhancing the distinctive physical properties of a liquid crystal host using embedded inclusions, such as dispersed colloidal particles. The introduction of foreign particles changes the local orientation of nematic molecules through surface interactions, and in some cases can induce several topological defect structures [30]. It has also been shown that dispersions of colloids in a nematic host can change material properties such as phase transition temperatures [31], and induce the self-assembly of highly organized defect structures and anisotropic clusters [32]. The inclusion of magnetic nanorods was first theoretically investigated by Brochard and de Gennes [33], who proposed that rod-shaped particles can drastically enhance the macroscopic responses of a nematic liquid crystal to external magnetic fields. This class of soft matter is referred to as a *ferronematic*, and is explored in more detail in Chapter 6.

For a time, the LCD industry dominated the focus of applied science, but we are now seeing a renaissance of advanced and complex applications that have liquid crystals at its core. Liquid crystals' optical birefringence, susceptibility to external fields, and interaction with solid surfaces, offers a wide range of potential functions. To name but just a few of them, they are now being used to improve the sensitivity of switchable metamaterials [34], to construct tunable photonic band-gap devices [35], and as an important material in visualizing the presence of proteins such as DNA [36].

1.3 Modelling nematic liquid crystals

Liquid crystals present a challenge to mathematical modellers due to their anisotropic properties. Nonetheless, several mathematical approaches have been used to understand both the molecular behaviour, and macroscopic configurations in the nematic phase. The first attempt at a theoretical formulation of nematic liquid crystals is the 'swarm theory', proposed by Bose in 1909 [11]. This simple theory adopts the notion that liquid crystal molecules group into collective bundles, or swarms, in approximately the same direction. Whilst quite basic, this theory was able to explain the cloudy appearance of liquid crystal samples at the time. It is clear that molecular interactions within a liquid crystal instigate the orientational behaviour that is observed, but the majority of liquid crystal applications involve samples of liquid crystal with many molecules. For that reason, accurate molecular models of these samples are computationally expensive and hard to achieve. A more manageable approach is to carry out molecular dynamics simulations, which utilise an empirical potential for the intermolecular interaction, such as the Gay-Berne potential [37]–[39]. Where these models succeed in modelling the microscopic interactions of a liquid crystal, they are inadequate for calculating the macroscopic outcome from these interactions, for which a continuum theory is needed.

1.3.1 The scalar order parameter

Any robust continuum theory of nematic liquid crystals requires some measure of the orientational order in the system. We have already touched on one such measure, the director $\mathbf{n}(\mathbf{x}, t)$. This unit vector effectively measures the mean orientation of the molecules in a uniaxial nematic liquid crystal, at a point $\mathbf{x}$

in space, and time t. In this thesis we focus on the static continuum theory of nematics, where any notion of flow can be ignored, and so we consider directors $\mathbf{n}(\mathbf{x})$. As explained previously, the sign of $\mathbf{n}$ has no physical significance due to the head-to-tail symmetry of the constituent molecules. Therefore it is conducive to think of the molecular orientations, not as elements of a vector field, but as elements of the real projective plane, $\mathbb{R}P^2$. Another crucial parameter used to describe a nematic liquid crystal is the *scalar order parameter*, typically denoted by s, which measures the degree of orientational order about the director.

Consider a small region of the material, say a small ball $\mathcal{B}(\mathbf{x}, \delta)$ centred at the point $\mathbf{x}$ with radius δ, containing a uniaxial nematic liquid crystal consisting of calamitic (or rod-like) molecules. We pick δ small enough to describe the material point $\mathbf{x}$ effectively, but large enough for a statistical approach to make sense. As in [19], we may consider the probability distribution function, $\rho(\theta_m)$, of the angle, $-\frac{\pi}{2} \leq \theta_m \leq \frac{\pi}{2}$, between each molecule and the average orientation of molecules in the region $\mathcal{B}(\mathbf{x}, \delta)$. The scalar order parameter is a measure of how spread out this probability distribution function is. The standard way to define this is to compute a Legendre polynomial decomposition of the probability distribution function ρ. The first non-zero term is given by

$$s = \frac{1}{2} \int_{\mathcal{B}} (3 \cos^2 \theta_m - 1) \rho(\theta_m) \, \mathrm{dV}. \tag{1.3.1}$$

In a state of perfect alignment, we have that $\theta_m = 0$ everywhere. Since $\rho(\theta_m)$ is a probability distribution, its integral over the region $\mathcal{B}$ is equal to 1, and so we have $s = 1$. In an isotropic fluid, the molecules are randomly oriented. In this scenario, we have that $\rho(\theta_m)$ is a constant, since it resembles a uniform distribution. From the head-to-tail symmetry of molecular orientations, this constant value is equal to $\frac{1}{2\pi}$ since the integration in equation (1.3.1) may be performed over half the

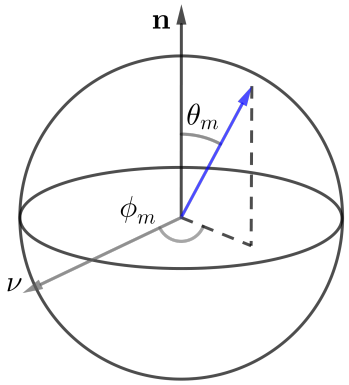

Figure 1.7: A diagram of the molecular orientation angles, adapted from [19]. The blue arrow represents the molecular orientation of a single molecule, and the average orientation of molecules in the region $\mathcal{B}$ is given by the director $\mathbf{n}$. θ_m is the zenithal angle between the molecule and director, and ϕ_m is the azimuthal angle, where ν is some fixed direction normal to the director.

boundary of the sphere, $\delta\mathcal{B}^+$, and

$$\int_{\delta\mathcal{B}^+} \mathrm{dA} = \int_0^{2\pi} \int_0^{\frac{\pi}{2}} \sin\theta_m \, \mathrm{d}\theta_m \mathrm{d}\phi_m = 2\pi,$$

where ϕ_m is the azimuthal angle of a molecule and the director. For clarity, we present a diagram of these molecular angles in Figure 1.7. Therefore in the isotropic setting, the scalar order parameter is given by

$$\begin{aligned} s &= \frac{1}{4\pi} \int_{\delta\mathcal{B}^+} (3\cos^2\theta_m - 1) \, \mathrm{dA} \\ &= \frac{1}{2\pi} \int_0^{2\pi} \int_0^{\frac{\pi}{2}} (3\cos^2\theta_m - 1) \sin\theta_m \, \mathrm{d}\theta_m \, \mathrm{d}\phi_m \\ &= -\int_1^0 (3x^2 - 1) \, \mathrm{d}x = 0, \end{aligned}$$

where we have used the substitution $x = \cos\theta_m$ in the last line. Another extreme possibility, is that all of the molecules are randomly oriented in the plane perpendicular to the director. In this scenario we have $\theta_m = \frac{\pi}{2}$ and so $s = -\frac{1}{2}$.

1.3.2 Defects

Defects in a nematic liquid crystal can appear as isolated points or lines in the material. They correspond to localised regions where the average orientation of molecules can no longer be defined, and they typically present themselves as mathematical singularities in several theoretical frameworks [6]. Defects can occur as a result of a phase transition, the application of an external field, or they simply exist in equilibrium due to confinement or from the inclusion of colloidal particles [30], [40]. For the purposes of this thesis, it is useful to introduce a topological classification of point defects, which can be difficult since it depends on the topological properties of the order parameter space being used [6]. For the case of planar vector fields in 2D domains, we say that a defect has degree/topological charge k, if the director rotates k times through 2π radians as an oriented circuit around the defect [41]. Since the director is sign-invariant, this particular classification allows for both integer and half-integer degrees. The archetypal configuration of some of these defects is shown in Figure 1.8. We may classify point defects in three dimensions using the homotopy invariant Brouwer degree [42], however most of this thesis considers 2D systems or the reduced LdG setting with two degrees of freedom. Informally speaking, the Brouwer degree is the oriented number of times the image of the director field, restricted to a closed surface, covers or wraps around the unit sphere when enclosing a point defect and, in work by [43], the authors use fractional Brouwer degrees (also called *wrapping numbers*) to classify a tangent unit-vector field on three-dimensional polyhedral geometries.

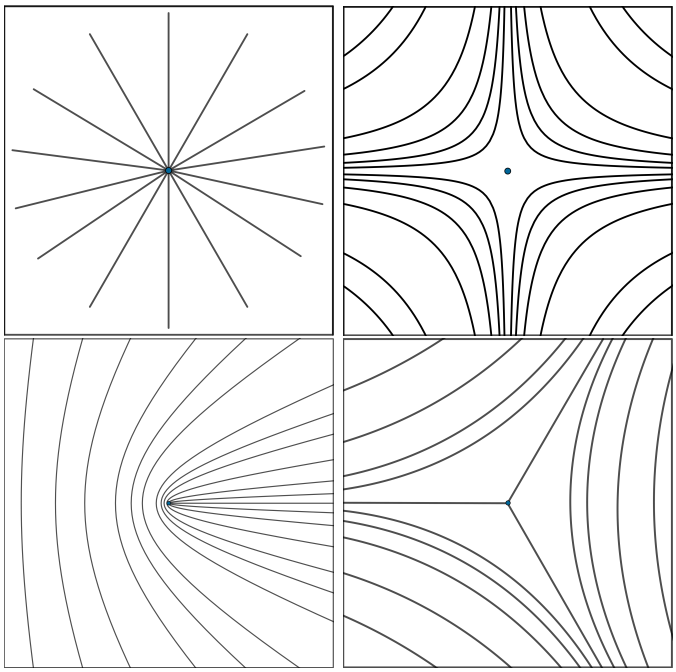

Figure 1.8: Illustrations of point defects with topological charge $+1$ (top left), -1 (top right), $+\frac{1}{2}$ (bottom left), and $-\frac{1}{2}$ (bottom right).

1.3.3 The Oseen-Frank theory

The key idea in any variational theory of nematic liquid crystals is that equilibrium configurations correspond to minimizers of some free energy functional. In the Oseen-Frank model, first proposed by Oseen [44] and later developed by Frank in 1958 [45], the total free energy of the system depends on just a single parameter - the director $\mathbf{n}$. For a uniaxial nematic sample, contained in some bounded open set $\Omega \subset \mathbb{R}^3$, the Oseen-Frank free energy is given by

$$\mathcal{F}_{OF}(\mathbf{n}) = \int_\Omega W(\mathbf{n}, \nabla \mathbf{n})\, \mathrm{d}\mathbf{x},$$

where W is the energy density

$$\begin{aligned} W(\mathbf{n}, \nabla \mathbf{n}) = {} & K_1(\nabla \cdot \mathbf{n})^2 + K_2(\mathbf{n} \cdot \nabla \times \mathbf{n})^2 + K_3(\mathbf{n} \times \nabla \times \mathbf{n})^2 \\ & + (K_2 + K_4)\nabla \cdot [(\mathbf{n} \cdot \nabla)\mathbf{n} - (\nabla \cdot \mathbf{n})\mathbf{n}]. \end{aligned} \tag{1.3.2}$$

Here, $K_1, \ldots, K_4$ are the Frank elastic constants, derived from the components of curvature, or curvature strains, obtained by considering a Taylor expansion for the components of the director, $\mathbf{n}$, about the origin [13]. These curvature strains are referred to as *splay*, *twist* an *bend*, and correspond to the elastic constants K_1, K_2 and K_3, respectively. Schematic representations of these curvature strains are shown in Figure 1.9.

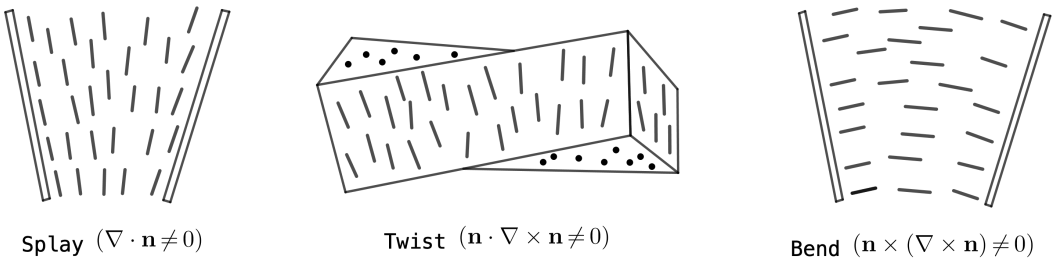

Figure 1.9: The splay, twist and bend curvature strains from the Oseen-Frank elastic energy density (1.3.2).

The last term in the elastic energy density (1.3.2) is referred to as the *saddle-splay* term, which is typically ignored in boundary value problems with prescribed strong anchoring, since its integral

$$(K_2 + K_4) \int_\Omega \nabla \cdot [(\mathbf{n} \cdot \nabla)\mathbf{n} - (\nabla \cdot \mathbf{n})\mathbf{n}] \, \mathrm{d}\mathbf{x},$$

depends only on values of $\mathbf{n}$ at the boundary, $\partial\Omega$. The elastic constants depend on temperature and, as an example, at $125°C$ the liquid crystal PAA has elastic constants

$$K_1 = 4.5 \times 10^{-12}\,\mathrm{N}, \quad K_2 = 2.9 \times 10^{-12}\,\mathrm{N}, \quad K_3 = 9.5 \times 10^{-12}\,\mathrm{N},$$

and these values typically decrease as the temperature of the system increases [13]. For analytical simplicity, the one-constant approximation of this energy functional

is often taken [46]. In this approximation, we have $K \equiv K_1 = K_2 = K_3$, $K_4 = 0$, which reduces the energy to the Dirichlet energy functional for harmonic maps given by

$$\mathcal{F}_{OF}(\mathbf{n}) = K \int_\Omega |\nabla \mathbf{n}|^2 \, \mathrm{d}\mathbf{x}.$$

This classical continuum theory is still widely used today however, it depends only on a single director and assumes a constant scalar order parameter throughout. As a result, the theory fails to predict the isotropic-nematic phase transition, biaxial nematic phases, and several classes of defects.

1.3.4 The Ericksen theory

Since not all defects can be accounted for within the Oseen-Frank framework, this inspired Jerald Ericksen to formulate a modified continuum theory for uniaxial nematics in 1991 [47]. Here, the free energy functional is designed to depend on both the director, $\mathbf{n}$, and the scalar order parameter, s, given by (1.3.1). The one-constant approximation of this energy can be written as:

$$\mathcal{F}_E[s, \mathbf{n}] = \int_\Omega k_{el}|\nabla s|^2 + s^2|\nabla \mathbf{n}|^2 + f_b(s) \, \mathrm{d}\mathbf{x},$$

where k_{el} is some elastic constant, and f_b is a bulk potential chosen to encapsulate the phase transition behaviour of the system. We will clarify the details of a suitable bulk potential in Section 1.4.2. The key idea of this theory is that the scalar order parameter, s, vanishes in regions where the director, $\mathbf{n}$, can no longer be defined, and so defects may be modelled by regions of the material where the molecular orientation is completely disordered, as in an isotropic fluid. This mathematical framework, allows for line defects (or disclinations) and two-

dimensional point defects, and can effectively model phase transitions from an isotropic fluid to a uniaxial nematic phase. However, it is not able to sufficiently describe biaxial nematic phases, for which a more sophisticated continuum theory is required.

1.4 The Landau-de Gennes theory

A biaxial nematic phase has no axis of rotational symmetry, as in a uniaxial phase, and two scalar order parameters are required to describe the degree of orientational order in the system [19]. For this reason, both the classical Oseen-Frank theory, and Ericksen theory for nematic liquid crystals, will be insufficient at accurately modelling a biaxial phase and transitions between biaxial, uniaxial and isotropic phases. We only consider calamitic or discotic molecules with only one molecular axis, but for a detailed description of the associated continuum theory involving plank-like molecules with two molecular axes, we refer the reader to the work by Sonnet & Virga [48].

1.4.1 The de Gennes Q-tensor

In our derivation of the scalar order parameter (1.3.1), we considered a probability distribution function of the angle between each molecule and the average molecular orientation within a small region. Following the approach in [49], we will now consider the probability distribution function, $\rho(\mathbf{x}, \mathbf{p})$, of the molecular orientations themselves. This distribution represents the probability of a randomly chosen molecule in the region $\mathcal{B}(\mathbf{x}, \delta)$ having an orientation given by the vector $\mathbf{p} \in S^2$ (where S^2 is the unit sphere). Since $\mathbf{p}$ and $-\mathbf{p}$ are equivalent, we

have that ρ satisfies the following properties:

$$\rho(\mathbf{x},\mathbf{p}) \geq 0, \quad \int_{S^2} \rho(\mathbf{x},\mathbf{p})\,\mathrm{d}\mathbf{p} = 1, \quad \rho(\mathbf{x},\mathbf{p}) = \rho(\mathbf{x},-\mathbf{p}).$$

Now consider the finite moments of the probability measure $\mathbf{p}$. We see that the first moment, $\int_{S^2} \mathbf{p}\,\rho(\mathbf{x},\mathbf{p})\,\mathrm{d}\mathbf{p}$, vanishes and we denote the second moment by the following symmetric second-order tensor:

$$\mathbf{M}(\mathbf{x}) = \int_{S^2} \mathbf{p}\otimes\mathbf{p}\,\rho(\mathbf{x},\mathbf{p})\,\mathrm{d}\mathbf{p},$$

where the tensor product is defined by the relation $(\mathbf{a}\otimes\mathbf{b})_{ij} = a_i b_j$, $i,j = 1,2,3$, for arbitrary vectors $\mathbf{a} = (a_1,a_2,a_3)$ and $\mathbf{b} = (b_1,b_2,b_3)$. The *de Gennes* $\mathbf{Q}$-*tensor* is defined as

$$\mathbf{Q}(\mathbf{x}) = \mathbf{M}(\mathbf{x}) - \frac{1}{3}\mathbf{I}, \tag{1.4.1}$$

and is a measure of the deviation of $\mathbf{M}$ from its isotropic value. It follows that $\mathbf{Q}$ is a traceless, symmetric 3×3 matrix i.e., $\mathbf{Q}\in\mathcal{S}_0$ where,

$$\mathcal{S}_0 = \{\mathbf{Q}\in M^{3\times 3} : \mathbf{Q} = \mathbf{Q}^T,\ \mathrm{tr}\mathbf{Q} = 0\}.$$

We note that $\mathcal{S}_0$ is a five-dimensional subspace of the space of 3×3 matrices and, as we will describe in more detail, the de Gennes $\mathbf{Q}$-tensor (1.4.1) carries sufficient information to describe the two directors, and two scalar order parameters, of a biaxial nematic phase. The $\mathbf{Q}$-tensor may be expressed in terms of its eigenvalues, $\{\lambda_i\}_{i=1}^3$, and its eigenvectors, $\{\mathbf{n}_i\}_{i=1}^3$,

$$\mathbf{Q} = \lambda_1\mathbf{n}_1\otimes\mathbf{n}_1 + \lambda_2\mathbf{n}_2\otimes\mathbf{n}_2 + \lambda_3\mathbf{n}_3\otimes\mathbf{n}_3. \tag{1.4.2}$$

However, since $\mathbf{Q}$ is traceless, we must have that $\lambda_1 + \lambda_2 + \lambda_3 = 0$, and since $\sum_{i=1}^{3} \mathbf{n}_i \otimes \mathbf{n}_i = \mathbf{I}_3$, we have that

$$\mathbf{Q} = (2\lambda_1 + \lambda_2)\mathbf{n}_1 \otimes \mathbf{n}_1 + (2\lambda_2 + \lambda_1)\mathbf{n}_2 \otimes \mathbf{n}_2 - (\lambda_1 + \lambda_2)\mathbf{I}_3.$$

We say that the $\mathbf{Q}$-tensor is *isotropic* if all its eigenvalues are equal and, by the tracelessness of $\mathbf{Q}$, we have that $\mathbf{Q} = \mathbf{0}$. The $\mathbf{Q}$-tensor is *uniaxial* if it has a pair of degenerate non-zero eigenvalues, in which case it may be written as [50]

$$\mathbf{Q} = s\left(\mathbf{n} \otimes \mathbf{n} - \frac{1}{3}\mathbf{I}\right), \tag{1.4.3}$$

where $s \in \mathbb{R}$ is the scalar order parameter and $\mathbf{n} \in S^2$ is the director, corresponding to the associated non-degenerate eigenvalue, which labels the distinct direction of uniaxial nematic alignment. Lastly, the $\mathbf{Q}$-tensor is *biaxial* if it has three distinct eigenvalues, in which case it can be written as

$$\mathbf{Q} = s\left(\mathbf{n} \otimes \mathbf{n} - \frac{1}{3}\mathbf{I}\right) + r\left(\mathbf{m} \otimes \mathbf{m} - \frac{1}{3}\mathbf{I}\right),$$

for unit-length eigenvectors $\mathbf{n}, \mathbf{m} \in S^2$, with $\mathbf{n}\cdot\mathbf{m} = 0$, and scalar order parameters $s, r \in \mathbb{R}$, which represent the two preferred directions of molecular alignment in a biaxial nematic liquid crystal, and the degree of orientational order about these directions, respectively.

We are now prepared to introduce the Landau-de Gennes continuum theory of nematic liquid crystals, which relies on the $\mathbf{Q}$-tensor order parameter (1.4.1) [9]. Suppose we have a sample of nematic liquid crystal, contained in an open bounded set $\Omega \subset \mathbb{R}^3$ with smooth boundary, $\partial\Omega$. The total free energy of the sample is given by

$$\mathcal{F} = \int_{\Omega} (f_{el} + f_b + f_{em})\,\mathrm{dV} + \int_{\partial\Omega} (f_s)\,\mathrm{dS},$$

where the energy densities, f_{el}, f_b, f_{em} and f_s, represent the energy potentials of elastic distortions, thermotropic contributions, externally applied electromagnetic fields, and surface interactions, respectively. Surface anchoring conditions may be broadly classified into two regimes: *strong anchoring* and *weak anchoring* [6]. Strong anchoring conditions, typically referred to as Dirichlet boundary conditions, encapsulate scenarios where the forces on the boundary are strong enough to essentially prescribe a value for the order parameter at the surface, that is,

$$\mathbf{Q} = \mathbf{Q}_b, \qquad \text{on} \quad \partial\Omega. \tag{1.4.4}$$

In this case, the surface energy contributions are so dominant in the free energy that we may reduce this minimization problem to the case where $f_s = 0$. When modelling a weak anchoring condition, we have $f_s \neq 0$. This surface energy is introduced to give a preference for the director orientation along the boundary, which may vary under the application of external fields [19]. One typical surface energy density used in the $\mathbf{Q}$-tensor framework is the Rapini-Papoular surface energy [51]

$$f_s^{(i)}(\mathbf{Q}) = \frac{w^{(i)}}{2}\mathrm{tr}(\mathbf{Q} - \mathbf{Q}_s^{(i)})^2, \tag{1.4.5}$$

which imposes a preferred orientation, determined by $\mathbf{Q}_s^{(i)}$, on the i^{th} lateral surface. The $w^{(i)}$ are the anchoring coefficients, which dictate the strength of surface anchoring [52]. For the purposes of this thesis, we will disregard externally applied electric/magnetic fields, but for an excellent review of how these terms contribute to the $\mathbf{Q}$-tensor model, see [9] and [19].

1.4.2 Thermotropic contributions

The bulk thermotropic term, f_b, essentially dictates which liquid crystalline state we are in. By design, this energy potential is minimized by the isotropic state, $\mathbf{Q} = \mathbf{0}$, at high enough temperatures. The simplest form of f_b that allows for a first-order nematic-isotropic phase transition is a truncated Taylor series in $\mathbf{Q}$ about the isotropic state i.e., the following quartic polynomial in the invariants of $\mathbf{Q}$:

$$f_b(\mathbf{Q}) = \frac{A}{2}\mathrm{tr}\mathbf{Q}^2 - \frac{B}{3}\mathrm{tr}\mathbf{Q}^3 + \frac{C}{4}(\mathrm{tr}\mathbf{Q}^2)^2. \tag{1.4.6}$$

For clarity, we denote $\mathrm{tr}\mathbf{Q}^2 = Q_{ij}Q_{ij}$, and $\mathrm{tr}\mathbf{Q}^3 = Q_{ij}Q_{jk}Q_{ki}$, where the Einstein summation convention is to be assumed, and Q_{ij} corresponds to the ij^{th} component of the tensor $\mathbf{Q}$. The parameter A is approximated to be linear in temperature i.e., $A = \alpha(T - T^*)$, where $\alpha > 0$ is a material-dependent constant, T is the absolute temperature of the system, and T^* represents the characteristic nematic supercooling temperature, at which the isotropic state becomes unstable. The other parameters $B, C > 0$ are to be considered material-dependent constants. We repeat an important result from [50], and its proof, concerning minimizers of the thermotropic bulk energy contribution (1.4.6).

Proposition 1.4.1. *[50] The bulk energy density defined by (1.4.6) attains its minimum for either the isotropic state, or a continuum of uniaxial* $\mathbf{Q}$*-tensors of the form*

$$\mathbf{Q}_u = s_+\left(\mathbf{n}\otimes\mathbf{n} - \frac{1}{3}\mathbf{I}\right), \tag{1.4.7}$$

where $\mathbf{n} \in S^2$ *is a unit eigenvector of* $\mathbf{Q}$ *and*

$$s_+ = \frac{B + \sqrt{B^2 - 24AC}}{4C}. \tag{1.4.8}$$

Proof. We recall that for a symmetric, traceless matrix $\mathbf{Q}$-tensor of the form (1.4.2), we have that $\mathrm{tr}\mathbf{Q}^n = \sum_{i=1}^3 \lambda_i^n$, subject to the tracelessness condition $\lambda_1 + \lambda_2 + \lambda_3 = 0$. Therefore, the thermotropic bulk energy density, f_b, only depends on the eigenvalues $\lambda_1, \lambda_2, \lambda_3$, and the stationary points of f_b are given by the stationary points of the function $f : \mathbb{R}^3 \to \mathbb{R}$ defined by

$$f(\lambda_1, \lambda_2, \lambda_3) := \frac{A}{2}\sum_{i=1}^3 \lambda_i^2 - \frac{B}{3}\sum_{i=1}^3 \lambda_i^3 + \frac{C}{4}\left(\sum_{i=1}^3 \lambda_i^2\right)^2 - 2\delta\sum_{i=1}^3 \lambda_i.$$

Here we have recast f_b in terms of the eigenvalues of $\mathbf{Q}$, and introduced a Lagrange multiplier δ to account for the tracelessness constraint. The stationary points of f_b then satisfy the following system of algebraic equations:

$$\frac{\partial f}{\partial \lambda_i} = 0 \iff A\lambda_i - B\lambda_i^2 + C\left(\sum_{k=1}^3 \lambda_k^2\right)\lambda_i = 2\delta, \quad i = 1, 2, 3, \tag{1.4.9}$$

or equivalently,

$$(\lambda_i - \lambda_j)\left[A - B(\lambda_i + \lambda_j) + C\sum_{k=1}^3 \lambda_k^2\right] = 0, \quad 1 \le i < j \le 3. \tag{1.4.10}$$

Suppose, for a contradiction, we let $\{\lambda_i\}$ be a solution of the system (4.2.10) with three distinct eigenvalues $\lambda_1 \neq \lambda_2 \neq \lambda_3$ i.e., f_b is minimized by a biaxial $\mathbf{Q}$-tensor. Without loss of generality, we consider equation (1.4.10) for the pairs (λ_1, λ_2) and (λ_1, λ_3). This yields two equations:

$$A - B(\lambda_1 + \lambda_2) + C\sum_{k=1}^3 \lambda_k^2 = 0,$$
$$A - B(\lambda_1 + \lambda_3) + C\sum_{k=1}^3 \lambda_k^2 = 0,$$

from which we obtain

$$-B(\lambda_2 - \lambda_3) = 0,$$

contradicting our initial hypothesis $\lambda_2 \neq \lambda_3$. We thus conclude that a stationary point f_b must have at least two equal eigenvalues, and therefore correspond to either a uniaxial or isotropic liquid crystal state. Without loss of generality, we consider an arbitrary uniaxial state given by $(\lambda_1, \lambda_2, \lambda_3) = \left(\frac{2s}{3}, -\frac{s}{3}, -\frac{s}{3}\right)$. The corresponding $\mathbf{Q}$-tensor is

$$\mathbf{Q} = s\left(\mathbf{e}_1 \otimes \mathbf{e}_1 - \frac{1}{3}\mathbf{I}\right).$$

The function f_b is then a quartic polynomial in the order parameter s, that is

$$f_b(s) = \frac{s^2}{27}(9A - 2Bs + 3Cs^2),$$

and the stationary points are solutions of the algebraic equation

$$\frac{df_b}{ds} = 0 \iff \frac{2As}{3} - \frac{2Bs^2}{9} + \frac{4Cs^3}{9} = 0.$$

This cubic equation admits three solutions:

$$s = 0, \quad \text{and} \quad s_\pm = \frac{B \pm \sqrt{B^2 - 24AC}}{4C},$$

where

$$f_b(0) = 0, \quad \text{and} \quad f_b(s_\pm) = \frac{s_\pm^2}{54}(9A - Bs_\pm),$$

and so $f_b(s_-) > f_b(s_+)$. Symmetry considerations show that we obtain the same set of stationary points for the remaining choices of eigenvalues. The global minimizer is therefore either the isotropic state $\mathbf{Q} = 0$, or an ordered nematic state of the form (1.4.3), where $s = s_+$. □

We may check the stability of this family of stationary points by computing $\frac{d^2 f_b}{ds^2}$. We see that the isotropic state, $s = 0$, is globally stable for $A > \frac{B^2}{27C}$, metastable for $0 < A < \frac{B^2}{27C}$, and unstable for $A < 0$. The nematic state, $s = s_+$, is globally

stable for $A < \frac{B^2}{27C}$, metastable for $\frac{B^2}{27C} < A < \frac{B^2}{24C}$, and undefined for $A > \frac{B^2}{24C}$. The $s = s_-$ state is metastable for $A < 0$, unstable for $0 < A < \frac{B^2}{24C}$, and undefined for $A > \frac{B^2}{24C}$. In summary there are 3 distinct temperature regimes for the variable A:

- $A = 0$, below which the isotropic state loses its stability. This is commonly referred to as the *nematic supercooling temperature*.
- $A = \frac{B^2}{27C}$, at which both the nematic state and isotropic state have equal energies ($f_b(s_+) = f_b(0)$). This represents the *nematic-isotropic transition temperature*.
- $A = \frac{B^2}{24C}$, above which the nematic states, $s_\pm$, are no longer defined and we refer to this as the *nematic superheating temperature*.

We present a plot of f_b as a function of the scalar order parameter s, for different values of A, in Figure 1.10. Here we take $B = 0.64 \times 10^4\,\mathrm{Nm}^{-2}$, $C = 0.35 \times 10^4\,\mathrm{Nm}^{-2}$ - typical values for the liquid crystal MBBA [8].

1.4.3 Elastic contributions

Liquid crystalline materials are anisotropic in their nature, and hence elicit a directionally-dependent response to elastic deformations [16]. The elastic energy density, f_{el} in the total free energy, penalises any spatial inhomogeneities in the system, and is composed of quadratic functions in $\nabla\mathbf{Q}$. That is,

$$\begin{aligned} f_{el}(\mathbf{Q}, \nabla\mathbf{Q}) =& \frac{L_1}{2} Q_{ij,k} Q_{ij,k} + \frac{L_2}{2} Q_{ij,j} Q_{ik,k} + \frac{L_3}{2} Q_{ik,j} Q_{ij,k} \\ &+ \frac{L_4}{2} \epsilon_{ijk} Q_{il} Q_{jl,k} + \frac{L_5}{2} Q_{lk} Q_{ij,l} Q_{ij,k}, \end{aligned}$$

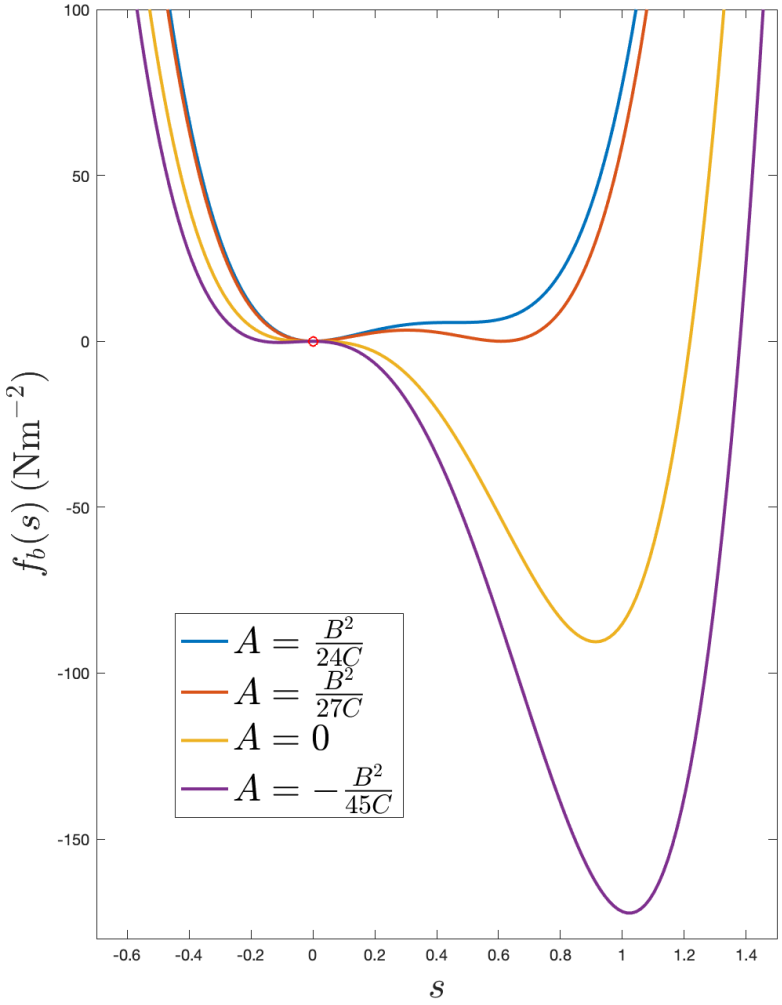

Figure 1.10: Plots of the thermotropic bulk energy density, f_b, as a function of the scalar order parameter, s, for various temperature regimes. The red circle represents the isotropic state, $s = 0$.

where $Q_{ij,k} = \frac{\partial Q_{ij}}{\partial x_k}$ for $i, j, k = 1, 2, 3$, and where the Einstein summation convention is to be assumed [53]. The $L_1, \ldots, L_5$ are material-dependent elastic constants which are related to the Frank elastic constants from (1.3.2). The fourth term accounts for any molecular chirality in the system and so for nematic liquid crystals we have $L_4 = 0$. The last term is one of several potential cubic

terms that can effectively model any broken symmetry of the K_1 and K_3 Frank elastic constants [54]. Furthermore, the difference of the second and third elastic terms, $Q_{ij,j}Q_{ik,k} - Q_{ik,j}Q_{ij,k}$, is a null lagrangian and so, for simplicity, we will only be considering the first two elastic terms i.e., $L_3 = L_4 = L_5 = 0$. The case where $L_i = 0$, for $i = 2, \ldots, 5$, is referred to as the one-constant approximation of the elastic energy density. For clarity, $\mathbf{Q}$-tensors in the space $\mathcal{S}_0$ have the corresponding matrix norm $|\mathbf{Q}|^2 = \mathrm{tr}\mathbf{Q}^2 = Q_{ij}Q_{ij}$, $i, j = 1, 2, 3$ and hence, the one-constant approximation of the elastic energy density can be written as $L|\nabla\mathbf{Q}|^2$.

1.4.4 The biaxiality parameter

In confined systems, localized regions of biaxiality within the liquid crystal sample can arise, especially in the vicinity of defects. For this reason, it is useful to utilize a measure of the degree of biaxiality, which will also be key in proving some results in this thesis. We define the biaxiality parameter, β^2, as in [55] and [40]:

$$\beta^2 := 1 - 6\frac{(\mathrm{tr}\mathbf{Q}^3)^2}{(\mathrm{tr}\mathbf{Q}^2)^3}. \tag{1.4.11}$$

It was shown in [56] that, for any $\mathbf{Q} \in \mathcal{S}_0 \setminus \{\mathbf{0}\}$, the biaxiality parameter (1.4.11) takes values in the interval $[0, 1]$, where $\beta^2 = 1$ corresponds to a state of maximum biaxiality if, and only if, one eigenvalue of $\mathbf{Q}$ vanishes, and $\beta^2 = 0$ for all uniaxial states of the form (1.4.3). Moreover, for any $\mathbf{Q} \in \mathcal{S}_0$, the following inequality holds:

$$-\frac{|\mathbf{Q}|^3}{\sqrt{6}}\left(1 - \frac{\beta^2}{2}\right) \leq \mathrm{tr}\mathbf{Q}^3 \leq \frac{|\mathbf{Q}|^3}{\sqrt{6}}\left(1 - \frac{\beta^2}{2}\right). \tag{1.4.12}$$

1.4.5 Results on minimizers

Throughout this thesis, we consider the equilibrium configurations of a nematic liquid crystal in confinement in the Landau-de Gennes theory. In this brief section, we reproduce some of the key results concerning minimizers of the one-constant approximation of the Landau-de Gennes energy functional in the absence of external electromagnetic fields and surface energies, $\mathcal{F}_{LG}$, given by

$$\mathcal{F}_{LG}[\mathbf{Q}] = \int_\Omega \frac{L}{2}|\nabla \mathbf{Q}|^2 + f_b(\mathbf{Q})\,\mathrm{dV}. \tag{1.4.13}$$

Confined nematic systems evolve to a configuration that minimizes the LdG free energy (1.4.13) i.e., $\mathcal{F}_{LG}$ will be a minimum when the system is in equilibrium. To this end, we consider the minimization problem of $\mathcal{F}_{LG}$ with respect to the tensor order parameter $\mathbf{Q}$. We choose Dirichlet boundary conditions (1.4.4) such that the thermotropic bulk potential is minimized along the boundary i.e., $\mathbf{Q}_b$ is of the form (1.4.7). We define our admissible space to be

$$\mathcal{A} := \{\mathbf{Q} \in W^{1,2}(\Omega; \mathcal{S}_0) : \mathbf{Q} = \mathbf{Q}_b \ \text{ on } \ \partial\Omega\}, \tag{1.4.14}$$

where the Sobolev space $W^{1,2}(\Omega; \mathcal{S}_0)$ is given by

$$W^{1,2}(\Omega; \mathcal{S}_0) = \left\{\mathbf{Q} \in \mathcal{S}_0 : \int_\Omega |\nabla \mathbf{Q}|^2 + |\mathbf{Q}|^2\,\mathrm{dV} < \infty\right\},$$

which is equipped with the following inner product:

$$(\mathbf{Q}, \mathbf{P})_{W^{1,2}(\Omega)} := \int_\Omega \{Q_{ij}P_{ij} + Q_{ij,k}P_{ij,k}\}\,\mathrm{dV}, \qquad i,j,k = 1,2,3;$$

and norm and seminorm, respectively

$$||\mathbf{Q}||^2_{W^{1,2}(\Omega)} := (\mathbf{Q}, \mathbf{Q}), \qquad |\mathbf{Q}|^2_{W^{1,2}(\Omega)} := \int_\Omega Q_{ij,k}Q_{ij,k}\,\mathrm{dV} = \int_\Omega |\nabla \mathbf{Q}|^2\,\mathrm{dV}.$$

The existence of a global minimizer of $\mathcal{F}_{LG}$, over the admissible space $\mathcal{A}$, is an immediate consequence from the direct methods in the calculus of variations [57]. Since the elastic energy density is convex in $\nabla\mathbf{Q}$, then we have that $\mathcal{F}_{LG}$ is weakly lower semi-continuous. That is,

$$\liminf_{n\to\infty} \mathcal{F}_{LG}[\mathbf{Q}_n] \geq \mathcal{F}_{LG}[\mathbf{Q}]$$

for all sequences $\mathbf{Q}_n$ weakly converging to $\mathbf{Q}$ in $W^{1,2}(\Omega)$ i.e., $(\mathbf{Q}_n, \phi)_{W^{1,2}(\Omega)} \to (\mathbf{Q}, \phi)_{W^{1,2}(\Omega)}$ for all $\phi \in W^{1,2}(\Omega)$. Furthermore, from (1.4.2), the bulk energy density f_b is bounded from below by some constant depending only on the material parameters A, B and C, hence $\mathcal{F}_{LG}$ is coercive over $\mathcal{A}$. That is,

$$\mathcal{F}_{LG}[\mathbf{Q}] \geq C_1||\mathbf{Q}||_{W^{1,2}(\Omega)} + C_2$$

for all $\mathbf{Q} \in \mathcal{A}$, and constants $C_1 > 0$ and $C_2 \in \mathbb{R}$. Furthermore, any critical point of the rescaled functional (1.4.13) in the admissible space (1.4.14) will satisfy the following Euler-Lagrange equations:

$$L\Delta\mathbf{Q} = A\mathbf{Q} - B\left(\mathbf{Q}\mathbf{Q} - \frac{\mathbf{I}}{3}|\mathbf{Q}|^2\right) + C|\mathbf{Q}|^2\mathbf{Q}, \tag{1.4.15}$$

which comprises of a system of up to five coupled partial differential equations. From Proposition 13 in [50], solutions of the Euler-Lagrange equations (1.4.15) are real analytic in Ω. For completeness, we now reproduce an important result, and its proof, from [56] and [50].

Proposition 1.4.2. *Suppose* $\mathbf{Q}$ *is a global minimizer of the LdG energy functional* $\mathcal{F}_{LG}$*, in the admissible space* $\mathcal{A}$*. Then we have the following a priori* L^∞ *bounds, independent of the elastic constant* L*:*

$$||\mathbf{Q}||_{L^\infty(\Omega)} = \operatorname*{ess\,sup}_{\mathbf{x}\in\Omega} |\mathbf{Q}(\mathbf{x})| \leq \sqrt{\frac{2}{3}} s_+ =: M(A, B, C),$$

where s_+ is defined in (1.4.8).

Proof. Suppose for a contradiction, that there exists some point $\mathbf{x}^* \in \bar{\Omega}$, where $|\mathbf{Q}|$ achieves its maximum, and $|\mathbf{Q}(\mathbf{x}^*)| > \sqrt{\frac{2}{3}}s_+$. The function $|\mathbf{Q}|^2 : \bar{\Omega} \to \mathbb{R}$ attains its maximum at the point $\mathbf{x}^* \in \Omega$, and hence

$$\Delta\left(\frac{1}{2}|\mathbf{Q}|^2\right)(\mathbf{x}^*) \leq 0. \tag{1.4.16}$$

Multiplying both sides of the Euler-Lagrange equations (1.4.15) by $\mathbf{Q}$, and using the inequality $\mathrm{tr}\mathbf{Q}^3 \leq \frac{|\mathbf{Q}|^3}{\sqrt{6}}$ in (1.4.12), we have that

$$\begin{aligned} L\Delta\left(\frac{1}{2}|\mathbf{Q}|^2\right) &= A\mathrm{tr}\mathbf{Q}^2 - B\mathrm{tr}\mathbf{Q}^3 + C(\mathrm{tr}\mathbf{Q}^2)^2 + L|\nabla\mathbf{Q}|^2 \\ &\geq A\mathrm{tr}\mathbf{Q}^2 - B\mathrm{tr}\mathbf{Q}^3 + C(\mathrm{tr}\mathbf{Q}^2)^2 \\ &\geq A|\mathbf{Q}|^2 - \frac{B}{\sqrt{6}}|\mathbf{Q}|^3 + C|\mathbf{Q}|^4 \\ &> 0 \end{aligned}$$

when $|\mathbf{Q}| > \sqrt{\frac{2}{3}}s_+$. This yields $\Delta\left(\frac{1}{2}|\mathbf{Q}|^2\right)(\mathbf{x}) > 0$, for all interior points $\mathbf{x} \in \Omega$, whenever $|\mathbf{Q}(\mathbf{x})| > \sqrt{\frac{2}{3}}s_+$, contradicting the statement in (1.4.16). □

1.5 Thesis outline

In Chapter 2, we review the relevant literature and motivate the topics addressed in this thesis.

In Chapter 3, we study nematic equilibria confined to three-dimensional square wells, given planar degenerate Dirichlet conditions on the lateral surfaces. We focus on the Well Order Reconstruction Solution (WORS), as a function of the well-size λ, and the well height ϵ. The WORS are distinctive equilibria reported in

[52] for square domains, without taking the third dimension into account, which have two mutually perpendicular defect lines running along the square diagonals, intersecting at the square centre. Firstly, assuming natural boundary conditions on the top and bottom surfaces and secondly, with realistic surface energies, we prove the existence of a general class of nematic equilibria (including the WORS) in three dimensions, for arbitrary well heights, and for temperatures below the nematic supercooling temperature. We show in both cases, that the WORS is globally stable for λ small enough, and unstable as λ increases.

In Chapter 4, we complement the analysis of three-dimensional nematic equilibria with numerical simulations using an energy-minimization based approach. We numerically compute novel mixed 3D solutions for large λ and ϵ, followed by a numerical investigation of the effects of surface anchoring on the WORS. These simulations are then extended to rectangular three-dimensional domains, where we study the effects of the confining geometrical aspect ratio, δ, as well as λ and ϵ on the (numerical) stability of equilibrium configurations.

In Chapter 5, we consider a two-term elastic energy density in the Landau-de Gennes framework, where the degree of 'elastic anisotropy' is given by the rescaled elastic constant L_2. We study nematic equilibria in two-dimensional square wells, with tangent Dirichlet boundary conditions, as a function of the well cross-sectional size λ, and L_2. We prove that, for λ small enough, there exists a unique global minimizer of the Landau-de Gennes energy. For $L_2 = 0$, we simply recover the WORS. For $L_2 \neq 0$, the solution landscape is more complex and the unique global minimizer corresponds to either: (i) the 'Ring' solution with a +1-defect at the square centre, for L_2 small enough or; (ii) a 'Constant' solution, for L_2 large enough, which is constantly uniaxial with negative scalar order parameter away from the edges of the square. We categorise the symmetries of these solutions

in the $\lambda \to 0$ limit. We also prove, in the physically relevant Oseen-Frank limit, $\lambda \to \infty$, that global minimizers converge strongly in $W^{1,2}$ to a global minimizer with constant order parameter. We also show that critical points of the Landau-de Gennes energy are stable, for L_2 larger than some critical threshold that depends on λ. This analysis is complemented by numerical simulations and several bifurcation diagrams, as a function of λ, for different values of L_2.

In Chapter 6, we study a dilute suspension of magnetic nanoparticles in a nematic host, or ferronematic, on regular two-dimensional polygons. These systems are described by the Landau-de Gennes $\mathbf{Q}$-tensor and a spontaneous magnetization, in the absence of any external fields. We study the stable states in terms of stable critical points of an appropriately defined ferronematic free energy, with a nemato-magnetic coupling energy. We numerically study the interplay between the shape of the regular polygon, the size of the polygon, and the strength of the nemato-magnetic coupling, for the multistability of this prototype system. We present the co-existence of stable states with domain walls, and stable interior and boundary defects, as well as the control of multistability through the nemato-magnetic coupling parameter.

In Chapter 7, we introduce a new methodology, based on the approach of Mihai et al. [58], [59], for stochastic elasticity. We consider a fourth-order thermotropic bulk potential (1.4.6), where the material-dependent parameter B is assumed to follow a non-Gaussian probability distribution. We then study the effects of stochasticity on the Landau-de Gennes order parameter, as a function of the temperature, by reviewing the classical bifurcation analysis of the nematic-isotropic phase transition within this new framework.

In Chapter 8, we summarize our results and discuss some open problems and

potential directions of future research based on this work.

1.6 Publication and collaboration details

Chapters 3 and 4 of thesis are joint work with Apala Majumdar, Giacomo Canevari and Yiwei Wang, which has been published in the International Journal of Nonlinear Mechanics as reference [1]. The code used in Chapter 4 was produced by Yiwei Wang and edited and implemented by the author.

Chapter 5 in this thesis is joint work with Apala Majumdar, Yucen Han and Lei Zhang, which has been submitted to the SIAM Journal on Mathematical Analysis, and with arxiv submission as reference [2].

Chapter 6 is joint work with Apala Majumdar, Yucen Han and Joshua Walton, which has been published in Physical Review E as reference [3]. The bifurcation diagrams and code for the stability checks in Chapter 5 and 6 were produced by Dr Yucen Han, with the stability checks being implemented by the author.

The bifurcation diagrams seen in Chapter 7 are a result of important collaboration with Angela Mihai and Thomas Woolley.

Chapter 2

Literature review

2.1 The planar bistable nematic device

Chapters 3 – 6 of this thesis are motivated by the bistable system reported in Tsakonas et al. [60]. Here, the authors experimentally, and numerically, study nematic liquid crystals (NLCs) inside a periodic array of shallow micron-sized wells, with a square cross-section. The height of these square wells, and hence the thickness of the NLC sample, was kept small enough to induce planar alignment of the nematic director. The surfaces of these wells were treated in order to induce planar degenerate molecular alignment on the lateral surfaces. We include a simple schematic of this device in Figure 2.1. A similar system was studied in Luo et al. [61], and then later Kralj and Majumdar [52], within the continuum Landau-de Gennes (LdG) theory for NLCs. Within this theory, experimentally observable states can be modelled by local or global minimizers of an appropriately defined LdG free energy. It is assumed that the well height is typically much smaller than the square cross-sectional length. In other words, the authors speculate that

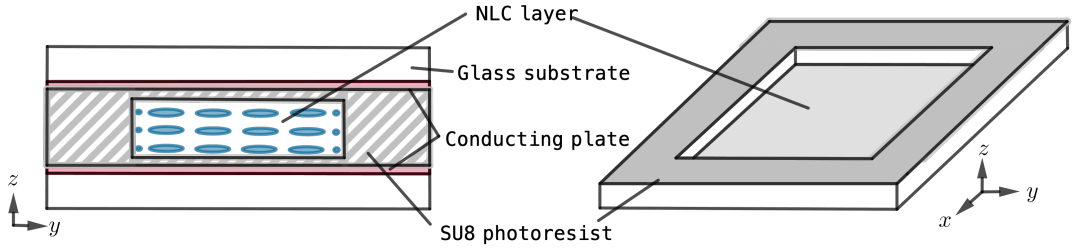

Figure 2.1: Side view and perspective view of the planar bistable nematic device. Adapted from [60].

the structural characteristics only vary in the plane of the square cross-section, and are translationally invariant along the height of the well, effectively reducing this to a two-dimensional (2D) problem. Hence, the authors restrict attention to the bottom square cross-section of the well geometry. They impose tangent boundary conditions (TBCs) on the well surfaces, consistent with the surface treatment of the well array i.e., the nematic directors, in the plane of the well surfaces, are constrained to be tangent to those well surfaces. More specifically, TBCs in their setup refer to planar degenerate anchoring on the well surfaces where the azimuthal anchoring in the plane of the square domain is free and there is no polar anchoring since the nematic molecules lie in the plane of these surfaces. However, this necessarily means that the nematic director has to be tangent to the square edges, creating defects at the connecting square vertices, where the director is not defined. In [61], the authors report a bistable configuration that exhibits six different equilibrium profiles. These profiles may be classified into two optically contrasting states: the *diagonal* (D) state, for which there are two, where the nematic director lies along one of the square diagonals; and the *rotated* (R) state, for which there are four, where the director rotates by π radians between a pair of parallel square edges. The authors also include a Rapini-Papoular surface

energy term, and study the multiplicity of solutions as a function of the anchoring strength. In [52], the authors study the nematic equilibria as a function of the square size (in terms of the biaxial correlation length). For micron-sized squares, the authors recover the D and R solutions, within a continuum LdG approach. It was shown that, for small enough wells (on the nano-scale), a unique pattern emerges with two mutually perpendicular defect lines, which emanate from the square vertices. Coined the Well Order Reconstruction Solution (WORS), this solution exhibits a constant set of eigenvectors, and is distinguished by a uniaxial cross with negative scalar order parameter, along the square diagonals. This can be physically interpreted as a nematic sample with preferred in-plane molecular orientation, as well as locally disordered molecules in the plane along the defect lines. These defect lines intersect at the centre of the square, partitioning the well into four quadrants, with approximately constant director profiles in each. Indeed, we speculate that this distinctive defect line could be a special optical feature of the WORS, if experimentally realised. For clarity, we plot the typical director profile of the diagonal, and rotated states, as well as the WORS, in Figure 2.2.

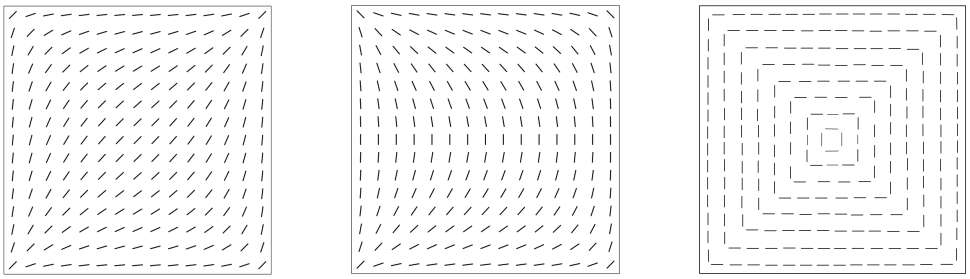

Figure 2.2: The director orientation of a diagonal (D) solution, rotated (R) solution and WORS.

The WORS was further analysed for a special temperature in Canevari et al. [62], in terms of solutions of the Allen-Cahn equation, and again in Wang et al. [63], for square domains with an isotropic inclusion. It is rigorously proven that the WORS is globally stable for sufficiently small squares i.e., for nano-scale

geometries.

Although the WORS has been proven to exist in molecular simulations by Robinson et al. [64], a possible criticism is that the WORS has not been studied in three-dimensional (3D) geometries with a finite height and thus, could just be an artefact of the 2D square domain. In Chapter 3, we address the important question - does the WORS survive in a 3D square box? We show that yes it does, and we identify two physically relevant 3D scenarios for which the WORS exists, for all values of the well height, and for all temperatures below the nematic supercooling temperature i.e., for temperatures that favour a bulk ordered nematic phase.

In Chapter 3, we study nematic equilibria within confining geometries on the nano-scale. NLC systems of this size are often difficult to study experimentally. Moreover, the governing Euler-Lagrange equations of the LdG free energy in three dimensions correspond to up to five nonlinear coupled partial differential equations, which makes this a hard mathematical problem to solve analytically. This motivates a numerical approach to studying this system, which is the aim of Chapter 4. In Canevari et al. [62], the authors numerically solve the gradient flow model for nematodynamics, in a 2D LdG framework. In this numerical scheme, the dynamic solutions evolve along a path of decreasing energy, yielding a stable equilibrium configuration, if a sufficiently good initial guess is chosen. They show numerically that, for $A < 0$, the WORS is the unique LdG critical point in a 2D square, for sufficiently small well size, λ. In Wang et al. [63], the authors numerically solve a similar system in a 2D square domain, by computing solutions of the associated Euler-Lagrange system using standard finite difference methods, and Newton's method. They also numerically check the stability of these solutions by minimizing the second variation of the LdG free energy, and they find two

'escaped' configurations, where the leading eigenvector of the solution escapes into the third dimension around a small isotropic inclusion, with a topological strength ± 1. 3D NLC systems are much harder to solve numerically. In Chapter 4, we employ the energy-minimization based numerical scheme from Wang, Zhang and Chen [65], where the authors compute numerical solutions of the LdG free energy, under the one-constant approximation, for systems of single and double spherical colloidal particles immersed in a uniformly aligned NLC host. This numerical scheme utilises the limited memory Broyden-Fletcher-Goldfarb-Shanno (L-BFGS) algorithm, which is a type of quasi-Newton method, and is sufficient for our 3D problem. The (numerical) local stability of solutions in [65], and in Robinson et al. [64], is justified by checking the sign of the smallest eigenvalue associated with the Hessian of the LdG free energy. We make similar justifications for numerical stability in Chapters 4 – 6. In Chapter 4 specifically, we assess this quantity using an optimization-based shrinking dimer method from Yin and Zhang [66], which minimizes one Rayleigh quotient simultaneously using gradient flow. A high index optimization-based shrinking dimer method was also used in Yin et al. [67], to compute the full solution landscape for the 2D square problem, as a function of the square cross-sectional size.

We complement this numerical study by computing nematic equilibria in 3D rectangular wells with tangent boundary conditions, employing the same energy-minimization based numerical scheme as for the 3D square wells. In Lewis et al. [68], the authors study micron-sized rectangular wells within a two-dimensional Oseen-Frank framework, with tangent boundary conditions. They obtain explicit analytical expressions for the director fields, and energies, of the diagonal and rotated solutions, and numerically show the existence of higher energy metastable states with internal defects. In Fang et al. [69], the authors model a rectangular

NLC system within a reduced 2D LdG framework, and compute limiting solution profiles in two distinguished limits for the cross-sectional size: $\lambda \to 0$, and $\lambda \to \infty$, in our framework. They also employ continuation methods to produce bifurcation plots for these reduced equilibria, at three distinct values of the geometric anisotropy, δ. In our work, we present novel mixed solutions which interpolate between rotated and diagonal states, and study the stability of these 3D solutions as a function of δ, λ, and the well height.

2.2 Elastic anisotropy

In the simplest setting, the LdG energy has two contributions - a bulk energy that only depends on the eigenvalues of the LdG $\mathbf{Q}$-tensor, and an elastic energy that penalises spatial inhomogeneities of the $\mathbf{Q}$-tensor (see Section 1.4). The elastic energy is typically a quadratic and convex function of $\nabla\mathbf{Q}$ and, in [52], [61], the authors work with an isotropic elastic energy - the Dirichlet elastic energy. However, NLCs are anisotropic in nature, and the inclusion of an anisotropic elastic energy to the model is a natural extension to the analysis of nematic equilibria in confinement in Chapter 3. To this end, we model NLCs in 2D square wells with tangent boundary conditions, and a two-term elastic energy density in the LdG theory in Chapter 5. In Golovaty, Montero and Sternberg [70], the authors rigorously justify the study of thin NLCs systems by a 2D LdG model using Gamma-convergence results. They show that it is sufficient to model this reduced 2D system when studying the behaviour of LdG equilibria in the limit of vanishing thickness, given strong Dirichlet boundary conditions on the lateral surfaces, and weak tangential anchoring on the top and bottom surfaces of the film. In Bauman et al. [71], the authors analyse thin NLC systems in general

simply connected bounded domains, with a three-term elastic energy density in the 2D LdG framework. They show that, for large domains, minimizers converge to a limiting uniaxial nematic texture, with a finite number of defects of degree $\pm\frac{1}{2}$. We adopt a similar approach in Chapter 5, and consider thin NLC systems in a 2D square with tangent Dirichlet boundary conditions. In the two papers by Golovaty et al. [72], [73], the authors conduct an asymptotic analysis of this model problem, for more general domains, where the elastic anisotropy is large.

To complement our analysis in Chapter 5, we also numerically compute the equilibrium configurations, using standard finite difference methods, and Newton's method, to solve a weak form of the Euler-Lagrange equations associated with the LdG free energy. This numerical approach is inspired by the work of Han et al. [74], where the authors numerically compute LdG equilibria in regular 2D polygons, given an isotropic elastic energy. The authors also employ continuation methods to produce bifurcation diagrams for the equilibrium configurations, as a function of the domain edge-length. In Chapter 5, we use the same numerical scheme to compute bifurcation diagrams, as a function of the edge-length, for different degrees of the elastic anisotropy.

2.3 Ferronematics

NLCs have historically relied on their dielectric responses to electric fields for applications because the NLC dielectric anisotropy is several orders of magnitude (e.g., 7 orders of magnitude) larger than the magnetic anisotropy [13]. This implies that (unrealistically) large magnetic fields are needed to elicit macroscopic NLC responses to magnetic fields, making it difficult to exploit the magneto-mechanical, and magneto-optic, properties of NLCs. The addition of magnetic

nanoparticles (MNPs) to a NLC host can substantially increase the magnetic susceptibility of the suspension [75], and influence phase transition temperatures and other material properties, all of which are largely determined by the surface anchoring on the MNP surfaces. Some of these composite systems are referred to as "ferronematics", with non-zero net magnetization in the absence of an external magnetic field. Ferronematics were theoretically predicted by the pioneering work of Brochard and de Gennes [33], with further notable theoretical developments by Burylov and Raikher [76], among others. Although ferronematic systems were experimentally realized rather early on by Rault, Cladis and Burger [77], stable MNP suspensions have only been recently achieved (see the papers by Mertelj et al. [78], [79]).

In the papers by Bisht et al. [80], [81], the authors study a dilute suspension of MNPs in a one-dimensional NLC-filled channel, and a NLC-filled 2D square, respectively. They report exotic stable morphologies for the nematic director, and the associated magnetization profile, without any external fields. They report the co-existence of stable states with interior nematic defects, interior magnetic vortices, states with defects pinned to the square vertices, and states with magnetic domain walls that separate *ordered polydomains* i.e., two distinct domains with different magnetizations. These results demonstrate the immense potential of 2D polygons for tailored multistability in ferronematic-type systems, which would be inaccessible in generic confined NLC systems (see e.g., [64], [61]). In Chapter 6, we build on this work by studying dilute suspensions of MNPs in a nematic host, on 2D regular polygons without external magnetic fields, as a natural generalisation of the work on square wells in [81]. A dilute suspension refers to a uniform suspension of small MNPs (on the nanometer scale with length greater than the diameter), such that the average distance between a pair of distinct MNPs is much

greater than the MNP size, and the total volume fraction of suspended MNPs is small. In [78], the authors designed a stable ferronematic suspension using barium hexaferrite (BaHF) platelets, with a thickness of $\sim 5\,\text{nm}$ and a mean diameter of $\sim 70\,\text{nm}$, with number concentrations in the range $10^{13} - 10^{14}\,\text{cm}^{-3}$ in 5CB. In the papers by Calderer et al. [82], and Canevari and Zarnescu [83], the authors show using homogenization techniques that, in this dilute limit, the MNP-interactions are "small" compared to other effects, and the NLC-MNP interactions are captured by an "effective energy". This effective NLC-MNP energy depends on the shape and size of the MNPs, the surface anchoring energies, and the nemato-magnetic coupling which couples the magnetization and the nematic directors.

The pure NLC system has been well described in Han et al. [74] on 2D polygons, where the authors demonstrate a unique *Ring* solution profile, with a unique nematic point defect at the center, which is the generic stable solution for large enough polygons except for the square. In large enough N-sided polygons, the authors find at least $\binom{N}{2}$ stable states. A key question we address in Chapter 6 is - how does the solution landscape respond to the NLC-MNP coupling in regular 2D polygons? We show that the multistability of solutions can be strongly enhanced by the NLC-MNP coupling parameter, the cross-sectional size, and an increased number sides for the domain. This work is accompanied by bifurcation diagrams for positive and negative coupling values, as a function of the cross-sectional size of the well.

2.4 Stochastic models for nematic liquid crystals

Throughout this thesis, we have modelled NLC systems in confinement given deterministic model parameter choices. In reality, experimental data is rarely deterministic, especially when it concerns small elastic constants or material-dependent parameters in the Landau-de Gennes energy which are difficult to measure. This intrinsic variability offers important information about the behaviour of nematic liquid crystals, motivating a stochastic framework for modelling these systems. In Staber and Guilleminot [84], and the related papers by Mihai et al. [58], [59], [85], the authors construct stochastic hyperelastic models described by strain-energy densities, where the parameters are characterised by non-Gaussian probability density functions. These are advanced phenomenological models that rely on the finite elasticity theory, and the maximum entropy principle for a discrete probability distribution introduced by Jaynes [86], to enable the propagation of uncertainties from input data to output quantities of interest. The derivation of such probability density functions was shown in Soize [87], in order to model random uncertainties in the finite element models of linear structural dynamics. One stochastic model of interest was constructed in [58], where the authors studied isotropic incompressible hyperelastic bodies under equitriaxial dead loads, where the random shear modulus follows a Gamma distribution, with hyperparameters that depend on the mean value, and variance, of data coming from experiments. In Chapter 7, we employ a similar approach to a simple problem in nematic liquid crystals namely, the nematic-isotropic phase transition for a fourth order thermotropic bulk potential in the Landau-de Gennes theory. In the deterministic case, the transition between these phases occurs at

a critical temperature. However, we argue that the inherent variability of the material parameter choices implies that there is always competition between these states of order. We ask the question: *what is the influence of the stochastic model parameter on the predicted order parameter responses?* We actually show that the isotropic and nematic phases which in the deterministic setting have distinct may coexist for fixed temperatures, and the stochastic model parameter allows us to quantify the likelihood of observing either state. This is different from the deterministic modelling perspective, where a first-order phase transition occurs at some critical temperature.

Chapter 3

Analysis of the well order reconstruction solution in three dimensions

In this chapter, we study nematic equilibria on three-dimensional (3D) square wells in the Landau-de Gennes (LdG) theory, with tangent boundary conditions on the lateral surfaces, motivated by the bistable system in [60]. To begin, we will introduce the LdG free energy of the system in the absence of external fields and surface energies, as well as the domain, and tangent Dirichlet boundary conditions on the lateral surfaces of the well. We prove the existence of the WORS on 3D square wells, for arbitrary well heights, with natural boundary conditions on the top and bottom surfaces, as well as stability and qualitative properties of the WORS as a special case of a more general family of LdG equilibria; we believe these results to be of general interest. Furthermore, we work with 3D wells that have realistic surface energies, that favour planar boundary conditions on the top

and bottom surfaces, and again prove the existence of the WORS for arbitrary well heights and low temperatures, accompanied by interesting companion results for surface energy.

3.1 Model formulation

We begin by considering the total free energy of a nematic liquid crystal, in the absence of external field effects and surface energies. Recall the following one-constant approximation of the Landau-de Gennes free energy:

$$\mathcal{F}[\mathbf{Q}] := \int_V \frac{L}{2}|\nabla \mathbf{Q}|^2 + f_b(\mathbf{Q})\,\mathrm{dV},$$

where V is our 3D domain. For clarity, $L > 0$ is the material-dependent elastic constant, and f_b is the thermotropic bulk energy density given by (1.4.6). We take

$$V := \Omega \times (0, h),$$

where h is the height of the well, and $\Omega \subset \mathbb{R}^2$ is some 2D cross-section to be determined later. For ease of notation, we define Γ to be the union of the top and bottom surfaces of the domain i.e., $\Gamma := \Omega \times \{0, h\}$. We will introduce a key characteristic geometric-length scale, λ, to non-dimensionalise the system. We define the change of variables $\bar{\mathbf{x}} = \frac{\mathbf{x}}{\lambda}$, and hence the rescaled domain becomes

$$\bar{V} := \bar{\Omega} \times (0, \epsilon), \tag{3.1.1}$$

where $\bar{\Omega}$ is the rescaled two-dimensional cross-section, and $\epsilon := \frac{h}{\lambda}$ is the rescaled height of the well. We rescale the LdG energy functional, $\mathcal{F}$, as follows:

$$\mathcal{F}_\lambda[\mathbf{Q}] := \frac{\mathcal{F}[\mathbf{Q}]}{L\lambda} = \int_{\bar{V}} \frac{1}{2}|\bar{\nabla}\mathbf{Q}|^2 + \frac{\lambda^2}{L} f_b(\mathbf{Q})\, \overline{\mathrm{dV}},$$

where $\bar{\nabla}$ is the gradient with respect to the new rescaled spatial coordinates $\bar{\mathbf{x}}$, and $\overline{\mathrm{dV}}$ is the rescaled volume element. It is to be made clear that, in the rest of this chapter, we will drop the '*bars*' in our notation, and all calculations should be thought of with respect to these rescaled quantities.

Now that we have rescaled the system with respect to the characteristic length scale λ, the next step in setting up the model problem is defining the working domain, and the boundary conditions, for our confining geometry.

3.1.1 The working domain

We wish to study nematic equilibria inside square wells of finite height, ϵ, with planar degenerate boundary conditions that mimic the surface treatment in [60]. To this end, we consider the minimization problem of $\mathcal{F}_\lambda$ in the three-dimensional rescaled domain (3.1.1). Following the literature on planar degenerate boundary conditions on square domains [88], [62], [63], we take $\Omega \subset \mathbb{R}^2$ to be a truncated unit square, whose diagonals lie along the coordinate axes. That is, for some small but fixed parameter $\eta \in (0, 1)$,

$$\Omega := \{(x, y) \in \mathbb{R}^2 : |x| < 1 - \eta, |y| < 1 - \eta, |x + y| < 1, |x - y| < 1\},$$

(see Figure 3.1).

The reason for truncating the vertices of the domain is due to the choice of boundary conditions we wish to impose. Tangent boundary conditions (TBCs) require

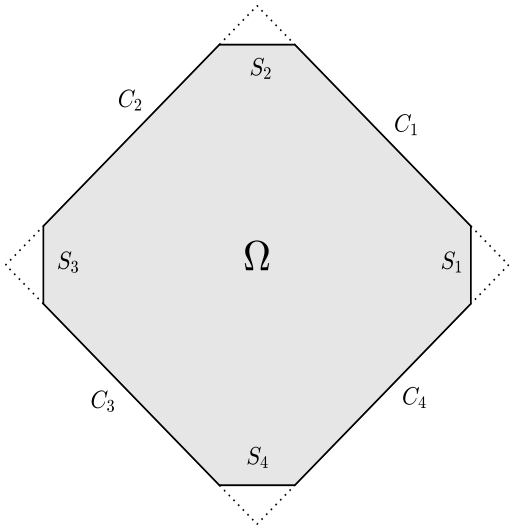

Figure 3.1: The truncated unit square $\Omega \subset \mathbb{R}^2$.

the nematic directors to be tangent to the square edges, creating a necessary mismatch at the square vertices. By choosing appropriate boundary conditions, we may avoid these discontinuities, whilst the qualitative solution trends you would expect for a square well are not affected [62]. The boundary of the cross-sectional geometry, $\partial\Omega$, has four "long" edges, parallel to the lines $y = x$ and $y = -x$, which we define as $C_1, \ldots, C_4$. In order to remove the sharp square vertices, we have four additional "short" edges of length 2η, parallel to the coordinate axes, which we define as $S_1, \ldots, S_4$. The four long edges are labelled counterclockwise, with C_1 being the edge contained in the first quadrant i.e., $C_1 := \{(x, y) \in \mathbb{R}^2 : x + y = 1, \eta \leq x \leq 1 - \eta\}$. The short edges are also labelled counterclockwise, with $S_1 := \{(1 - \eta, y) \in \mathbb{R}^2 : |y| \leq \eta\}$.

3.1.2 Boundary conditions on the lateral surfaces

There are a number of boundary conditions that are consistent with experimentally induced tangential anchoring on the lateral surfaces of the domain, $\partial\Omega \times (0, \epsilon)$.

In this chapter, we follow the approach taken in [61], [52] and [62], by imposing tangent uniaxial Dirichlet conditions on the lateral surfaces of the well:

$$\mathbf{Q} = \mathbf{Q}_b \qquad \text{on} \qquad \partial V \setminus \Gamma = \partial\Omega \times (0, \epsilon), \tag{3.1.2}$$

where $\mathbf{Q}_b$ minimises the bulk energy density (1.4.6). As was shown in Proposition 1.4.1, it is suitable to impose

$$\mathbf{Q}_b(x, y, z) := \begin{cases} s_+ \left(\mathbf{n}_1 \otimes \mathbf{n}_1 - \frac{1}{3}\mathbf{I} \right), & (x, y) \in C_1 \cup C_3, \\ s_+ \left(\mathbf{n}_2 \otimes \mathbf{n}_2 - \frac{1}{3}\mathbf{I} \right), & (x, y) \in C_2 \cup C_4, \end{cases}$$

where $\mathbf{n}_1 := \frac{1}{\sqrt{2}}(-1, 1, 0)$, $\mathbf{n}_2 := \frac{1}{\sqrt{2}}(1, 1, 0)$, and s_+ is defined as in (1.4.8). The Dirichlet conditions on the short edges, $S_1, \ldots, S_4$, must be taken more carefully as to eliminate the discontinuities of the tangent Dirichlet boundary condition. We define

$$\mathbf{Q}_b(x, y, z) := \begin{cases} g(y)(\mathbf{n}_1 \otimes \mathbf{n}_1 - \mathbf{n}_2 \otimes \mathbf{n}_2) - \frac{s_+}{2} \left(\hat{\mathbf{z}} \otimes \hat{\mathbf{z}} - \frac{1}{3}\mathbf{I} \right) & (x, y) \in S_1 \cup S_3, \\ g(x)(\mathbf{n}_1 \otimes \mathbf{n}_1 - \mathbf{n}_2 \otimes \mathbf{n}_2) - \frac{s_+}{2} \left(\hat{\mathbf{z}} \otimes \hat{\mathbf{z}} - \frac{1}{3}\mathbf{I} \right) & (x, y) \in S_2 \cup S_4, \end{cases}$$

where $g : [-\eta, \eta] \to [-\frac{s_+}{2}, \frac{s_+}{2}]$ is a smoothing function, such as

$$g(\upsilon) = \frac{s_+}{2\eta}\upsilon, \qquad -\eta \leq \upsilon \leq \eta.$$

Although the boundary condition, $\mathbf{Q}_b$, does not minimize the bulk energy on $S_1, \ldots, S_4$, and the $\mathbf{Q}$-tensor is not tangent to these edges, they are short by construction, and are chosen purely for mathematical convenience.

3.2 The 3D WORS and related results

Consider the minimization problem of $\mathcal{F}_\lambda$, with respect to the tensor order parameter $\mathbf{Q}$. Given the Dirichlet TBCs (3.1.2), we define our admissible space to be

$$\mathcal{A} := \{\mathbf{Q} \in W^{1,2}(V; \mathcal{S}_0) : \mathbf{Q} = \mathbf{Q}_b \ \text{ on } \ \partial\Omega \times (0, \epsilon)\},$$

where $\mathcal{S}_0$ is defined by the space of traceless, symmetric 3×3 matrices. The choice of function space $W^{1,2}$ ensures the elastic energy in the Landau-de Gennes free energy is finite. Furthermore, any critical point of the rescaled functional, $\mathcal{F}_\lambda$, in the admissible space, $\mathcal{A}$, will satisfy the following Euler-Lagrange equations:

$$\Delta\mathbf{Q} = \frac{\lambda^2}{L}\left\{A\mathbf{Q} - B\left(\mathbf{Q}\mathbf{Q} - \frac{\mathbf{I}}{3}|\mathbf{Q}|^2\right) + C|\mathbf{Q}|^2\mathbf{Q}\right\}, \tag{3.2.1}$$

which comprises a system of up to five coupled partial differential equations. In [52], the authors numerically compute critical points of $\mathcal{F}_\lambda$, satisfying the Dirichlet boundary conditions (3.1.2), on the 2D cross-section Ω. In [62], the authors analyse these critical points at the special fixed temperature, $A = -\frac{B^2}{3C}$. In this regime, the WORS corresponds to a classical solution of the Euler-Lagrange equations, (3.2.1), of the form

$$\mathbf{Q}_{WORS}(x, y) = q(\mathbf{n}_1 \otimes \mathbf{n}_1 - \mathbf{n}_2 \otimes \mathbf{n}_2) - \frac{B}{6C}(2\hat{\mathbf{z}} \otimes \hat{\mathbf{z}} - \mathbf{n}_1 \otimes \mathbf{n}_1 - \mathbf{n}_2 \otimes \mathbf{n}_2).$$

This solution is described by a single degree of freedom, $q : \Omega \to \mathbb{R}$, which satisfies the Allen-Cahn equation, and exhibits the following symmetry properties:

$$q(x, 0) = q(0, y) = 0, \qquad xyq(x, y) \geq 0.$$

They prove that, solutions of this type are globally stable for λ small enough, and unstable for λ large enough in the 2D domain. Their analysis was restricted

to the specific temperature, but numerically they were able to show the WORS exists for all $A < 0$. The negative eigenvalue associated with $\hat{\mathbf{z}}$ implies that nematic molecules lie in the (x, y)-plane and, for non-zero q, there is a locally defined nematic director in the (x, y)-plane. In this section, we show that the WORS survives in 3D scenarios, given natural boundary conditions on the top and bottom surfaces of the well.

3.2.1 Natural boundary conditions on the top and bottom plates

In this section, we will assume that the material dependent parameters $L, B, C > 0$ are fixed, while λ and A may vary. We consider all temperatures below the nematic supercooling temperature ($A < 0$) that is, all temperatures that favour a bulk ordered nematic phase. We also assume *natural*, or Neumann, boundary conditions on the top and bottom plates of the well i.e.,

$$\partial_z \mathbf{Q} = \mathbf{0} \quad \text{on} \quad \Gamma, \tag{3.2.2}$$

that is, the outward normal derivative is equal to zero on the top and bottom surfaces of the well, and the liquid crystal sample is modelled to have planar degenerate alignment on these surfaces. Whilst a surface anchoring term in the free energy is more physically realistic, this is a boundary condition chosen for mathematical simplicity which can shed more light on the physical set up in [60] in three dimensions. In their experiment, the authors consider an array of shallow square wells where each of the square edges were consistent with planar degenerate alignment due to the treatment of SU8 photoresist onto each glass substrate. Under the assumption (3.2.2), we may use a classic result in the

calculus of variations to simplify the minimization problem.

Proposition 3.2.1. *For any $\lambda > 0$ and $A < 0$, there exist minimizers $\mathbf{Q}$, of $\mathcal{F}_\lambda$, in the admissible class $\mathcal{A}$. Moreover, these minimizers are independent of the z-variable, that is $\partial_z \mathbf{Q} = \mathbf{0}$ on V, and they minimize the 2D functional*

$$\mathcal{I}[\mathbf{Q}] := \int_\Omega \left(\frac{1}{2}|\nabla \mathbf{Q}|^2 + \frac{\lambda^2}{L} f_b(\mathbf{Q}) \right) \mathrm{dA},$$

in the admissible class

$$\mathcal{A}' := \{ \mathbf{Q} \in W^{1,2}(\Omega, \mathcal{S}_0) \, : \, \mathbf{Q} = \mathbf{Q}_b \quad \text{on} \quad \partial\Omega \}.$$

Proof. For this proof, we follow the argument used in Theorem 0 from [89]. Suppose that there exists some $\mathbf{V}_0 \in \mathcal{A}'$ which minimizes the 2D energy functional $\mathcal{I}$ i.e.,

$$\kappa = \mathcal{I}[\mathbf{V}_0] = \min_{\mathbf{V} \in \mathcal{A}'} \int_\Omega \frac{1}{2}|\nabla \mathbf{V}|^2 + \frac{\lambda^2}{L} f_b(\mathbf{V}) \, \mathrm{d}x \, \mathrm{d}y.$$

Then for each $\mathbf{Q} \in \mathcal{A}$, we have

$$\begin{aligned} \int_V \frac{1}{2}|\nabla \mathbf{Q}|^2 + \frac{\lambda^2}{L} f_b(\mathbf{Q}) \, \mathrm{d}x \, \mathrm{d}y \, \mathrm{d}z &\geq \int_V \frac{1}{2}|\nabla_{x,y} \mathbf{Q}|^2 + \frac{1}{2}|\partial_z \mathbf{Q}|^2 + \frac{\lambda^2}{L} f_b(\mathbf{Q}) \, \mathrm{d}x \, \mathrm{d}y \, \mathrm{d}z \\ &\geq \int_\Omega \frac{1}{2}|\nabla_{x,y} \mathbf{Q}|^2 + \frac{\lambda^2}{L} f_b(\mathbf{Q}) \, \mathrm{d}x \, \mathrm{d}y \geq \kappa \end{aligned} \tag{3.2.3}$$

and since we may choose $\mathbf{Q} \in \mathcal{A}$ such that $\mathbf{Q}(x, y, z) = \mathbf{V}_0(x, y)$, we have

$$\kappa = \min_{\mathbf{Q} \in \mathcal{A}} \int_V \frac{1}{2}|\nabla \mathbf{Q}|^2 + \frac{\lambda^2}{L} f_b(\mathbf{Q}) \, \mathrm{d}x \, \mathrm{d}y \, \mathrm{d}z.$$

Furthermore, if a given $\mathbf{Q}$ is a minimizer of the 3D functional $\mathcal{F}_\lambda$ in the admissible class $\mathcal{A}$, that is if

$$\int_V \frac{1}{2}|\nabla \mathbf{Q}|^2 + \frac{\lambda^2}{L} f_b(\mathbf{Q}) \, \mathrm{d}x \, \mathrm{d}y \, \mathrm{d}z = \kappa,$$

then, by (3.2.3),

$$\int_V \frac{1}{2}|\nabla_{x,y}\mathbf{Q}|^2 + \frac{\lambda^2}{L} f_b(\mathbf{Q})\,\mathrm{d}x\,\mathrm{d}y = \kappa,$$

which yields $\partial_z \mathbf{Q} = \mathbf{0}$. □

We conclude, that any (z-independent) critical point of the energy functional $\mathcal{I}$, in the admissible class $\mathcal{A}'$, is also a solution of the 3D system (3.2.1), subject to the Dirichlet boundary conditions on the lateral surfaces (3.1.2), and the natural boundary conditions on the top and bottom plates (3.2.2). This implies that the WORS is a LdG critical point on 3D wells V, for arbitrary height ϵ, with natural boundary conditions (3.2.2) on Γ. Hence, in the rest of this section, we will restrict ourselves to a 2D problem - the analysis of critical points of $\mathcal{I}$ in $\mathcal{A}'$.

Our first result concerns the existence of a WORS-like solution for all $A < 0$, as proven below.

Proposition 3.2.2. *For any $\lambda > 0$ and $A < 0$, there exists a solution, (q_1^{WORS}, q_3^{WORS}), of the system*

$$\begin{cases} \Delta q_1 &= \frac{\lambda^2}{L} q_1 \left\{A + 2Bq_3 + 2C(q_1^2 + 3q_3^2)\right\}, \\ \Delta q_3 &= \frac{\lambda^2}{L} q_3 \left\{A - Bq_3 + 2C(q_1^2 + 3q_3^2)\right\} + \frac{\lambda^2 B}{3L} q_1^2, \end{cases} \tag{3.2.4}$$

subject to the boundary conditions

$$q_1(x,y) = q_{1b}(x,y) := \begin{cases} \frac{s_+}{2}, & (x,y) \in C_1 \cup C_3, \\ -\frac{s_+}{2}, & (x,y) \in C_2 \cup C_4, \\ g(y), & (x,y) \in S_1 \cup S_3, \\ g(x), & (x,y) \in S_2 \cup S_4, \end{cases} \tag{3.2.5}$$

and $q_3 = -\frac{s_+}{6}$ *on* $\partial\Omega$*, that satisfies*

$$xyq_1(x,y) \geq 0, \text{ and } \quad q_3(x,y) < 0 \quad \text{for any} \quad (x,y) \in \Omega. \tag{3.2.6}$$

Then

$$\mathbf{Q}(x,y) = q_1^{WORS}(\mathbf{n}_1 \otimes \mathbf{n}_1 - \mathbf{n}_2 \otimes \mathbf{n}_2) + q_3^{WORS}(2\hat{\mathbf{z}} \otimes \hat{\mathbf{z}} - \mathbf{n}_1 \otimes \mathbf{n}_1 - \mathbf{n}_2 \otimes \mathbf{n}_2), \tag{3.2.7}$$

is a WORS solution of the Euler-Lagrange system (3.2.1) on V*, subject to the Dirichlet boundary conditions (3.1.2), and natural boundary conditions (3.2.2), on* Γ*.*

Proof. We use a similar approach to the one adopted by [62]. Define the following portion of Ω that is contained in the positive quadrant of the square:

$$\Omega_+ := \{(x,y) \in \Omega \,:\, x > 0, y > 0\}. \tag{3.2.8}$$

We first note that, for solutions of the form (3.2.7), the LdG energy $\mathcal{I}$ reduces to the following energy functional, in terms of the scalar order parameters $q_1, q_3 \in W^{1,2}(\Omega_+;\mathbb{R})$:

$$G[q_1,q_3] := \int_{\Omega_+} \left\{ |\nabla q_1|^2 + 3|\nabla q_3|^2 + \frac{\lambda^2}{L} f_b(q_1,q_3) \right\} \mathrm{dA},$$

where

$$f_b(q_1,q_3) := A(q_1^2 + 3q_3^2) + C(q_1^2 + 3q_3^2)^2 + 2Bq_3(q_1^2 - q_3^2)$$

is the associated bulk energy term for solutions (3.2.7). We wish to minimise G in the restricted admissible class

$$\mathcal{G} := \Big\{ (q_1,q_3) \in W^{1,2}(\Omega_+;\mathbb{R}^2) \,:\, q_3 \leq 0 \text{ in } \Omega_+,\ q_1 = q_{1b} \text{ on } \partial\Omega \cap \overline{\Omega_+},$$

$$q_3 = -\frac{s_+}{6} \text{ on } \partial\Omega \cap \overline{\Omega_+},\ q_1 = 0 \text{ on } \partial\Omega_+ \setminus \partial\Omega \Big\}.$$

We impose no boundary conditions for q_3 on $\partial\Omega_+ \setminus \partial\Omega$. We note that the function q_{1b} is compatible with the Dirichlet boundary conditions, (3.1.2), imposed on Ω. Since the boundary conditions here are continuous and piecewise of class C^1, there exist functions $(q_1, q_3) \in W^{1,2}(\Omega_+; \mathbb{R}^2)$ belonging to the admissible space $\mathcal{G}$. An example of such a function could be $(q_1, -\frac{s_+}{6})$, where

$$q_1(x,y) = \begin{cases} \frac{s_+}{2\eta^2}xy, & x \in [0,\eta), y \in [0,\eta), \\ \frac{s_+}{2\eta}x, & x \in [0,\eta), y \in [\eta, 1-\eta], \\ \frac{s_+}{2\eta}y, & x \in [\eta, 1-\eta], y \in [0,\eta), \\ \frac{s_+}{2}, & \text{otherwise.} \end{cases}$$

For clarity, we include an illustration of this choice of q_1, in Figure 3.2. The

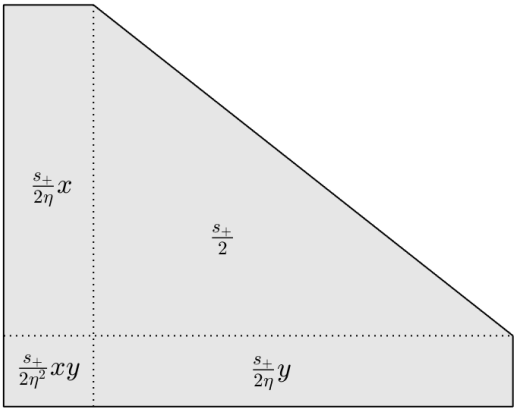

Figure 3.2: $q_1 \in W^{1,2}(\Omega_+)$ in the admissible space $\mathcal{G}$.

existence of a global minimizer of G, in the admissible class $\mathcal{G}$, follows from a routine application of the direct methods in the calculus of variations. We include the proof here for clarity. As the bulk energy term $f_b(q_1, q_3)$ is a quartic polynomial with positive quartic coefficient, it is bounded below by some function independent of q_1 and q_3. We recall that for $A < 0$, the bulk energy density is

minimized by a uniaxial state prescribed on the edge $\partial\Omega \cap \overline{\Omega_+}$. That is,

$$f_b(q_1, q_3) \geq f_b\left(\frac{s_+}{2}, -\frac{s_+}{6}\right) = \frac{As_+^2}{3} - \frac{2Bs_+^3}{27} + \frac{Cs_+^4}{9} =: K(A, B, C).$$

We therefore conclude that G is coercive in $\mathcal{G}$. Furthermore, by linearity of ∇, and the Minkowski's inequality for 2-norms, we have that for any $u, v \in \mathbb{R}$ and $\alpha \in (0, 1)$,

$$|\nabla(\alpha u + (1-\alpha)v)|^2 = |\alpha\nabla u + (1-\alpha)\nabla v|^2 \leq \alpha|\nabla u|^2 + (1-\alpha)|\nabla v|^2.$$

Hence, the elastic energy potential in G is convex in both ∇q_1 and ∇q_3. This condition, along with the fact that the admissible space $\mathcal{G}$ is non-empty, ensures the weak lower semi-continuity of the reduced energy functional G (see Theorem 8.2.1 from [57]). Therefore, there exists a global minimizer (q_1^{WORS}, q_3^{WORS}) of the reduced LdG energy G, in the admissible space $\mathcal{G}$. Moreover, we may assume without loss of generality, that $q_1^{WORS} \geq 0$ on Ω_+. If not, we can replace q_1^{WORS} with $|q_1^{WORS}|$, since we have that

$$G[q_1^{WORS}, q_3^{WORS}] = G[|q_1^{WORS}|, q_3^{WORS}].$$

We now claim that $q_3^{WORS} < 0$ in Ω_+. To prove this, consider a function $\varphi \in W^{1,2}(\Omega_+)$, such that $\varphi \geq 0$ in Ω_+ and $\varphi = 0$ on $\partial\Omega \cap \overline{\Omega_+}$. For sufficiently small $t \geq 0$, the function $\overline{q_3} := q_3^{WORS} - t\varphi$ is an admissible perturbation of q_3^{WORS}, and hence we have

$$\left.\frac{\mathrm{d}}{\mathrm{d}t}\right|_{t=0} G[q_1^{WORS}, \overline{q_3}] \geq 0 \tag{3.2.9}$$

because (q_1^{WORS}, q_3^{WORS}) is a minimizer. Therefore, by explicitly computing the left-hand side of (3.2.9), we obtain

$$\int_{\Omega_+} \left\{-6\nabla q_3^{WORS} \cdot \nabla\varphi - \frac{\lambda^2}{L} f(q_1^{WORS}, q_3^{WORS})\varphi\right\} \mathrm{dA} \geq 0, \tag{3.2.10}$$

where

$$f(q_1, q_3) := 6q_3(A - Bq_3 + 6Cq_3^2) + 2(B + 6Cq_3)q_1^2.$$

For $|q_3|$ sufficiently small, we have that $A - Bq_3 + 6Cq_3^2 < 0$ and $B + 6Cq_3 > 0$. Therefore, there exists some $\delta \in (0, \frac{s_+}{6})$ (depending only on A, B, C), such that

$$f(q_1, q_3) > 0 \quad \text{for any} \quad q_1 \in \mathbb{R} \text{ and } q_3 \in [-\delta, 0]. \tag{3.2.11}$$

Now, we define

$$\varphi := \begin{cases} q_3^{WORS} + \delta & \text{if} \quad q_3^{WORS} > -\delta, \\ 0 & \text{if} \quad q_3^{WORS} \leq -\delta. \end{cases}$$

As we have chosen $\delta < \frac{s_+}{6}$, we can make sure that $\varphi = 0$ on $\partial\Omega \cap \overline{\Omega_+}$. By substituting φ into (3.2.10), we obtain

$$\int_{\{q_3^{WORS} > -\delta\}} \left\{ 6|\nabla q_3^{WORS}|^2 + \frac{\lambda^2}{L} f(q_1^{WORS}, q_3^{WORS})(q_3^{WORS} + \delta) \right\} \mathrm{dA} \leq 0.$$

By (3.2.11), we conclude that $q_3^{WORS} \leq -\delta < 0$ in Ω_+. In particular, (q_1^{WORS}, q_3^{WORS}) lies in the interior of the admissible space $\mathcal{G}$ and hence, solves the Euler-Lagrange system (3.2.4) for the functional G, together with the natural boundary condition $\partial_\nu q_3 = 0$ on $\partial\Omega_+ \setminus \partial\Omega$. We extend (q_1^{WORS}, q_3^{WORS}) to the whole of Ω by odd reflections of q_1^{WORS}, and even reflections of q_3^{WORS}, about the coordinate axes $\{x = 0\}$ and $\{y = 0\}$:

$$q_1^{WORS}(x, y) := \mathrm{sign}(xy) q_1^{WORS}(|x|, |y|), \quad q_3^{WORS}(x, y) := q_3^{WORS}(|x|, |y|),$$

for any $(x, y) \in \Omega \setminus \overline{\Omega_+}$. The new solution, (q_1^{WORS}, q_3^{WORS}), is a weak solution of the system of equations (3.2.4) everywhere in Ω except at the origin, and satisfies the necessary sign properties (3.2.6). We now follow an argument based

on elliptic regularity, as in Theorem 3 of [90], to show that (q_1^{WORS}, q_3^{WORS}) is indeed a solution of (3.2.4), on the whole of Ω. By considering some small ball around the origin, $B_\xi(\mathbf{0})$, for any test function $\phi \in W_0^{1,2}(\Omega)$, we have

$$\begin{aligned}\int_{\Omega\setminus B_\xi(\mathbf{0})} \phi(x,y) f_1(q_1^{WORS}, q_3^{WORS}) &= \int_{\Omega\setminus B_\xi(\mathbf{0})} \phi(x,y)\Delta q_1^{WORS} \\ &= -\int_{\Omega\setminus B_\xi(\mathbf{0})} \nabla\phi\cdot\nabla q_1^{WORS} - \int_{\partial B_\xi(\mathbf{0})} \phi\partial_r q_1^{WORS}\end{aligned}$$

where ∂_r is the radial derivative on $\partial B_\xi(\mathbf{0})$, and

$$f_1(q_1,q_3) = \frac{\lambda^2}{L} q_1 \left\{A + 2Bq_3 + 2C(q_1^2+3q_3^2)\right\}.$$

Since ∇q_1^{WORS} is uniformly bounded in $\Omega\setminus\{\mathbf{0}\}$, as we pass to the limit $\xi\downarrow 0$, we obtain

$$\int_\Omega \phi f_1(q_1^{WORS}, q_3^{WORS}) + \int_\Omega \nabla\phi\cdot\nabla q_1^{WORS} = 0.$$

Similarly, we have that

$$\int_\Omega \phi f_2(q_1^{WORS}, q_3^{WORS}) + \int_\Omega \nabla\phi\cdot\nabla q_3^{WORS} = 0,$$

for any test function $\phi \in W_0^{1,2}(\Omega)$ and $f_2(q_1,q_3) = \frac{\lambda^2}{L} q_3\{A - Bq_3 + 2C(q_1^2+3q_3^2)\} + \frac{\lambda^2 B}{3L} q_1^2$. Therefore, the solution pair (q_1^{WORS}, q_3^{WORS}) is a weak solution of (3.2.4) on the whole of Ω including the origin, and satisfies the Dirichlet boundary conditions (3.2.5), and sign properties (3.2.6), by construction. □

In the remainder of this section, we show that the WORS-like solution (3.2.7) of the Euler-Lagrange system (3.2.1) is the unique LdG critical point, for $A < 0$ and small enough λ. By adapting a general criterion for uniqueness of critical points (see Lemma 8.2 from [91]), we can show that the energy functional $\mathcal{F}_\lambda$ has a unique critical point in the admissible class $\mathcal{A}$, when λ is below some critical

threshold, irrespective of the well height ϵ.

Proposition 3.2.3. *There exists a positive number λ_0 such that, for $\lambda < \lambda_0$, the Euler-Lagrange system (3.2.1) has a unique solution that satisfies the boundary conditions (3.1.2) and (3.2.2).*

Proof. Consider the constant M given in Proposition 1.4.2, the maximum principle result from [50] which shows that, all solutions of the Euler-Lagrange equations (3.2.1) are naturally bounded. Given the natural boundary conditions (3.2.2) on Γ, Proposition 3.2.1, and by a criterion for the uniqueness of critical points (as in [91]), it suffices to show that there exists a positive number $\lambda_0 = \lambda_0(M, A, B, C, L, \Omega)$ such that, for $\lambda < \lambda_0$, the energy functional $\mathcal{I}$ is strictly convex in the admissible class

$$\mathcal{X}_\Omega = \{\mathbf{Q} \in W^{1,2}(\Omega; \mathcal{S}_0) : |\mathbf{Q}| \leq M,\ \mathbf{Q} = \mathbf{Q}_b \text{ on } \partial\Omega\}.$$

Suppose that $\mathbf{Q}_1, \mathbf{Q}_2 \in \mathcal{X}_\Omega$, where $\mathbf{Q}_1 \neq \mathbf{Q}_2$. Then

$$\begin{aligned}
\mathcal{I}\left(\frac{\mathbf{Q}_1 + \mathbf{Q}_2}{2}\right) &= \int_\Omega \frac{1}{8}|\nabla(\mathbf{Q}_1 + \mathbf{Q}_2)|^2 + \frac{\lambda^2}{L} f_b\left(\frac{\mathbf{Q}_1 + \mathbf{Q}_2}{2}\right) \mathrm{dA} \\
&= \int_\Omega \frac{1}{4}\left\{|\nabla \mathbf{Q}_1|^2 + |\nabla \mathbf{Q}_2|^2 - \frac{1}{2}|\nabla(\mathbf{Q}_1 - \mathbf{Q}_2)|^2\right\} \mathrm{dA} \\
&\quad + \frac{\lambda^2}{L}\int_\Omega f_b\left(\frac{\mathbf{Q}_1 + \mathbf{Q}_2}{2}\right) \mathrm{dA} \\
&= \frac{1}{2}\mathcal{I}(\mathbf{Q}_1) + \frac{1}{2}\mathcal{I}(\mathbf{Q}_2) - \frac{1}{8}\int_\Omega |\nabla(\mathbf{Q}_1 - \mathbf{Q}_2)|^2 \,\mathrm{dA} \\
&\quad + \frac{\lambda^2}{L}\int_\Omega \left\{f_b\left(\frac{\mathbf{Q}_1 + \mathbf{Q}_2}{2}\right) - \frac{1}{2}f_b(\mathbf{Q}_1) - \frac{1}{2}f_b(\mathbf{Q}_2)\right\} \mathrm{dA} \qquad (3.2.12)
\end{aligned}$$

Since $\mathbf{Q}_1, \mathbf{Q}_2 \in \mathcal{X}_\Omega$, we have that $\mathbf{Q}_1 - \mathbf{Q}_2 = \mathbf{0}$ on $\partial\Omega$. By the Poincaré inequality on Ω, there exists some positive constant, c_1, that only depends on the geometry of Ω, such that

$$\int_\Omega |\mathbf{Q}_1 - \mathbf{Q}_2|^2 \,\mathrm{dA} \leq c_1 \int_\Omega |\nabla(\mathbf{Q}_1 - \mathbf{Q}_2)|^2 \,\mathrm{dA}. \qquad (3.2.13)$$

Since $|\mathbf{Q}_1| \leq M$ and $|\mathbf{Q}_2| \leq M$ everywhere in Ω, we have that

$$\int_\Omega \left| f_b\left(\frac{\mathbf{Q}_1+\mathbf{Q}_2}{2}\right) - \frac{1}{2}f_b(\mathbf{Q}_1) - \frac{1}{2}f_b(\mathbf{Q}_2)\right| \,\mathrm{dA} \leq ||f_b||_{W^{2,\infty}(B_M)} \int_\Omega |\mathbf{Q}_1-\mathbf{Q}_2|^2 \,\mathrm{dA}, \tag{3.2.14}$$

where $B_M = \{\mathbf{Q} \in \mathcal{S}_0 : |\mathbf{Q}| \leq M\}$ and $||f_b||_{W^{2,\infty}(B_M)}$ is a positive constant, depending only on M, A, B and C, that bounds the second derivatives of f_b in B_M. Combining both (3.2.13) and (3.2.14), there exists a positive constant $c_2 = c_2(\Omega, M, A, B, C) := c_1(\Omega)||f_b||_{W^{2,\infty}(B_M)}$ such that

$$\int_\Omega \left\{ f_b\left(\frac{\mathbf{Q}_1+\mathbf{Q}_2}{2}\right) - \frac{1}{2}f_b(\mathbf{Q}_1) - \frac{1}{2}f_b(\mathbf{Q}_2)\right\} \,\mathrm{dA} \leq c_2 \int_\Omega |\nabla(\mathbf{Q}_1-\mathbf{Q}_2)|^2 \,\mathrm{dA}. \tag{3.2.15}$$

Substituting the inequality (3.2.15) into (3.2.12), we have that

$$\mathcal{I}\left(\frac{\mathbf{Q}_1+\mathbf{Q}_2}{2}\right) \leq \frac{1}{2}\mathcal{I}(\mathbf{Q}_1) + \frac{1}{2}\mathcal{I}(\mathbf{Q}_2) + \left(\frac{c_2\lambda^2}{L} - \frac{1}{8}\right)\int_\Omega |\nabla(\mathbf{Q}_1-\mathbf{Q}_2)|^2 \,\mathrm{dA}.$$

If we take $\lambda < \lambda_0 := \left(\frac{L}{8c_2}\right)^{1/2}$, then we have

$$\mathcal{I}\left(\frac{\mathbf{Q}_1+\mathbf{Q}_2}{2}\right) \leq \frac{1}{2}\mathcal{I}(\mathbf{Q}_1) + \frac{1}{2}\mathcal{I}(\mathbf{Q}_2)$$

with equality if, and only if, $\mathbf{Q}_1 = \mathbf{Q}_2$. Thus, $\mathcal{I}$ is strictly convex in the admissible class $\mathcal{X}_\Omega$ and hence, must have at most one critical point in $\mathcal{X}_\Omega$. □

We conclude that the WORS survives in 3D wells, independently of the well height, ϵ, given natural boundary conditions on the top and bottom surfaces. Moreover, for sufficiently small λ and $A < 0$, the WORS is the unique LdG energy minimizer in three dimensions.

3.2.2 A more general class of critical points

It was shown in [52] that, for sufficiently large λ, there exist multiple critical points of the LdG energy $\mathcal{I}$. In this work, the authors consider the multiplicity of solutions as a function of the bare biaxial correlation length, studying its dependence on temperature and anchoring strength. In our framework, they show the WORS exists for wells with side length $\lambda \sim 78 - 138\,\text{nm}$, for temperatures in the deep-nematic regime. Therefore, wells with $\lambda \sim \mu\text{m}$ will be sufficiently large to observe the diagonal and rotated states reported in [60]. Indeed, the WORS $\mathbf{Q}$-tensor solution (3.2.7) belongs to a more general class of critical points, with constant eigenvector $\hat{\mathbf{z}}$. Solutions of this type can be completely described by three degrees of freedom i.e., they can be written as

$$\begin{aligned}\mathbf{Q}(x,y) = q_1(x,y)(\mathbf{n}_1 \otimes \mathbf{n}_1 - \mathbf{n}_2 \otimes \mathbf{n}_2) + q_2(x,y)(\mathbf{n}_1 \otimes \mathbf{n}_2 + \mathbf{n}_2 \otimes \mathbf{n}_1) \\ + q_3(x,y)(2\hat{\mathbf{z}} \otimes \hat{\mathbf{z}} - \mathbf{n}_1 \otimes \mathbf{n}_1 - \mathbf{n}_2 \otimes \mathbf{n}_2),\end{aligned} \tag{3.2.16}$$

where q_1, q_2, q_3 are scalar functions, and $\mathbf{n}_1, \mathbf{n}_2$ are as before. Solutions of the form (3.2.16) mimic the WORS if we have $q_2 = 0$ and $q_3 < 0$ everywhere in V, while $q_1 = 0$ in the coordinate axes $\{x = 0\}$ and $\{y = 0\}$. We again impose the Dirichlet boundary conditions (3.1.2) on the lateral surfaces of the well, and the natural boundary conditions (3.2.2) on Γ. By constructing a similar argument, we may show that there exists solutions of the Euler-Lagrange system (3.2.1), of the form (3.2.16), that satisfy these boundary conditions in the three-dimensional domain V. For solutions of the form (3.2.16), the Landau-de Gennes energy $\mathcal{I}$ reduces to the following energy functional, with respect to the three scalar functions $q_1, q_2, q_3 \in W^{1,2}(\Omega; \mathbb{R})$:

$$J[q_1, q_2, q_3] := \int_\Omega \left\{ |\nabla q_1|^2 + |\nabla q_2|^2 + 3|\nabla q_3|^2 + \frac{\lambda^2}{L} f_b(q_1, q_2, q_3) \right\} \text{dA},$$

where

$$f_b(q_1, q_2, q_3) := A(q_1^2 + q_2^2 + 3q_3^2) + 2Bq_3(q_1^2 + q_2^2 - q_3^2) + C(q_1^2 + q_2^2 + 3q_3^2)^2$$

is the associated bulk energy potential for solutions of the form (3.2.16). Critical points of J satisfy the following Euler-Lagrange system

$$\begin{cases} \Delta q_1 &= \frac{\lambda^2}{L} q_1 \left\{A + 2Bq_3 + 2C(q_1^2 + q_2^2 + 3q_3^2)\right\}, \\ \Delta q_2 &= \frac{\lambda^2}{L} q_2 \left\{A + 2Bq_3 + 2C(q_1^2 + q_2^2 + 3q_3^2)\right\}, \\ \Delta q_3 &= \frac{\lambda^2}{L} q_3 \left\{A - Bq_3 + 2C(q_1^2 + q_2^2 + 3q_3^2)\right\} + \frac{\lambda^2 B}{3L}(q_1^2 + q_2^2); \end{cases} \tag{3.2.17}$$

and the Dirichlet boundary condition, $\mathbf{Q}_b$, on the lateral surfaces (3.1.2) corresponds to the following boundary conditions for q_1, q_2 and q_3:

$$q_1 = q_{1b} \quad \text{(as in (3.2.5))}, \quad q_2 = 0, \quad q_3 = -\frac{s_+}{6}, \quad \text{on} \quad \partial\Omega. \tag{3.2.18}$$

We minimize $J[q_1, q_2, q_3]$ in the admissible class

$$\mathcal{J} := \{(q_1, q_2, q_3) \in W^{1,2}(\Omega; \mathbb{R}^3) : \, q_1 = q_{1b}, \quad q_2 = 0, \quad q_3 = -\frac{s_+}{6} \quad \text{on } \partial\Omega\}.$$

Following the methods in [92], we can construct solutions (q_1, q_2, q_3) to the system (3.2.17), of the form (3.2.16), subject to the boundary conditions (3.2.18), that satisfy $q_3 < 0$ in Ω and are locally stable. The WORS is a specific example of such a solution with constant eigenframe. In fact, the results in [63] show that the WORS loses stability with respect to solutions of the form (3.2.16) with $q_2 \neq 0$, as λ increases.

Definition 3.2.4. We say that a solution (q_1, q_2, q_3) of the Euler-Lagrange system (3.2.17) is locally stable if, for any perturbations $\varphi_1, \varphi_2, \varphi_3 \in C_c^1(\Omega)$, the second

variation of J satisfies

$$\delta^2 J(q_1, q_2, q_3)[\varphi_1, \varphi_2, \varphi_3] := \left.\frac{\mathrm{d}^2}{\mathrm{d}t^2}\right|_{t=0} J[q_1 + t\varphi, q_2 + t\varphi_2, q_3 + t\varphi_3] \geq 0.$$

Given a locally stable solution (q_1, q_2, q_3) of (3.2.17), the corresponding $\mathbf{Q}$-tensor, defined by (3.2.16), is a solution of (3.2.1) and is locally stable in the restricted class of $\mathbf{Q}$-tensors that have the constant eigenvector $\hat{\mathbf{z}}$.

Proposition 3.2.5. *For any $A < 0$ and $\lambda > 0$, there exists a solution (q_1^*, q_2^*, q_3^*) of the system (3.2.17), subject to the boundary conditions (3.2.18), that is locally stable and has $q_3^* < 0$ everywhere in Ω.*

Proof. The boundary data (3.2.18) are compatible with the Dirichlet boundary conditions (3.1.2). Furthermore, the boundary conditions in (3.2.18) are continuous piecewise of class C^1, so there exist functions $(q_1, q_2, q_3) \in W^{1,2}(\Omega; \mathbb{R}^3)$ that satisfy (3.2.18). Therefore, the admissible class $\mathcal{J}$ is non-empty. To construct solutions with $q_3 < 0$, we first introduce the following restricted admissible class

$$\mathcal{J}^- := \{(q_1, q_2, q_3) \in \mathcal{J} : \, q_3 \leq 0 \text{ a.e. on } \Omega\}.$$

Note that $\mathcal{J}^-$ is a non-empty, closed and convex subset of $W^{1,2}(\Omega; \mathbb{R}^3)$. As in Proposition 3.2.2, we have that the LdG energy functional J is coercive in $\mathcal{J}^-$, and weak lower semi-continuous. By the direct method in the calculus of variations, we know that there exists a global minimizer (q_1^*, q_2^*, q_3^*) of the functional J, in the class $\mathcal{J}^-$. To complete the proof, it suffices to show that $q_3^* \leq -\delta$ in Ω, for some strictly positive constant δ. Once this is proven, it follows that (q_1^*, q_2^*, q_3^*) lies in the interior of $\mathcal{J}^-$ and hence, it is a locally stable solution of the Euler-Lagrange system (3.2.17).

To prove that $q_3^* \leq -\delta$ in Ω, we follow the same method as in Proposition 3.2.2.

Let Ω_+ be the positive quadrant of Ω defined by (3.2.8), and let $\varphi \in W^{1,2}(\Omega_+)$ be such that $\varphi \geq 0$ in Ω, and $\varphi = 0$ on $\partial\Omega$, then

$$\left.\frac{\mathrm{d}}{\mathrm{d}t}\right|_{t=0} J[q_1^*,\, q_2^*,\, q_3^* - t\varphi] \geq 0,$$

since (q_1^*, q_2^*, q_3^*) is a minimizer and hence,

$$\int_{\Omega_+} \left\{ -6\nabla q_3^* \cdot \nabla\varphi - \frac{\lambda^2}{L} f^*(q_1^*, q_2^*, q_3^*)\varphi \right\} \mathrm{dA} \geq 0,$$

where

$$f^*(q_1, q_2, q_3) := 6q_3(A - Bq_3 + 6Cq_3^2) + 2(B + 6Cq_3)(q_1^2 + q_2^2).$$

As in Proposition 3.2.2, there exists a number $\delta > 0$ (depending only on A, B, C), such that

$$f^*(q_1, q_2, q_3) > 0 \quad \text{for any} \quad q_1, q_2 \in \mathbb{R} \quad \text{and} \quad q_3 \in [-\delta, 0].$$

By repeating the same arguments of Proposition 3.2.2, we can show that $q_3^* \leq -\delta$ in Ω. □

We now consider the constructed solutions of (3.2.17), satisfying the boundary conditions (3.2.18), with $q_3 < 0$ in Ω, and prove bounds for q_3 in the deep-nematic temperature regime, $A < 0$.

Lemma 3.2.6. *Any solution (q_1, q_2, q_3) of the system (3.2.17), subject to (3.2.18), satisfies the following inequality*

$$q_1^2 + q_2^2 + 3q_3^2 \leq \frac{s_+^2}{3} \quad \textit{in} \quad \Omega.$$

Proof. Note that for any solutions $\mathbf{Q} \in \mathcal{A}$ of the form (3.2.16), one can easily

verify that

$$|\mathbf{Q}|^2 = 2q_1^2 + 2q_2^2 + 6q_3^2.$$

Hence, the proof of this lemma follows immediately from the corresponding maximum principle approach for the full LdG system (3.2.1) in Proposition 1.4.2. □

Lemma 3.2.7. *Let (q_1, q_2, q_3) be a solution of the system (3.2.17), subject to (3.2.18), such that $q_3 < 0$ everywhere in Ω. Then the following inequality holds:*

$$q_1^2 + q_2^2 < 9q_3^2, \qquad \text{everywhere in} \qquad \Omega. \tag{3.2.19}$$

Proof. Define the functions $v_1 := -\frac{q_1}{q_3}$, and $v_2 := -\frac{q_2}{q_3}$. Then, for $k \in \{1, 2\}$, we have

$$\nabla v_k = -\frac{1}{q_3}\nabla q_k + \frac{q_k}{q_3^2}\nabla q_3$$

$$\begin{aligned}\Delta v_k =& -\frac{1}{q_3}\Delta q_k + \frac{q_k}{q_3^2}\Delta q_3 + \frac{2}{q_3^2}\nabla q_3 \cdot \nabla q_k - \frac{2q_k}{q_3^3}|\nabla q_3|^2 \\ =& -\frac{1}{q_3}\Delta q_k + \frac{q_k}{q_3^2}\Delta q_3 - \frac{2}{q_3}\nabla q_3 \cdot \nabla v_k\end{aligned}$$

Using the system (3.2.17), we have for $k \in \{1, 2\}$,

$$\begin{aligned}\Delta v_k + \frac{2}{q_3}\nabla q_3 \cdot \nabla v_k =& \frac{\lambda^2}{L}\left\{-\frac{q_k}{q_3}(A + 2Bq_3 + 2C(q_1^2 + q_2^2 + 3q_3^2))\right. \\ &\left. + \frac{q_k}{q_3}(A - Bq_3 + 2C(q_1^2 + q_2^2 + 3q_3^2))\right\} + \frac{\lambda^2 B}{3L}\frac{q_k}{q_3^2}(q_1^2 + q_2^2) \\ =& \frac{\lambda^2 B}{3L}q_k(-9 + v_1^2 + v_2^2).\end{aligned} \tag{3.2.20}$$

Now, we define a non-negative function v by $v^2 := v_1^2 + v_2^2$. Then, we obtain

$$\Delta(v^2/2) = v_1\Delta v_1 + v_2\Delta v_2 + |\nabla v_1|^2 + |\nabla v_2|^2.$$

Therefore, using (3.2.20), we have

$$\Delta(v^2/2) + \frac{2}{q_3}\nabla q_3 \cdot (v_1\nabla v_1 + v_2\nabla v_2) = \frac{\lambda^2 B}{3L}(q_1 v_1 + q_2 v_2)(v^2 - 9) + |\nabla v_1|^2 + |\nabla v_2|^2.$$

Finally, we obtain the following differential inequality:

$$\Delta(v^2/2) + \frac{2}{q_3}\nabla q_3 \cdot \nabla(v^2/2) \geq \underbrace{-\frac{\lambda^2 B}{3L}\frac{q_1^2 + q_2^2}{q_3}}_{\geq 0}(v^2 - 9). \tag{3.2.21}$$

From the boundary conditions (3.2.18), we know that $v = v_1 \leq 3$ on $\partial\Omega$. Then, the strong maximum principle applied to (3.2.21) implies that $v^2 < 9$, everywhere inside Ω. Thus, the lemma is proved. □

Recall the definition of the s_+ and s_- ordered nematic states from Proposition 1.4.1. We note that for temperatures below the nematic super-cooling temperature ($A < 0$), we have the following equivalent definition:

$$s_\pm := \frac{B \pm \sqrt{B^2 + 24|A|C}}{4C}.$$

Proposition 3.2.8. *Let (q_1, q_2, q_3) be any solution of the system (3.2.17), subject to the boundary conditions (3.2.18), with $q_3 < 0$ in Ω. Then the following bounds on q_3 hold:*

- *If $-\frac{B^2}{3C} \leq A < 0$, then $-\frac{s_+}{6} \leq q_3 \leq \frac{s_-}{3}$ in Ω;*
- *If $A = -\frac{B^2}{3C}$, then $q_3 \equiv -\frac{s_+}{6}$ in Ω;*
- *If $A \leq -\frac{B^2}{3C}$, then $\frac{s_-}{3} \leq q_3 \leq -\frac{s_+}{6}$ in Ω.*

Proof. If $-\frac{B^2}{3C} \leq A < 0$, then we necessarily have that

$$-\frac{B}{6C} \leq -\frac{s_+}{6} \leq \frac{s_-}{3}. \tag{3.2.22}$$

We will have to prove the inequalities separately, in several steps.

Step 1: *We show the upper bound, $q_3 \leq \frac{s_-}{3}$ in Ω, holds.* Assume for a contradiction, that the maximum of q_3 is attained at some point $(x_0, y_0) \in \Omega$, where $0 > q_3(x_0, y_0) > \frac{s_-}{3}$. Then the following inequalities hold at the point (x_0, y_0):

$$\begin{aligned} Aq_3 - Bq_3^2 + 6Cq_3^3 &> A\left(-\frac{B}{6C}\right) + B\left(-\frac{B^2}{36C^2}\right) + 6C\left(-\frac{B^3}{216C^3}\right) \\ &> \left(-\frac{B^2}{3C}\right)\left(-\frac{B}{6C}\right) - \frac{B^3}{18C^2} = 0, \end{aligned}$$

and

$$2Cq_3 + \frac{B}{3} > 2C\left(-\frac{B}{6C}\right) + \frac{B}{3} = 0.$$

Evaluating both sides of the equation for q_3 in (3.2.17) at the point (x_0, y_0):

$$\begin{aligned} \underbrace{\Delta q_3(x_0, y_0)}_{\leq 0} = &\underbrace{\frac{\lambda^2}{L}\left\{Aq_3(x_0, y_0) - Bq_3^2(x_0, y_0) + 6Cq_3^3(x_0, y_0)\right\}}_{>0} \\ &+ \underbrace{\frac{\lambda^2}{L}\left\{2Cq_3(x_0, y_0) + \frac{B}{3}\right\}(q_1^2(x_0, y_0) + q_2^2(x_0, y_0))}_{>0} \end{aligned}$$

which leads to a contradiction. By (3.2.22), we have $q_3 = -\frac{s_+}{6} \leq \frac{s_-}{3}$ on $\partial\Omega$. Therefore, we can conclude that $q_3 \leq \frac{s_-}{3}$ everywhere in Ω.

Step 2: *Now we will prove a weaker lower bound $q_3 \geq -\frac{B}{6C}$ in Ω.* Assume for a contradiction, that the minimum of q_3 is attained at some point $(x_1, y_1) \in \Omega$, with $q_3(x_1, y_1) < -\frac{B}{6C}$. Then the following inequalities hold at the point (x_1, y_1):

$$\begin{aligned} Aq_3 - Bq_3^2 + 6Cq_3^3 &< A\left(-\frac{B}{6C}\right) + B\left(-\frac{B^2}{36C^2}\right) + 6C\left(-\frac{B^3}{216C^3}\right) \\ &< \left(\frac{B^2}{3C}\right)\left(\frac{B}{6C}\right) - \frac{B^3}{18C^2} = 0, \end{aligned}$$

and

$$2Cq_3 + \frac{B}{3} < 2C\left(-\frac{B}{6C}\right) + \frac{B}{3} = 0.$$

Again, by evaluating both sides of the equation for q_3 in (3.2.17) at the point (x_1, y_1), we obtain a contradiction. The boundary conditions (3.2.18) conclude the weak lower bound $q_3 \geq -\frac{B}{6C}$ in Ω.

Step 3: *We now prove the optimal lower bound* $q_3 \geq -\frac{s_+}{6}$ *in* Ω. Using (3.2.17), the weak lower bound $q_3 \geq -\frac{B}{6C}$ and Lemma 3.2.7, we obtain

$$\begin{aligned}
\Delta q_3 &= \frac{\lambda^2}{L}\left\{Aq_3 - Bq_3^2 + 6Cq_3^3\right\} + \frac{\lambda^2}{L}\left\{2Cq_3 + \frac{B}{3}\right\}(q_1^2 + q_2^2) \\
&\leq \frac{\lambda^2}{L}\left\{Aq_3 - Bq_3^2 + 6Cq_3^3\right\} + \frac{\lambda^2}{L}\left\{2Cq_3 + \frac{B}{3}\right\} 9q_3^2 \\
&= \frac{\lambda^2}{L}\left\{Aq_3 + 2Bq_3^2 + 24Cq_3^3\right\} \quad \text{in} \quad \Omega
\end{aligned}$$

Now we may apply the same maximum principle argument as in Step 2. Assume for a contradiction, that the minimum of q_3 is attained at some point $(x_2, y_2) \in \Omega$, with $q_3(x_2, y_2) < -\frac{s_+}{6}$, then the following inequality holds at the point (x_2, y_2):

$$\begin{aligned}
Aq_3 + 2Bq_3^2 + 24Cq_3^3 &< A\left(-\frac{s_+}{6}\right) - 2B\left(-\frac{s_+^2}{36}\right) + 24C\left(-\frac{s_+^3}{216}\right) \\
&< \left(\frac{B^2}{3C}\right)\left(\frac{s_+}{6}\right) + 2B\left(\frac{B^2}{36C^2}\right) + 24C\left(-\frac{s_+^3}{216}\right) \\
&< \frac{B^3}{9C^2} - \frac{B}{9}\left(\frac{B^2}{C}\right) = 0.
\end{aligned}$$

Therefore,

$$\underbrace{\Delta q_3(x_2, y_2)}_{\geq 0} \leq \underbrace{\frac{\lambda^2}{L}\left\{Aq_3(x_2, y_2) + 2Bq_3^2(x_2, y_2) + 24Cq_3^3(x_2, y_2)\right\}}_{<0}$$

which leads to contradiction and hence proves the optimal lower bound $q_3 \geq -\frac{s_+}{6}$ in Ω.

Note that if we had chosen $A = -\frac{B^2}{3C}$, then we necessarily have that

$$\frac{s_-}{3} \equiv q_3 \equiv -\frac{s_+}{6} \quad \text{in} \quad \Omega.$$

Proving the last set of inequalities is completely analogous to the above arguments, with inequalities reversed. Assuming $A \leq -\frac{B^2}{3C}$, we first prove the lower bound $q_3 \geq \frac{s_-}{3}$, then the weaker upper bound $q_3 \leq -\frac{B}{6C}$, and finally the optimal upper bound $q_3 \leq -\frac{s_+}{6}$. Each step is obtained by repeating almost word by word the above arguments. We omit the details for brevity. □

Now that we have proved bounds on q_3 for various temperature regimes, we are in a position to study the stability/instability of the WORS, with natural boundary conditions on the top and bottom plates. As is standard in variational problems, a solution is stable if it satisfies the requirement in Definition 3.2.4, and is unstable if we can find any perturbation for which the second variation of the energy is negative. With this in mind, we look at in-plane perturbations of solutions $\mathbf{Q}$, of the form (3.2.16), with $q_2 \neq 0$. First, consider a function $\varphi \in C_c^1(\Omega)$, and consider the perturbation

$$\mathbf{Q}_t(x,y) := \mathbf{Q}(x,y) + t\varphi(x,y)(\mathbf{n}_1 \otimes \mathbf{n}_2 + \mathbf{n}_2 \otimes \mathbf{n}_1)$$

where $t \in \mathbb{R}$ is a small parameter. When considering the WORS-type solutions of the form (3.2.7), as discussed in Proposition 3.2.2, the second variation of the LdG energy is

$$\begin{aligned} H_\lambda[\varphi] :=& \frac{1}{2}\frac{\mathrm{d}^2}{\mathrm{d}t^2}\mathcal{I}[\mathbf{Q}_t]\bigg|_{t=0} \\ =& \frac{1}{2}\frac{\mathrm{d}^2}{\mathrm{d}t^2}J[q_1, q_2 + t\varphi, q_3]\bigg|_{t=0} \\ =& \int_\Omega \left\{ |\nabla\varphi|^2 + \frac{\lambda^2}{L}\varphi^2(A + 2Bq_3 + 2C(q_1^2 + 3q_3^2)) \right\} \mathrm{dA} \end{aligned} \tag{3.2.23}$$

(see Section 5.3 in [63]). The following result shows that, for A low enough and when λ is large, the WORS is unstable with respect to in-plane perturbations.

Proposition 3.2.9. *Let $A \leq -\frac{B^2}{3C}$, and suppose (q_1, q_2, q_3) is a solution of (3.2.17), subject to the boundary conditions (3.2.18), such that $q_2 = 0$ and $q_3 < 0$ everywhere in Ω. For any function $\varphi \in C_c^1(\Omega)$, that is not identically equal to zero, there exists a number $\lambda_0 > 0$ (depending on A, B, C, L and φ) such that $H_\lambda[\varphi] < 0$ when $\lambda \geq \lambda_0$.*

Proof. By Lemma 3.2.6 and Proposition 3.2.8, we have

$$\begin{aligned} A + 2Bq_3 + 2C(q_1^2 + 3q_3^2) &\leq A - \frac{Bs_+}{3} + \frac{2Cs_+^2}{3} \\ &= A - \frac{B}{3}\left(\frac{B + \sqrt{B^2 + 24|A|C}}{4C}\right) \\ &\quad + \frac{2C}{3}\left(\frac{2B^2 + 2B\sqrt{B^2 + 24|A|C} + 24|A|C}{16C^2}\right) \\ &= A + |A| = 0 \end{aligned}$$

The equality holds if, and only if, $q_3 = -\frac{s_+}{6}$ and $q_1^2 + 3q_3^2 = \frac{s_+^2}{3}$, that is if, and only if, $|q_1| = \frac{s_+}{2}$ and $q_3 = -\frac{s_+}{6}$. However, from Lemma 3.2.7, we know that $3q_3 < q_1 < -3q_3$ inside Ω. Therefore we must have

$$A + 2Bq_3 + 2C(q_1^2 + 3q_3^2) < 0, \quad \text{everywhere inside} \quad \Omega.$$

Then, for any fixed $\varphi \in C_c^1(\Omega)$, that is not identically equal to zero, the quantity $H_\lambda[\varphi]$ defined by (3.2.23) becomes strictly negative for λ large enough. □

3.2.3 Weak anchoring on the top and bottom plates

Experimentally, the surfaces of a confined nematic cell are treated chemically in order induce the planar boundary conditions, which forces the liquid crystal molecules to lie in plane of the surfaces [70], [93], [94]. With this in mind, a purely z-independent condition on the top and bottom plates is less realistic. In this section, we impose a surface energy term which is consistent with the preferred planar orientation that is usually achieved on the top and bottom plates. We define a revised Landau-de Gennes energy

$$\mathcal{F}_{\lambda,s}[\mathbf{Q}] := \int_V \left(\frac{1}{2}|\nabla \mathbf{Q}|^2 + \frac{\lambda^2}{L} f_b(\mathbf{Q}) \right) \mathrm{dV} + \frac{\lambda}{L} \int_\Gamma f_s(\mathbf{Q}) \, \mathrm{dS},$$

where f_s is the surface anchoring energy density defined by

$$f_s(\mathbf{Q}) := \alpha_z \left(\mathbf{Q}\hat{\mathbf{z}} \cdot \hat{\mathbf{z}} + \frac{s_+}{3} \right)^2 + \gamma_z |(\mathbf{I} - \hat{\mathbf{z}} \otimes \hat{\mathbf{z}})\mathbf{Q}\hat{\mathbf{z}}|^2,$$

where $\alpha_z, \gamma_z > 0$. This form of surface energy may be derived from the "bare" surface energy with respect to $\mathbf{Q}$-tensors, as in [70], with its minimum being achieved by uniaxial or biaxial $\mathbf{Q}$-tensors in the plane tangent to the surface of the liquid crystal. The polar anchoring on these surfaces is fixed because molecules lie in the plane of these surfaces, and the azimuthal anchoring is free because the nematic molecules are free to rotate in the plane. Note that the term, $(\mathbf{I} - \hat{\mathbf{z}} \otimes \hat{\mathbf{z}})\mathbf{Q}\hat{\mathbf{z}} = (Q_{13}, Q_{23}, 0)$, and hence $|(\mathbf{I} - \hat{\mathbf{z}} \otimes \hat{\mathbf{z}})\mathbf{Q}\hat{\mathbf{z}}|^2$ is equal to zero if, and only if, $\mathbf{Q}\hat{\mathbf{z}}$ is parallel to $\hat{\mathbf{z}}$. Hence, the surface energy density term, f_s, favours $\mathbf{Q}$-tensors that have $\hat{\mathbf{z}}$ as an eigenvector, with constant eigenvalue $-\frac{s_+}{3}$, on the top and bottom plates. We maintain the Dirichlet boundary conditions (3.1.2) on the lateral surfaces of the well, and seek to minimize the revised LdG energy $\mathcal{F}_{\lambda,s}$ in the admissible class $\mathcal{A}$.

Lemma 3.2.10. *Critical points of $\mathcal{F}_{\lambda,s}$, in the admissible class $\mathcal{A}$, satisfy the Euler-Lagrange system (3.2.1), subject to Dirichlet boundary conditions (3.1.2) on the lateral surfaces and*

$$\partial_\nu \mathbf{Q} + \frac{\lambda}{L}\mathbf{H}(\mathbf{Q}) = \mathbf{0} \quad on \quad \Gamma, \tag{3.2.24}$$

where ν is the outward-pointing unit normal to V and $\mathbf{H}$ is defined by

$$\mathbf{H}(\mathbf{Q}) := \begin{pmatrix} -\frac{2}{3}\alpha_z\left(Q_{33}+\frac{s_+}{3}\right) & 0 & \gamma_z Q_{13} \\ 0 & -\frac{2}{3}\alpha_z\left(Q_{33}+\frac{s_+}{3}\right) & \gamma_z Q_{23} \\ \gamma_z Q_{13} & \gamma_z Q_{23} & \frac{4}{3}\alpha_z\left(Q_{33}+\frac{s_+}{3}\right) \end{pmatrix}$$

Proof. Suppose $\mathbf{Q} \in W^{1,2}(V;\mathcal{S}_0)$ minimizes the revised LdG energy functional $\mathcal{F}_{\lambda,s}$ in the admissible class $\mathcal{A}$. Now, suppose $\mathbf{P} \in W^{1,2}(V;\mathcal{S}_0)$ is some perturbation such that $\mathbf{P} = \mathbf{0}$ on $\partial V \setminus \Gamma$. We wish to calculate the first variation of the LdG energy $\mathcal{F}_{\lambda,s}$, with respect to the perturbations $\mathbf{P}$. We have that,

$$\begin{aligned}\mathcal{F}_{\lambda,s}[\mathbf{Q}+t\mathbf{P}] = &\int_V \frac{1}{2}|\nabla(\mathbf{Q}+t\mathbf{P})|^2 \,\mathrm{dV} \\ &+ \int_V \frac{\lambda^2}{L}\left(\frac{A}{2}(\mathbf{Q}+t\mathbf{P})^2 - \frac{B}{3}\mathrm{tr}(\mathbf{Q}+t\mathbf{P})^3 + \frac{C}{4}(\mathbf{Q}+t\mathbf{P})^4\right)\mathrm{dV} \\ &+ \frac{\lambda}{L}\int_\Gamma \alpha_z\left((\mathbf{Q}+t\mathbf{P})\hat{\mathbf{z}}\cdot\hat{\mathbf{z}} + \frac{s_+}{3}\right)^2 + \gamma_z|(\mathbf{I}-\hat{\mathbf{z}}\otimes\hat{\mathbf{z}})(\mathbf{Q}+t\mathbf{P})\hat{\mathbf{z}}|^2 \,\mathrm{dS}\end{aligned}$$

Therefore, the first variation of $\mathcal{F}_{\lambda,s}$ with respect to $\mathbf{P}$ is:

$$\begin{aligned}0 &= \left.\frac{\mathrm{d}}{\mathrm{d}t}\right|_{t=0} \mathcal{F}_{\lambda,s}[\mathbf{Q}+t\mathbf{P}] \\ &= \int_V \left(\nabla\mathbf{Q} : \nabla\mathbf{P} + \frac{\lambda^2}{L}(A\mathbf{Q}\cdot\mathbf{P} - B\mathbf{Q}^2\cdot\mathbf{P} + C|\mathbf{Q}|^2\mathbf{Q}\cdot\mathbf{P})\right)\mathrm{dV} \\ &\quad + \frac{\lambda}{L}\int_\Gamma \left(2\alpha_z(\mathbf{P}\hat{\mathbf{z}}\cdot\hat{\mathbf{z}})\left(\mathbf{Q}\hat{\mathbf{z}}\cdot\hat{\mathbf{z}} + \frac{s_+}{3}\right) + 2\gamma_z(\mathbf{I}-\hat{\mathbf{z}}\otimes\hat{\mathbf{z}})\mathbf{Q}\hat{\mathbf{z}}\cdot(\mathbf{I}-\hat{\mathbf{z}}\otimes\hat{\mathbf{z}})\mathbf{P}\hat{\mathbf{z}}\right)\mathrm{dS}.\end{aligned}$$

Since $\mathbf{Q},\mathbf{P} \in \mathcal{S}_0$, we have that $\mathbf{Q}\cdot\mathbf{P} := \mathrm{tr}(\mathbf{QP}) = Q_{ij}P_{ij}$. Integrating by parts,

and noting that tr$\mathbf{P} = 0$, gives

$$\begin{aligned} 0 = &\int_V \left(-\Delta\mathbf{Q} + \frac{\lambda^2}{L}\left(A\mathbf{Q} - B\mathbf{Q}^2 + \frac{B}{3}|\mathbf{Q}|^2\mathbf{I} + C|\mathbf{Q}|^2\mathbf{Q}\right)\right)\cdot\mathbf{P}\,\mathrm{dV} \\ &+ \underbrace{\int_V \nabla\mathbf{Q}\cdot\mathbf{P}\,\mathrm{dV}}_{\underset{div.thm.}{=}\int_\Gamma \partial_\nu\mathbf{Q}\cdot\mathbf{P}\,\mathrm{dS}} \\ &+ \frac{\lambda}{L}\int_\Gamma \left(2\alpha_z(\mathbf{P}\hat{\mathbf{z}}\cdot\hat{\mathbf{z}})\left(\mathbf{Q}\hat{\mathbf{z}}\cdot\hat{\mathbf{z}} + \frac{s_+}{3}\right) + 2\gamma_z(\mathbf{I}-\hat{\mathbf{z}}\otimes\hat{\mathbf{z}})\mathbf{Q}\hat{\mathbf{z}}\cdot(\mathbf{I}-\hat{\mathbf{z}}\otimes\hat{\mathbf{z}})\mathbf{P}\hat{\mathbf{z}}\right)\mathrm{dS} \end{aligned} \tag{3.2.25}$$

We consider the surface energy terms in (3.2.25) separately. We remark that

$$\begin{aligned} (\mathbf{P}\hat{\mathbf{z}}\cdot\hat{\mathbf{z}})\left(\mathbf{Q}\hat{\mathbf{z}}\cdot\hat{\mathbf{z}} + \frac{s_+}{3}\right) &= \left(Q_{33} + \frac{s_+}{3}\right)P_{33} \\ &= \begin{pmatrix} -\frac{1}{3}\left(Q_{33}+\frac{s_+}{3}\right) & 0 & 0 \\ 0 & -\frac{1}{3}\left(Q_{33}+\frac{s_+}{3}\right) & 0 \\ 0 & 0 & \frac{2}{3}\left(Q_{33}+\frac{s_+}{3}\right) \end{pmatrix}\cdot\mathbf{P} \end{aligned} \tag{3.2.26}$$

and

$$(\mathbf{I}-\hat{\mathbf{z}}\otimes\hat{\mathbf{z}})\mathbf{Q}\hat{\mathbf{z}}\cdot(\mathbf{I}-\hat{\mathbf{z}}\otimes\hat{\mathbf{z}})\mathbf{P}\hat{\mathbf{z}} = \sum_{i=1}^{2} Q_{i3}P_{i3} = \frac{1}{2}\begin{pmatrix} 0 & 0 & Q_{13} \\ 0 & & Q_{23} \\ Q_{13} & Q_{23} & 0 \end{pmatrix}\cdot\mathbf{P} \tag{3.2.27}$$

By combining (3.2.25), (3.2.26) and (3.2.27), we finally obtain

$$\begin{aligned} \int_V \left(-\Delta\mathbf{Q} + \frac{\lambda^2}{L}\left(A\mathbf{Q} - B\mathbf{Q}^2 + \frac{B}{3}|\mathbf{Q}|^2\mathbf{I} + C|\mathbf{Q}|^2\mathbf{Q}\right)\right)\cdot\mathbf{P}\,\mathrm{dV} \\ + \int_\Gamma \left(\partial_\nu\mathbf{Q} + \frac{\lambda}{L}\mathbf{H}(\mathbf{Q})\right)\cdot\mathbf{P}\,\mathrm{dS} = 0, \end{aligned}$$

for any perturbation $\mathbf{P} \in W^{1,2}(V, \mathcal{S}_0)$ such that $\mathbf{P} = \mathbf{0}$ on $\partial V \setminus \Gamma$, and the lemma follows. □

Due to the boundary conditions (3.2.24) on Γ, z-independent solutions ($\partial_z \mathbf{Q} = \mathbf{0}$) may not, in general, be solutions of the 3D problem with weak anchoring on the top and bottom plates. However, we may infer from previous results, that there are z-independent 3D solutions for a specific temperature.

Corollary 3.2.11. *There exist z-independent solutions of (3.2.1), that satisfy (3.1.2) and (3.2.24), if $A = -\frac{B^2}{3C}$.*

Proof. We note from Proposition 3.2.5, the existence of solutions of (3.2.1) of the form (3.2.16), that satisfy the Dirichlet boundary conditions (3.1.2) on the lateral surfaces. Furthermore, from Proposition 3.2.8, we know that at the special temperature $A = -\frac{B^2}{3C}$, we have $q_3 = -\frac{s_+}{6}$ everywhere in $\Omega \times (0, \epsilon)$. It is necessarily the case that $Q_{33} = -\frac{s_+}{3}$, and hence the condition (3.2.24) reduces to the z-independent condition $\partial_z \mathbf{Q} = \mathbf{0}$ on Γ. □

Lemma 3.2.12. *There exists a constant M (depending only on A, B, and C) such that any solution $\mathbf{Q}$ of the Euler-Lagrange system (3.2.1), subject to the boundary conditions (3.1.2) and (3.2.24), satisfies*

$$|\mathbf{Q}| \leq M \quad \textit{in} \quad V. \tag{3.2.28}$$

Proof. This proof is analogous to the one in Proposition 1.4.2, where surface energy terms were neglected in the LdG energy. To begin, we define $\mathbf{P} := \mathbf{Q} + \frac{s_+}{2}(\hat{\mathbf{z}} \otimes \hat{\mathbf{z}})$. We have that $\partial_\nu(\frac{1}{2}|\mathbf{P}|^2) = \partial_\nu \mathbf{P} \cdot \mathbf{P} = \partial_\nu \mathbf{Q} \cdot \mathbf{P}$. Then, by the constraint on the top and bottom plates (3.2.24), we deduce that

$$\begin{aligned} -\frac{L}{\lambda}\partial_\nu(\frac{1}{2}|\mathbf{P}|^2) &= \mathbf{H}(\mathbf{Q}) \cdot \mathbf{P} \\ &= 2\gamma_z \sum_{i=1}^{2} Q_{i3}^2 + \frac{2}{3}\alpha_z \left(Q_{33} + \frac{s_+}{3}\right)(-Q_{11} - Q_{22} + 2Q_{33} + s_+) \end{aligned}$$

$$= 2\gamma_z \sum_{i=1}^{2} Q_{i3}^2 + 2\alpha_z \left(Q_{33} + \frac{s_+}{3} \right)^2 \geq 0 \quad \text{on} \quad \Gamma. \tag{3.2.29}$$

Similarly, we manipulate the Euler-Lagrange system (3.2.1) to obtain

$$\begin{aligned} \frac{L}{\lambda^2}\Delta(|\mathbf{P}|^2/2) &= \frac{L}{\lambda^2}\Delta\mathbf{Q} \cdot \left(\mathbf{Q} + \frac{s_+}{2}\hat{\mathbf{z}} \otimes \hat{\mathbf{z}} \right) + \frac{L}{\lambda^2}|\nabla\mathbf{Q}|^2 \\ &\geq A|\mathbf{Q}|^2 - B\mathrm{tr}\mathbf{Q}^3 + C|\mathbf{Q}|^4 \\ &\quad + \frac{s_+}{2}\left(\left(A + C|\mathbf{Q}|^2\right) Q_{33} - BQ_{3k}Q_{3k} + \frac{B}{3}|\mathbf{Q}|^2 \right) \end{aligned} \tag{3.2.30}$$

The right-hand side of (3.2.30) is a quartic polynomial in $\mathbf{Q}$, with leading order term $C|\mathbf{Q}|^4$ and $C > 0$. Therefore, there exists some positive number $M_1 := M_1(A, B, C)$ such that the right-hand side of (3.2.30) is positive when $|\mathbf{Q}| \geq M_1$. By the triangle inequality, we have

$$|\mathbf{P}| \geq M_2 := M_1 + \frac{s_+}{2} \quad \Longrightarrow \quad |\mathbf{Q}| = \left| \mathbf{P} - \frac{s_+}{2}\hat{\mathbf{z}} \otimes \hat{\mathbf{z}} \right| \geq M_1$$

and hence, the right-hand side of (3.2.30) is positive when $\mathbf{P} \geq M_2$. Finally, the boundary datum $\mathbf{Q}_b$ on the lateral surfaces, defined by (3.1.2), satisfies $|\mathbf{Q}_b| \leq \sqrt{\frac{2}{3}}s_+$ on $\partial\Omega \times (0, \epsilon)$. By applying the maximum principle to (3.2.29) and (3.2.30), we obtain that

$$|\mathbf{P}| \leq \max\left\{ M_2, \left(\sqrt{\frac{2}{3}} + \frac{1}{2} \right) s_+ \right\} \quad \text{in} \quad V.$$

By the triangle inequality, $\mathbf{Q}$ is also bounded in terms of A, B and C only. □

We wish to construct WORS-like solutions for this 3D problem, with imposed surface energies on the top and bottom plates. Recall that we may completely describe these solutions in terms of two degree of freedom. In 3D, these solutions

have the following form:

$$\mathbf{Q} = q_1(x,y,z)(\mathbf{n}_1 \otimes \mathbf{n}_1 - \mathbf{n}_2 \otimes \mathbf{n}_2) + q_3(x,y,z)(2\hat{\mathbf{z}} \otimes \hat{\mathbf{z}} - \mathbf{n}_1 \otimes \mathbf{n}_1 - \mathbf{n}_2 \otimes \mathbf{n}_2). \tag{3.2.31}$$

We shall adapt the methods in [62], for all values of λ and ϵ, to prove the existence of WORS-type solutions satisfying these boundary conditions.

Proposition 3.2.13. *For any λ, ϵ and A, there exists a solution of the form (3.2.31), of the system (3.2.1), subject to the boundary conditions (3.1.2) and (3.2.24), which satisfies the symmetry property*

$$xyq_1(x,y,z) \geq 0, \quad \textit{for any} \quad (x,y,z) \in V,$$

with $q_1 = 0$ along the square diagonals, and has $q_3 < 0$ on V.

Proof. We use a similar approach to that used in Proposition 3.2.5. We define the following quadrant of the 3D square well, V:

$$V_+ := \{(x,y,z) \in V : \, x,y > 0\}.$$

Consider the associated LdG energy functional among the finite energy pairs $(q_1, q_3) \in W^{1,2}(V_+; \mathbb{R}^2)$:

$$\begin{aligned} G[q_1,q_3] := &\int_{V_+} |\nabla q_1|^2 + 3|\nabla q_3|^2 \, \mathrm{dV} \\ &+ \frac{\lambda^2}{L} \int_{V_+} \left\{ A(q_1^2 + q_3^2) + C(q_1^2 + 3q_3^2)^2 + 2Bq_3(q_1^2 - q_3^2) \right\} \mathrm{dV} \\ &+ \frac{2\lambda\alpha_z}{L} \int_{\Gamma \cap \overline{V_+}} \left(q_3 + \frac{s_+}{6} \right)^2 \mathrm{dS}, \end{aligned}$$

obtained by substituting the ansatz (3.2.31) into $\mathcal{F}_{\lambda,s}$. We minimize G, subject

to the constraint $q_3 \leq 0$ on V, and the following boundary conditions:

$$(q_1, q_3) = (q_{1b}, -\frac{s_+}{6}) \quad \text{on} \quad (\partial\Omega \times (0, \epsilon)) \cap \overline{V_+}, \quad q_1 = 0 \quad \text{on} \quad \partial V_+ \setminus \partial V, \tag{3.2.32}$$

where the function q_{1b} is defined by (3.2.5). As in Proposition 3.2.5, a routine application of the direct method of the calculus of variations shows that a minimizer (q_1^*, q_3^*) exists. Without loss of generality, we may assume $q_1^* \geq 0$ on V_+; otherwise we replace q_1^* with $|q_1^*|$, and note that

$$G[q_1^*, q_3^*] = G[|q_1^*|, q_3^*].$$

We claim that $q_3^* \leq -\delta$ for some strictly positive constant δ, depending only on A, B and C. The proof of this claim follows the same argument as in Proposition 3.2.2. Consider a function $\varphi \in W^{1,2}(V_+)$ such that $\varphi \geq 0$ in V_+, and $\varphi = 0$ on $\partial V \cap \overline{V_+}$. Then the admissible perturbation $\bar{q_3} := q_3^* - t\varphi$, for some small parameter $t \geq 0$, satisfies the following optimality condition

$$\left.\frac{\mathrm{d}}{\mathrm{d}t}\right|_{t=0} G[q_1^*, \bar{q_3}] \geq 0.$$

We deduce that

$$\int_{V_+} \left\{ -6\nabla q_3^* \cdot \nabla\varphi - \frac{\lambda^2}{L} f(q_1^*, q_3^*)\varphi \right\} \mathrm{dV} - \frac{4\lambda\alpha_z}{L} \int_{\Gamma \cap \overline{V_+}} \left(q_3 + \frac{s_+}{6} \right) \varphi \, \mathrm{dS} \geq 0, \tag{3.2.33}$$

where the function $f(q_1^*, q_3^*)$ is defined in Proposition 3.2.2 and analogously, we know that there exists a constant $\delta \in (0, \frac{s_+}{6})$ such that $f(q_1, q_3) > 0$ for any $q_1 \in \mathbb{R}$ and any $q_3 \in [-\delta, 0]$. We choose φ as in Proposition 3.2.2 and, due to (3.2.33), we deduce that $q_3^* \leq -\delta$ in V_+.

Since q_3^* is strictly negative, we can consider perturbations of the form $q_3^t :=$

$q_3^* + t\varphi$, irrespective of the sign of φ, provided that $|t|$ is sufficiently small. As a consequence, (q_1^*, q_3^*) solves the Euler-Lagrange system (3.2.4) on V_+ as well as the boundary conditions

$$\partial_\nu q_1 = 0, \quad \partial_\nu q_3 + \frac{4\lambda\alpha_z}{3L}\left(q_3 + \frac{s_+}{6}\right) = 0 \quad \text{on} \quad \Gamma \cap \overline{V_+}, \tag{3.2.34}$$

and $\partial_\nu q_3 = 0$ on $\partial V_+ \setminus \partial V$. We extend (q_1^*, q_3^*) to the whole of V by reflections about the planes $\{x = 0\}$ and $\{y = 0\}$:

$$q_1^*(x, y, z) := \text{sign}(xy) q_1^*(|x|, |y|, z), \quad q_3^*(x, y, z) := q_3^*(|x|, |y|, z),$$

for any $(x, y, z) \in V \setminus \overline{V_+}$. The functions q_1^*, q_3^*, defined as above, solve the Euler-Lagrange system (3.2.4) on $\Omega \setminus (\{x = 0\} \cup \{y = 0\})$. Applying the same argument based on elliptic regularity as in Proposition 3.2.2, shows that (q_1^*, q_3^*) is a solution of (3.2.4) on the whole of Ω. Finally, using (3.2.4), (3.2.32) and (3.2.34), we can check that the $\mathbf{Q}$-tensor associated with (q_1^*, q_3^*), as defined by (3.2.31), has all the required properties. □

Proposition 3.2.14. *There exists a positive number λ_0 (depending only on A, B, C) such that, when $\lambda < \lambda_0$ the system (3.2.1) has a unique solution that satisfies the boundary conditions (3.1.2) and (3.2.24).*

Proof. Consider the constant $M := M(A, B, C)$ given by Proposition 1.4.2. Any solution of the system (3.2.1), subject to the boundary conditions (3.1.2), (3.2.24), must belong to the class

$$\mathcal{X}_V = \{\mathbf{Q} \in W^{1,2}(V, \mathcal{S}_0) : |\mathbf{Q}| \leq M \quad \text{on} \quad V, \quad \mathbf{Q} = \mathbf{Q}_b \quad \text{on} \quad \partial\Omega \times (0, \epsilon)\}.$$

As in Proposition 3.2.3, it suffices to show that for any $M > 0$, there exists a number $\lambda_0 = \lambda_0(M, A, B, C, L, \Omega)$ such that, for $\lambda < \lambda_0$, the functional $\mathcal{F}_{\lambda,s}$ is strictly convex in $\mathcal{X}_V$. For any $\mathbf{Q}_1, \mathbf{Q}_2 \in \mathcal{X}_V$, we have

$$\begin{aligned}\mathcal{F}_{\lambda,s}\left(\frac{\mathbf{Q}_1+\mathbf{Q}_2}{2}\right) &= \int_V \left\{\frac{1}{8}|\nabla(\mathbf{Q}_1+\mathbf{Q}_2)|^2 + \frac{\lambda^2}{L} f_b\left(\frac{\mathbf{Q}_1+\mathbf{Q}_2}{2}\right)\right\} \mathrm{dV} \\ &\quad + \frac{\lambda}{L}\int_\Gamma f_s\left(\frac{\mathbf{Q}_1+\mathbf{Q}_2}{2}\right) \mathrm{dS} \\ &= \int_V \frac{1}{4}\left\{|\nabla\mathbf{Q}_1|^2 + |\nabla\mathbf{Q}_2|^2 - \frac{1}{2}|\nabla(\mathbf{Q}_1-\mathbf{Q}_2)|^2\right\} \mathrm{dV} \\ &\quad + \frac{\lambda^2}{L}\int_V f_b\left(\frac{\mathbf{Q}_1+\mathbf{Q}_2}{2}\right) \mathrm{dV} + \frac{\lambda}{L}\int_\Gamma f_s\left(\frac{\mathbf{Q}_1+\mathbf{Q}_2}{2}\right) \mathrm{dS}\end{aligned} \tag{3.2.35}$$

Since $f_s(\mathbf{Q})$ is a convex function of $\mathbf{Q}$, then we have

$$\int_\Gamma f_s\left(\frac{\mathbf{Q}_1+\mathbf{Q}_2}{2}\right) \mathrm{dS} \leq \frac{1}{2}\int_\Gamma \left(f_s(\mathbf{Q}_1) + f_s(\mathbf{Q}_2)\right) \mathrm{dS}. \tag{3.2.36}$$

We now focus our attention to the bulk term, f_b. Both $\mathbf{Q}_1$ and $\mathbf{Q}_2$ are equal to $\mathbf{Q}_b$ on the lateral surfaces of the well, $\partial\Omega \times (0,\epsilon)$, and hence, $\mathbf{Q}_1 - \mathbf{Q}_2 = \mathbf{0}$ on $\partial\Omega \times (0,\epsilon)$. For a.e. fixed $z_0 \in (0,\epsilon)$, by the Poincaré inequality on Ω, we have

$$||\mathbf{Q}_1(\cdot,\cdot,z_0) - \mathbf{Q}_2(\cdot,\cdot,z_0)||^2_{L^2(\Omega)} \leq c_1(\Omega)||\nabla_{x,y}(\mathbf{Q}_1(\cdot,\cdot,z_0) - \mathbf{Q}_2(\cdot,\cdot,z_0))||^2_{L^2(\Omega)} \tag{3.2.37}$$

where $c_1 > 0$ is a constant that only depends on the cross-sectional geometry Ω. By integrating (3.2.37) with respect to z_0, we deduce that

$$\int_V |\mathbf{Q}_1 - \mathbf{Q}_2|^2 \,\mathrm{dV} \leq c_1(\Omega)\int_V |\nabla(\mathbf{Q}_1 - \mathbf{Q}_2)|^2 \,\mathrm{dV}. \tag{3.2.38}$$

Since, $|\mathbf{Q}_1|$ and $|\mathbf{Q}_2|$ are bounded by M everywhere in V, we have

$$\int_V \left|f_b\left(\frac{\mathbf{Q}_1+\mathbf{Q}_2}{2}\right) - \frac{1}{2}f_b(\mathbf{Q}_1) - \frac{1}{2}f_b(\mathbf{Q}_2)\right| \mathrm{dV} \leq ||f_b||_{W^{2,\infty}(B_M)}\int_V |\mathbf{Q}_1 - \mathbf{Q}_2|^2 \,\mathrm{dV} \tag{3.2.39}$$

where $B_M := \{\mathbf{Q} \in \mathcal{S}_0 : |\mathbf{Q}| \leq M\}$ and $||f_b||_{W^{2,\infty}(B_M)}$ is a positive constant that bounds the second derivatives of f_b in B_M (in particular, $||f_b||_{W^{2,\infty}(B_M)}$ only

depends on M, A, B and C). Combining (3.2.38) and (3.2.39), we find a positive constant $c_2 = c_2(f_b, \Omega, M) := c_1(\Omega)||f_b||_{W^{2,\infty}(B_M)}$ such that

$$\int_V f_b\left(\frac{\mathbf{Q}_1+\mathbf{Q}_2}{2}\right)\,\mathrm{dV} \leq \frac{1}{2}\int_V (f_b(\mathbf{Q}_1)+f_b(\mathbf{Q}_2))\,\mathrm{dV} + c_2\int_V |\nabla(\mathbf{Q}_1-\mathbf{Q}_2)|^2\,\mathrm{dV} \tag{3.2.40}$$

Using (3.2.36) and (3.2.40) to bound the right-hand side of (3.2.35), we obtain

$$\mathcal{F}_{\lambda,s}\left(\frac{\mathbf{Q}_1+\mathbf{Q}_2}{2}\right) \leq \frac{1}{2}(\mathcal{F}_{\lambda,s}(\mathbf{Q}_1)+\mathcal{F}_{\lambda,s}(\mathbf{Q}_2)) + \left(\frac{c_2\lambda^2}{L}-\frac{1}{8}\right)\int_V |\nabla(\mathbf{Q}_1-\mathbf{Q}_2)|^2\,\mathrm{dV}$$

If we take $\lambda < \lambda_0 := \left(\frac{L}{8c_2}\right)^{1/2}$, then we have

$$\mathcal{F}_{\lambda,s}\left(\frac{\mathbf{Q}_1+\mathbf{Q}_2}{2}\right) \leq \frac{1}{2}(\mathcal{F}_{\lambda,s}(\mathbf{Q}_1)+\mathcal{F}_{\lambda,s}(\mathbf{Q}_2))$$

and the equality holds if, and only if, $\mathbf{Q}_1 = \mathbf{Q}_2$. Thus proving that $\mathcal{F}_{\lambda,s}$ is strictly convex in the class $\mathcal{X}_V$. □

We conclude that for λ small enough, the LdG energy functional $\mathcal{F}_{\lambda,s}$ has at most one critical point described by $\mathbf{Q}$-tensor solutions of the form (3.2.31), where (q_1, q_3) are the minimizers of the associated functional G from Proposition 3.2.13.

3.3 Summary

In this chapter we have analytically studied nematic equilibria on 3D square wells, with an emphasis on the WORS as a function of the well size, characterized by λ, and the well height, denoted by ϵ. Given the batch of papers on NLCs in square wells [52], [61]–[63], which consider shallow wells and model equilibria on a 2D square with tangent boundary conditions, it is natural to ask if the WORS is relevant for 3D domains or if they are a 2D artefact. Our essential findings in this

chapter show that the WORS is in fact a LdG critical point for 3D wells with a square cross-section and experimentally relevant tangent boundary conditions on the lateral surfaces. We have shown that the WORS exists, for arbitrary well height, with both natural boundary conditions and realistic surface energies on the top and bottom surfaces. In fact, for sufficiently small λ, the WORS is the global LdG minimizer for these 3D problems, exemplifying the 3D relevance of the WORS for all temperatures below the nematic supercooling temperature.

Chapter 4

Numerical simulations of three-dimensional nematic equilibria in confinement

Recently, there has been substantial interest in new applications for NLCs, where the typical confining geometry is microscopic. NLC systems of this size are often difficult to study experimentally, motivating a numerical approach to studying these problems. In this chapter, we build upon the analysis of nematic equilibrium solutions in 3D wells, in Chapter 3. We employ an energy-minimization based numerical approach to compute novel equilibrium solutions for square and rectangular 3D wells, and a Rayleigh-quotient iterative minimization method to assess the stability of these solutions. In Chapter 3, we proved that for small enough wells in three dimensions, the WORS is the unique global minimizer of the LdG free energy, given two physically relevant boundary conditions. In this chapter, we numerically compute the WORS in three dimensions, and study the

effects of varying domain size and anchoring strengths on the lateral surfaces of the well. For large enough wells, we numerically compute 3D diagonal and rotated configurations (as seen in [60] and [61] in the 2D case), as well as novel mixed equilibrium configurations that interpolate between two different diagonal director profiles on the top and bottom plates. We also compute two stable *escaped* configurations by employing weak anchoring conditions on the top and bottom surfaces of the domain. Furthermore, we study the effects of choosing a rectangular cross-sectional geometry for this 3D problem, and how the added geometrical anisotropy changes the solution landscape.

4.1 The computational model

Recall that we take a three-dimensional domain $V = \Omega \times (0, \epsilon)$, where ϵ is the rescaled height of the well, Ω is the 2D cross-sectional domain, and $\Gamma := \Omega \times \{0, \epsilon\}$ is the union of the top and bottom surfaces of the well. We wish to (numerically) minimize the rescaled LdG energy, $\mathcal{F}_\lambda$, defined in Chapter 3. As explained in Chapter 1, we may describe the preferred directions of the constituent liquid crystal molecules by the eigenvectors of the LdG $\mathbf{Q}$-tensor (1.4.1), and the degree of order about these preferred directions is given by the associated eigenvalues. We consider the most general form of $\mathbf{Q} \in \mathcal{S}_0$, in three dimensions:

$$\begin{aligned}\mathbf{Q}(x,y,z) = {} & q_1(x,y,z)(\hat{\mathbf{x}} \otimes \hat{\mathbf{x}} - \hat{\mathbf{y}} \otimes \hat{\mathbf{y}}) + q_2(x,y,z)(\hat{\mathbf{x}} \otimes \hat{\mathbf{y}} + \hat{\mathbf{y}} \otimes \hat{\mathbf{x}}) \\ & + q_3(x,y,z)(2\hat{\mathbf{z}} \otimes \hat{\mathbf{z}} - \hat{\mathbf{x}} \otimes \hat{\mathbf{x}} - \hat{\mathbf{y}} \otimes \hat{\mathbf{y}}) \\ & + q_4(x,y,z)(\hat{\mathbf{x}} \otimes \hat{\mathbf{z}} + \hat{\mathbf{z}} \otimes \hat{\mathbf{x}}) + q_5(x,y,z)(\hat{\mathbf{y}} \otimes \hat{\mathbf{z}} + \hat{\mathbf{z}} \otimes \hat{\mathbf{y}}),\end{aligned} \tag{4.1.1}$$

where $\hat{\mathbf{x}}$, $\hat{\mathbf{y}}$ and $\hat{\mathbf{z}}$ are unit-vectors in the x-, y- and z-directions, respectively. Instead of solving the Euler-Lagrange equations for $\mathcal{F}_\lambda$, we reduce the problem

to that of finding solutions $\mathbf{Q}$ that make it stationary i.e., $\mathcal{D}\mathcal{F}_\lambda(\mathbf{Q}) = 0$, where $\mathcal{D}\mathcal{F}_\lambda(\mathbf{Q})$ is the Fréchet derivative of $\mathcal{F}_\lambda$, evaluated at $\mathbf{Q}$. To this end, we use an energy-minimization based numerical method to find the minimizer of the current system [65]. Furthermore, computing finite-energy $\mathbf{Q}$-tensors is computationally expensive. To remedy this problem, we may follow the approach of [95], by analysing a function of the scalar coordinates $\mathbf{q} = (q_1, \dots, q_5)$, rather than the energy functional $\mathcal{F}_\lambda$ directly. This is because the macroscopic order parameter $\mathbf{Q} \in \mathcal{S}_0$ is described by the unique representation $\mathbf{Q} = q_i E_i$, where $\{E_i\}_{i=1}^5$ is an orthonormal basis of $\mathcal{S}_0$, and $q_i = \mathrm{tr}(\mathbf{Q}E_i)$ - forming an isometric isomorphism between $W^{1,2}(V;\mathcal{S}_0)$ and $W^{1,2}(V;\mathbb{R}^5)$. For $\mathbf{Q}$-tensors of the form (4.1.1), the LdG energy functional reduces to the following functional with respect to the scalar functions $q_i \in W^{1,2}(V;\mathbb{R})$:

$$\begin{aligned}\mathcal{F}_\lambda[q_1,\dots,q_5] = \int_V \Big\{ &|\nabla q_1|^2 + |\nabla q_2|^2 + 3|\nabla q_3|^2 + |\nabla q_4|^2 + |\nabla q_5|^2 \Big\}\ \mathrm{dV} \\ &+ \frac{\lambda^2}{L}\int_V \Big\{ A(q_1^2 + q_2^2 + 3q_3^2 + q_4^2 + q_5^2) \\ &\quad + B\left(q_3(-2q_1^2 - 2q_2^2 + 2q_3^2 + q_4^2 + q_5^2) + q_1(q_4^2 - q_5^2) + 2q_2q_4q_5\right) \\ &\quad + C(q_1^2 + q_2^2 + 3q_3^2 + q_4^2 + q_5^2)^2 \Big\}\ \mathrm{dV} \end{aligned} \tag{4.1.2}$$

For computational convenience, we take $\Omega \subset \mathbb{R}^2$ to be a square with sides parallel to the coordinate axes i.e., $\Omega = (-1,\, 1)^2$. We note that in the analysis of the system, subject to infinite anchoring boundary conditions, it was necessary to truncate the corners of Ω. Without this truncation, the boundary condition leads to a natural mismatch at the vertices of the well, leading to point defects at each corner with infinite Dirichlet/elastic energy in 2D. This can be rectified by introducing a scalar order parameter which vanishes at the point defects. In our numerical simulations, we will employ a surface energy term that mimics the behaviour of an infinite anchoring condition, for sufficiently large values of the

anchoring coefficient. This is a more physically realistic modelling choice, and is computationally convenient as it allows us to study solutions without excluding the corners of the well [88]. More precisely, we minimize the LdG energy functional

$$\mathcal{F}_\lambda[\mathbf{Q}] + \int_{\partial V} f_s(\mathbf{Q})\,\mathrm{dS}. \tag{4.1.3}$$

We impose surface energies on $\partial\Omega \times (0, \epsilon)$, given by [52] in the non-dimensionlized setting:

$$\begin{aligned} f_s(\mathbf{Q}) &= \omega \left(\mathbf{Q} - g(x) \left(\hat{\mathbf{x}} \otimes \hat{\mathbf{x}} - \frac{1}{3}\mathbf{I} \right) \right)^2, \quad y = -1, 1; \\ f_s(\mathbf{Q}) &= \omega \left(\mathbf{Q} - g(y) \left(\hat{\mathbf{y}} \otimes \hat{\mathbf{y}} - \frac{1}{3}\mathbf{I} \right) \right)^2, \quad x = -1, 1. \end{aligned} \tag{4.1.4}$$

In this weak anchoring condition, we take $\omega = \frac{W\lambda}{L}$ to be the non-dimensionalized anchoring strength, where W is the surface anchoring on the lateral surfaces of the well. We take the function $g \in C^\infty([-1, 1])$ so as to eliminate the discontinuity at the corners. In our simulations we choose

$$g(s) = s_+, \quad \forall s \in [-1 + \eta, 1 - \eta], \qquad g(-1) = g(1) = 0,$$

for a small, but fixed value, η. The choice of g does not affect the numerical results qualitatively. Note how the form of (4.1.4) enforces a preferred tangential orientation on each of the lateral surfaces. Unless stated otherwise, we take $W = 10^{-2}\mathrm{Jm}^{-2}$, which is a suitable value to mimic strong anchoring on the lateral sides of well [96]. In order to complement the analysis in Section 3.2.3, we also impose finite tangential anchoring on the top and bottom surfaces, Γ, given by

$$f_s(\mathbf{Q}) = w_z \left(\alpha_z \left(\mathbf{Q}\hat{\mathbf{z}} \cdot \hat{\mathbf{z}} + \frac{1}{3}s_+ \right)^2 + \gamma_z \left| \left(\mathbf{I} - \hat{\mathbf{z}} \otimes \hat{\mathbf{z}} \right) \mathbf{Q}\hat{\mathbf{z}} \right|^2 \right), \tag{4.1.5}$$

where $w_z = \frac{W_z\lambda}{L}$ is the non-dimensionalized anchoring strength on Γ, W_z is the surface anchoring on Γ, and $\alpha_z, \gamma_z > 0$. The surface energy (4.1.5) favours $\mathbf{Q}$-tensors with $\hat{\mathbf{z}}$ as an eigenvector, with associated eigenvalue $-\frac{s_+}{3}$, and hence this

choice of surface energy induces planar boundary conditions on Γ.

4.2 The numerical methods

In the Landau-de Gennes framework, numerical simulations of equilibrium configurations within these confining geometries have so far been restricted to the two-dimensional case [61], [62]. The extension to solving the full 3D system is computationally expensive and hence, we employ an energy minimization based numerical scheme which we describe in this section. To begin, we re-scale the physical domain to be

$$V_c = \{(\bar{x}, \bar{y}, \bar{z}) \mid \bar{x} \in [0, 2\pi], \bar{y} \in [0, 2\pi], \bar{z} \in [-1, 1]\}.$$

Since $\mathbf{Q} \in \mathcal{S}_0$ is a symmetric and traceless matrix, it may be written as a matrix involving five scalar order parameters, $p_i \in W^{1,2}(V_c; \mathbb{R})$, $i = 1, \ldots, 5$:

$$\mathbf{Q} = \begin{pmatrix} p_1 & p_2 & p_3 \\ p_2 & p_4 & p_5 \\ p_3 & p_5 & -p_1 - p_4 \end{pmatrix}.$$

The p_i are simply linear combinations of the original q_i scalar order parameters in (4.1.1). We expand the p_i in terms of special functions: Fourier series on $\bar{x}$ and $\bar{y}$, and Chebyshev polynomials on $\bar{z}$ i.e.,

$$p_i(\bar{x}, \bar{y}, \bar{z}) = \sum_{l=1-L}^{L-1} \sum_{m=1-M}^{M-1} \sum_{n=0}^{N-1} p_i^{lmn} X_l(\bar{x}) Y_m(\bar{y}) Z_n(\bar{z}), \tag{4.2.1}$$

where L, M, N specify the truncation limits of the expanded series, and X_l and Y_m are defined as

$$X_l(\bar{x}) = \begin{cases} \cos l\bar{x}, & l \geq 0, \\ \sin |l|\bar{x}, & l < 0, \end{cases} \qquad Y_m(\bar{y}) = \begin{cases} \cos m\bar{y}, & m \geq 0, \\ \sin |m|\bar{y}, & m < 0. \end{cases}$$

The derivative of this periodic extension is continuous, and the smoothing function, $g \in C^\infty([-1,1])$, prevents any discontinuities that form around the corners of the domain. Inserting the coefficients of the spectral expansion of $\mathbf{Q}$, (4.2.1), into the LdG free energy (4.1.3), we obtain a function of $\mathbf{p} = (p_i^{lmn}) \in \mathbb{R}^D$, where $D = (2L-1) \times (2M-1) \times N$. We wish to minimize this discretized energy using numerical optimization methods which we shall describe below. By discretizing the LdG free energy, with respect to $\mathbf{p}$, we avoid any computation of nonlinear terms in the Euler-Lagrange equations. By using the chain rule, and numerical integration, we may obtain the derivatives of the discrete free energy required.

4.2.1 Limited-memory BFGS

Define the LdG free energy (4.1.3), with with respect to the discretized $\mathbf{Q}$-tensor, as $F(\mathbf{p})$. Minimizers of $F(\mathbf{p})$ can be found by some standard optimization methods. In any numerical optimization method, one key concept is that of a line search. This is an iterative approach to find the local minimum of an objective function. The iteration itself is given by

$$\mathbf{p}_{k+1} = \mathbf{p}_k + \alpha_k \mathbf{d}_k, \tag{4.2.2}$$

where α_k is a positive scalar value called the 'step length', and a 'search direction', d_k. In our numerical method, we use the strong Wolfe conditions for our line search requirements [97]. These conditions guarantee that the step length at the

k^{th} iteration, α_k, should give a sufficient decrease in the objective function F, measured by

$$F(\mathbf{p}_k + \alpha_k \mathbf{d}_k) \leq F(\mathbf{p}_k) + c_1 \alpha_k \nabla F_k^T \mathbf{d}_k, \qquad c_1 \in (0, 1). \tag{4.2.3}$$

This condition enforces the reduction in F to be proportional to the step length α_k, and the directional derivative $\nabla F_k^T \mathbf{d}_k$. To avoid step lengths that are unacceptably short, a second requirement is employed - typically referred to as the 'curvature condition', which requires α_k to satisfy the following inequality:

$$|\nabla F(\mathbf{p}_k + \alpha_k \mathbf{d}_k)^T \mathbf{d}_k| \geq c_2 |\nabla F_k^T \mathbf{d}_k|, \qquad c_2 \in (c_1, 1). \tag{4.2.4}$$

This condition guarantees that, the gradient of the new objective function at α_k, is greater than c_2 times the original gradient, whilst excluding points that are far from the stationary points. A backtracking approach ensures that these line search conditions are fulfilled. In the following simulation, we mainly use L-BFGS, which is a type of quasi-Newton method, and approximates the Broyden-Fletcher-Goldfarb-Shanno (BFGS) algorithm using a restricted amount of computer memory [98]. The benefit of using a quasi-Newton method is that search directions do not require the expensive computation of the Hessian (as in regular Newton methods), but an approximation B_k, which is updated after each iteration. The new Hessian approximation, B_{k+1}, is given by the following formula:

$$B_{k+1} = B_k - \frac{B_k \mathbf{s}_k \mathbf{s}_k^T B_k}{\mathbf{s}_k^T B_k \mathbf{s}_k} + \frac{g_k g_k^T}{g_k^T \mathbf{s}_k}, \tag{4.2.5}$$

where the displacement vector, $\mathbf{s}_k$, and change of gradient vector, g_k, are given by

$$\mathbf{s}_k = \mathbf{p}_{k+1} - \mathbf{p}_k, \qquad g_k = \nabla F_{k+1} - \nabla F_k. \tag{4.2.6}$$

Note that the Hessian approximation, according to (4.2.5), will satisfy the secant equation $B_{k+1}\mathbf{s}_k = g_k$. This is a requirement of any quasi-Newton scheme in order to simulate the properties of the true Hessian. In the BFGS method, each update can be derived by imposing conditions on the inverses of the Hessian approximations, $H_k = B_k^{-1}$. The solution to the new approximation is then given by the following formula

$$H_{k+1} = (\mathbf{I} - \rho_k \mathbf{s}_k g_k^T) H_k (\mathbf{I} - \rho_k g_k \mathbf{s}_k^T) + \rho_k \mathbf{s}_k \mathbf{s}_k^T, \tag{4.2.7}$$

where $\rho_k = \frac{1}{g_k^T \mathbf{s}_k}$. Provided a sufficiently good initial guess for the Hessian is chosen, this method usually converges to a local minimizer, but it is not necessarily guaranteed. Limited-memory BFGS (L-BFGS) is based on this updating formula, but only stores recent information to construct the Hessian approximations, and is therefore less computationally expensive. The L-BFGS algorithm uses the curvature information from the m most recent iterations and, in our simulations, we have $m = 20$ which is sufficient for our problem. We state the typical L-BFGS algorithm below for clarity.

Choose starting point $\mathbf{p}_0$, integer $m > 0$;
$k \leftarrow 0$;
repeat
  Choose initial matrix H_k^0;
  Compute $\mathbf{d}_k \leftarrow -H_k \nabla F_k$;
  Compute $\mathbf{p}_{k+1} \leftarrow \mathbf{p}_k + \alpha_k \mathbf{d}_k$, where α_k satisfies the strong Wolfe conditions (4.2.3);
  if $k > m$ **then**
    Discard the vector pair $\{\mathbf{s}_{k-m}, g_{k-m}\}$ from storage;
  end
  Compute and save $\mathbf{s}_k \leftarrow \mathbf{p}_{k+1} - \mathbf{p}_k$, $g_k = \nabla F_{k+1} - \nabla F_k$;
  $k = k + 1$;
until *convergence*;

Algorithm 1: L-BFGS

Provided we have set a suitable initial guess, this algorithm runs until the termin-

ation criterion $||\nabla F|| \leq 10^{-5}$ is satisfied.

4.2.2 Stability of solutions

Given the twice Fréchet differentiable energy functional $F(\mathbf{p})$, found numerically by the procedure described above, we denote its Hessian by $\mathbf{G}(\mathbf{p}) = \nabla^2 F(\mathbf{p})$. A point $\mathbf{p}$ is called a critical point of $F(\mathbf{p})$, if $||\nabla F(\mathbf{p})|| = 0$ holds. A saddle point of $F(\mathbf{p})$ is any unstable critical point which is not a local extremum. As stated in Morse theory, the index of a saddle point $\mathbf{p}$ is defined as the maximal dimension of a subspace $\mathcal{K}$, on which the operator $\mathbf{G}(\mathbf{p})$ is negative definite. Similarly to [64], we can justify the stability of an obtained solution $\mathbf{p}$ by computing the smallest eigenvalue, λ_1, of Hessian matrix $\mathbf{G}(\mathbf{p})$ corresponding to $\mathbf{p}$:

$$\lambda_1 = \min_{\mathbf{v}\neq 0, \mathbf{v}\in\mathbb{R}^D} \frac{\langle \mathbf{G}(\mathbf{p})\mathbf{v},\, \mathbf{v}\rangle}{\langle \mathbf{v}, \mathbf{v}\rangle}, \tag{4.2.8}$$

where $\langle \cdot,\, \cdot \rangle$ is the standard inner product in $\mathbb{R}^D$. This optimization problem corresponds to searching for index-1 saddle points numerically (see [66] for further explanation on the numerical methodology of finding saddle point solutions). The right-hand side of (4.2.8) is equivalent to taking general admissible perturbations with respect to the five independent basis directions, and minimizing the second variation of the discretized LdG energy, $F(\mathbf{p})$, with respect to those perturbations - a common approach to studying the stability of solutions in the calculus of variations. If the smallest eigenvalue λ_1 is positive, this indicates that the second variation is positive for all admissible perturbations, and hence a solution is (numerically) locally stable. Note that the optimization problem in (4.2.8) is equivalent to minimizing $\langle \mathbf{G}(\mathbf{p})\mathbf{v}, \mathbf{v}\rangle$, provided we impose the constraint $\langle \mathbf{v}, \mathbf{v}\rangle = 1$.

The associated Lagrangian function is then given by

$$\mathcal{L}(\mathbf{v};\xi) = \frac{\langle \mathbf{G}(\mathbf{p})\mathbf{v}, \mathbf{v}\rangle}{\langle \mathbf{v}, \mathbf{v}\rangle} - \xi(\langle \mathbf{v}, \mathbf{v}\rangle - 1),$$

where ξ is a Lagrangian multiplier. The dynamics of $\mathbf{v}$ is then given by the equation

$$\frac{\partial \mathbf{v}}{\partial t} = -\gamma \frac{\partial}{\partial \mathbf{v}} \mathcal{L}(\mathbf{v};\xi) = -2\gamma \left(\frac{\mathbf{G}(\mathbf{p})\mathbf{v}}{\langle \mathbf{v}, \mathbf{v}\rangle} - \xi \mathbf{v} \right), \tag{4.2.9}$$

where $\gamma > 0$ is a relaxation parameter. Since we assume $\langle \mathbf{v}, \mathbf{v}\rangle = 1$ always holds, the dynamics in (4.2.9) should satisfy $\langle \mathbf{v}, \frac{\partial \mathbf{v}}{\partial t}\rangle = 0$, which implies $\xi = \frac{\langle \mathbf{G}(\mathbf{p})\mathbf{v}, \mathbf{v}\rangle}{\langle \mathbf{v}, \mathbf{v}\rangle}$, and hence we are left with the the following gradient flow equation for $\mathbf{v}$:

$$\frac{\partial \mathbf{v}}{\partial t} = -\frac{2\gamma}{\langle \mathbf{v},\, \mathbf{v}\rangle} \left(\mathbf{G}\mathbf{v} - \frac{\langle \mathbf{G}\mathbf{v},\, \mathbf{v}\rangle}{\langle \mathbf{v},\, \mathbf{v}\rangle} \mathbf{v} \right). \tag{4.2.10}$$

The key idea behind this method is that the dynamic solutions evolve along a path of decreasing energy, and hence converge to a stable equilibrium over long times [99]. In our code, we find the smallest eigenvalue of the Hessian matrix $\mathbf{G}(\mathbf{p})$, by solving (4.2.10), and $\mathbf{G}\mathbf{v} = \mathbf{G}(\mathbf{p})\mathbf{v}$ is approximated by a central difference formula:

$$\mathbf{G}(\mathbf{p})\mathbf{v} \approx -\frac{\nabla_D F(\mathbf{p} + \ell \mathbf{v}) - \nabla_D F(\mathbf{p} - \ell \mathbf{v})}{2\ell},$$

for some small constant ℓ. The approximation error here is $\mathcal{O}(\ell)$. We can choose γ to appropriately accelerate the convergence of the dynamic system (4.2.10) but in our numerical simulations, we simply take $\gamma = 1$.

4.2.3 Initial guesses

It was shown in [64], that for λ large enough, there exist multiple stable states within the two-dimensional setting. Therefore, a 'close' initial guess is important

in achieving proper convergence in the 3D numerical procedure. The states we are referring to are commonly called the *diagonal* and *rotated* configurations. These are solutions described by $\mathbf{Q}$-tensors of the form

$$\mathbf{Q} = q\left(\mathbf{n}\otimes\mathbf{n} - \frac{\mathbf{I}_2}{2}\right) + q_3\left(\hat{\mathbf{z}}\otimes\hat{\mathbf{z}} - \frac{\mathbf{I}_3}{3}\right), \tag{4.2.11}$$

where $\mathbf{n} = (\cos\theta, \sin\theta, 0)$, and $\mathbf{I}_2, \mathbf{I}_3$ are the identity matrices in two and three dimensions, respectively. Furthermore, $q > 0$, $q_3 < 0$. What this means physically is that, nematic molecules prefer to orient themselves perpendicular to the z-direction i.e., molecules lie in the (x, y)-plane. In this chapter, we will frequently refer to the two diagonal states as D_1, D_2, where the nematic director $\mathbf{n}$ roughly aligns along one of the diagonals of Ω. We also refer to the four possible rotated states as $R_1, \ldots, R_4$, where θ rotates approximately π radians between a pair of opposite edges. In our numerical simulations, when choosing an initial step for the L-BFGS algorithm, we set $\mathbf{Q} = s_+(\mathbf{n}\otimes\mathbf{n} - \frac{1}{3}\mathbf{I}_3)$, where our choice of $\mathbf{n}$ determines the director profile. In order to simulate any of the diagonal/rotated configurations in the domain, we choose the director as follows:

Configuration	Director $\mathbf{n}(x,y,z)$
(D1)	$\frac{1}{\sqrt{2}}(1,1,0)$
(D2)	$\frac{1}{\sqrt{2}}(-1,1,0)$
(R1)	$\begin{cases} (0,1,0), & x \le 0, \\ \frac{1}{\sqrt{2}}(1,1,0), & x,y > 0, \\ \frac{1}{\sqrt{2}}(-1,1,0), & x > 0, y \le 0, \end{cases}$
(R2)	$\begin{cases} (1,0,0), & y \ge 0, \\ \frac{1}{\sqrt{2}}(1,1,0), & x,y < 0, \\ \frac{1}{\sqrt{2}}(-1,1,0), & x \ge 0, y < 0, \end{cases}$
(R3)	$\begin{cases} (0,1,0), & x \ge 0, \\ \frac{1}{\sqrt{2}}(1,1,0), & x,y < 0, \\ \frac{1}{\sqrt{2}}(-1,1,0), & x < 0, y \ge 0, \end{cases}$
(R4)	$\begin{cases} (1,0,0), & y < 0, \\ \frac{1}{\sqrt{2}}(1,1,0), & x,y \ge 0, \\ \frac{1}{\sqrt{2}}(-1,1,0), & x < 0, y \ge 0. \end{cases}$

We frequently refer to these initial choices (configurations in the table above) when presenting the numerical results.

4.3 Numerical results

In this section, we present **Q**-tensor solutions which minimize the discretized LdG energy described in the previous section. We choose different initial guesses for a solution **Q** in the L-BFGS algorithm, and plot the results. We regularly plot

the biaxiality parameter $\beta^2(\mathbf{Q})$ (defined in (1.4.11)), which takes values from 0 to 1, given by colours blue to red, respectively. We also plot the director $\mathbf{n}$, which is found by computing the eigenvector corresponding to the largest positive eigenvalue of $\mathbf{Q}$. Following [63] for the two-dimensional numerical study, we fix the material constants in the LdG free energy to be typical values for the liquid crystal MBBA, and choose $A = -\frac{B^2}{3C}$ where

$$B = 0.64 \times 10^4\,\mathrm{Nm}^{-2}, \quad C = 0.35 \times 10^4\,\mathrm{Nm}^{-2}, \quad L = 4 \times 10^{-11}\,\mathrm{N}.$$

As expected from our analysis in Proposition 3.2.8, at this special temperature we have $q_3 = -\frac{s_+}{6} = -\frac{B}{6C}$ everywhere. The two key dimensionless variables are

$$\bar{\lambda}^2 = \frac{2C\lambda^2}{L}, \quad \epsilon = \frac{h}{\lambda},$$

which describe the cross-sectional size and height of the well, respectively.

4.3.1 Strong anchoring on the lateral surfaces

In this section, we focus on nematic equilibria inside wells with strong anchoring conditions on the lateral surfaces. More specifically, we find minimizers of the LdG energy functional $\mathcal{F}_\lambda$ using the numerical scheme described above, subject to infinite tangential Dirichlet conditions on $\partial\Omega\times(0,\epsilon)$. As described in the numerical methods section, we mimic the strong anchoring condition by minimizing the energy functional (4.1.3), with $W = 10^{-2}\mathrm{Jm}^{-2}$ in (4.1.4). For the top and bottom surfaces, we also take $W_z = 10^{-2}\mathrm{Jm}^{-2}$ in (4.1.5), which is sufficient to mimic the natural boundary condition on Γ from (3.2.2). We recall from Chapter 3, there exist z-independent critical points of the Landau-de Gennes energy $\mathcal{F}_\lambda$, subject to natural boundary conditions on the top and bottom plates, indeed our numerical

simulations throughout this section have $|\partial_z \mathbf{Q}|^2 \approx 10^{-12}$.

For sufficiently small values of $\bar{\lambda}^2$, we always get the WORS for arbitrary ϵ, in accordance with the uniqueness results for small λ in Chapter 3. Since we run our numerical simulations at the fixed temperature $A = -\frac{B^2}{3C}$, the WORS corresponds (see [62]) to a solution of the form

$$\mathbf{Q}_{WORS}(x, y, z) = q_1(\hat{\mathbf{x}} \otimes \hat{\mathbf{x}} - \hat{\mathbf{y}} \otimes \hat{\mathbf{y}}) - \frac{B}{6C}(2\hat{\mathbf{z}} \otimes \hat{\mathbf{z}} - \hat{\mathbf{x}} \otimes \hat{\mathbf{x}} - \hat{\mathbf{y}} \otimes \hat{\mathbf{y}}). \quad (4.3.1)$$

We plot the WORS for $\bar{\lambda}^2 = 5$ and $\epsilon = 4$ in Figure 4.1. This includes plots of (from left to right): a 3D representation of the full solution; the biaxiality parameter; the director profile; and the q_1 and q_2 components of the numerical solution $\mathbf{Q}$ in (4.1.1). As expected, we see that q_2 is close to zero throughout the domain. Each 2D plot is taken from the middle slice of the full 3D solution ($z = \frac{\epsilon}{2}$). Since this solution is the global minimizer for $\bar{\lambda}^2 = 5$, the choice of initial guess in the numerical procedure does not affect the final solution.

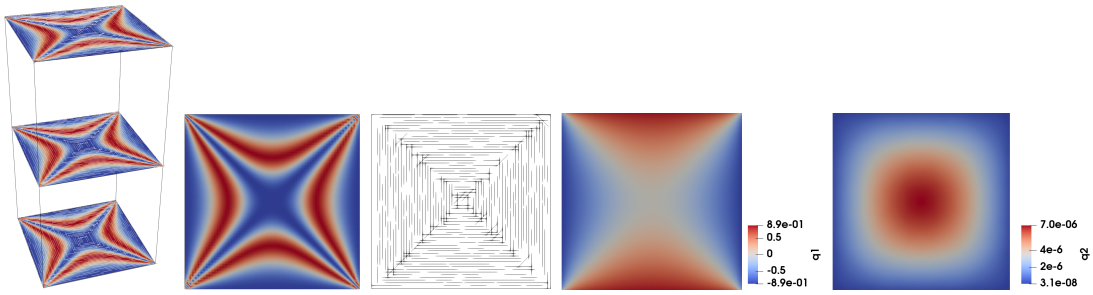

Figure 4.1: The 3D WORS with $\bar{\lambda}^2 = 5$ and $\epsilon = 4$.

For relatively large values of $\bar{\lambda}^2$, we find the well-known diagonal and rotated solutions. More specifically, the diagonal solutions exist for $\bar{\lambda}^2 \geq 6$, and the rotated solutions exist for $\bar{\lambda}^2 \geq 29$, in our simulations. If we consider the dimensionless parameters $\bar{\lambda}$ and ϵ, as well as our choice of material-dependent parameters (based on the typical values for the liquid crystal MBBA), diagonal solutions exist for

wells with an edge-length on the order of 180nm, and rotated solutions exist for wells with an edge-length on the order of 440nm. This is consistent with the work by [52], where the authors report the WORS is observable for cells with edge length $\lambda \sim 78 - 138$nm with respect to the bare biaxial correlation length. Another liquid crystal such as 5CB would typically take values $B = 2.1 \times 10^6\,\mathrm{Jm}^{-3}$ and $C = 1.7 \times 10^6\,\mathrm{Jm}^{-3}$ (as in [96]), but this does not drastically change the order of magnitude of our numerical findings with respect to molecular length scales. In fact, as stated in [52], the size of well for which we would expect to see the WORS does depend on temperature, with larger wells on the order of $\lambda \sim 240 - 420$nm exhibiting the WORS for larger temperatures. In our simulations, we have simply taken $A = -\frac{B^2}{3C}$ to complement our analysis in Chapter 3, and a further exploration of different temperature regimes would be an exciting avenue for future research. These z-invariant solutions were numerically reported in [60] in two dimensions, and are stable configurations in our simulations, for arbitrary well height, ϵ. These solutions are presented in Figures 4.2 and 4.3, respectively, where $\bar{\lambda}^2 = 100$ an $\epsilon = 4$. We obtain the diagonal solution by choosing the (D1) initial guess, and the rotated solution by choosing the (R1) initial guess. In both figures we plot: 3D representations of the numerical solution; the biaxiality parameter; the director profile $\mathbf{n}$; and the contributions from the q_1, q_2 scalar order parameters in (4.1.1). At the special temperature regime $A = -\frac{B^2}{3C}$ we have $q_3 = -\frac{B}{6C}$ everywhere in these numerical solutions, as expected from our analysis in Chapter 3. We may find the other diagonal and rotated configurations but they are equivalent under rotation about the z-axis, so we do not present these plots for brevity.

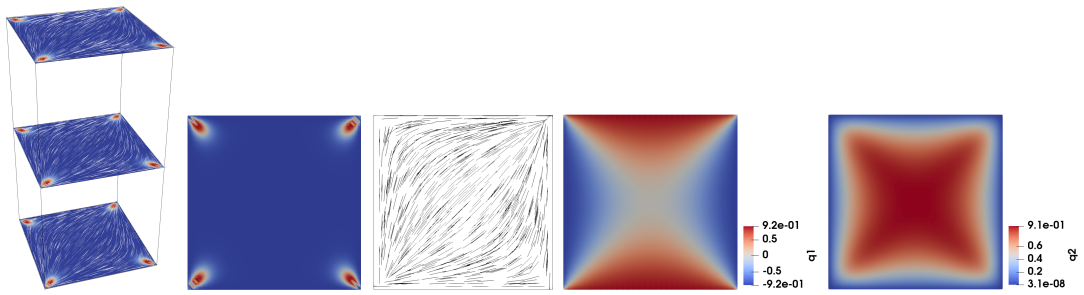

Figure 4.2: The 3D diagonal solution with $\bar{\lambda}^2 = 100$ and $\epsilon = 4$.

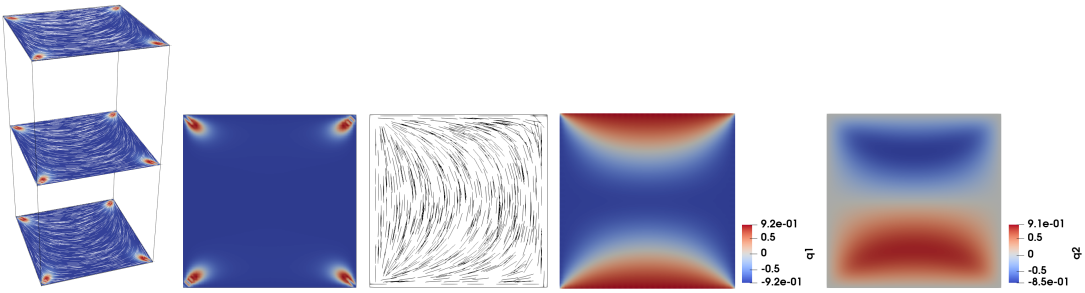

Figure 4.3: The 3D rotated solution with $\bar{\lambda}^2 = 100$ and $\epsilon = 4$.

Interestingly, for ϵ large enough, we observe locally stable solutions with mixed diagonal profiles on the top and bottom plates. These are obtained by prescribing the (D1) and (D2) initial conditions described earlier, on the top and bottom surfaces of the domain, respectively. For example, we set $\mathbf{Q} = s_+ \left(\mathbf{n} \otimes \mathbf{n} - \frac{1}{3}\mathbf{I}_3\right)$ with

$$\mathbf{n}(x, y, z) = \begin{cases} \frac{1}{\sqrt{2}}(1, 1, 0), & z \geq \frac{\epsilon}{2} \\ \frac{1}{\sqrt{2}}(1, -1, 0), & z < \frac{\epsilon}{2}. \end{cases}$$

This leads to a 3D solution with two different diagonal profiles on the top and bottom surfaces, with a mismatch at the centre of the well. In the middle slice, the L-BFGS procedure converges to a BD-like profile (referring to the terminology in [62]), where the corresponding $\mathbf{Q}$-tensor is of the form

$$\mathbf{Q}_{BD} = q_1(\hat{\mathbf{x}} \otimes \hat{\mathbf{x}} - \hat{\mathbf{y}} \otimes \hat{\mathbf{y}}) + q_3 \left(2\hat{\mathbf{z}} \otimes \hat{\mathbf{z}} - \hat{\mathbf{x}} \otimes \hat{\mathbf{x}} - \hat{\mathbf{y}} \otimes \hat{\mathbf{y}}\right).$$

The two-dimensional BD solution is characterized by uniaxial bands of $q_1 = 0$ near a pair of parallel square edges. These $q_1 = 0$ nodal lines form transition layers between two distinct values of q_1. At the special temperature $A = -\frac{B^2}{3C}$, we have $q_3 = -\frac{B}{6C}$ everywhere in the domain. We present these mixed 3D solutions in Figures 4.4 and 4.5, for wells of height $\epsilon = 4$, and where $\bar{\lambda}^2 = 100$ and 10, respectively. By computing the smallest eigenvalue of the Hessian matrix corresponding to these solutions, we find that they are numerically stable. Indeed, these solutions actually have a lower energy than the rotated solutions seen in Figure 4.3, for the same size of domain. In both figures, we plot: a 3D representation of the mixed solution; the biaxiality parameter; and the director profile. We show five cross-sections in the (x, y)-plane to illustrate how the profile changes in the z-direction. These cross-sections are at $z = \epsilon, \frac{9\epsilon}{16}, \frac{\epsilon}{2}, \frac{7\epsilon}{16}, 0$, respectively. In Figure 4.4, we additionally present the q_1 and q_2 components of the solution at the respective cross-sections. We see that $q_2 = 0$ at $z = \frac{\epsilon}{2}$ in both of these mixed solutions - an indicator that the solution resembles the BD profile described above. Numerical simulations show that these mixed profiles cease to exist when $\bar{\lambda}^2$ or ϵ is too small. For example when $\bar{\lambda}^2 = 100$, we cannot observe such solutions for $\epsilon \leq 0.8$. If we consider our choice of material-dependent parameters, this would correspond to wells with $\lambda \sim 820\,\text{nm}$ for roughly $h \leq 330\,\text{nm}$. This does pose an interesting question, however - can wells of this size be physically produced? As indicated by these numerical results, we may only observe height invariant solutions for wells with sufficiently small height, and we must consider wells with edge-length on the order of one hundred nanometers for the WORS configuration to be numerically stable. This is a difficult system to produce in practice however, as was discussed in [52], we may enhance the stability of the WORS in larger domains if we consider higher temperatures, or

even polymeric liquid crystals with a larger molecular length. Whilst we do not consider these regimes numerically, this would be a very interesting topic of future research which would shed light on the possibility of observing these interesting equilibrium configurations in practice.

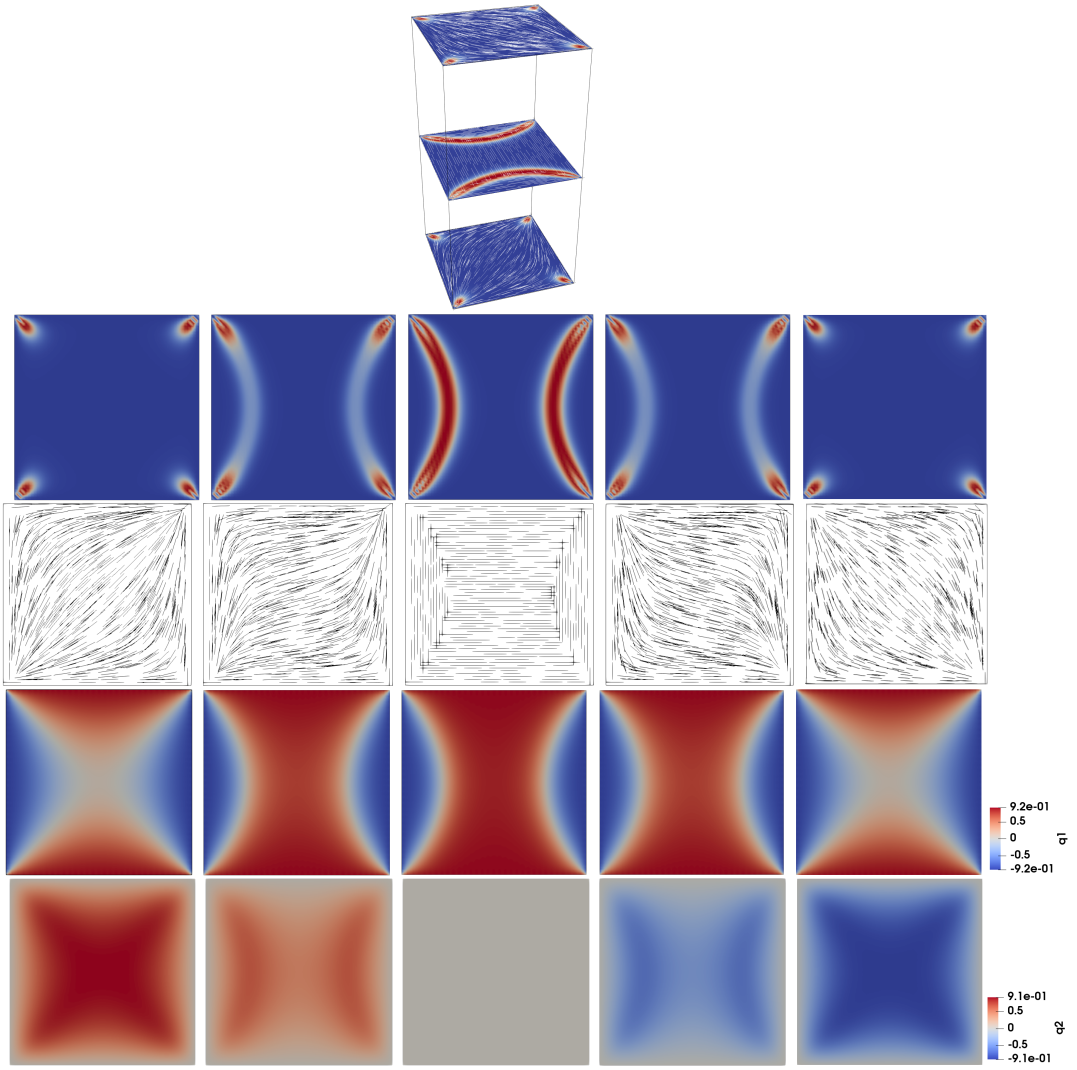

Figure 4.4: A locally stable mixed diagonal solution for $\bar{\lambda}^2 = 100$ and $\epsilon = 4$ with 2D cross-sections (from left to right) at $z = \epsilon$, $z = \frac{9\epsilon}{16}$, $z = \frac{\epsilon}{2}$, $z = \frac{7\epsilon}{16}$ and $z = 0$, respectively.

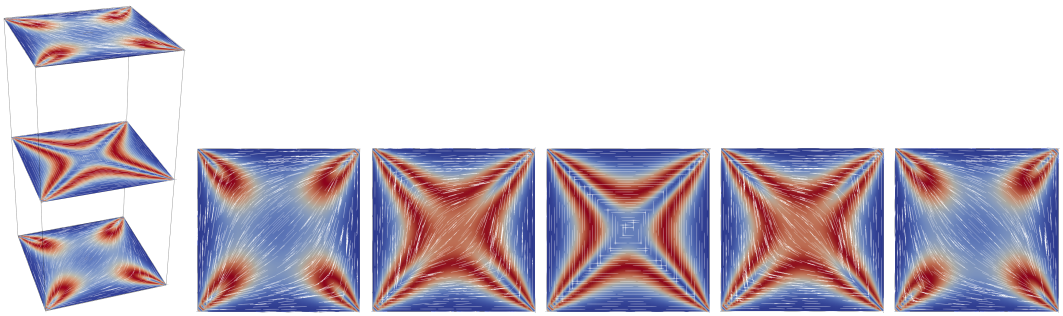

Figure 4.5: A mixed diagonal solution for $\bar{\lambda}^2 = 10$ and $\epsilon = 4$. Colours given by the biaxiality parameter and the director orientation is given by white lines. Cross-sectional heights as in Figure 4.4.

We can generate more 3D configurations by mixing combinations of the 2 diagonal and 4 rotated configurations on the top and bottom surfaces, but these are unstable according to our numerics. We may even simulate a repeated twist in the director profile in the domain by taking the (D1) initial condition in the top and bottom thirds of the well, and the (D2) condition elsewhere. More specifically, to take $\mathbf{Q} = s_+\left(\mathbf{n}\otimes\mathbf{n} - \frac{1}{3}\mathbf{I}_3\right)$ where

$$\mathbf{n}(x,y,z) = \begin{cases} \frac{1}{\sqrt{2}}(1,1,0), & z \geq \frac{2\epsilon}{3} \\ \frac{1}{\sqrt{2}}(1,-1,0), & \frac{\epsilon}{3} \leq z < \frac{2\epsilon}{3} \\ \frac{1}{\sqrt{2}}(1,1,0), & z < \frac{\epsilon}{3}. \end{cases}$$

however, the L-BFGS procedure converges to a z-invariant diagonal solution, as in Figure 4.2.

4.3.2 Weak anchoring on the lateral surfaces

In this section, we study the effect of weak anchoring conditions on the lateral surfaces. Our main findings in this subsection are:

- For a small enough anchoring strength coefficient, we lose the defect cross structure of the WORS, and solutions approach a uniformly aligned nematic director is preferred as we weaken the anchoring.

- The anchoring strength on the lateral surfaces has a stabilising effect on the WORS, and this is corroborated by a bifurcation diagram as a function of the cross-sectional size.

- We may tailor the defect pattern of the WORS by employing different surface anchoring terms in the LdG free energy.

To begin, we minimize the LdG energy functional (4.1.3), where the strong anchoring condition simulation on the top and bottom plates is preserved by taking $W_z = 10^{-2}\text{Jm}^{-2}$ in (4.1.5). We vary the anchoring strength coefficient, W, in the surface energy term (4.1.4), defined on $\partial\Omega \times (0, \epsilon)$. In Figures 4.6 – 4.8, we plot numerical solutions for $\bar{\lambda}^2 = 5$ and $\epsilon = 0.2$, with $W = 2 \times 10^{-3}, 1 \times 10^{-3}$ and $1 \times 10^{-4}\text{Jm}^{-2}$, respectively. As expected, W_z is sufficiently large to mimic the natural boundary conditions on Γ from (3.2.2). Therefore, all of these numerical solutions are z-invariant and thus, we present the 2D cross-sections from $z = \frac{\epsilon}{2}$. For each solution, we plot: the biaxiality parameter described by (1.4.11); the director profile, $\mathbf{n}$; and the q_1 and q_2 components of the solution. We have $q_3 = -\frac{B}{6C}$ throughout the well in each simulation. All three solutions are obtained by using the (D1) initial condition. In the strong anchoring case ($W = 10^{-2}\text{Jm}^{-2}$), we get the WORS as expected, since the WORS is the unique critical point when $\bar{\lambda}^2$ is small enough. However, for $W = 10^{-3}\text{Jm}^{-2}$, we get a diagonal-like solution in which maximal biaxiality is achieved around the corners of the well. By further decreasing the anchoring strength, the nematic director is almost uniformly aligned along the diagonal direction. Similar results were reported in [52]. According to

our numerical procedure, all three of these solutions are numerically stable.

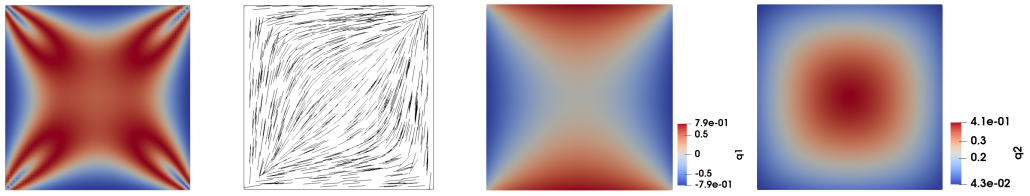

Figure 4.6: A locally stable solution with $\bar{\lambda}^2 = 5$ and $\epsilon = 0.2$ and $W = 2 \times 10^{-3}\text{Jm}^{-2}$ in (4.1.4).

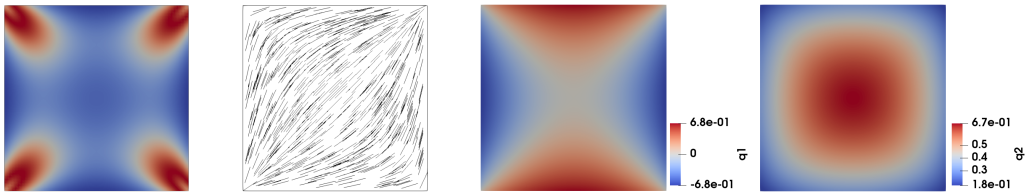

Figure 4.7: A locally stable solution with $\bar{\lambda}^2 = 5$ and $\epsilon = 0.2$ and $W = 10^{-3}\text{Jm}^{-2}$ in (4.1.4).

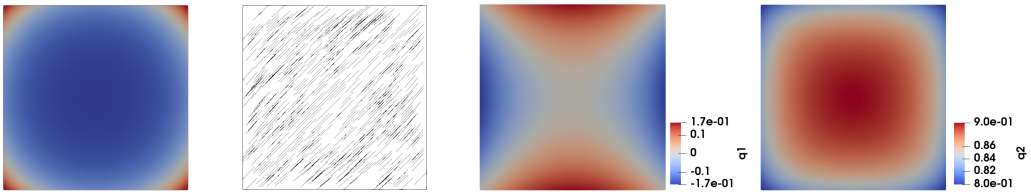

Figure 4.8: A locally stable solution with $\bar{\lambda}^2 = 5$ and $\epsilon = 0.2$ and $W = 10^{-4}\text{Jm}^{-2}$ in (4.1.4).

We see from Figures 4.6 – 4.8, that the numerical solution converges to a uniform profile close to the initial guess, as the anchoring strength is weakened. By taking different initial guesses in our code, we are able to find other, unstable states, for W small enough. These solutions have $q_2 = 0$ everywhere in the well but exhibit different defect patterns. In Figure 4.9, we plot the numerical solution for $W = 10^{-4}\text{Jm}^{-2}$, with $\bar{\lambda}^2 = 5$ and $\epsilon = 0.2$, when an isotropic solution ($\mathbf{Q} = 0$) was chosen as the initial guess. For W small enough, we get a WORS-like solution with strong biaxial regions near the lateral surfaces of the well. In Figure 4.10, we

plot the numerical solution for $W = 8 \times 10^{-4}\text{Jm}^{-2}$, also with $\bar{\lambda}^2 = 5$ and $\epsilon = 0.2$, where we take a uniform horizontal initial condition $\mathbf{Q} = s_+\left(\hat{\mathbf{x}} \otimes \hat{\mathbf{x}} - \frac{1}{3}\mathbf{I}_3\right)$. For W small enough, we get a BD-like solution with a pair of uniaxial bands across two opposing sides of the well.

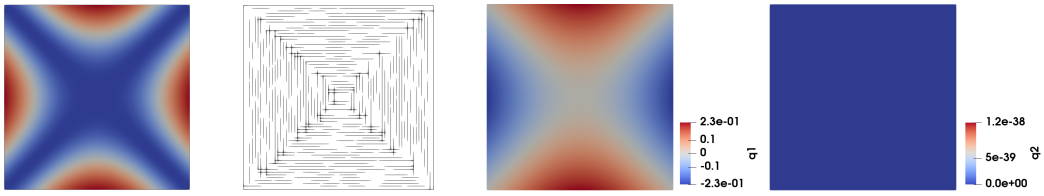

Figure 4.9: An unstable numerical solution with $\bar{\lambda}^2 = 5$ and $\epsilon = 0.2$ and $W = 10^{-4}\text{Jm}^{-2}$ given an isotropic initial guess ($\mathbf{Q} = 0$).

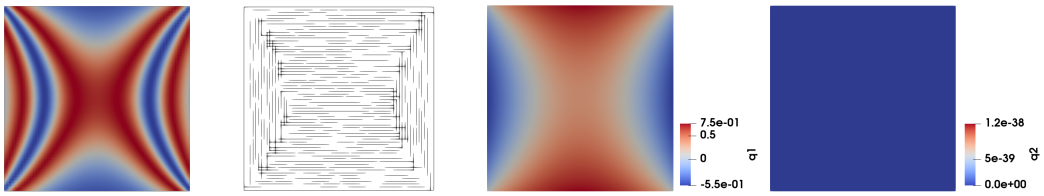

Figure 4.10: An unstable numerical solution with $\bar{\lambda}^2 = 5$ and $\epsilon = 0.2$ and $W = 8 \times 10^{-4}\text{Jm}^{-2}$ given a uniform horizontal initial guess.

For $W = 10^{-3}\text{Jm}^{-2}$, we can get the WORS by further decreasing $\bar{\lambda}^2$. However, the WORS ceases to exist for $W = 10^{-4}\text{Jm}^{-2}$. Quantitatively, we can compute bifurcation points $\bar{\lambda}^2_*$, such that the WORS is the unique solution for $\bar{\lambda}^2 < \bar{\lambda}^2_*$, as a function of anchoring strength W, shown in Figure 4.11. We can find $\bar{\lambda}^2_*$ by decreasing $\bar{\lambda}^2$ till diagonal-like (D1) initial conditions converge to the WORS, since diagonal solutions cease to exist for $\bar{\lambda}^2 < \bar{\lambda}^2_*$. The result in Figure 4.11 is computed with $\epsilon = 0.2$. However, this result is independent of ϵ, as both diagonal and the WORS are z-invariant solutions for $A = -\frac{B^2}{3C}$. By comparing with our choice of values for L and C, we find that the WORS is the unique solution for

wells with an edge-length, λ, of the order $\sim 60\,\text{nm}$ with an anchoring strength $W = 5 \times 10^{-4}\,\text{Jm}^2$ and, as indicated by the blue dashed line in Figure 4.11, the WORS is the unique solution for wells smaller than $\lambda \sim 190\,\text{nm}$ with a Dirichlet boundary condition in a 2D square domain.

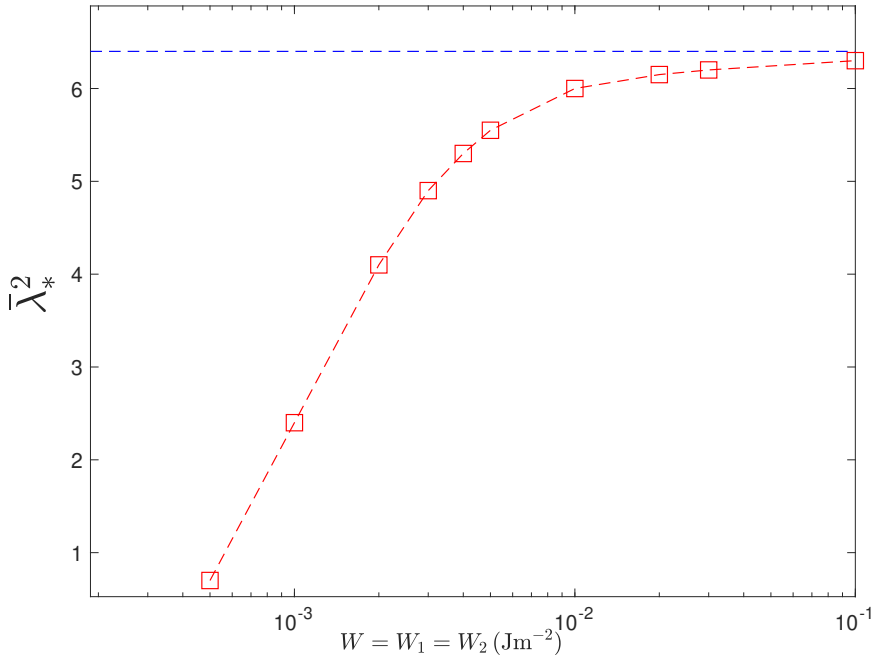

Figure 4.11: Bifurcation points $\bar{\lambda}^*$, such that the WORS is the unique solution for $\bar{\lambda}^2 < \bar{\lambda}^2_*$, as a function of anchoring strength W. The blue dashed line indicates the bifurcation point of the WORS for Dirichlet boundary condition in a 2D square domain ($\bar{\lambda}^2 \approx 6.4$).

Another way to relax the surface anchoring is to consider the surface energy

$$\begin{aligned} f_s(\mathbf{Q}) &= \omega \left(\alpha \left(\mathbf{Q}\hat{\mathbf{x}} \cdot \hat{\mathbf{x}} - \frac{2}{3} s_+ \right)^2 + \gamma \left| \left(\mathbf{I} - \hat{\mathbf{x}} \otimes \hat{\mathbf{x}} \right) \mathbf{Q}\hat{\mathbf{x}} \right|^2 \right); \quad y = -1, 1; \\ f_s(\mathbf{Q}) &= \omega \left(\alpha \left(\mathbf{Q}\hat{\mathbf{y}} \cdot \hat{\mathbf{y}} - \frac{2}{3} s_+ \right)^2 + \gamma \left| \left(\mathbf{I} - \hat{\mathbf{y}} \otimes \hat{\mathbf{y}} \right) \mathbf{Q}\hat{\mathbf{y}} \right|^2 \right); \quad x = -1, 1; \end{aligned} \tag{4.3.2}$$

where $\omega = \frac{W\lambda}{L}$ is the non-dimensionalized anchoring strength, and $\alpha > 0$ and $\gamma > 0$ are constants. We minimize the LdG energy (4.1.3) with surface energy

terms (4.3.2) and (4.1.5). Here, we fix $W_z = W = 10^{-2}\text{Jm}^{-2}$, and vary the constants α and γ. Note how the surface energy term (4.3.2) enforces a preferred tangential boundary condition on the lateral surfaces of the domain. For example, the condition on the planes $y = -1, 1$ in (4.3.2) favours $\mathbf{Q}$-tensors with an $\hat{\mathbf{x}}$ eigenvector, with corresponding eigenvalue of $\frac{2}{3}s_+$. Furthermore, since the second term in (4.3.2) can be zero if we take $\mathbf{Q} = s_+\left(\hat{\mathbf{z}} \otimes \hat{\mathbf{z}} - \frac{1}{3}\mathbf{I}\right)$, which also makes the surface energy on the top and bottom plates (Γ) zero, we keep α non-zero to get interesting defect patterns. In Figures 4.12 – 4.15, we show different configurations in wells of size $\bar{\lambda}^2 = 5$, and height $\epsilon = 0.2$, as we vary both α and γ. For each of the four solutions, we use the (D1) configuration as the initial guess, and they are locally stable according to our numerical check. In Figure 4.12, we choose $\alpha = \gamma = 1$. We obtain a WORS-like solution with strong biaxial regions near the corners of the square cross-section, and q_2 approximately zero everywhere. As we reduce α in Figure 4.13, these biaxial regions extend to the edges of the square, and therefore the lateral surfaces of the well, whilst the distinctive uniaxial cross of the WORS is maintained. If we fix α and reduce γ, as presented in Figures 4.14 and 4.15, we see the nematic director (the leading eigenvector of the $\mathbf{Q}$-tensor) is no longer tangent to the square edges and the WORS ceases to exist - indicated by non-zero q_2. In each plot, we show the middle slice ($z = \frac{\epsilon}{2}$) of the well, showing the biaxiality parameter, the nematic director profile, q_1 and q_2. In all of these solutions, we have $q_3 = -\frac{B}{6C}$ everywhere in the domain. These examples show that the WORS ceases to exist if the anchoring on the lateral surfaces is weak enough, and we always get a diagonal-like solution when the WORS ceases to exist (the non-diagonal solutions like in Figures 4.9 and 4.10 are unstable). It should be remarked that the diagonal-like solutions tend to be defect-free around the corners with weak anchoring, as the nematic directors aren't forced to be

tangential to the square edges, and there is no biaxial-uniaxial or biaxial-isotropic interface near the corners.

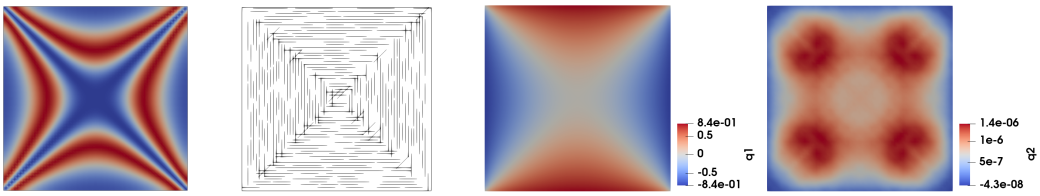

Figure 4.12: The stable WORS-like solution with $\bar{\lambda}^2 = 5$, $\epsilon = 0.2$ and $\alpha = \gamma = 1$ in (4.3.2).

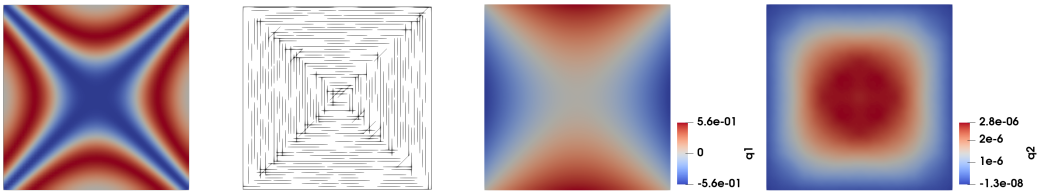

Figure 4.13: A locally stable numerical solution with $\bar{\lambda}^2 = 5$, $\epsilon = 0.2$ and $\alpha = 0.1$, $\gamma = 1$ in (4.3.2).

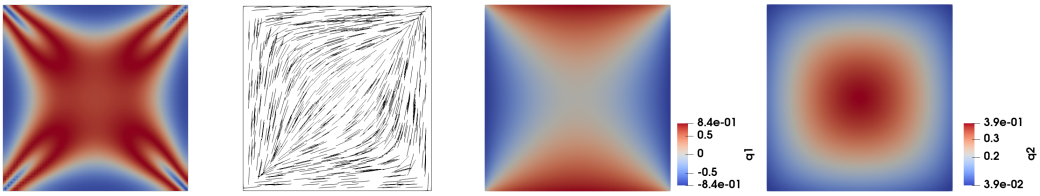

Figure 4.14: A locally stable numerical solution with $\bar{\lambda}^2 = 5$, $\epsilon = 0.2$ and $\alpha = 1$, $\gamma = 0.2$ in (4.3.2).

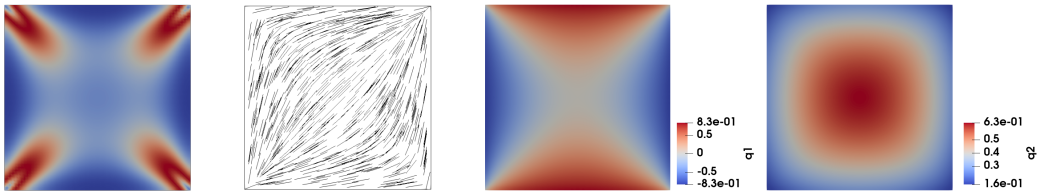

Figure 4.15: A locally stable numerical solution with $\bar{\lambda}^2 = 5$, $\epsilon = 0.2$ and $\alpha = 1$, $\gamma = 0.1$ in (4.3.2).

4.3.3 Escaped solutions

In this subsection, we show that:

- By weakening the anchoring strength on the top and bottom surfaces of the well, we may observe two stable configurations with a non-zero z-component, which exhibit a ± 1-disclination line along the z-axis.
- These out-of-plane configurations cease to exist if either the well height, ϵ, is small enough or if the anchoring on the top and bottom plates, W_z, is large enough.

The numerical simulations so far have only presented solutions (4.1.1) that have $q_4 = q_5 = 0$, along with $q_3 < 0$. This implies that solutions lie in the (x, y)-plane and do not '*escape*' to the z-direction. In [63], the authors show that there exists two escaped solutions with non-zero q_4 and q_5, and $q_3 > 0$, in the reduced 2D square domain, for relatively large $\bar{\lambda}^2$. Our simulations show that these two escaped solutions can exist in 3D wells, for similar values of $\bar{\lambda}^2$, if the anchoring strength on the top and bottom plates is weak enough. We find that these escaped solutions are locally stable according to our numerical check. As done previously in this chapter, we minimize the LdG energy functional (4.1.3) with surface energy terms (4.1.4) on $\partial\Omega \times (0, \epsilon)$, and (4.1.5) on Γ. We mimic strong anchoring conditions on the lateral surfaces by taking $W = 10^{-2}\text{Jm}^{-2}$ in (4.1.4). In this section, we weaken the anchoring on the top and bottom plates to see if escaped solutions can exist in 3D. To this end, we take $W_z = 10^{-5}\text{Jm}^{-2}$ in (4.1.5).

Both of the stable escaped configurations that we present are taken with $\bar{\lambda}^2 = 100$, and $\epsilon = 4$. We see that both are quite similar to the escaped configurations in a

cylindrical cavity [100]. In both figures, we plot a 3D representation of the solution by plotting both the biaxiality parameter (1.4.11), and the nematic director profile. In the remaining plots, we take the middle 2D slice ($z = \frac{\epsilon}{2}$) of the domain. As well as the biaxiality parameter and director profile, we plot all five of the scalar order components of the **Q**-tensor solution in (4.1.1). We see that $q_3 > 0$ in the centre of the well. In Figure 4.16, we present an escaped configuration with a -1-disclination line in the centre of the well along the z-axis and, in Figure 4.17, we present an escaped configuration with a $+1$-disclination line in the centre of the well. We see that the escaped solutions in Figures 4.16 and 4.17 cease to

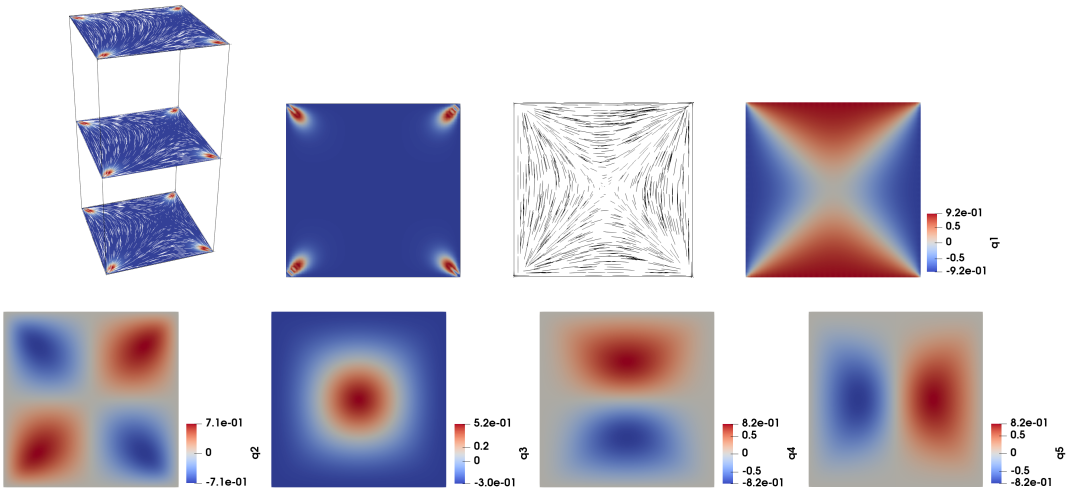

Figure 4.16: Escaped configuration with -1-disclination line in the center of the well where $\bar{\lambda}^2 = 100$, $\epsilon = 4$ and $W_z = 10^{-5}\text{Jm}^{-2}$ in (4.1.5).

exist if either, ϵ is small enough, or if the anchoring W_z is large enough. We can compute the critical anchoring strength, W_z, on the top and bottom plates, for which the escaped configurations cease to exist, as a function of ϵ, for $\bar{\lambda}^2 = 100$, and this is shown in Figure 4.18. Comparing with our choice of values for L and C, we can see that the escaped configurations lose (numerical) stability for an anchoring strength, W_z, of $10^{-6}\,\text{Jm}^{-2}$ for wells with a height, h, of $\sim 80\,\text{nm}$, and

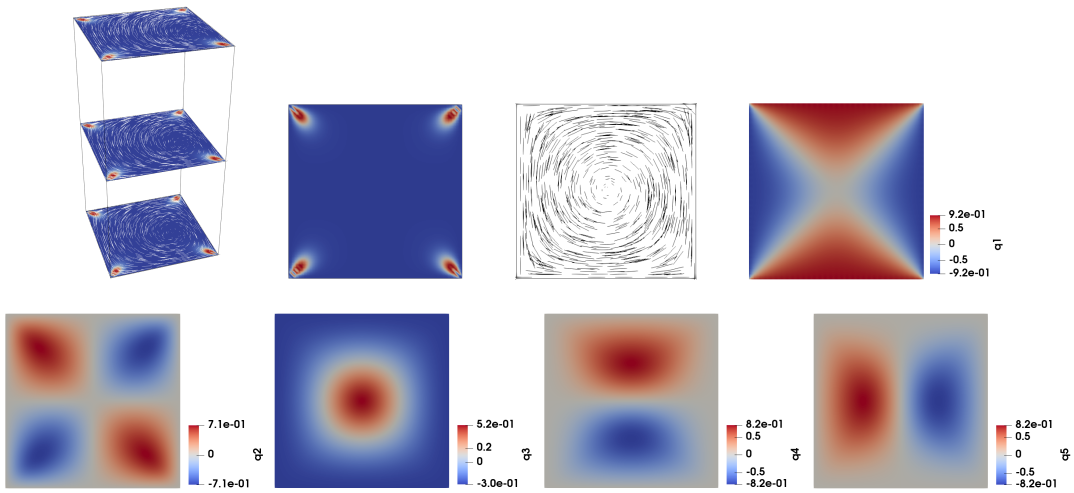

Figure 4.17: Escaped configuration with +1-disclination line in the center of the well where $\bar{\lambda}^2 = 100$, $\epsilon = 4$ and $W_z = 10^{-5}\mathrm{Jm}^{-2}$ in (4.1.5).

$7 \times 10^{-5}\,\mathrm{Jm}^{-2}$ for wells with a height of $\sim 3\,\mu$m.

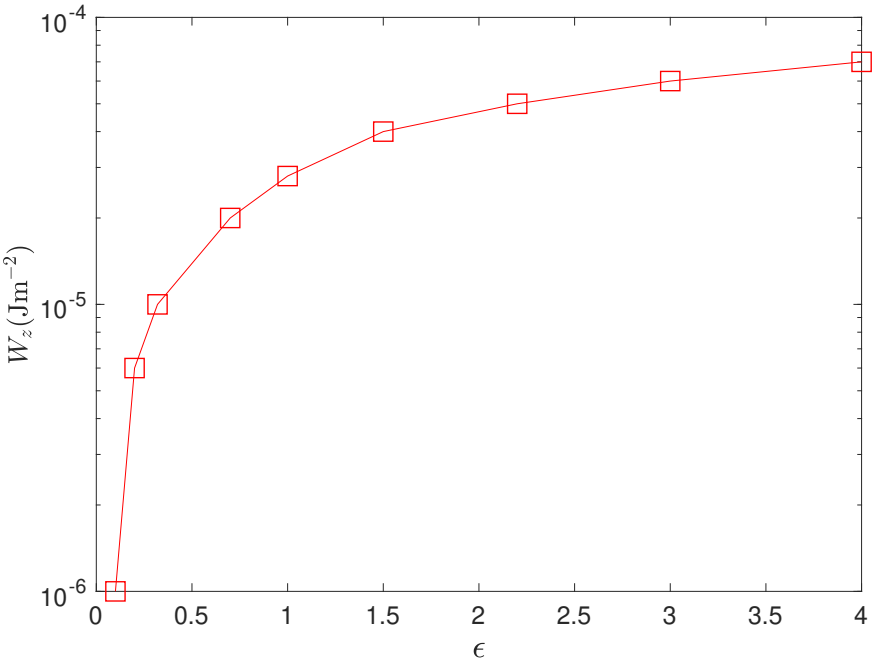

Figure 4.18: Critical anchoring strength W_z, in (4.1.5), for which the escaped configurations lose stability as a function of ϵ.

4.3.4 Simulations in a rectangular domain

In this section, we build upon the analytical and numerical study of nematic equilibrium solutions in three-dimensional square wells, by extending our numerical search for 3D rectangular wells. To this end, we consider minimizers of the rescaled LdG energy functional, $\mathcal{F}_\lambda$, in the 3D domain $V = \Omega \times (0, \epsilon)$. However, we take the 2D cross-section of the well to be

$$\Omega := \{(x, y) \in \mathbb{R}^2 : |x| \leq 1, |y| \leq \delta\},$$

where $\delta > 0$ represents the *geometric anisotropy* of the cross-sectional domain, and measures the ratio of the side lengths of the rectangle. All other parts of the computational model remain unchanged however, the y-coordinate should be thought of with respect to the rescaling $\bar{y} := \delta y$ e.g., in the definition of the surface energies (4.1.4). Clearly, when $\delta = 1$, we recover the square cross-sectional domain as shown earlier in this chapter. We avoid values of the aspect ratio $0 < \delta < 1$, since the solutions are equivalent, up to a rotation of 90° about the z-axis, to those solutions with aspect ratio $\frac{1}{\delta}$. However it must be noted, that due to choice of boundary conditions on q_1, the sign of q_1 is reversed by taking the aspect ratio $\frac{1}{\delta}$, instead of δ. This is essentially because transition lines for q_1, that separate the two distinct values on the boundary, traverse either the short, or long edges of the rectangle, and so it is dependent on whether the rectangle is 'portrait' or 'landscape'. All other solutions such as the biaxiality parameter, the director profile, and q_2 remain unchanged. In this section, we show:

- For $\delta \neq 1$, we lose the defect cross-structure of the WORS, and the globally minimizing solution corresponds to the 3D sBD2 profile (referring to the terminology in [69]), with two bands of uniaxiality across each of the shorter

rectangle edges.

- The geometrical anisotropy has a stabilising effect on the sBD2 profile and lower energy rotated states, shown by a complete bifurcation diagram for the various profiles, as a function of δ.

- The height of the well, and the geometric anisotropy, also have a stabilising effect on mixed configurations which interpolate between diagonal and rotated profiles. Novel mixed solutions, with mixed rotated cross-sectional profiles, exist for δ and ϵ large enough.

Similarly to the numerical simulations on 3D square wells, we consider $\mathbf{Q}$-tensors of the form (4.1.1) that minimize the LdG energy functional (4.1.3), subject to surface anchoring conditions which mimic strong tangential boundary conditions ($W = W_z = 10^{-2}\text{Jm}^{-2}$ in (4.1.4) and (4.1.5)). The parameters A, B, C and L remain at their fixed values, and we vary the key dimensionless parameters for the size and height of the well: $\bar{\lambda}$ and ϵ, respectively. In these figures, we present a 3D representation of the solution, as well as the biaxiality parameter (1.4.11), the nematic director profile, and the q_1 and q_2 components of the $\mathbf{Q}$-tensor solution. We recall that the director profile is given by the eigenvector corresponding to the largest eigenvalue of the numerical solution. All of these solutions exhibit almost zero z-component (indeed in our simulations we have $|\partial_z \mathbf{Q}|^2 \sim 10^{-12}$), which is expected given such strong anchoring, W_z, on the top and bottom surfaces, Γ. At the special temperature, $A = -\frac{B^2}{3C}$, we have $q_3 = -\frac{B}{6C}$ everywhere in the domain.

For $\bar{\lambda}^2$ large enough, there exist multiple stable states within the two-dimensional setting. These states are similar in nature to that of a square well, however the geometrical anisotropy of the rectangular well does lead to some differences. As mentioned previously, the *diagonal* and *rotated* configurations are solutions

described by **Q**-tensors of the form (4.2.11). The two diagonal (D_1 and D_2) states are distinguished by the nematic director, $\mathbf{n} = (\cos\theta, \sin\theta, 0)$, which roughly aligns along one of the diagonals of Ω. The main difference involves the four possible rotated states. These states prescribe the director angle, θ, to rotate approximately π radians between a pair of opposite edges, as in the square case. However, in a rectangular geometry, two of the rotated states (which we will refer to as R_1 and R_2) involve a director rotation about the shorter opposing sides, meanwhile the remaining two rotated states (which we refer to as U_1 and U_2) correspond to higher energy states, and involve a director rotation across the two longer opposing sides [68]. We plot illustrations of the typical director formation of these states in Figure 4.19.

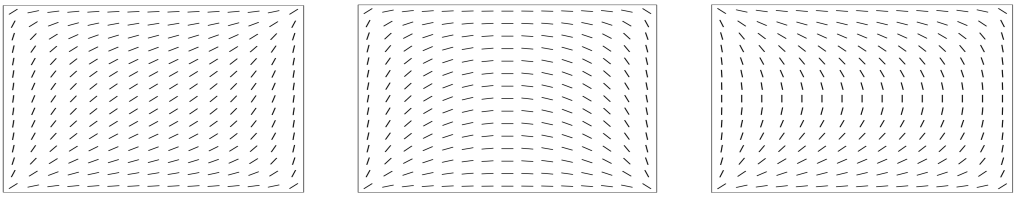

Figure 4.19: Director orientations for the D, R and U states in a rectangular domain.

As before, when choosing an initial step for the L-BFGS algorithm, we set $\mathbf{Q} = s_+(\mathbf{n} \otimes \mathbf{n} - \frac{1}{3}\mathbf{I}_3)$, where our choice of $\mathbf{n}$ determines the solution profile. The (D1) and (D2) initial configurations remain unchanged in the rectangular geometry, and are sufficient at finding diagonal solutions. In order to simulate any of the rotated R and U configurations in the domain, we choose the director as follows:

(R1)	$\begin{cases} (0,1,0), & x \le 0, \\ \frac{1}{\sqrt{2}}(1,1,0), & x,y > 0, \\ \frac{1}{\sqrt{2}}(-1,1,0), & x > 0, y \le 0, \end{cases}$	(R2)	$\begin{cases} (0,1,0), & x \ge 0, \\ \frac{1}{\sqrt{2}}(1,1,0), & x,y < 0, \\ \frac{1}{\sqrt{2}}(-1,1,0), & x < 0, y \ge 0, \end{cases}$
(U1)	$\begin{cases} (1,0,0), & y \ge 0, \\ \frac{1}{\sqrt{2}}(1,1,0), & x,y < 0, \\ \frac{1}{\sqrt{2}}(-1,1,0), & x \ge 0, y < 0, \end{cases}$	(U2)	$\begin{cases} (1,0,0), & y < 0, \\ \frac{1}{\sqrt{2}}(1,1,0), & x,y \ge 0, \\ \frac{1}{\sqrt{2}}(-1,1,0), & x < 0, y \ge 0. \end{cases}$

For relatively large $\bar{\lambda}^2$, we find the 6 possible diagonal and rotated states, for arbitrary ϵ. However, in our numerical simulations, we can only find the higher energy U_1 and U_2 rotated states for $\delta \le 1.5$. In Figures 4.20 – 4.22, we plot three-dimensional solutions for $\bar{\lambda}^2 = 100$, $\epsilon = 4$ and $\delta = 1.45$, where the 2D cross-sections are taken from the middle slice ($z = \frac{\epsilon}{2}$). In Figure 4.20, we plot a diagonal solution, where the (D1) initial guess was taken in the numerical procedure. We plot a lower energy rotated state in Figure 4.21, where the (R1) initial guess was chosen, and a higher energy rotated state in Figure 4.22, given the (U1) condition.

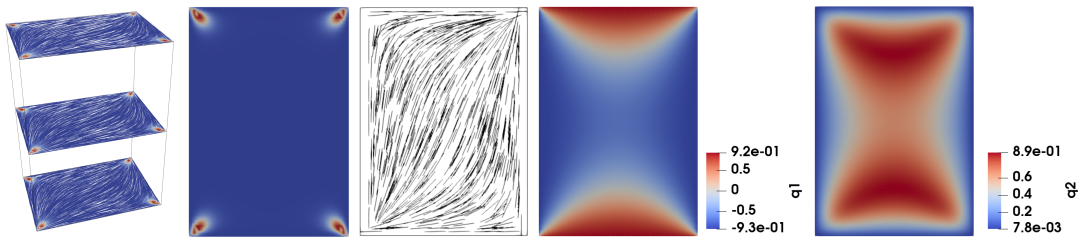

Figure 4.20: A 3D diagonal (D) solution in a rectangle with $\delta = 1.45$, $\bar{\lambda}^2 = 100$ and $\epsilon = 4$.

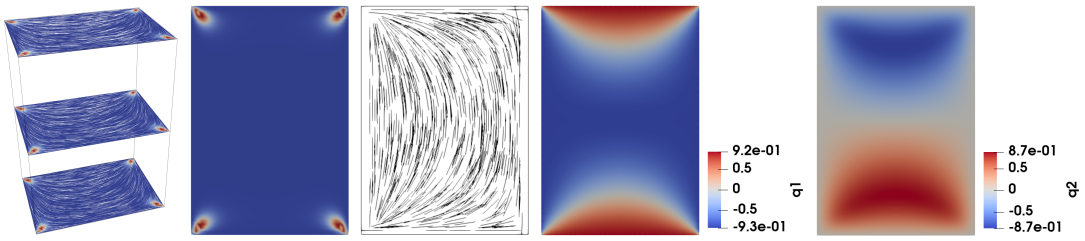

Figure 4.21: A 3D lower energy rotated (R) solution in a rectangle with $\delta = 1.45$, $\bar{\lambda}^2 = 100$ and $\epsilon = 4$.

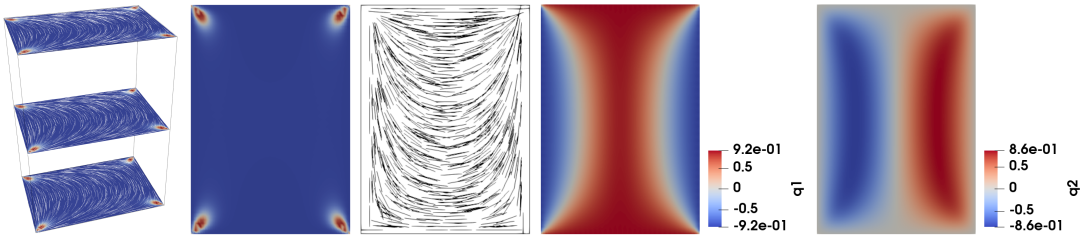

Figure 4.22: A 3D higher energy rotated (U) state in a rectangle with $\delta = 1.45$, $\bar{\lambda}^2 = 100$ and $\epsilon = 4$.

For sufficiently small $\bar{\lambda}^2$, we obtain a solution with nodal lines along the shorter rectangular edges. This solution matches the description of the limiting profile in a two-dimensional framework, described as the sBD2 solution in [69] where, at the special temperature $A = -\frac{B^2}{3C}$, the corresponding $\mathbf{Q}$-tensor is of the form

$$\mathbf{Q}_{sBD2} = q_1(\hat{\mathbf{x}} \otimes \hat{\mathbf{x}} - \hat{\mathbf{y}} \otimes \hat{\mathbf{y}}) - \frac{B}{6C}\left(2\hat{\mathbf{z}} \otimes \hat{\mathbf{z}} - \hat{\mathbf{x}} \otimes \hat{\mathbf{x}} - \hat{\mathbf{y}} \otimes \hat{\mathbf{y}}\right).$$

This two-dimensional solution is characterized by nodal $q_1 = 0$ lines of uniaxiality. These lines form transition layers between two distinct values of q_1. In Figure 4.23, we plot this solution profile in three dimensions, for $\bar{\lambda}^2 = 5$, $\delta = 1.45$ and $\epsilon = 4$. This profile is characterised by an approximately zero q_2-component, everywhere in the domain.

We know that for $\delta = 1$, the WORS is the unique global minimizer, for $\bar{\lambda}^2$ small enough. Similarly, for any $\delta > 1$, we can get the sBD2 solution for $\bar{\lambda}^2$ small

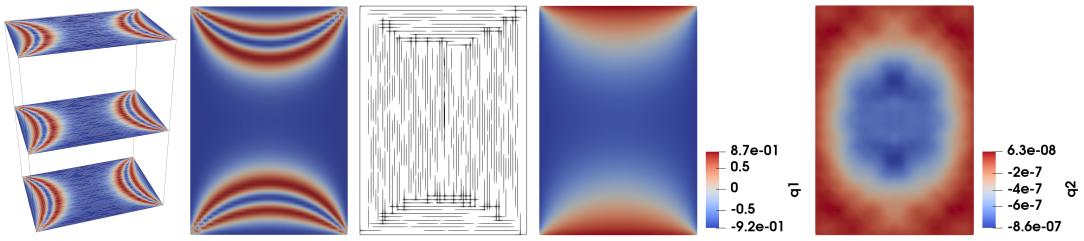

Figure 4.23: The 3D sBD2 state with $\delta = 1.45$, $\bar{\lambda}^2 = 5$ and $\epsilon = 4$.

enough. For example, when $\delta = 2$, the sBD2 solution ceases to exist for $\bar{\lambda}^2 \geq 13$. Comparing with our choice of values for L and C, we see that wells of this size would correspond to dimensions $270 \times 550\,\mathrm{nm}^2$. Quantitatively, we can compute bifurcation points $\bar{\lambda}_c^2$, such that the sBD2 is the unique solution for $\bar{\lambda}^2 < \bar{\lambda}_c^2$, as a function of the geometric anisotropy δ, shown by the red markers in Figure 4.24. We can find $\bar{\lambda}_c^2$ by decreasing $\bar{\lambda}^2$ till diagonal-like (D1) initial conditions converge to the sBD2, since diagonal solutions cease to exist for $\bar{\lambda}^2 < \bar{\lambda}_c^2$. This is difficult to see numerically, but we may justify the loss of stability of the sBD2 by a sudden increase in the q_2-component of the numerical solution. For clarity, we take $\bar{\lambda}_c^2$ to be the smallest well size, $\bar{\lambda}^2$, such that

$$\max_{(x,y)\in\Omega} q_2(x,y) > 0.01.$$

Furthermore, we observe an interesting interplay between the appearance of the rotated states, and the geometric anisotropy δ. By choosing appropriate initial conditions, we find both the R rotated states (for any δ), and the U rotated states (for $\delta \leq 1.5$), provided $\bar{\lambda}^2$ is sufficiently large. If $\bar{\lambda}^2$ is too small, then the numerical procedure converges to a diagonal state. To visualize this, we can compute bifurcation points such that the rotated states lose their stability, as a function of δ. The blue markers in Figure 4.25 present the critical well size, $\bar{\lambda}_c^2$, such that the R rotated states lose their stability. The green markers

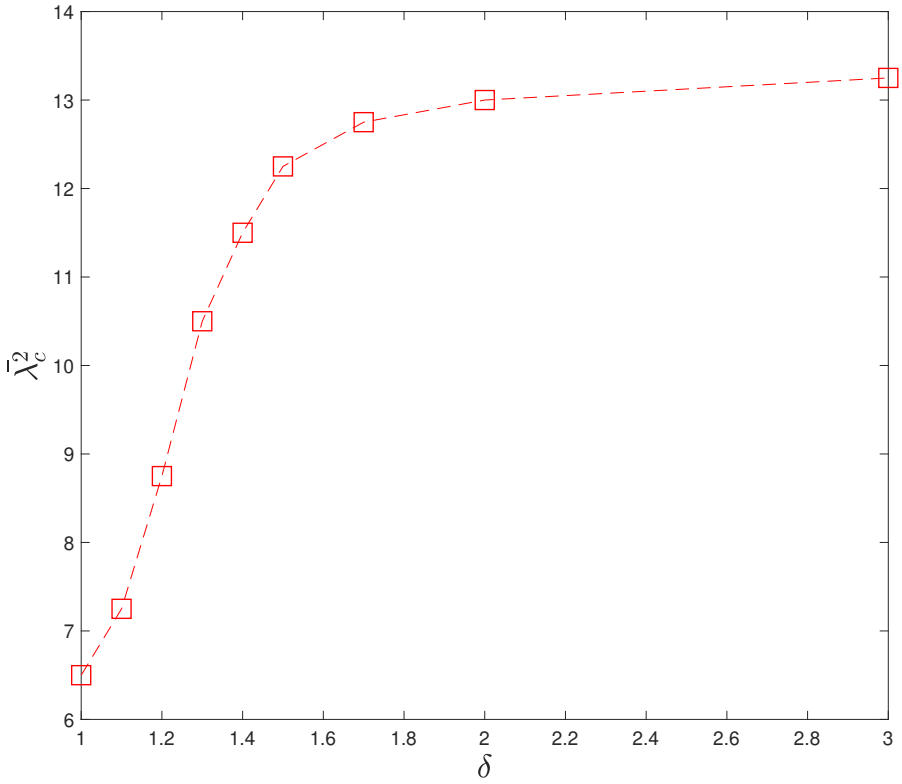

Figure 4.24: Bifurcation points $\bar{\lambda}_c^2$, such that the sBD2 is the unique solution for $\bar{\lambda}^2 < \bar{\lambda}_c^2$, as a function of δ.

in Figure 4.25 present the critical well size, $\bar{\lambda}_c^2$, such that the higher energy U rotated states lose their stability. Figure 4.25 also includes the bifurcation points from Figure 4.24, for comparison. The results in these figures are computed with $\epsilon = 0.2$. However, this is independent of ϵ, since the diagonal, rotated and the sBD2 solutions are z-invariant for $A = -\frac{B^2}{3C}$.

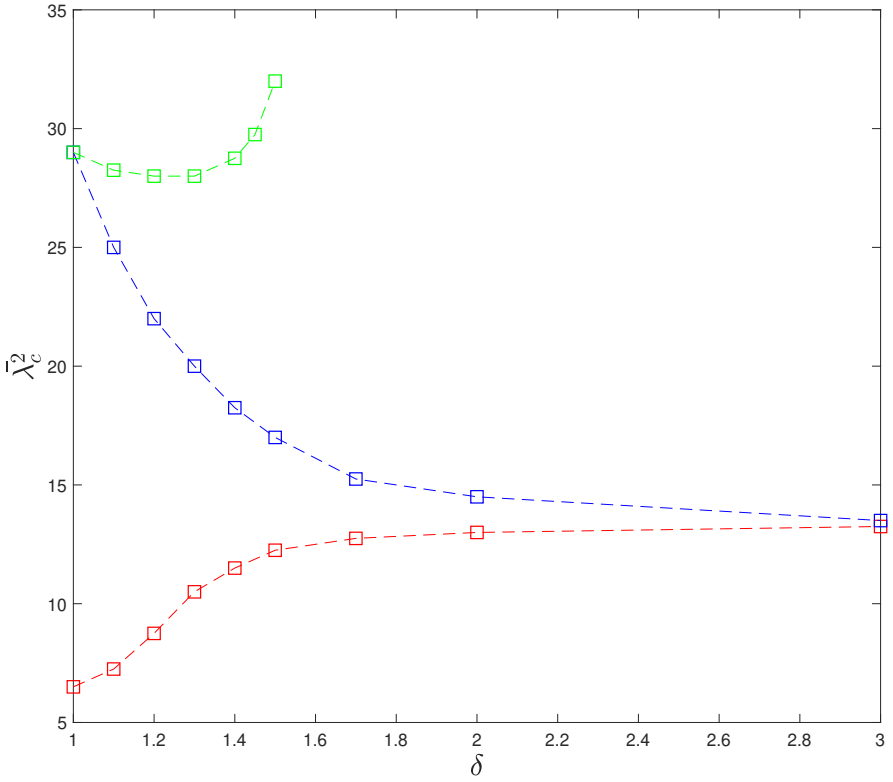

Figure 4.25: Bifurcation points $\bar{\lambda}_c^2$, such that the rotated states lose their stability for $\bar{\lambda}^2 < \bar{\lambda}_c^2$, as a function of geometric anisotropy δ. Blue markers for the R states and green markers for the U states. For $\delta > 1.5$ we cannot obtain the U rotated states in our numerical simulations. We include the bifurcation points from Figure 4.24, shown by the red markers.

In the case $\delta = 1$, for ϵ large enough, we find (numerically) locally stable mixed 3D solutions consisting of two distinct diagonal profiles on the top and bottom surfaces of the well. These solutions exhibit a BD-type solution in the middle cross-section of the domain. We now study the effect that geometric anisotropy has on the stability of mixed 3D solutions. Similarly to when $\delta = 1$, we find a locally stable mixed diagonal solution, with an sBD2-type profile in the middle cross-section of the domain, for any $\delta > 1$, if ϵ is large enough. For example, if

we take $\delta = 1.5$ then we find mixed diagonal solutions for $\epsilon \geq 1.1$. This mixed solution can be obtained by taking a mixed initial condition $\mathbf{Q} = s_+(\mathbf{n} \otimes \mathbf{n} - \frac{1}{3}\mathbf{I}_3)$ with

$$\mathbf{n}(x, y, z) = \begin{cases} (\text{D1}), & z \geq \frac{\epsilon}{2} \\ (\text{D2}), & z < \frac{\epsilon}{2}. \end{cases} \tag{4.3.3}$$

In Figure 4.26, we plot a mixed 3D diagonal solution, for $\bar{\lambda}^2 = 100$, $\delta = 1.45$ and $\epsilon = 4$. We present the solution as a 3D representation, taking three 2D cross-sections at $z = \epsilon, \frac{\epsilon}{2}, 0$. We also show: the biaxiality parameter; the director profile; q_1; and q_2 at (from left to right) $z = \epsilon, \frac{9\epsilon}{16}, \frac{\epsilon}{2}, \frac{7\epsilon}{16}, 0$.

Interestingly, for δ and ϵ large enough, we find another mixed 3D solution. This solution consists of two distinct (R_1 and R_2) rotated configurations on the top and bottom surfaces, with an sBD2-type profile in the middle cross-section of the domain. These solutions are locally stable according to our numerical simulations. In Figure 4.27, we plot a mixed 3D rotated solution, for $\bar{\lambda}^2 = 100$, $\delta = 1.45$ and $\epsilon = 4$. This mixed solution can be obtained by taking a mixed initial condition $\mathbf{Q} = s_+(\mathbf{n} \otimes \mathbf{n} - \frac{1}{3}\mathbf{I}_3)$, with

$$\mathbf{n}(x, y, z) = \begin{cases} (\text{R1}), & z \geq \frac{\epsilon}{2}, \\ (\text{R2}), & z < \frac{\epsilon}{2}. \end{cases} \tag{4.3.4}$$

For $\epsilon = 4$, mixed rotated solutions lose their stability if $\delta < 1.4$. In both mixed solutions, we see that $q_3 = -\frac{B}{6C}$ throughout the domain and $q_2 = 0$ in the middle cross-section of the well - a distinctive feature of the sBD2 profile.

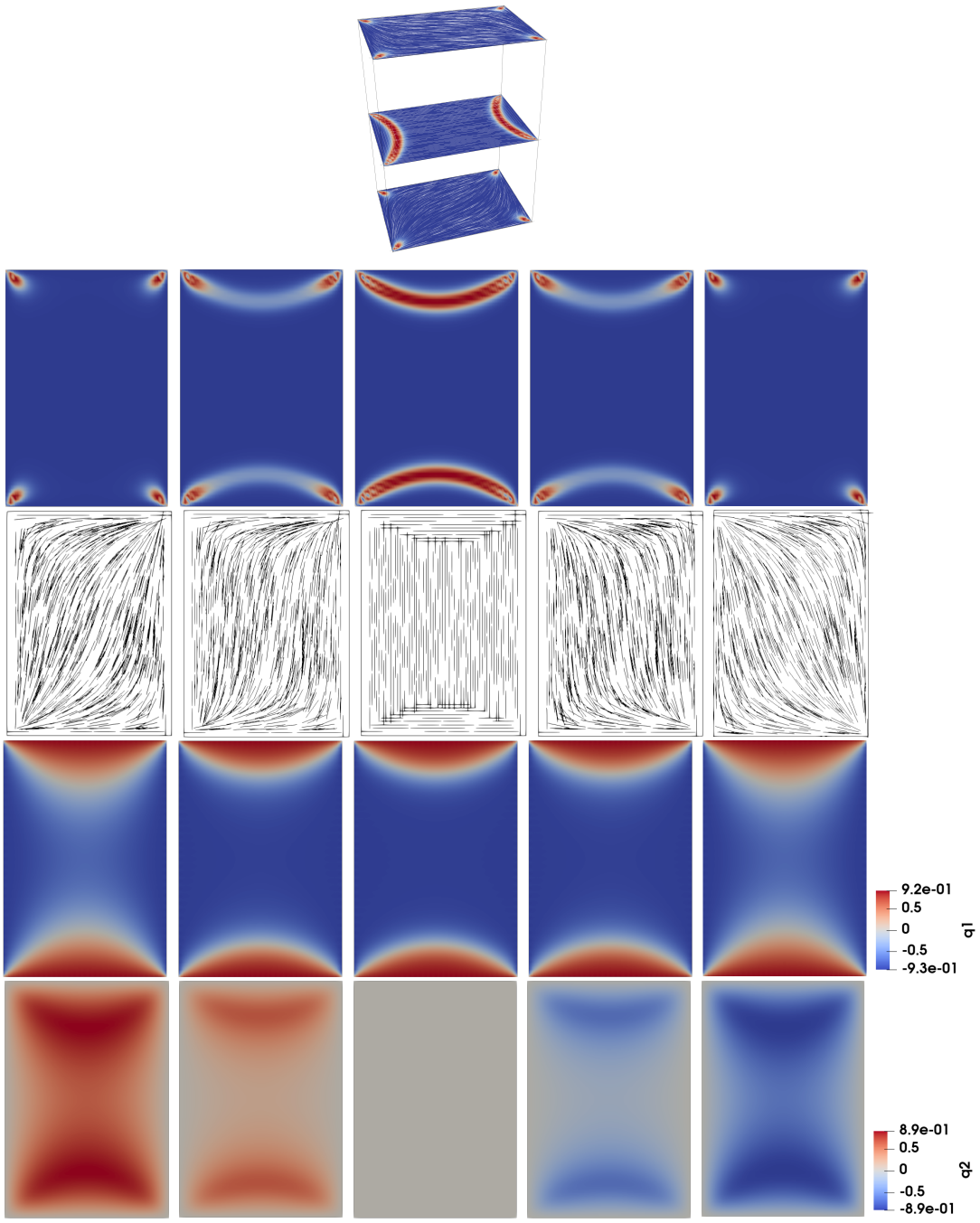

Figure 4.26: A locally stable mixed 3D diagonal solution in a rectangle with $\bar{\lambda}^2 = 100$, $\epsilon = 4$ and $\delta = 1.45$. Cross-sectional heights as in Figure 4.4.

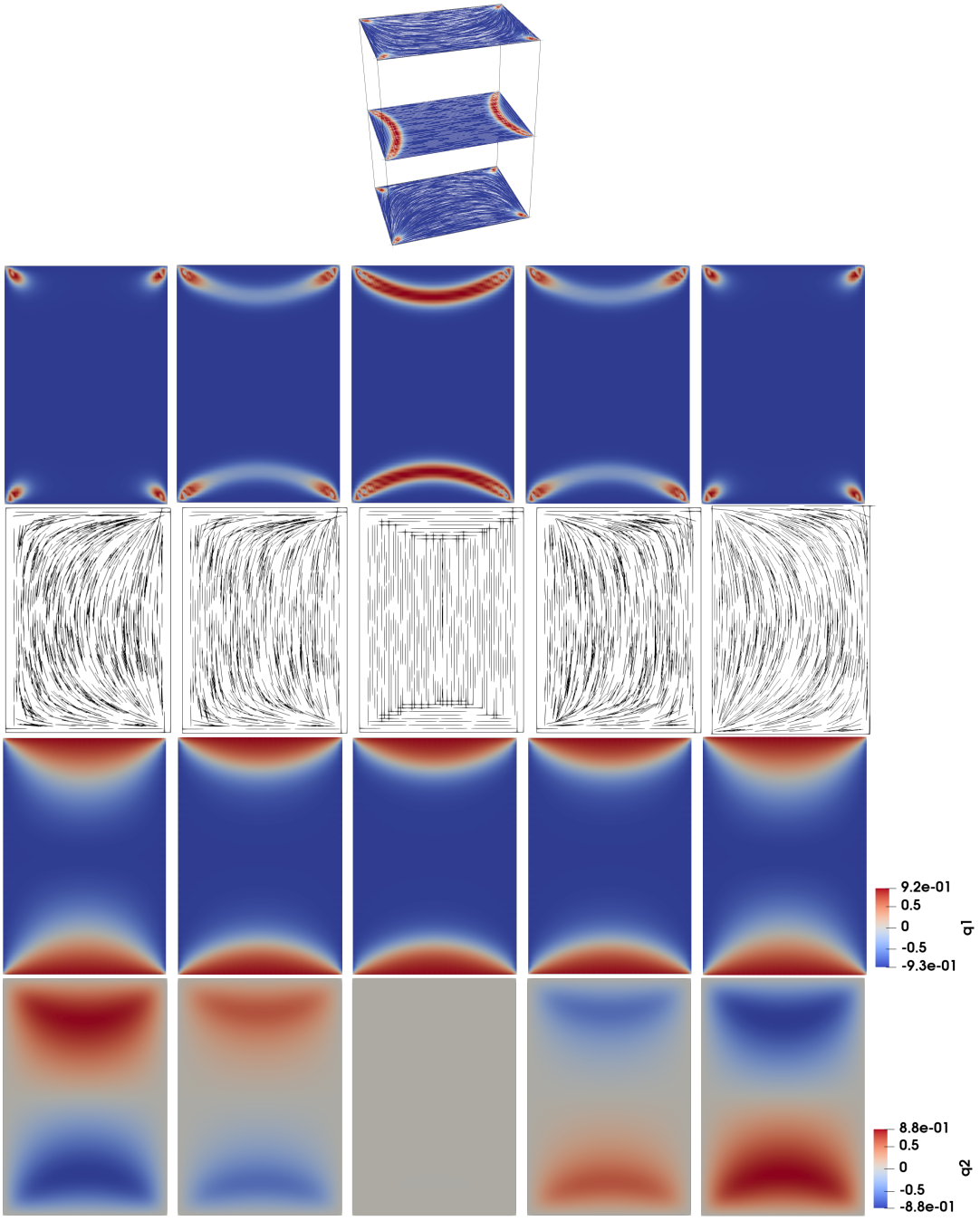

Figure 4.27: A locally stable mixed 3D rotated (R_1 and R_2) solution in a rectangle with $\bar{\lambda}^2 = 100$, $\epsilon = 4$ and $\delta = 1.45$. Cross-sectional heights as in Figure 4.4.

For δ and ϵ large enough, we find other mixed combinations, such as the mixed D and R configuration. This solution, presented in Figure 4.28, consists of two distinct nematic profiles on the top and bottom plates. On the top surface of the well, we have a diagonal D_1 state, while on the bottom surface, we have a rotated R_2 state. This particular simulation was obtained by taking the (D1) and (R2) initial configurations in the top and bottom halves of the well, respectively. This mixed solution exhibits a different type of profile in the interior of the well, but not at the middle slice ($z = \frac{\epsilon}{2}$). This profile involves one nodal $q_1 = 0$ line across a short edge of the rectangle, which separates two distinct values of q_1. In Figure 4.28, we present the mixed diagonal and rotated solution by a 3D representation, with 2D cross-sections at $z = 4, 1.53$, and 0. We also plot: the biaxiality parameter; the director profile; q_1; and q_2 at the (asymmetric) cross-sectional heights $z = 4, 1.8, 1.53, 1.26, 0$. We only observe solutions of this type if ϵ and δ are large enough.

Indeed, all of these mixed 3D configurations exhibit some dependence on ϵ and δ. In Figure 4.29, we plot the critical well-height, ϵ_*, such that for $\epsilon < \epsilon_*$, the mixed solutions lose their stability, as a function of δ. We see that we can only find the mixed rotated solutions, as in Figure 4.27, for $\delta \geq 1.3$, and mixed diagonal and rotated solutions, as in Figure 4.28, for $\delta \geq 1.9$. These findings are in accordance with the numerical study of mixed solutions for $\delta = 1$, in Section 4.3.1.

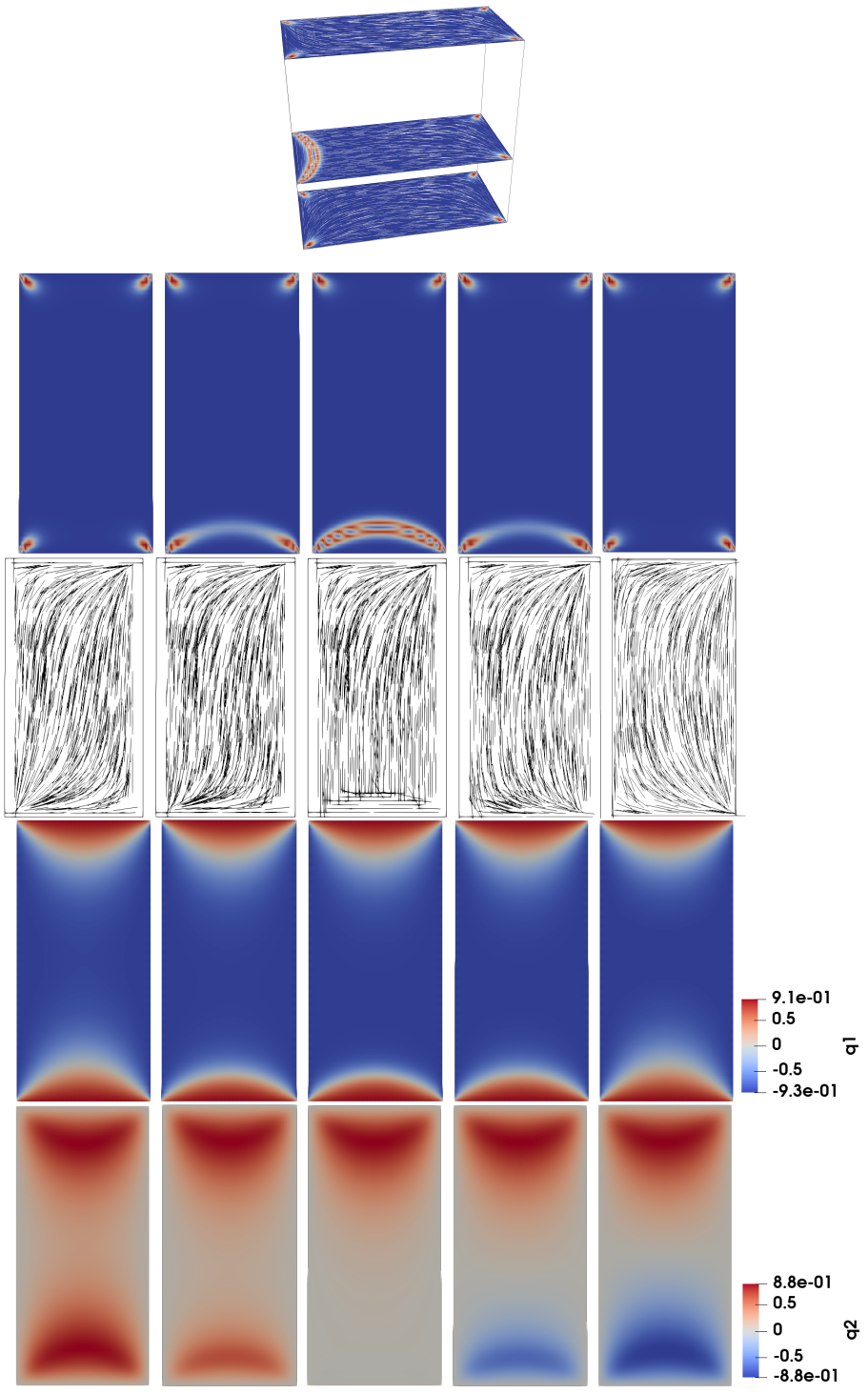

Figure 4.28: A mixed 3D diagonal (D) and rotated (R) solution in a rectangle with $\bar{\lambda}^2 = 100$, $\epsilon = 4$ and $\delta = 2.1$. 2D cross-sections (from left to right) at $z = 4, 1.8, 1.53, 1.26, 0$.

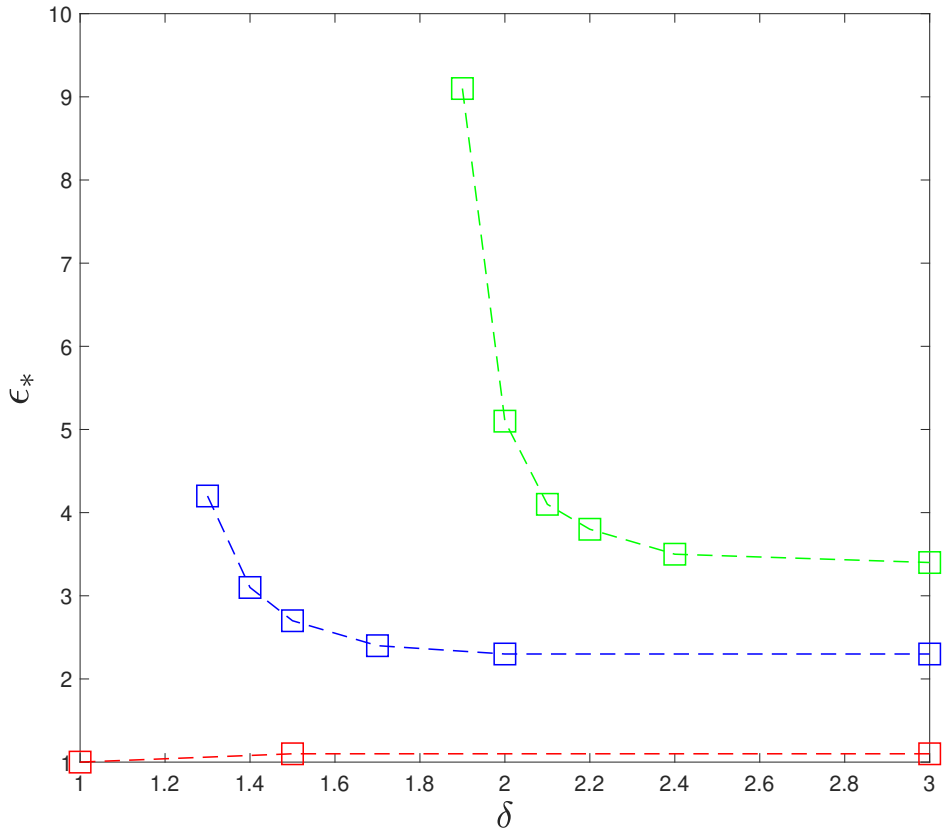

Figure 4.29: Bifurcation points ϵ_*, such that the mixed solutions lose their stability for $\epsilon < \epsilon_*$, as a function of δ. The red markers indicate the critical well heights for the mixed diagonal solutions, the blue markers for the mixed rotated solutions, and the green markers for the mixed diagonal and rotated solutions.

4.4 Summary

In this chapter, we have employed an energy minimization based numerical scheme to simulate nematic equilibria, in three-dimensional confinement. In order to complement the analysis of three-dimensional nematic equilibria in Chapter 3, we have computed local minimizers of the LdG free energy in the absence of external fields, in square wells of finite height. We imposed strong anchoring conditions on the lateral surfaces, as well as surface energies on the top and bottom surfaces with a large anchoring coefficient. We have also numerically studied the stability of these solutions, by solving the dynamic equation of a Rayleigh quotient corresponding to the Hessian of the computational solution. This essentially determines the sign of the smallest eigenvalue of the Hessian, which is sufficient at verifying (at least numerically) locally stable configurations.

We have presented solutions in a square with either a diagonal or rotated profile in the (x, y)-plane for λ large enough, or the 3D WORS for λ small enough, for arbitrary well height, as predicted by the analysis of LdG minimizers. We also numerically demonstrated the existence of stable mixed 3D solutions with two different diagonal profiles on the top and bottom well surfaces, for wells with sufficiently large ϵ and λ. These are again interesting from an applications point of view, and are 3D solutions that are not covered by a purely 2D study. It is interesting to see that whilst the BD solution is an unstable LdG critical point on a 2D square domain, it interpolates between the two distinct diagonal profiles for a stable mixed 3D solution. This was then followed by a numerical investigation of the effect of surface anchoring on the WORS, exemplifying the relevance of this solution in a 3D context. We showed that the WORS loses its stability, at smaller values of well-size, as the anchoring strength on the lateral surfaces is reduced, and

that the numerical procedure will converge to a uniform configuration, if anchoring is weak enough. We completed our numerical investigation on square wells by reporting two novel escaped configurations, given a weak anchoring condition on the top and bottom surfaces of the well. These escaped configurations exhibit ± 1-disclination lines in the centre of the well, along the z-axis, and are stable for ϵ large enough and W_z small enough. Furthermore, the anchoring, W_z, required to find these stable escaped solutions, must decrease as we lower the height of the well.

We have extended our numerical investigation to three-dimensional rectangular wells. We considered minimizers of the LdG free energy, and the effects of the geometric anisotropy δ, λ and ϵ, on the stability of equilibrium configurations in this 3D geometry. We showed that for large enough λ, we can find diagonal and rotated states. However, the higher energy rotated (U) states may only be found for δ small enough. For λ small enough, we always find the sBD2 limiting profile in three dimensions, for arbitrary ϵ. For λ less than some critical value, the diagonal and rotated states cease to exist. However, as δ increases, the U states are increasingly hard to find, and the R states become easier to find. We present a bifurcation diagram which demonstrates how these critical values of λ change, as a function of δ, for the D, R and U states. Interestingly, δ has a stabilising effect on the appearance of mixed solutions. For δ and ϵ large enough, we find stable mixed 3D solutions not previously found in 3D square wells, such as mixed combinations of the D_1, D_2, R_1, and R_2 states on the top and bottom surfaces. This is different from the 3D square wells as only mixed diagonal solutions were found to be stable, for ϵ large enough. We complement this with bifurcation diagrams for the mixed configurations, which illustrate the stabilising effect of δ and the well height.

Chapter 5

Elastic anisotropy in a 2D square domain

In [60], the authors experimentally and numerically study NLCs inside periodic arrays of 3D wells, with a square cross-section, such that the well height is typically much smaller than the square cross-sectional length. In other words, the authors speculate that the structural characteristics only vary in the plane of the square cross-section, and are translationally invariant along the height of the well, effectively reducing this to a two-dimensional (2D) problem. Hence, the authors restrict attention to the bottom square cross-section of the well geometry, where the square edge length is denoted by λ, and typically on the micron scale. The authors impose tangent boundary conditions (TBCs) on the well surfaces i.e., the nematic directors, in the plane of the well surfaces, are constrained to be tangent to those well surfaces. As we explained in Chapter 3, the authors observe two classes of stable NLC states in this geometry: the diagonal (D) states, for which the nematic director aligns along one of the square diagonals; and the rotated (R) states, for which the director rotates by π radians between a pair of opposite

square edges. The typical nematic director profile for these states is shown in Figure 2.2. In [52], [61], the authors model this square system within the 2D LdG framework, where the elastic energy is an isotropic elastic energy - the Dirichlet elastic energy. In this chapter, we study the same problem of NLCs on a 2D square domain, with Dirichlet TBCs on the square edges, but with a two-term anisotropic elastic energy as opposed to the isotropic energy.

We model the degree of elastic anisotropy by the anisotropy parameter, L_2. We prove that, for λ small enough, there exists a unique global minimizer of the revised LdG energy, for all values of L_2. We show that with the addition of elastic anisotropy to our model, the solution landscape is more complex, and the unique global minimizer corresponds to either: (i) the 'Ring' solution with a +1-defect at the square centre, for L_2 small enough or; (ii) a 'Constant' solution, for L_2 large enough, which is constantly uniaxial with negative scalar order parameter away from the edges of the square. This corresponds to a NLC system which is uniformly aligned in the direction of the well height. We then categorise the symmetries of these solutions in the $\lambda \to 0$ limit. We show that critical points of the Landau-de Gennes energy are stable, for L_2 larger than some critical threshold that depends on λ. This analysis is then complemented by numerical simulations and several bifurcation diagrams as a function of λ, for different values of L_2.

5.1 Model formulation

As we described in Chapter 1, the LdG $\mathbf{Q}$-tensor (1.4.1) describes the nematic state of order. The eigenvectors of $\mathbf{Q}$ represent the averaged directions of preferred molecular alignment, and the corresponding eigenvalues measure the degree of order about these eigen-directions. In this chapter, we assume a 2D confining

geometry, $\Omega \subset \mathbb{R}^2$, in the context of modelling *thin* 3D systems. Consider a 3D well, such as

$$\mathcal{B} = \left\{(x, y, z) \in \mathbb{R}^3 : (x, y) \in \Omega,\ z \in (0, h)\right\},$$

where $h \ll \lambda$, and λ is a characteristic length scale associated with Ω e.g., edge length of a regular 2D polygon. In this limit, one can assume (at least for modelling purposes) that physically relevant $\mathbf{Q}$-tensors are independent of the z-coordinate i.e., the profiles are invariant across the height of the well, and that $\hat{\mathbf{z}}$ is a fixed eigenvector (see [70] and [71] for some rigorous analysis and justification). This implies that we can restrict ourselves to $\mathbf{Q}$-tensors with three degrees of freedom (see (3.2.16)). For clarity, we consider

$$\begin{aligned}\mathbf{Q} = q_1(x, y)(\hat{\mathbf{x}} \otimes \hat{\mathbf{x}} - \hat{\mathbf{y}} \otimes \hat{\mathbf{y}}) + q_2(x, y)(\hat{\mathbf{x}} \otimes \hat{\mathbf{y}} + \hat{\mathbf{y}} \otimes \hat{\mathbf{x}}) \\ + q_3(x, y)(2\hat{\mathbf{z}} \otimes \hat{\mathbf{z}} - \hat{\mathbf{x}} \otimes \hat{\mathbf{x}} - \hat{\mathbf{y}} \otimes \hat{\mathbf{y}}),\end{aligned} \tag{5.1.1}$$

where $\hat{\mathbf{x}}, \hat{\mathbf{y}}$ and $\hat{\mathbf{z}}$ are unit vectors in the x-, y- and z-axis, respectively. The degree of nematic order in the plane is captured by the scalar functions q_1, and q_2, whereas q_3 measures the out-of-plane order, such that positive (negative) q_3 implies that the nematic director lies out of the plane (in the plane) of the square, respectively. The TBCs will naturally constrain q_3 to be negative on the square edges, but q_3 could be positive in the interior, away from the square edges, for energetic reasons.

In the absence of a surface anchoring energy and external electric/magnetic fields, the LdG free energy is given by

$$\mathcal{F}[\mathbf{Q}] := \int_\Omega f_{el}(\mathbf{Q}, \nabla\mathbf{Q}) + f_b(\mathbf{Q})\,\mathrm{dA},$$

where f_{el} and f_b are the elastic and thermotropic bulk energy densities, respectively. We define our thermotropic energy density by (1.4.6), just as we did in the

preceding analysis, in Chapter 3. For clarity, we take

$$f_b(\mathbf{Q}) = \frac{A}{2}\text{tr}\mathbf{Q}^2 - \frac{B}{3}\text{tr}\mathbf{Q}^3 + \frac{C}{4}(\text{tr}\mathbf{Q}^2)^2,$$

where A encodes the temperature of the system, and $B, C > 0$ are material-dependent constants. We work with low temperatures, $A < 0$, for which f_b is minimized by a continuum of uniaxial states of the form (1.4.7). In this model problem, we consider a two-term elastic energy density given by

$$f_{el}(\mathbf{Q}) = \frac{L}{2}\left(|\nabla\mathbf{Q}|^2 + L_2(\text{div}\,\mathbf{Q})^2\right),$$

where $L > 0$ is an elastic constant, and $L_2 \in (-1, \infty)$ is the "elastic anisotropy" parameter. In terms of notation, we use $|\nabla\mathbf{Q}|^2 := Q_{ij,k}Q_{ij,k}$, and $(\text{div}\,\mathbf{Q})^2 := Q_{ij,j}Q_{ik,k}$, for $i, j, k = 1, 2, 3$, where the Einstein summation convention is assumed and $Q_{ij,k} = \frac{\partial Q_{ij}}{\partial x_k}$. Since we assume a 2D confining geometry, Ω, we have that $Q_{ij,3} = 0$, for all $1 \leq i, j \leq 3$. Comparing the $\mathbf{Q}$-tensor elastic constants above with the Frank elastic constants described in (1.3.2), we see that $L \propto K_2$ and $L_2 \propto \frac{K_1 - K_2}{K_2}$, where $K_1 = K_3$ (see [19]). This implies that, for our choice of elastic energy density, splay and bend deformations of the nematic director (see Figure 1.9) are energetically expensive compared to out-of-plane twist deformations, for L_2 positive i.e., we would expect the physically observable states to have positive q_3 in the square interior, as L_2 increases. Therefore, we would expect to see competing effects between the TBCs on the square edges, and the preferred out-of-plane director orientation in the square interior, for larger values of L_2. We may consider the measured Frank elastic constants for real liquid crystals given in the table below and, utilizing the relation to the elastic constants in the Landau-de Gennes free energy in [19], estimate real values for the elastic anisotropy L_2.

	PAA at $120^{\circ C}$ [9]	MBBA at $25^{\circ C}$ [13]
K_1	5×10^{-12} N	6×10^{-12} N
K_2	3.8×10^{-12} N	3.8×10^{-12} N
L_2	~ 0.6	~ 1.2

We non-dimensionalize the system using a change of variables, $\bar{\mathbf{x}} = \frac{\mathbf{x}}{\lambda}$, where λ is the characteristic edge length of Ω. The rescaled LdG energy functional (up to a multiplicative constant) is given by:

$$\mathcal{F}_\lambda[\mathbf{Q}] := \frac{\mathcal{F}[\mathbf{Q}]}{L\lambda} = \int_{\bar{\Omega}} \left\{ \frac{1}{2}|\nabla_{\bar{\mathbf{x}}}\mathbf{Q}|^2 + \frac{L_2}{2}(\operatorname{div}_{\bar{\mathbf{x}}}\mathbf{Q})^2 + \frac{\lambda^2}{L} f_b(\mathbf{Q}) \right\} \overline{\mathrm{dA}}, \tag{5.1.2}$$

where differentiation is with respect to the new rescaled coordinates, $\bar{\Omega}$ is the rescaled domain in $\mathbb{R}^2$, and $\overline{\mathrm{dA}}$ is the rescaled area element. We drop the 'bars' in the rest of this chapter, but all computations should be interpreted in terms of the rescaled variables.

Next, we define the working domain and Dirichlet boundary conditions for this model problem, although we believe that our methods can be generalised to arbitrary 2D domains and other types of Dirichlet conditions. We focus on square domains, building on the substantial work in [88], [62], [63], and following the same approach as the one taken in Chapter 3. We impose Dirichlet tangent boundary conditions on the square edges, which require the nematic director to be tangent to the edges, necessarily creating a mismatch at the square vertices. To avoid the discontinuities at the vertices, we take $\Omega \subset \mathbb{R}^2$ to be a truncated unit square, whose edges are parallel to the coordinate axes:

$$\Omega := \{(x, y) \in \mathbb{R}^2 : |x| < 1, |y| < 1, |x + y| < 2 - \eta, |x - y| < 2 - \eta\}.$$

Provided $\eta << 1$, the truncation does not change the qualitative properties of the

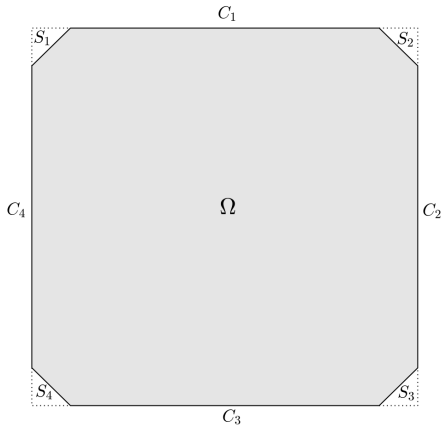

Figure 5.1: The truncated unit square, $\Omega \subset \mathbb{R}^2$.

LdG energy minimizers, away from the square vertices. The boundary, $\partial\Omega$, has four "long" edges, parallel to the coordinate axes, which we define in a clockwise fashion as $C_1, \ldots, C_4$, where C_1 lies parallel to the x-axis at $y = 1$. The truncation creates four additional "short" edges of length $\sqrt{2}\eta$, parallel to the lines $y = x$ and $y = -x$, which we label as $S_1, \ldots, S_4$ in a clockwise fashion, starting at the top-left corner of the domain. The domain is illustrated in Figure 5.1.

We impose tangent uniaxial Dirichlet conditions on the long edges, consistent with the experimentally and numerically investigated TBCs in [60], [61] and [52]. In particular, we fix the director to be $\mathbf{n} = (\pm 1, 0)$ on the edges, C_1 and C_3, and $\mathbf{n} = (0, \pm 1)$ on C_2 and C_4. From a physical standpoint, this constitutes *strong* (infinite) anchoring on the long edges. One could also model a weak (finite) anchoring condition with an additional surface energy in the LdG free energy [19], but that would make the analysis more complicated for the time being. We set

$$\mathbf{Q} = \mathbf{Q}_b \qquad \text{on} \qquad \partial\Omega, \tag{5.1.3}$$

where

$$\mathbf{Q}_b(x,y) := \begin{cases} s_+\left(\hat{\mathbf{x}}\otimes\hat{\mathbf{x}} - \frac{1}{3}\mathbf{I}\right), & (x,y)\in C_1\cup C_3, \\ s_+\left(\hat{\mathbf{y}}\otimes\hat{\mathbf{y}} - \frac{1}{3}\mathbf{I}\right), & (x,y)\in C_2\cup C_4, \end{cases} \tag{5.1.4}$$

where $\mathbf{I}$ is the identity matrix in 3 dimensions. In particular, $\mathbf{Q}_b$ minimizes the thermotropic bulk potential on $C_1,\dots,C_4$. On the short edges, $S_1,\dots,S_4$, we effectively prescribe a continuous interpolation between the boundary conditions on the associated long edges (5.1.4), given by:

$$\mathbf{Q}_b(x,y) := \begin{cases} g(x+y)(\hat{\mathbf{x}}\otimes\hat{\mathbf{x}} - \hat{\mathbf{y}}\otimes\hat{\mathbf{y}}) - \frac{s_+}{2}\left(\hat{\mathbf{z}}\otimes\hat{\mathbf{z}} - \frac{1}{3}\mathbf{I}\right), & (x,y)\in S_1, \\ g(y-x)(\hat{\mathbf{x}}\otimes\hat{\mathbf{x}} - \hat{\mathbf{y}}\otimes\hat{\mathbf{y}}) - \frac{s_+}{2}\left(\hat{\mathbf{z}}\otimes\hat{\mathbf{z}} - \frac{1}{3}\mathbf{I}\right), & (x,y)\in S_2, \\ g(-x-y)(\hat{\mathbf{x}}\otimes\hat{\mathbf{x}} - \hat{\mathbf{y}}\otimes\hat{\mathbf{y}}) - \frac{s_+}{2}\left(\hat{\mathbf{z}}\otimes\hat{\mathbf{z}} - \frac{1}{3}\mathbf{I}\right), & (x,y)\in S_3, \\ g(x-y)(\hat{\mathbf{x}}\otimes\hat{\mathbf{x}} - \hat{\mathbf{y}}\otimes\hat{\mathbf{y}}) - \frac{s_+}{2}\left(\hat{\mathbf{z}}\otimes\hat{\mathbf{z}} - \frac{1}{3}\mathbf{I}\right), & (x,y)\in S_4, \end{cases} \tag{5.1.5}$$

where $g : [-\eta,\eta] \to [-\frac{s_+}{2}, \frac{s_+}{2}]$ is a smoothing function, defined as

$$g(\upsilon) = \frac{s_+}{2\eta}\upsilon, \qquad -\eta \le \upsilon \le \eta.$$

Although the boundary conditions (5.1.5) do not minimize f_b on $S_1,\dots,S_4$, and do not respect TBCs, they are short by construction and are chosen purely for mathematical convenience. Given the Dirichlet boundary conditions (5.1.4) and (5.1.5), we define our admissible space to be

$$\mathcal{A} := \{\mathbf{Q}\in W^{1,2}(\Omega;\mathcal{S}_0) : \mathbf{Q} = \mathbf{Q}_b \ \text{ on } \ \partial\Omega\}, \tag{5.1.6}$$

where we recall $\mathcal{S}_0$ is the space of traceless symmetric 3×3 matrices. The energy minimizers, indeed any critical point of the LdG energy (5.1.2), are solutions of

the associated Euler-Lagrange equations:

$$\begin{aligned}\Delta Q_{ij}+&\frac{L_2}{2}\left(Q_{ik,kj}+Q_{jk,ki}-\frac{2}{3}\delta_{ij}Q_{kl,kl}\right)\\&=\frac{\lambda^2}{L}\left\{AQ_{ij}-B\left(Q_{ik}Q_{kj}-\frac{1}{3}\delta_{ij}\mathrm{tr}\mathbf{Q}^2\right)+CQ_{ij}\mathrm{tr}\mathbf{Q}^2\right\},\end{aligned}\tag{5.1.7}$$

which comprise a system of up to five nonlinear, coupled partial differential equations. The terms $\frac{2}{3}Q_{kl,kl}$, and $\frac{1}{3}\mathrm{tr}\mathbf{Q}^2$, are simply Lagrange multipliers associated with the tracelessness constraint. Given that we restrict ourselves to studying $\mathbf{Q}$-tensors of the form (5.1.1), the Euler-Lagrange equations (5.1.7), and the TBCs (5.1.3), reduce to the following system of PDEs, and constraints, on the scalar functions q_1, q_2, q_3:

$$\left(1+\frac{L_2}{2}\right)\Delta q_1+\frac{L_2}{2}(q_{3,yy}-q_{3,xx})=\frac{\lambda^2}{L}q_1(A+2Bq_3+2C(q_1^2+q_2^2+3q_3^2)),\tag{5.1.8}$$

$$\left(1+\frac{L_2}{2}\right)\Delta q_2-L_2q_{3,xy}=\frac{\lambda^2}{L}q_2(A+2Bq_3+2C(q_1^2+q_2^2+3q_3^2)),\tag{5.1.9}$$

$$\left(1+\frac{L_2}{6}\right)\Delta q_3+\frac{L_2}{6}(q_{1,yy}-q_{1,xx}-2q_{2,xy})=\frac{\lambda^2}{L}q_3(A-Bq_3+2C(q_1^2+q_2^2+3q_3^2))+\frac{\lambda^2B}{3L}(q_1^2+q_2^2),\tag{5.1.10}$$

subject to the boundary conditions

$$q_1(x,y) = q_b(x,y) = \begin{cases} \frac{s_+}{2}, & (x,y) \in C_1 \cup C_3; \\ -\frac{s_+}{2}, & (x,y) \in C_2 \cup C_4; \\ g(x+y), & (x,y) \in S_1; \\ g(y-x), & (x,y) \in S_2; \\ g(-x-y), & (x,y) \in S_3; \\ g(x-y), & (x,y) \in S_4, \end{cases} \tag{5.1.11}$$

and

$$q_3(x,y) = -\frac{s_+}{6}, \quad \text{and} \quad q_2 = 0 \quad \text{on} \quad \partial\Omega. \tag{5.1.12}$$

It is easy to verify that the boundary conditions (5.1.11), and (5.1.12), are equivalent to the Dirichlet conditions in (5.1.3).

5.2 Numerical methods

In this chapter, we numerically compute the solutions of the nonlinear system of equations (5.1.8)–(5.1.10), subject to the tangent Dirichlet boundary conditions (5.1.11) and (5.1.12), which are necessarily critical points of (5.3.1). In our simulations, we set the square vertices at $(-1, \pm 1)$ and $(+1, \pm 1)$, such that $(q_1, q_2, q_3) = (q_b, 0, -\frac{s_+}{6})$ on the square edges. We use the DOLFIN library [101], from the popular open-source computing platform FEniCS [102], to solve the weak formulation of (5.1.8)–(5.1.10) given by

$$
\begin{aligned}
0 = \int_\Omega \Big\{ & \left(1 + \frac{L_2}{2}\right) \nabla q_1 \cdot \nabla v_1 + \frac{L_2}{2} \left(q_{3,y} \cdot v_{1,y} - q_{3,x} \cdot v_{1,x}\right) \\
& + \frac{\lambda^2}{L} q_1 \left(A + 2Bq_3 + 2C(q_1^2 + q_2^2 + 3q_3^2)\right) \cdot v_1 \Big\} \, \mathrm{dA} \\
0 = \int_\Omega \Big\{ & \left(1 + \frac{L_2}{2}\right) \nabla q_2 \cdot \nabla v_2 - L_2 q_{3,x} \cdot v_{2,y} \\
& + \frac{\lambda^2}{L} q_2 \left(A + 2Bq_3 + 2C(q_1^2 + q_2^2 + 3q_3^2)\right) \cdot v_2 \Big\} \, \mathrm{dA} \\
0 = \int_\Omega \Big\{ & \left(1 + \frac{L_2}{6}\right) \nabla q_3 \cdot \nabla v_3 + \frac{L_2}{6} \left(q_{1,y} \cdot v_{3,y} - q_{1,x} \cdot v_{3,x} - 2q_{2,x} \cdot v_{3,y}\right) \\
& + \frac{\lambda^2}{L} q_1 \left(A - Bq_3 + 2C(q_1^2 + q_2^2 + 3q_3^2)\right) \cdot v_3 + \frac{\lambda^2 B}{3L} (q_1^2 + q_2^2) \cdot v_3 \Big\} \, \mathrm{dA}
\end{aligned}
$$

for arbitrary test functions $v_1, v_2, v_3 \in W_0^{1,2}(\Omega)$. We apply the finite element method on a triangular mesh, with mesh-size $h \leq \frac{1}{256}$, for the discretization of the square domain. This then defines a large, but finite-dimensional nonlinear problem of the form: $F(\mathbf{q}) = 0$, where $\mathbf{q}$ is the finite element approximation of (q_1, q_2, q_3), and F is the sum of the integrals above. This nonlinear system is solved using Newton's method [103]. In Chapter 4, we described standard line search algorithms and properties of quasi-Newton methods, which optimize the nonlinear problem, without the expensive computation of the Hessian, $\mathbf{G}(\mathbf{q}) = \nabla^2 F(\mathbf{q})$. For our purposes, Newton's method is sufficient [104], [105], and DOLFIN automates much of this computation using a linear LU solver for each iteration. The iterative scheme has converged when the residual at an iteration k, $||F(\mathbf{q}_k)||$, is less than the absolute tolerance which we set to 10^{-13}. Due to the high multiplicity of the solutions, convergence may be highly sensitive to the choice of initial condition.

We also check the stability of the solutions by numerically calculating the smallest real eigenvalue, λ_1, of the Hessian $\mathbf{G}(\mathbf{q})$ of the computed solution, $\mathbf{q}$, with three

degrees of freedom using the LOBPCG (locally optimal block preconditioned conjugate gradient) method [106]. This method follows a similar approach to the Rayleigh quotient iterative minimization method explained in Chapter 4, where $\lambda_1 > 0$ is essentially a signature of local stability, and the numerical solution is unstable if $\lambda_1 < 0$. A full description of this iterative algorithm can be found in [66].

In the figures of our numerical solutions, we regularly plot the scalar order parameter $s^2 = q_1^2 + q_2^2$, labelled by the colour chart, and the nematic director, $\mathbf{n}$, shown by white lines, where $\mathbf{n}$ is given by

$$\mathbf{n} = (\cos\theta, \sin\theta), \qquad \theta = \frac{1}{2}\text{atan2}(q_2, q_1). \tag{5.2.1}$$

Here, the function atan2 is found in many modern programming languages and $\text{atan2}(y, x)$ returns the angle θ between the ray to the point (x, y) and the positive x-axis, confined to $(-\pi, \pi]$. These measures capture the nematic order parameter for the system. In order to make comparisons with the numerical simulations in [62], [63], and the results in Chapter 4, we fix $B = 0.64 \times 10^4\,\text{Nm}^{-2}$, $C = 0.35 \times 10^4\,\text{Nm}^{-2}$ and the special temperature $A = -\frac{B^2}{3C}$, and we define the dimensionless parameter

$$\bar{\lambda}^2 := \frac{2C\lambda^2}{L}.$$

We frequently refer to this rescaled parameter, which describes the cross-sectional size of the domain, in our numerical simulations. We also compute bifurcation diagrams as a function of $\bar{\lambda}^2$, for various fixed values of L_2. In these diagrams, we plot solid lines to represent stable solution branches, and dashed lines correspond to unstable branches. The numerical computation of the bifurcation diagrams requires continuation techniques, for which we first locate different stable solutions,

for fixed L_2 and $\bar{\lambda}^2$. Depending on the solution branch, we perform a increasing/decreasing $\bar{\lambda}^2$ sweep to produce these diagrams (we solve for a value of λ, and then use that numerical solution as the initial guess in the procedure to solve for a larger/smaller λ), and we plot two measures to distinguish between separate solution branches: $\int_\Omega q_1 \, (1 + x + y) \, \mathrm{d}x\mathrm{d}y$ and $\int_\Omega q_2 \, (1 + x + y) \, \mathrm{d}x\mathrm{d}y$. These particular measures were chosen in order to compare with the results in [64], [74] for the $L_2 = 0$ modelling scenario. The multiplier $(1 + x + y)$ has been chosen in order to distinguish between the symmetry of the diagonal solutions and the Ring and WORS configurations.

5.3 Qualitative properties of the equilibrium configurations

In [52], the authors numerically compute critical points of (5.1.2) with $L_2 = 0$, satisfying the Dirichlet boundary conditions (5.1.3), on the square cross-section Ω, with edge length λ. For λ small enough, the authors report a new Well Order Reconstruction Solution (WORS). The WORS has a constant set of eigenvectors, $\hat{\mathbf{x}}, \hat{\mathbf{y}}$, and $\hat{\mathbf{z}}$, which are the coordinate unit vectors. The WORS is further distinguished by a uniaxial cross, with negative scalar order parameter, along the square diagonals. Physically, this indicates the nematic molecules prefer to be in the plane of the square, there is a planar defect cross along the square diagonals, and the nematic molecules are disordered in the square plane along the square diagonals. In [62], the authors analyse this system at the fixed temperature $A = -\frac{B^2}{3C}$, at which, the WORS is a classical solution of the associated

Euler-Lagrange equations given by:

$$\mathbf{Q}_{WORS}(x,y) = q(\hat{\mathbf{x}}\otimes\hat{\mathbf{x}} - \hat{\mathbf{y}}\otimes\hat{\mathbf{y}}) - \frac{B}{6C}(2\hat{\mathbf{z}}\otimes\hat{\mathbf{z}} - \hat{\mathbf{x}}\otimes\hat{\mathbf{x}} - \hat{\mathbf{y}}\otimes\hat{\mathbf{y}}).$$

There is a single degree of freedom, $q : \Omega \to \mathbb{R}$, which satisfies the Allen-Cahn equation

$$\Delta q = \frac{\lambda^2}{L}\left(2Cq^3 - \frac{B^2}{2C}q\right),$$

and exhibits the following symmetry properties:

$$q = 0 \quad \text{on} \quad \{y = x\} \cup \{y = -x\}, \qquad (y^2 - x^2)q(x,y) \geq 0.$$

Notably, $q_2 = 0$ everywhere for the WORS, which is equivalent to having a set of constant eigenvectors in the plane of Ω. They prove that the WORS is globally stable for λ small enough, and unstable for λ large enough, demonstrating a pitchfork bifurcation in a scalar setting. Their analysis is restricted to the specific temperature and, in Chapter 3, we have extended the analysis to all $A < 0$, with $L_2 = 0$. In this section, we analyse the equilibrium configurations with $L_2 \neq 0$, in the small λ limit, including their symmetry properties. Notably, we show that the cross-structure of the WORS does not survive with $L_2 \neq 0$, in the following propositions. Our first result concerns the existence of minimizers of the rescaled LdG energy functional (5.1.2).

Proposition 5.3.1. *There exists at least one solution to the Euler-Lagrange equations (5.1.7) of the form (5.1.1) in $\mathcal{A}$, given the Dirichlet boundary conditions (5.1.4) and (5.1.5), provided the functions q_1, q_2, q_3 satisfy the PDE system (5.1.8)–(5.1.10) subject to the boundary conditions (5.1.11) and (5.1.12).*

Proof. Our proof is analogous to Theorem 2.2 in [71]. Substituting the **Q**-tensor ansatz (5.1.1) into the general form of the LdG energy (5.1.2), we let

$$J[q_1, q_2, q_3] := \int_\Omega f_{el}(q_1, q_2, q_3) + \frac{\lambda^2}{L} f_b(q_1, q_2, q_3)\, \mathrm{dA}, \tag{5.3.1}$$

where we have substituted our **Q**-tensor (5.1.1) into our elastic and thermotropic bulk energy densities to obtain

$$\begin{aligned} f_{el}(q_1, q_2, q_3) := &\left(1 + \frac{L_2}{2}\right) |\nabla q_1|^2 + \left(1 + \frac{L_2}{2}\right) |\nabla q_2|^2 + \left(3 + \frac{L_2}{2}\right) |\nabla q_3|^2 \\ &+ L_2(q_{1,y} q_{3,y} - q_{1,x} q_{3,x} - q_{2,y} q_{3,x} - q_{2,x} q_{3,y}) + |L_2|(q_{2,y} q_{1,x} - q_{1,y} q_{2,x}), \end{aligned} \tag{5.3.2}$$

and

$$f_b(q_1, q_2, q_3) := A(q_1^2 + q_2^2 + 3q_3^2) + C(q_1^2 + q_2^2 + 3q_3^2)^2 + 2Bq_3(q_1^2 + q_2^2 - q_3^2), \tag{5.3.3}$$

respectively. We prove the existence of minimizers of J in the admissible class

$$\mathcal{A}_0 := \{(q_1, q_2, q_3) \in W^{1,2}(\Omega; \mathbb{R}^3) : q_1 = q_b,\ q_2 = 0,\ q_3 = -\frac{s_+}{6} \text{ on } \partial\Omega\},$$

which will also be solutions of (5.1.7), in the admissible space $\mathcal{A}$. Since the boundary conditions (5.1.11) and (5.1.12) are piece-wise of class C^1, we have that the admissible space $\mathcal{A}_0$ is non-empty. The next step, is to check that J is coercive in $\mathcal{A}_0$. The elastic energy density can be rewritten as a function of $q_1, q_2, q_3 \in W^{1,2}(\Omega; \mathbb{R})$ in the following two ways (depending on the sign of L_2):

$$f_{el} = |\nabla q_1|^2 + |\nabla q_2|^2 + 3|\nabla q_3|^2 + \frac{L_2}{2}((q_{1,x} + q_{2,y} - q_{3,x})^2 + (q_{2,x} - q_{1,y} - q_{3,y})^2), \tag{5.3.4}$$

if $L_2 \in [0, \infty)$, and

$$f_{el} = (1+L_2)(|\nabla q_1|^2 + |\nabla q_2|^2 + 3|\nabla q_3|^2) \\ - \frac{L_2}{2}((-q_{3,x} - q_{1,x} - q_{2,y})^2 + (q_{2,x} - q_{1,y} + q_{3,y})^2 + 4|\nabla q_3|^2), \tag{5.3.5}$$

if $L_2 \in (-1, 0)$. The difference between the expressions for f_{el} in (5.3.4) and (5.3.5), is a null Lagrangian, and hence can be ignored under the Dirichlet boundary condition. Since we assume that $1 + L_2 > 0$, we see that the elastic energy density can be written as the sum of non-negative terms, for any $L_2 > -1$ and, furthermore,

$$f_{el}(q_1, q_2, q_3) \geq \min\{1, 1+L_2\} \left(|\nabla q_1|^2 + |\nabla q_2|^2 + 3|\nabla q_3|^2\right). \tag{5.3.6}$$

Also, the bulk energy potential, f_b, is minimized along the boundary of the domain by design and hence it also satisfies

$$f_b(q_1, q_2, q_3) \geq f_b(\pm\frac{s_+}{2}, 0, -\frac{s_+}{6}) =: M_1(A, B, C),$$

for some constant M_1, depending only on A, B and C. Hence $J[q_1, q_2, q_3]$ is coercive in $\mathcal{A}_0$. Finally, we note that J is weakly lower semi-continuous on $W^{1,2}(\Omega)$, which follows immediately from the fact that f_{el} is quadratic and convex in $\nabla(q_1, q_2, q_3)$. Thus, the direct method in the calculus of variations yields the existence of a global minimizer of the functional J among the finite energy triplets $(q_1, q_2, q_3) \in W^{1,2}(\Omega; \mathbb{R}^3)$, satisfying the boundary conditions (5.1.11) and (5.1.12) [57]. One can verify that the semilinear elliptic system (5.1.8)–(5.1.10) corresponds to the Euler-Lagrange equations associated with J, and the minimizers for J are $C^\infty(\Omega) \cap C^2(\bar{\Omega})$ solutions of (5.1.8)–(5.1.10). The corresponding $\mathbf{Q}$-tensor is an exact solution of the LdG Euler-Lagrange equations (5.1.7). □

Now that we have proved the existence of a critical point of the LdG energy (5.1.2) of the form (5.1.1), our next result constructs a symmetric critical point, for any $L_2 > -1$, for which $q_1 = 0$ on the square diagonals, and $q_2 = 0$ on the coordinate axes, where the axes are parallel to the square edges. Furthermore, the WORS is simply a special case of this critical point with $q_2 = 0$ everywhere in the square domain, for $L_2 = 0$.

Proposition 5.3.2. *There exists a critical point, (q_1^s, q_2^s, q_3^s), of the energy functional (5.3.1) in the admissible space $\mathcal{A}_0$, for all $\lambda > 0$, such that $q_1 = 0$ on the square diagonals $y = x$ and $y = -x$, and $q_2 = 0$ on $x = 0$ and $y = 0$.*

Proof. We follow the approach in [62] and in Proposition 3.2.2. We define the following octant of a square, located in the positive quadrant of Ω:

$$\Omega_q := \{(x, y) \in \Omega : 0 < y < x,\ 0 < x < 1\}.$$

The boundary conditions (5.1.11) and (5.1.12), on the whole of Ω, are consistent with the following boundary conditions on Ω_q:

$$\begin{cases} q_1 = q_b,\ q_2 = 0,\ q_3 = -\frac{s_+}{6}, & (x, y) \in \partial\Omega_q \cap \partial\Omega; \\ q_1 = \partial_\nu q_2 = \partial_\nu q_3 = 0, & (x, y) \in \partial\Omega_q \cap \{y = x\}; \\ \partial_\nu q_1 = q_2 = \partial_\nu q_3 = 0, & (x, y) \in \partial\Omega_q \cap \{y = 0\}, \end{cases} \tag{5.3.7}$$

where ∂_ν represents the outward normal derivative. We minimize the associated LdG energy functional in Ω_q, given by:

$$J[q_1, q_2, q_3] = \int_{\Omega_q} f_{el}(q_1, q_2, q_3) + \frac{\lambda^2}{L} f_b(q_1, q_2, q_3)\, \mathrm{dA},$$

on the admissible space

$$\mathcal{A}_q := \{(q_1, q_2, q_3) \in W^{1,2}(\Omega_q; \mathbb{R}^3) : (5.3.7) \quad \text{is satisfied}\}.$$

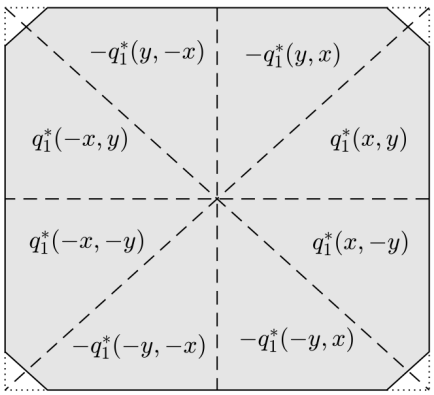

Figure 5.2: The reflected solution $q_1^s(x,y)$.

As the boundary conditions on Ω_q are continuous and piecewise of class C^1, we have that $\mathcal{A}_q$ is non-empty. Furthermore, we have shown that J is coercive on $\mathcal{A}_q$, and convex in the gradient $\nabla(q_1,q_2,q_3)$. Thus, by the direct method in the calculus of variations, we have the existence of a minimizer $(q_1^*,q_2^*,q_3^*)\in\mathcal{A}_q$. We define a function $q_1^s\in\Omega$, by odd reflection of $q_1^*\in\Omega_q$ about the square diagonals, and even reflection about x- and y-axis. An illustration of the reflected solution $q_1^s(x,y)$ is given in Figure 5.2. We can do the same for the function $q_2^s\in\Omega$, defined by even reflections of q_2^* about the square diagonals, and odd reflection about x- and y-axis and lastly, for the function $q_3^s\in\Omega$, defined by even reflections of q_3^* about the square diagonals and the x- and y-axis. By repeating the arguments in [90], and Proposition 3.2.2, we can prove that the new triple, (q_1^s,q_2^s,q_3^s), is a weak solution of the associated Euler-Lagrange equation on Ω. One can verify that (q_1^s,q_2^s,q_3^s) is a critical point of J on $\mathcal{A}_0$, with the desired properties. □

As we mentioned previously, the WORS is distinguished by its uniaxial cross structure, with $q_1=0$ on the square diagonals, and $q_2\equiv 0$ in the square domain. Our next result shows that the symmetric critical point from Proposition 5.3.2

cannot have q_2 identically zero on the domain, for $L_2 \neq 0$. This essentially proves that the addition of anisotropy to the elastic energy destroys the perfect cross symmetry of the WORS.

Proposition 5.3.3. *For $A < 0$ and $L_2 \neq 0$, the critical point constructed in Proposition 5.3.2, denoted by (q_1^s, q_2^s, q_3^s), has non-constant q_2^s on Ω, for all $\lambda > 0$.*

Proof. We proceed by contradiction. Assume that q_2^s is constant on Ω. Recalling the boundary conditions (5.1.12), we necessarily have that $q_2^s \equiv 0$ in Ω. Substituting $q_2^s \equiv 0$ into (5.1.9), we obtain

$$q_3^s(x, y) = F(x) + G(y),$$

for arbitrary real-valued functions F, G, with $q_3^s = -\frac{s_+}{6}$ on $\partial\Omega$. Therefore, $q_3^s \equiv -\frac{s_+}{6}$ in Ω. Substituting $q_2^s \equiv 0$ and $q_3^s \equiv -\frac{s_+}{6}$ into (5.1.8) and (5.1.10) yields the following reduced PDEs:

$$q_{1,yy}^s + q_{1,xx}^s = f(q_1^s), \tag{5.3.8}$$

$$q_{1,yy}^s - q_{1,xx}^s = g(q_1^s) + C_g, \tag{5.3.9}$$

where $f, g : \mathbb{R} \to \mathbb{R}$ and C_g is a constant given by:

$$\begin{aligned} f(q_1^s) &= \frac{4C\lambda^2}{(2+L_2)L}(q_1^s)^3 + \frac{2\lambda^2}{(2+L_2)L}\left(A - \frac{Bs_+}{3} + \frac{Cs_+^2}{6}\right) q_1^s, \\ g(q_1^s) &= \frac{2\lambda^2}{LL_2}(B - Cs_+)(q_1^s)^2, \\ C_g &= -\frac{\lambda^2 s_+}{LL_2}\left(A + \frac{Bs_+}{6} + \frac{Cs_+^2}{6}\right). \end{aligned}$$

By manipulating the equations (5.3.8) and (5.3.9), and taking second derivatives by applications of the chain rule and product rule of differentiation, one can

calculate

$$2(q^s_{1,xx})_{yy} - 2(q^s_{1,yy})_{xx} = f''(q^s_1)((q^s_{1,y})^2 - (q^s_{1,x})^2) - g''(q^s_1)((q^s_{1,y})^2 + (q^s_{1,x})^2) + f'(q^s_1)(\underbrace{q^s_{1,yy} - q^s_{1,xx}}_{=g(q^s_1)+C_g}) - g'(q^s_1)(\underbrace{q^s_{1,yy} + q^s_{1,xx}}_{=f(q^s_1)}) \tag{5.3.10}$$

From the symmetry properties of q^s_1 in Proposition 5.3.2, we have

$$q^s_1|_{(0,0)} = q^s_{1,x}|_{(0,0)} = q^s_{1,y}|_{(0,0)} = 0.$$

Substituting this into (5.3.10), we obtain

$$\begin{aligned}(2q^s_{1,xxyy} - 2q^s_{1,yyxx})|_{(0,0)} &= (f'(q^s_1)C_g)|_{(0,0)} \\ &= -\frac{2\lambda^4 s_+}{(2L_2 + L_2^2)L^2}(A - \frac{Bs_+}{3} + \frac{Cs_+^2}{6})(A + \frac{Bs_+}{6} + \frac{Cs_+^2}{6})\end{aligned} \tag{5.3.11}$$

If $A \neq -\frac{B^2}{3C}$, then the right hand side of equation (5.3.11) at $(0,0)$ is non-zero which, from the equality of mixed partial derivatives, leads to a contradiction. If $A = -\frac{B^2}{3C}$, then $q^s_3 \equiv -\frac{s_+}{6} = -\frac{B}{6C}$ and (5.3.9) reduces to

$$q^s_{1,yy} - q^s_{1,xx} = 0,$$

which implies that q^s_1 is of the following form:

$$q^s_1(x,y) = F_1(x-y) + F_2(x+y),$$

for arbitrary real-valued functions F_1, F_2. By construction of the symmetric critical point from Proposition 5.3.2, we know that for any $\lambda > 0$, q^s_1 satisfies the symmetry property $q^s_1(x,y) = q^s_1(x,-y)$ and hence,

$$F_1(x-y) + F_2(x+y) = F_1(x+y) + F_2(x-y), \qquad \forall (x,y) \in \Omega. \tag{5.3.12}$$

Subtracting $F_2(x-y)+F_2(x+y)$ on both sides of the equality (5.3.12), we get

$$\begin{aligned} G(x-y) &= F_1(x-y) - F_2(x-y) \\ &= F_1(x+y) - F_2(x+y) = G(x+y), \qquad \forall (x,y) \in \Omega. \end{aligned}$$

Therefore, defining another real-valued function with zero derivative,

$$G(z) = F_1(z) - F_2(z) \equiv K, \qquad z \in (-2,2),$$

for some constant K (as a result of the property $G' = -G'$). Given this fact, the function q_1^s may now be rewritten as

$$q_1^s(x,y) = F_1(x+y) + F_1(x-y) - K, \qquad (x,y) \in \Omega.$$

This formulation cannot be extended continuously on the boundary since, for $(x,y) = (0,1)$, $(-1,0)$ and $(1,0)$, we have

$$F_1(1) + F_1(-1) - K = \frac{s_+}{2}, \qquad 2F_1(-1) - K = -\frac{s_+}{2}, \qquad 2F_1(1) - K = -\frac{s_+}{2},$$

which again, leads to the required contradiction. □

Proposition 5.3.4. *There exists some critical edge length, $\lambda_0 > 0$, such that for any $\lambda < \lambda_0$, the critical point, (q_1, q_2, q_3), constructed in Proposition 5.3.2 is the unique critical point of the LdG energy (5.3.1).*

Proof. We adapt the uniqueness criterion argument in Lemma 8.2 of [91]. Let $(q_1^\lambda, q_2^\lambda, q_3^\lambda)$ be a global minimizer of energy functional J in (5.3.1), for some fixed $\lambda > 0$. Let $(q_1^\infty(x,y), q_2^\infty(x,y), q_3^\infty(x,y)) \in \mathcal{A}_0$ be such that $f_b(q_1^\infty, q_2^\infty, q_3^\infty) = \min f_b$, a.e. $(x,y) \in \Omega$. Defining the always positive quantity, $\bar{f}_b(q_1,q_2,q_3) =$

$\frac{1}{L}(f_b(q_1,q_2,q_3) - \min f_b(q_1,q_2,q_3))$, where L is fixed, we have

$$\begin{aligned}\int_\Omega f_{el}(q_1^\lambda, q_2^\lambda, q_3^\lambda)\,\mathrm{dA} &\leq \int_\Omega f_{el}(q_1^\lambda, q_2^\lambda, q_3^\lambda) + \lambda^2 \bar{f}_b(q_1^\lambda, q_2^\lambda, q_3^\lambda)\,\mathrm{dA} \\ &\leq \int_\Omega f_{el}(q_1^\infty, q_2^\infty, q_3^\infty)\,\mathrm{dA} \\ &= M_2(A,B,C,L_2),\end{aligned} \tag{5.3.13}$$

where $M_2 > 0$ is some constant, depending only on A, B, C and the elastic anisotropy L_2. For more details, see Section 5.4.3. Thus, we restrict ourselves to the following admissible space of $\mathbf{Q}$-tensors:

$$\mathcal{A}_{upper} = \left\{ \mathbf{Q} \in \mathcal{A} : \int_\Omega \frac{1}{2}|\nabla \mathbf{Q}|^2 \mathrm{dA} \leq M_2(A,B,C,L_2) \right\}.$$

We aim to prove the strict convexity of the LdG energy functional J in $\mathcal{A}_{upper}$. Firstly, we note that the second derivatives of f_b are quadratic polynomials in (q_1, q_2, q_3). By an application of the relevant embedding theorem in [107] (Theorem 9.16 which implies that for a bounded domain Ω in $\mathbb{R}^N$ with Lipschitz boundary, for any $u \in C_c^1(\Omega)$, $||u||_{L^p} \leq C||u||_{W^{1,2}}$, $\forall p \in [N, \infty)$, with constant C depending only on Ω), we have that there exists some constant c_0, depending only on A, B, C and Ω, such that

$$\left(\int_\Omega |f_b''|^2 \mathrm{dA} \right)^{1/2} \leq c_0(A,B,C,\Omega) \int_\Omega |\nabla \mathbf{Q}|^2\,\mathrm{dA} \leq c_0 M_2.$$

Utilizing the second order central finite difference formula for f_b, and by an application of the Hölder inequality we get, for any $x, y \in \mathcal{A}_{upper}$,

$$\begin{aligned}\int_\Omega f_b\left(\frac{x+y}{2}\right) - \frac{1}{2}f_b(x) - \frac{1}{2}f_b(y)\,\mathrm{dA} &\leq \frac{1}{8}\sup_{\mathcal{A}_{upper}} \left(\int_\Omega |f_b''|^2 \mathrm{dA} \right)^{\frac{1}{2}} \left(\int_\Omega |x-y|^4 \mathrm{dA} \right)^{\frac{1}{2}} \\ &\leq \frac{c_0 M_2}{8} ||x-y||_{L_4}^2\end{aligned}$$

Therefore, for any $(q_1, q_2, q_3), (\tilde{q_1}, \tilde{q_2}, \tilde{q_3}) \in \mathcal{A}_{upper}$, we have

$$\int_\Omega \left\{ f_b\left(\frac{q_1+\tilde{q_1}}{2}, \frac{q_2+\tilde{q_2}}{2}, \frac{q_3+\tilde{q_3}}{2}\right) - \frac{1}{2}f_b(q_1,q_2,q_3) - \frac{1}{2}f_b(\tilde{q_1},\tilde{q_2},\tilde{q_3})\right\} \mathrm{dA} \\ \leq c_1 ||q_1-\tilde{q_1}, q_2-\tilde{q_2}, q_3-\tilde{q_3}||^2_{L_4} \tag{5.3.14}$$

where $c_1 = c_1(\Omega, A, B, C, L_2) > 0$. We note that f_{el} is positive definite quadratic in the gradient of (q_1, q_2, q_3), for all $L_2 > -1$ (see (5.3.6)). By an application of the Poincaré inequality, and by repeating the same arguments as above using the relevant embedding theorem, we have for any $(q_1, q_2, q_3), (\tilde{q_1}, \tilde{q_2}, \tilde{q_3}) \in \mathcal{A}_{upper}$:

$$\begin{aligned}
&\int_\Omega f_{el}(q_1-\tilde{q_1}, q_2-\tilde{q_2}, q_3-\tilde{q_3})\,\mathrm{dA} \\
&\quad \geq \min\{1, 1+L_2\} \int_\Omega \left\{ |\nabla(q_1-\tilde{q_1})|^2 + |\nabla(q_2-\tilde{q_2})|^2 + 3|\nabla(q_3-\tilde{q_3})|^2 \right\} \mathrm{dA} \\
&\quad \geq \min\{1, 1+L_2\} K(\Omega) \left(||q_1-\tilde{q_1}||^2_{W^{1,2}} + ||q_2-\tilde{q_2}||^2_{W^{1,2}} + 3||q_3-\tilde{q_3}||^2_{W^{1,2}} \right) \\
&\quad \geq \ c_2(\Omega, L_2) ||q_1-\tilde{q_1}, q_2-\tilde{q_2}, q_3-\tilde{q_3}||^2_{L^4}
\end{aligned} \tag{5.3.15}$$

for some constant c_2, depending only on Ω and the sign of L_2. Using both (5.3.14) and (5.3.15) we have, where $\mathbf{q} = (q_1, q_2, q_3)$ and $\tilde{\mathbf{q}} = (\tilde{q_1}, \tilde{q_2}, \tilde{q_3})$:

$$\begin{aligned}
J\left[\frac{\mathbf{q}+\tilde{\mathbf{q}}}{2}\right] &= \frac{1}{2}J[\mathbf{q}] + \frac{1}{2}J[\tilde{\mathbf{q}}] - \frac{1}{4}\int_\Omega f_{el}(\mathbf{q}-\tilde{\mathbf{q}})\,\mathrm{dA} \\
&\qquad + \frac{\lambda^2}{L}\int_\Omega \left\{ f_b\left(\frac{\mathbf{q}+\tilde{\mathbf{q}}}{2}\right) - \frac{1}{2}f_b(\mathbf{q}) - \frac{1}{2}f_b(\tilde{\mathbf{q}}) \right\} \mathrm{dA} \\
&\leq \frac{1}{2}J[\mathbf{q}] + \frac{1}{2}J[\tilde{\mathbf{q}}] - \frac{c_2}{4}||\mathbf{q}-\tilde{\mathbf{q}}||^2_{L^4} + \frac{c_1\lambda^2}{L}||\mathbf{q}-\tilde{\mathbf{q}}||^2_{L^4} \\
&= \frac{1}{2}J[\mathbf{q}] + \frac{1}{2}J[\tilde{\mathbf{q}}] - \frac{c_2}{8}||\mathbf{q}-\tilde{\mathbf{q}}||^2_{L^4} - c_1\left(\frac{c_2}{8c_1} - \frac{\lambda^2}{L}\right)||\mathbf{q}-\tilde{\mathbf{q}}||^2_{L^4}
\end{aligned}$$

Thus, J is strictly convex for the finite energy triplets (q_1, q_2, q_3), for $\lambda \leq \lambda_0 := \sqrt{\frac{c_2 L}{8c_1}}$, and has a unique critical point, for $\lambda < \lambda_0$. We deduce that the symmetric critical point, constructed in Proposition 5.3.2, is the unique minimizer of $J[q_1, q_2, q_3]$ and, in fact, the unique global LdG energy minimizer (when we consider $\mathbf{Q}$-tensors with the full five degrees of freedom as opposed to this reduced

setting, (5.1.1), with three degrees of freedom), for sufficiently small λ. □

Lemma 5.3.5. *Suppose that $(q_1, q_2, q_3) \in W^{1,2}(\Omega, \mathbb{R}^3)$ is the unique global minimizer of the energy (5.3.1), for $\lambda < \lambda_0$ given by Proposition 5.3.4. Then for any $L_2 > -1$, the function $q_1 : \Omega \to \mathbb{R}$ vanishes along the square diagonals $y = x$ and $y = -x$ and the function $q_2 : \Omega \to \mathbb{R}$ vanishes along $y = 0$ and $x = 0$.*

Proof. This is in fact an immediate consequence of Proposition 5.3.2 but we present an alternative short proof based on symmetry observations. Suppose that $(q_1, q_2, q_3) \in W^{1,2}(\Omega, \mathbb{R}^3)$ is a global minimizer of the associated energy functional J, in the admissible class $\mathcal{A}_0$, for a given $\lambda > 0$. Then $(q_1(x, y), q_2(x, y), q_3(x, y))$ is a solution of the Euler-Lagrange system (5.1.8)–(5.1.10), subject to the boundary conditions (5.1.11) and (5.1.12). It is easy to verify from applications of the chain rule that the triples

$$(q_1(-x, y), -q_2(-x, y), q_3(-x, y)), \quad (q_1(x, -y), -q_2(x, -y), q_3(x, -y)),$$
$$(-q_1(y, x), q_2(y, x), q_3(y, x))$$

also solve the Euler-Lagrange system and are compatible with the imposed boundary conditions. We combine this symmetry result with the uniqueness result in Proposition 5.3.4 to get the desired conclusion. For example, we simply use $q_1(x, y) = -q_1(y, x)$, with $x = y$, to deduce that $q_1(x, x) = 0$. Also, $q_1(-x, y) = q_1(x, y)$, with $x = y$, yields that $q_1(x, -x) = q_1(x, x) = 0$. Furthermore, we use the relation $q_2(x, y) = -q_2(-x, y)$, with $x = 0$, to deduce that $q_2(0, y) = 0$, and similarly, $q_2(x, y) = -q_2(x, -y)$, with $y = 0$, to deduce that $q_2(x, 0) = 0$. □

Corollary 5.3.6. *For $A < 0$ and $L_2 \neq 0$, the unique global minimizer, (q_1, q_2, q_3), given in Proposition 5.3.4 when $\lambda < \lambda_0$, also has the symmetry property $q_1(x, y) =$*

$q_1(-x, y) = q_1(x, -y)$ in Lemma 5.3.5. If q_3 is constant in Ω then, in order to satisfy the boundary conditions, we must have $q_3 \equiv -\frac{s_+}{6}$ in Ω. Therefore, equations (5.1.8)–(5.1.9) become

$$\left(1 + \frac{L_2}{2}\right)\Delta q_1 = \frac{\lambda^2}{L} q_1 \left(A - \frac{Bs_+}{3} + 2C(q_1^2 + q_2^2) + \frac{Cs_+^2}{6}\right),$$
$$\left(1 + \frac{L_2}{2}\right)\Delta q_2 = \frac{\lambda^2}{L} q_2 \left(A - \frac{Bs_+}{3} + 2C(q_1^2 + q_2^2) + \frac{Cs_+^2}{6}\right).$$

From Proposition 5.3.4, we know that for $\lambda < \lambda_0(A, B, C, L, L_2)$, the solution is unique, and hence we have $q_2 \equiv 0$ in Ω. This directly contradicts the result of Proposition 5.3.3, and thus we have q_2 and q_3 non-constant throughout Ω.

In Figure 5.3, we plot the unique stable solution of (5.1.8)–(5.1.10), with $\bar{\lambda}^2 = \frac{2C\lambda^2}{L} = 5$, for $L_2 = -0.5,\ 0,\ 1,\ 10$. When $L_2 = 0$, the solution is the WORS with $q_2 \equiv 0$ and $q_3 \equiv -\frac{s_+}{6} = -\frac{B}{6C}$ in Ω. When $L_2 = -0.5$, 1, and 10, q_2 and q_3 are non-constant, as proven above. One can check that $q_1 : \Omega \to \mathbb{R}$ vanishes along the square diagonals, $y = x$ and $y = -x$, and the function $q_2 : \Omega \to \mathbb{R}$ vanishes along $y = 0$ and $x = 0$, as proven in Lemma 5.3.5. When $L_2 = -0.5, 1,$ and 10, we observe a central $+1$-point defect in the profile of (q_1, q_2), and we label this as the *Ring*$^+$ solution. By comparing our elastic constants with those in [71], and utilising the connection with the Frank elastic constants in [19], we see that the $L_2 \in (-1, 0)$ regime corresponds to materials with $K_1 < K_2$ i.e., out-of-plane twist deformations are energetically expensive compared to splay and bend deformations of the nematic director. This is substantiated by the strictly negative value of q_3 throughout the domain in the first row of Figure 5.3 - indicating the nematic molecules strongly prefer in-plane alignment.

We perform a parameter sweep of $\bar{\lambda}^2$, from 5 to 500, and find one of the symmetric solution branches constructed in Proposition 5.3.2, such that $q_1 : \Omega \to \mathbb{R}$ vanishes along the square diagonals, $y = x$ and $y = -x$, and $q_2 : \Omega \to \mathbb{R}$ vanishes along $y = 0$ and $x = 0$. This branch is a continuation of the Ring$^+$ branch. The solutions with $\bar{\lambda}^2 = 500$ are plotted in Figure 5.4. When $L_2 = 0$, we find the WORS for all $\lambda > 0$, although it is unstable for λ large enough. When $-1 < L_2 < 0$, the solution exhibits a $+1$-defect at the square center, continued from the Ring$^+$ branch and hence, we refer to it as the Ring$^+$ solution. When L_2 is positive and moderate in value, we recover the Ring$^+$ solution branch and, the essential

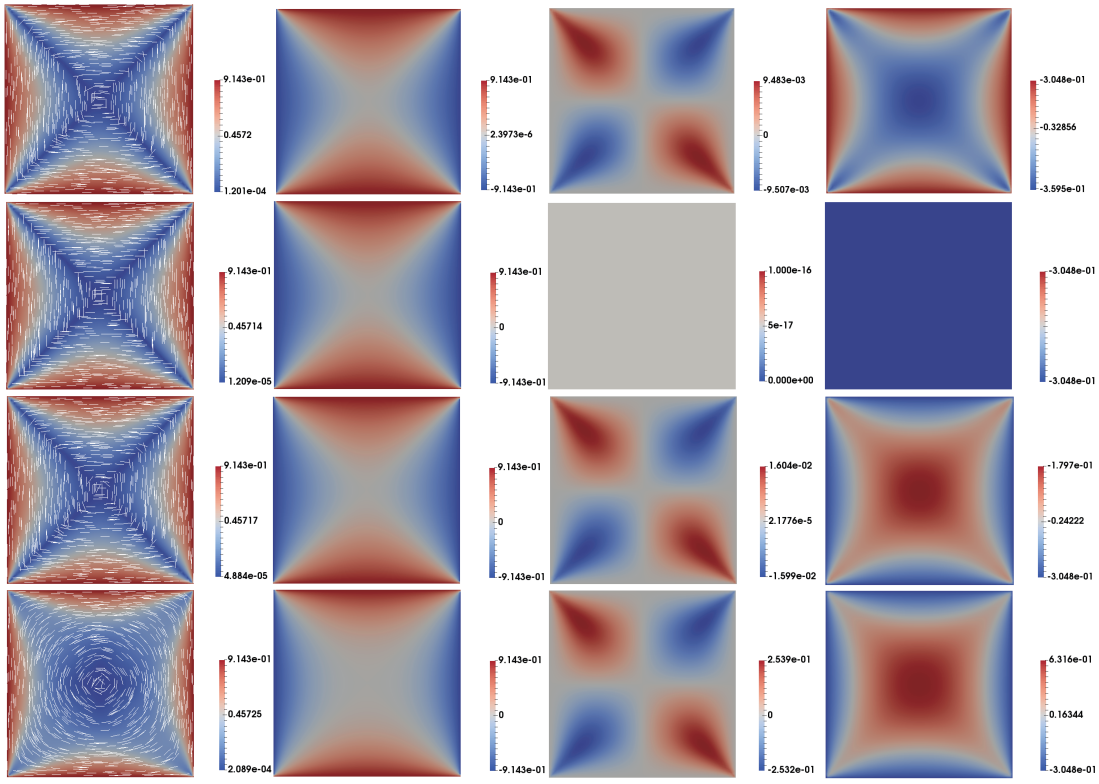

Figure 5.3: The unique stable solution of the Euler-Lagrange equations (5.1.8)–(5.1.10) with $\bar{\lambda}^2 = 5$, and (from the first to fourth row) $L_2 = -0.5$, 0, 1 and 10, respectively. We plot s^2, q_1, q_2 and q_3, in the first to fourth columns, respectively.

difference between Ring$^+$ for positive and negative L_2, is that $q_3 < -\frac{s_+}{6}$ at the center for negative L_2, but $q_3 > -\frac{s_+}{6}$ for positive L_2. When L_2 is large enough, we recover a solution which is approximately constant $(0, 0, \frac{s_+}{3})$, away from the square edges, as shown in the third row of Figure 5.4, for $L_2 = 10$, and labelled as the *Constant* solution branch in the remainder of this chapter. This is the only stable solution in Figure 5.4, for $\bar{\lambda}^2 = 500$.

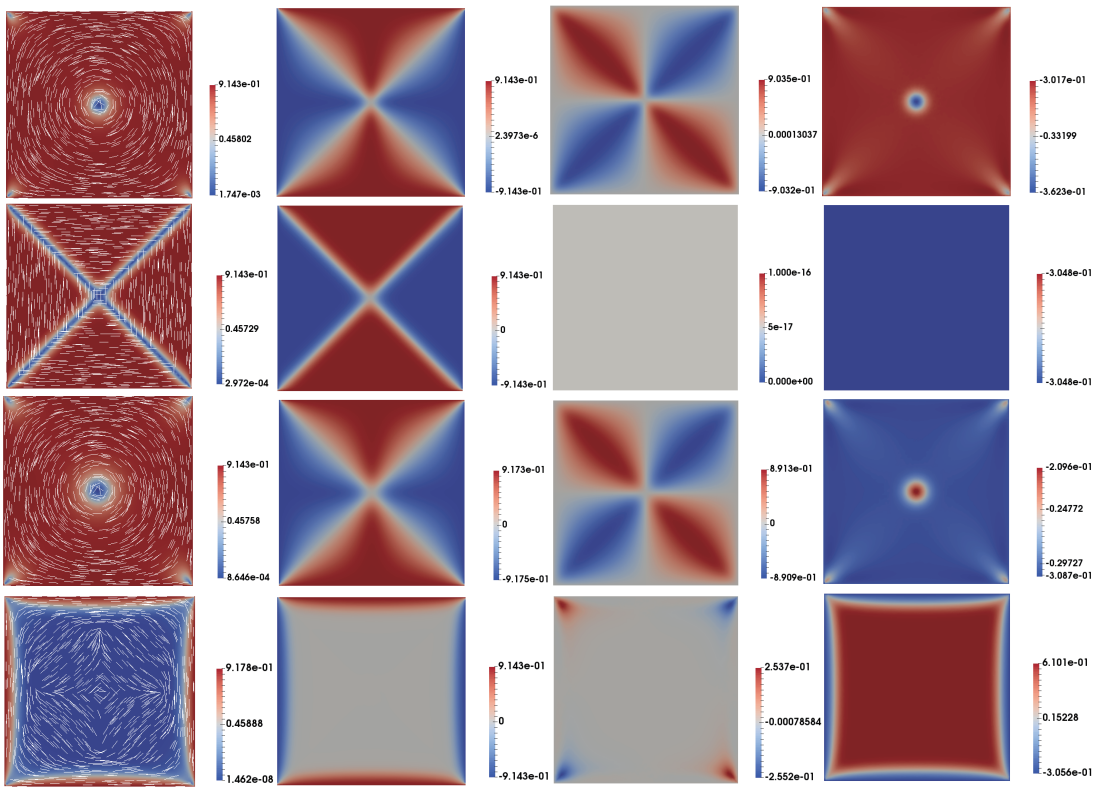

Figure 5.4: Solutions of (5.1.8)–(5.1.10) with $\bar{\lambda}^2 = 500$, and (on the first, second and third row) $L_2 = -0.5$, 0, 1 and 10, respectively. We plot s^2, q_1, q_2 and q_3, in the first to fourth columns, respectively.

5.4 Asymptotic studies

In Figures 5.3 and 5.4, we present solutions of the Euler-Lagrange system (5.1.8)–(5.1.10), in the small and large λ regimes, for several values of L_2, and it is clear that the solution landscape is affected by these parameters. For small λ, and $L_2 \neq 0$, we lose the uniaxial cross-structure of the WORS, and observe stable Ring$^+$ solutions with a central +1-point defect in the square. For large λ, the WORS and Ring$^+$ lose their stability and, for large L_2, we find the Constant solution. In this section, we study these solutions in three asymptotic limits: the $L_2 \to 0$ limit, about the uniquely minimizing solution for small λ; the $L_2 \to \infty$ limit and; the $\lambda \to \infty$ limit, for $L_2 \neq 0$.

5.4.1 The $L_2 \to 0$ limit for small λ

We work at the special temperature, $A = -\frac{B^2}{3C}$, to facilitate comparison with the results in [108], where the authors investigate solution landscapes with $L_2 = 0$. Notably, for $L_2 = 0$ and $A = -\frac{B^2}{3C}$, reduced LdG solutions have $q_3 \equiv -\frac{s_+}{6} = -\frac{B}{6C}$ for our choice of TBCs on 2D polygons, and it is natural to investigate the effects of the elastic anisotropy parameter, L_2, in these 2D frameworks. We consider solutions, (q_1, q_2, q_3), of the Euler-Lagrange equations (5.1.8)–(5.1.10) at the special temperature, satisfying $q_1 = q_b$, $q_2 = 0$, and $q_3 = -\frac{B}{6C}$, on $\partial\Omega$. We take a regular perturbation expansion of the functions q_1, q_2, q_3, in the $L_2 \to 0$ limit. The leading order approximation is given by the WORS, $(q, 0, -\frac{B}{6C})$, where q satisfies the Allen-Cahn equation, as in [62]:

$$\Delta q = \frac{2C\lambda^2}{L} q \left(q^2 - \frac{B^2}{4C^2} \right), \qquad q = q_b \quad \text{on} \quad \partial\Omega. \tag{5.4.1}$$

We may assume that q_1, q_2, q_3 can be expanded in powers of L_2, as follows:

$$\begin{aligned} q_1(x,y) &= q(x,y) + L_2 f(x,y) + \dots \\ q_2(x,y) &= L_2 g(x,y) + \dots \\ q_3(x,y) &= -\frac{B}{6C} + L_2 h(x,y) + \dots \end{aligned} \tag{5.4.2}$$

for some functions f, g, h, which vanish on the boundary. Up to $\mathcal{O}(L_2)$, the governing partial differential equations for f, g, h are given by:

$$\Delta f = \frac{C\lambda^2}{L}\left(4q^2 f + (2f - q)\left(q^2 - \frac{B^2}{4C^2}\right)\right), \tag{5.4.3}$$

$$\Delta g = \frac{2C\lambda^2}{L} g\left(q^2 - \frac{B^2}{4C^2}\right), \tag{5.4.4}$$

$$\Delta h = \frac{2C\lambda^2}{L} h\left(q^2 + \frac{B^2}{4C^2}\right) - \frac{1}{6}(q_{,yy} - q_{,xx}), \tag{5.4.5}$$

where $q = q_b, f = g = h = 0$, on $\partial\Omega$. One can easily verify that system (5.4.3)–(5.4.5) are the Euler-Lagrange equations for the following energy functional, with respect to f, g and h:

$$\begin{aligned} F(f,g,h) := &\int_\Omega \left\{ |\nabla f|^2 + |\nabla g|^2 + |\nabla h|^2 + \frac{1}{3}(q_{,y} h_{,y} - q_{,x} h_{,x}) \right\} \mathrm{dA} \\ &+ \frac{2C\lambda^2}{L} \int_\Omega \left\{ (f^2 + g^2 - fq)(q^2 - \frac{B^2}{4C^2}) + h^2(q^2 + \frac{B^2}{4C^2}) - 2f^2 q^2 \right\} \mathrm{dA}. \end{aligned}$$

For λ small enough, there exists a unique solution $(f, g, h) \in W_0^{1,2}(\Omega; \mathbb{R}^3)$ of the system (5.4.3)–(5.4.5), by following the approach in [91] to show that F is strictly convex in $W_0^{1,2}(\Omega; \mathbb{R}^3)$, for sufficiently small λ. Hence, for λ small enough, we have $g \equiv 0$ on Ω. Similarly to Proposition 5.3.5, we can check that if $(q(x,y), f(x,y), g(x,y), h(x,y))$ is a solution of (5.4.1),(5.4.3)–(5.4.5), then the quadruplets,

$$(-q(y,x), -f(y,x), g(y,x), h(y,x)), \quad (q(-x,y), f(-x,y), g(-x,y), h(-x,y)),$$

are also solutions of (5.4.1),(5.4.3)–(5.4.5). Thus, we have $f(x, y) = 0$ on the square diagonals, for λ small enough. Hence, for λ small enough, the cross structure of the WORS is lost, mainly because of effects of L_2 on the component q_3, as we show below.

From [69], the solutions of (5.4.1) with $\lambda = 0$ (the limiting equations for small λ or equivalently, the leading order approximations in the asymptotic limit of large elastic constant), are a good approximation to the solutions of (5.4.1), for sufficiently small λ. When $\lambda = 0$, $q = q_0$ where

$$\begin{aligned} \Delta q_0(x, y) = 0, \quad (x, y) \in \Omega, \\ q_0 = q_b, \quad \text{on} \quad \partial\Omega. \end{aligned} \tag{5.4.6}$$

The analytical solution of (5.4.6) is given by [68]:

$$q_0(x, y) = \frac{s_+}{2} \sum_{k \ odd} \frac{4}{k\pi \sinh(k\pi)} \Xi(x, y; k), \tag{5.4.7}$$

where

$$\begin{aligned} \Xi(x, y; k) = \Bigg\{ &\sin\left(\frac{k\pi(x+1)}{2}\right)\left(\sinh\left(\frac{k\pi(1-y)}{2}\right) + \sinh\left(\frac{k\pi(1+y)}{2}\right)\right) \\ &- \sin\left(\frac{k\pi(y+1)}{2}\right)\left(\sinh\left(\frac{k\pi(1-x)}{2}\right) + \sinh\left(\frac{k\pi(1+x)}{2}\right)\right)\Bigg\}. \end{aligned}$$

When $\lambda = 0$, the unique solution of (5.4.3)–(5.4.5) is $f = f_0 \equiv 0$, $g = g_0 \equiv 0$, and $h = h_0$, where

$$\Delta h_0 = -\frac{1}{6}(q_{0,yy} - q_{0,xx}), \tag{5.4.8}$$

with boundary condition $h_0 = 0$ on $\partial\Omega$. In Figure 5.5, we plot the difference between the solution of (5.1.8)–(5.1.10), (q_1, q_2, q_3), and the $\lambda = 0$ approximation of the leading asymptotic term of (5.4.2), $(q_0, 0, -\frac{s_+}{6} + L_2 h_0)$.

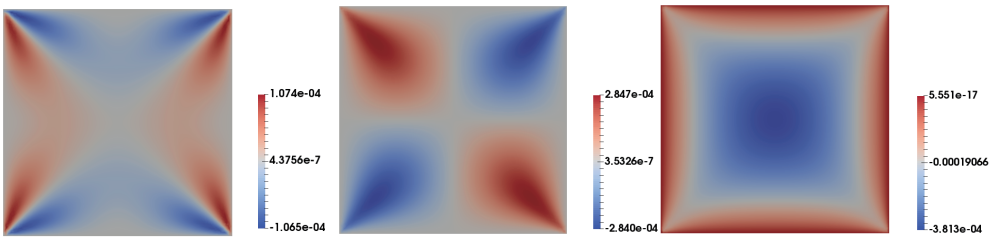

Figure 5.5: Error of the $\mathcal{O}(L_2)$ small λ approximations. Plots (from left to right) of $q_1 - q_0$, q_2, and $q_3 + \frac{s_+}{6} - L_2 h_0$, respectively, with $\bar{\lambda}^2 = 0.01$, $L_2 = 0.1$.

Proposition 5.4.1. *The analytical solution of* (5.4.8) *is given by*

$$h_0(x,y) = \sum_{m,n \ odd} \frac{16 s_+ mn}{3\pi^2 (m^2+n^2)^2} \sin\left(\frac{m\pi(x+1)}{2}\right) \sin\left(\frac{n\pi(y+1)}{2}\right), \tag{5.4.9}$$

where $h_0(0,0)$ *is positive.*

Proof. Firstly, we calculate the analytical solution of (5.4.8). Substituting (5.4.7) into (5.4.8), we have

$$\Delta h_0 = -\sum_{k \ odd} \frac{s_+}{3k\pi \sinh(k\pi)} (\Xi_{yy} - \Xi_{xx}),$$

which is the homogeneous Poisson equation on Ω. For mathematical convenience, we consider the transformations $\hat{x} = x+1$, $\hat{y} = y+1$, such that $h_0(\hat{x},\hat{y}) : [0,2]^2 \to \mathbb{R}$. We apply a method of eigenfunction expansion,

$$h_0(\hat{x},\hat{y}) = \sum_{n=1}^{\infty} \sum_{m=1}^{\infty} E_{mn} \sin\left(\frac{m\pi\hat{x}}{2}\right) \sin\left(\frac{n\pi\hat{y}}{2}\right),$$

where E_{mn} are double Fourier sine series coefficients. Following standard Fourier series calculations, we obtain:

$$h_0(\hat{x},\hat{y}) = \sum_{m,n \ odd} \frac{16 s_+ mn}{3\pi^2 (m^2+n^2)^2} \sin\left(\frac{m\pi\hat{x}}{2}\right) \sin\left(\frac{n\pi\hat{y}}{2}\right),$$

which yields the desired series expansion (5.4.9). Substituting $(x,y) = (0,0)$ into

(5.4.9), we obtain

$$\begin{aligned} h_0(0,0) &= \frac{16s_+}{3\pi^2}\sum_{m,n\ odd}\frac{mn}{(m^2+n^2)^2}\sin\left(\frac{m\pi}{2}\right)\sin\left(\frac{n\pi}{2}\right) \\ &= \frac{16s_+}{3\pi^2}\sum_{m,n\ odd}\frac{mn}{(m^2+n^2)^2}(-1)^{\frac{m+n-2}{2}} \\ &= \frac{16s_+}{3\pi^2}\left\{\sum_{m\ odd}\frac{1}{4m^2}+2\sum_{m>n\ odd}\frac{mn}{(m^2+n^2)^2}(-1)^{\frac{m+n-2}{2}}\right\} \\ &= \frac{s_+}{6}+\frac{32s_+}{3\pi^2}\sum_{m>n\ odd}\frac{mn}{(m^2+n^2)^2}(-1)^{\frac{m+n-2}{2}} \end{aligned} \tag{5.4.10}$$

We rewrite the summed term in (5.4.10), in terms of the positive and negative terms, for $s\in\mathbb{N}$, $s\geq 1$:

$$\begin{aligned} &\sum_{m>n\ odd}\frac{mn}{(m^2+n^2)^2}(-1)^{\frac{m+n-2}{2}} \\ &= \sum_{n\ odd,m=n+4s-2}\frac{mn}{(m^2+n^2)^2}(-1)^{\frac{m+n-2}{2}} \quad + \sum_{n\ odd,m=n+4s}\frac{mn}{(m^2+n^2)^2}(-1)^{\frac{m+n-2}{2}} \\ &\geq \sum_{n\ odd,m=n+4s-2}\frac{mn}{(m^2+n^2)^2}(-1)^{\frac{m+n-2}{2}} \end{aligned} \tag{5.4.11}$$

We now set $k=m+n$, and $l=m-n$. Therefore, we have $\frac{mn}{(m^2+n^2)^2}=\frac{k^2-l^2}{(k^2+l^2)^2}$ and, for integers $s,r\geq 1$, $p\geq 0$. Since n is odd, we have $k=m+n=2n+4s-2=2(2p+1)+4s-2=4(p+s)=4r$ and $l=m-n=4s-2$. Substituting this into (5.4.11), we obtain

$$\begin{aligned} \sum_{n\ odd,m=n+4s-2}\frac{mn}{(m^2+n^2)^2}(-1)^{\frac{m+n-2}{2}} &= \sum_{k>l,k=4r,l=4s-2}\frac{k^2-l^2}{(k^2+l^2)^2}(-1)^{\frac{k-2}{2}} \\ &= -\sum_{k>l,k=4r,l=4s-2}\frac{k^2-l^2}{(k^2+l^2)^2} \\ &\geq -\sum_{k=4r}\frac{1}{k^2}=-\sum_{r=1}^{\infty}\frac{1}{16r^2}=-\frac{\pi^2}{96} \end{aligned}$$

Hence, from (5.4.10), we have $h_0(0,0)\geq\frac{s_+}{6}+\frac{32s_+}{3\pi^2}\left(-\frac{\pi^2}{96}\right)>0$. □

5.4.2 The $L_2 \to \infty$ limit

Consider a regular perturbation expansion, in powers of $\frac{1}{L_2}$, of the solutions, q_1, q_2, q_3, of the Euler-Lagrange system (5.1.8)–(5.1.10), subject to the boundary conditions (5.1.11) and (5.1.12). Let ρ, σ, τ be the leading order approximations of q_1, q_2, q_3, respectively in the $L_2 \to \infty$ limit. Then we have:

$$\frac{1}{2}\Delta\rho + \frac{1}{2}(\tau_{yy} - \tau_{xx}) = 0, \tag{5.4.12}$$

$$\frac{1}{2}\Delta\sigma - \tau_{xy} = 0, \tag{5.4.13}$$

$$\frac{1}{6}\Delta\tau + \frac{1}{6}(\rho_{yy} - \rho_{xx}) - \frac{1}{3}\sigma_{xy} = 0, \tag{5.4.14}$$

with $\rho = q_b$, $\sigma = 0$, $\tau = -\frac{s_+}{6}$, on $\partial\Omega$.

Proposition 5.4.2. *The leading order system of Euler-Lagrange equations in the $L_2 \to \infty$ limit, (5.4.12)–(5.4.14), is not an elliptic PDE system.*

Proof. The system of equations (5.4.12)–(5.4.14) can be written as

$$A\mathbf{q}_{0,xx} + 2B\mathbf{q}_{0,xy} + C\mathbf{q}_{0,yy} = \mathbf{0},$$

where $\mathbf{q}_0 = (\rho, \sigma, \tau)$, and

$$A = \begin{pmatrix} \frac{1}{2} & 0 & -\frac{1}{2} \\ 0 & \frac{1}{2} & 0 \\ -\frac{1}{6} & 0 & \frac{1}{6} \end{pmatrix}, \quad B = \begin{pmatrix} 0 & 0 & 0 \\ 0 & 0 & -\frac{1}{2} \\ 0 & -\frac{1}{6} & 0 \end{pmatrix}, \quad C = \begin{pmatrix} \frac{1}{2} & 0 & \frac{1}{2} \\ 0 & \frac{1}{2} & 0 \\ \frac{1}{6} & 0 & \frac{1}{6} \end{pmatrix}.$$

The system is said to be *elliptic*, in the sense of I.G. Petrovsky [109], if the determinant

$$|A\alpha^2 + 2B\alpha\beta + C\beta^2| \neq 0,$$

for any real numbers $\alpha, \beta \neq 0$. We can check that for this system, we have

$$|A\alpha^2 + 2B\alpha\beta + C\beta^2| \equiv 0.$$

for any real numbers α, β. Hence, the limiting problem (5.4.12)–(5.4.14) is not an elliptic problem. □

Proposition 5.4.3. *There is no classical solution, $\mathbf{q}_0 \in C^2(\Omega)$, of the limiting problem (5.4.12)–(5.4.14), with the boundary conditions (5.1.11) (in the $\eta \to 0$ limit) and (5.1.12), where η is the short edge length of the truncated unit square, Ω.*

Proof. As $L_2 \to \infty$, the minimizers (q_1, q_2, q_3) of the energy J in (5.3.1), with f_{el} as in (5.3.4), are constrained to satisfy

$$f_{div}(q_1, q_2, q_3) = (q_{1,x} + q_{2,y} - q_{3,x})^2 + (q_{2,x} - q_{1,y} - q_{3,y})^2 = 0, \quad \text{a.e.} \quad (x, y) \in \Omega,$$

subject to the Dirichlet TBCs, (5.1.11) and (5.1.12). Up to $\mathcal{O}(L_2)$, this corresponds to the following PDEs for the leading order approximations, ρ, σ, τ:

$$(\rho - \tau)_x + \sigma_y = 0, \tag{5.4.15}$$

$$\sigma_x - (\rho + \tau)_y = 0, \tag{5.4.16}$$

almost everywhere, subject to the same TBCs, $\rho = q_b$, $\sigma = 0$, $\tau = -\frac{s_+}{6}$, on $\partial\Omega$. As $\eta \to 0$, the boundary conditions for ρ, σ, τ are piecewise constant, and hence the tangential derivatives of ρ, σ and τ vanish on the long square edges. On $y = \pm 1$, the tangential derivative $(\rho - \tau)_x = 0$, hence we obtain $\sigma_y = 0$ in (5.4.15). Similarly, we have $\sigma_x = 0$ on $x = \pm 1$. This implies that $\frac{\partial \sigma}{\partial \nu} = 0$ on $\partial\Omega$, where $\frac{\partial}{\partial \nu}$ is the outward pointing normal derivative, and we view the equation (5.4.13) to

be of the form

$$\Delta\sigma = f(x,y), \qquad \left.\frac{\partial\sigma}{\partial\nu}\right|_{\partial\Omega} = 0.$$

By the Hopf Lemma, when $\frac{\partial\sigma}{\partial\nu} = 0$ on the boundary, we have $\sigma \equiv 0$. Following the same arguments as in Proposition 5.3.3, this requires that $\tau \equiv -\frac{s_+}{6}$, and substituting $\tau \equiv -\frac{s_+}{6}$ into equations (5.4.15) and (5.4.16), we obtain $\rho_x = \rho_y = 0$, contradicting the boundary condition (5.1.11). Hence, there are no classical solutions of the system (5.4.12)–(5.4.14). □

Although there is no classical solution of (5.4.12)–(5.4.14) subject to the imposed boundary conditions, we can use finite difference methods to calculate a numerical solution, see Figure 5.6. We label this solution, $(\rho,\sigma,\tau) \equiv (0,0,\frac{s_+}{3})$ on Ω, as the *Constant* solution, where ρ and τ are discontinuous on $\partial\Omega$.

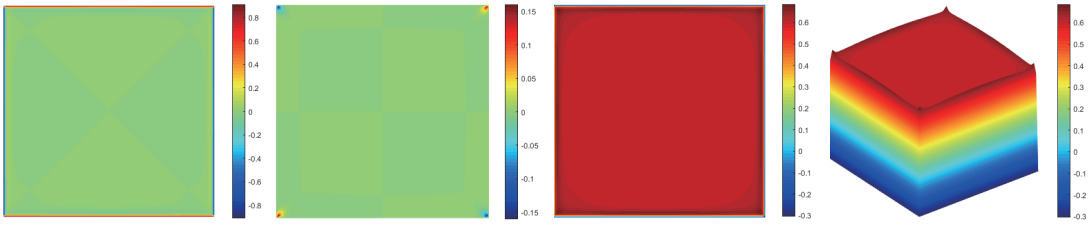

Figure 5.6: Solutions, ρ,σ,τ, of the leading order Euler-Lagrange system (5.4.12)–(5.4.14) in the $L_2 \to \infty$ limit. Plots of (from left to right) ρ,σ,τ, and (x,y,τ). Taken from [2].

We now give a heuristic argument to explain the emergence of the Constant solution in the interior of Ω, as $L_2 \to \infty$. Assuming $\rho = a$, $\sigma = b$, and $\tau = c$, where $a,b,c \in \mathbb{R}$ are constants, we have $f_{div} = 0$ in Ω, up to $\mathcal{O}(L_2)$. On the boundary, using finite difference methods, the first derivatives e.g., ρ_x, are calculated from the difference between the interior value, and the value on the boundary i.e.,

$\rho_x|_{x=-1} = \frac{\rho|_{interior} - \rho|_{boundary}}{h} = \frac{a-(-\frac{s_+}{2})}{h}$, where h is the size of the square mesh. We compute the choices of a, b, and c, that ensure $f_{div} = 0$ on the boundary, below:

$$\begin{aligned}
(a + \frac{s_+}{2} - c - \frac{s_+}{6})^2 + b^2 = 0 \quad &\text{on } x = -1, \\
(-a - \frac{s_+}{2} + c + \frac{s_+}{6})^2 + (-b)^2 = 0 \quad &\text{on } x = 1, \\
b^2 + (-a + \frac{s_+}{2} - c - \frac{s_+}{6})^2 = 0 \quad &\text{on } y = -1, \\
(-b)^2 + (a - \frac{s_+}{2} + c + \frac{s_+}{6})^2 = 0 \quad &\text{on } y = 1,
\end{aligned}$$

and hence $a = b = 0$, $c = \frac{s_+}{3}$. Therefore, $\rho = \sigma = 0$, $\tau = \frac{s_+}{3}$, is the unique stable solution of (5.4.12)–(5.4.13), except for zero measure sets, and we label $(q_1, q_2, q_3) = (0, 0, \frac{s_+}{3})$ as the physically relevant Constant solution, in the $L_2 \to \infty$ limit. This is consistent with the numerical results in Figure 5.6.

5.4.3 The $\lambda \to \infty$ limit

The set of minimizers of the thermotropic bulk energy density, f_b, in the (q_1, q_2, q_3)-plane can be written as $\mathbb{S} = \mathbb{S}_1 \cup \mathbb{S}_2$, where

$$\mathbb{S}_1 = \left\{ (q_1, q_2, q_3) : q_1^2 + q_2^2 = \frac{s_+^2}{4},\ q_3 = -\frac{s_+}{6} \right\}, \qquad \mathbb{S}_2 = \left(0, 0, \frac{s_+}{3} \right).$$

The $\lambda \to \infty$ limit is equivalent to the vanishing elastic constant limit, and the bulk energy density, f_b, converges uniformly to its minimum value in this limit [56].

Proposition 5.4.4. *Let $\Omega \in \mathbb{R}^2$ be a simply connected bounded open set with smooth boundary. Let $(q_1^\lambda, q_2^\lambda, q_3^\lambda)$ be a global minimizer of $J(q_1, q_2, q_3)$ in the admissible class $\mathcal{A}_0$ when $L_2 > -1$. Then there exists a sequence $\lambda_k \to \infty$ such that $(q_1^{\lambda_k}, q_2^{\lambda_k}, q_3^{\lambda_k}) \to (q_1^\infty, q_2^\infty, q_3^\infty)$ strongly in $W^{1,2}(\Omega; \mathbb{R}^3)$ where $(q_1^\infty, q_2^\infty, q_3^\infty) \in \mathbb{S}$.*

If $(q_1^\infty, q_2^\infty, q_3^\infty) \in \mathbb{S}_1$*, i.e.,*

$$q_1^\infty = s_+ \cos(2\theta^\infty), \quad q_2^\infty = s_+ \sin(2\theta^\infty), \quad q_3^\infty = -\frac{s_+}{6},$$

then θ^∞ *is a minimizer of*

$$\int_\Omega |\nabla\theta|^2 dA, \tag{5.4.17}$$

in the admissible class

$$\mathcal{A}_\theta = \{\theta \in W^{1,2}(\Omega); \theta = \theta_b \text{ on } \partial\Omega\},$$

where the boundary condition, θ_b*, is compatible with* (q_1, q_2) *on* $\partial\Omega$ *by the relation* $(q_{1b}, q_{2b}) = \frac{s_+}{2}(\cos(2\theta_b), \sin(2\theta_b))$*. Otherwise,* $(q_1^\infty, q_2^\infty, q_3^\infty)(x, y) \in \mathbb{S}_2$*, i.e.,*

$$(q_1^\infty, q_2^\infty, q_3^\infty) = \left(0, 0, \frac{s_+}{3}\right).$$

Proof. Our proof is analogous to Lemma 3 of [56]. Firstly, we note that the limiting solution, $(q_1^\infty, q_2^\infty, q_3^\infty)$, belongs to the admissible space $\mathcal{A}_0$. As in Proposition 5.3.4, we can show that the $W^{1,2}$-norms of the $(q_1^\lambda, q_2^\lambda, q_3^\lambda)$'s are uniformly bounded. Hence, there exists a weakly convergent subsequence, $(q_1^{\lambda_k}, q_2^{\lambda_k}, q_3^{\lambda_k})$, such that $(q_1^{\lambda_k}, q_2^{\lambda_k}, q_3^{\lambda_k}) \rightharpoonup (q_1^1, q_2^1, q_3^1)$ in $W^{1,2}$, for some $(q_1^1, q_2^1, q_3^1) \in \mathcal{A}_0$, as $\lambda_k \to \infty$. Using the lower semicontinuity of the $W^{1,2}$ norm with respect to the weak convergence, we have that

$$\int_\Omega |\nabla(q_1^1, q_2^1, q_3^1)|^2 \,\mathrm{dA} \leq \int_\Omega |\nabla(q_1^\infty, q_2^\infty, q_3^\infty)|^2 \,\mathrm{dA}. \tag{5.4.18}$$

The relation in (5.3.13) shows that

$$\int_\Omega \bar{f}_b(q_1^{\lambda_k}, q_2^{\lambda_k}, q_3^{\lambda_k}) \,\mathrm{dA} \leq \frac{1}{\lambda_k^2} \int_\Omega f_{el}(q_1^\infty, q_2^\infty, q_3^\infty) \,\mathrm{dA} \to 0 \qquad \text{as} \quad \lambda_k \to \infty,$$

where $\bar{f}_b = \frac{1}{L}(f_b - \min f_b)$. Since $\bar{f}_b(q_1, q_2, q_3) \geq 0$, $\forall (q_1, q_2, q_3) \in \mathbb{R}^3$, we have that,

on a subsequence λ_{k_j},

$$\bar{f}_b(q_1^{\lambda_{k_j}}(x,y), q_2^{\lambda_{k_j}}(x,y), q_3^{\lambda_{k_j}}(x,y)) \to 0,$$

for almost all $(x,y) \in \Omega$. We know that $\bar{f}_b(q_1,q_2,q_3) = 0$ if, and only if, $(q_1,q_2,q_3) \in \mathbb{S}$. On the other hand, the sequence $(q_1^{\lambda_k}, q_2^{\lambda_k}, q_3^{\lambda_k})$ converges weakly in $W^{1,2}$ and, on a subsequence, strongly in L^2 to (q_1^1, q_2^1, q_3^1). Therefore, the weak limit (q_1^1, q_2^1, q_3^1) is in the set $\mathbb{S}$ a.e. Ω. If (q_1^1, q_2^1, q_3^1) is in the set $\mathbb{S}_1$, then $|\nabla(q_1^1, q_2^1, q_3^1)|^2 = s_+^2 |\nabla\theta^1|^2$, where $q_1^1 = s_+\cos(2\theta^1)$ and $q_2^1 = s_+\sin(2\theta^1)$. Also, recalling $(q_1^\infty, q_2^\infty, q_3^\infty) \in \mathbb{S}_1$, we have that $|\nabla(q_1^\infty, q_2^\infty, q_3^\infty)|^2 = s_+^2|\nabla\theta^\infty|^2$, where $q_1^\infty = s_+\cos(2\theta^\infty)$ and $q_2^\infty = s_+\sin(2\theta^\infty)$. If (q_1^1, q_2^1, q_3^1) is in the set $\mathbb{S}_2$, then $(q_1^\infty, q_2^\infty, q_3^\infty) = (q_1^1, q_2^1, q_3^1) = (0, 0, \frac{s_+}{3})$. Combining (5.4.18) with the definition of $(q_1^\infty, q_2^\infty, q_2^\infty)$, we obtain that $\int_\Omega |\nabla\theta^1|^2 \,\mathrm{dA} = \int_\Omega |\nabla\theta^\infty|^2 \,\mathrm{dA}$ and therefore,

$$\begin{aligned}
\int_\Omega |\nabla(q_1^\infty, q_2^\infty, q_3^\infty)|^2 \,\mathrm{dA} &= \int_\Omega |\nabla(q_1^1, q_2^1, q_3^1)|^2 \,\mathrm{dA} \\
&\le \liminf_{\lambda_{k_j}\to\infty} \int_\Omega |\nabla(q_1^{\lambda_{k_j}}, q_2^{\lambda_{k_j}}, q_3^{\lambda_{k_j}})|^2 \,\mathrm{dA} \\
&\le \limsup_{\lambda_{k_j}\to\infty} \int_\Omega |\nabla(q_1^{\lambda_{k_j}}, q_2^{\lambda_{k_j}}, q_3^{\lambda_{k_j}})|^2 \,\mathrm{dA} \\
&\le \int_\Omega |\nabla(q_1^\infty, q_2^\infty, q_3^\infty)|^2 \,\mathrm{dA},
\end{aligned}$$

which demonstrates that $\lim_{\lambda_{k_j}\to\infty} ||\nabla(q_1^{\lambda_{k_j}}, q_2^{\lambda_{k_j}}, q_3^{\lambda_{k_j}})||_{L^2(\Omega)} = ||\nabla(q_1^\infty, q_2^\infty, q_3^\infty)||_{L^2(\Omega)}$. This, together with the weak convergence $(q_1^{\lambda_{k_j}}, q_2^{\lambda_{k_j}}, q_3^{\lambda_{k_j}}) \to (q_1^\infty, q_2^\infty, q_3^\infty)$, suffices to show the strong convergence $(q_1^{\lambda_{k_j}}, q_2^{\lambda_{k_j}}, q_3^{\lambda_{k_j}}) \to (q_1^\infty, q_2^\infty, q_3^\infty)$ in $W^{1,2}$. Since $f_b(q_1^\infty, q_2^\infty, q_3^\infty)$ is constant for $(q_1^\infty, q_2^\infty, q_3^\infty) \in \mathbb{S}_1$, we can recast our minimization problem to minimizing the elastic energy alone i.e., minimization of the limiting functional:

$$J_\infty[q_1,q_2,q_3] = \int_\Omega f_{el}\,(q_1,q_2,q_3)\ \mathrm{dA}.$$

Substituting $q_1 = \frac{s_+}{2}\cos(2\theta)$, $q_2 = \frac{s_+}{2}\sin(2\theta)$, and $q_3 = -\frac{s_+}{6}$, into J_∞, we obtain a

natural upper bound for the elastic energy density, which we utilized in (5.3.13):

$$J_\infty = s_+^2 \left(1 + \frac{L_2}{2}\right) \int_\Omega |\nabla\theta|^2 \, \mathrm{dA}.$$

The corresponding Euler-Lagrange equation for (5.4.17) is simply the Laplace equation:

$$\Delta\theta = 0,$$

subject to $\theta = \theta_b$ on $\partial\Omega$, where $(q_1, q_2, q_3) = (\frac{s_+}{2}\cos(2\theta_b), \frac{s_+}{2}\sin(2\theta_b), -\frac{s_+}{6})$ on $\partial\Omega$. □

For large λ i.e., large square domains, there are two classes of stable equilibria which are almost in the set $\mathbb{S}_1$. The diagonal (D) states are such that the nematic director (in the plane) is aligned along one of the square diagonals. The rotated (R) states are such that the director rotates by π radians between a pair of opposite square edges. There are 2 rotationally equivalent D states, and 4 rotationally equivalent R states, and the corresponding boundary conditions in terms of θ above are given by $\theta_b = \theta_b^D$ or θ_b^R respectively, where

$$\begin{cases} \theta_b^D &= \frac{\pi}{2}, \text{ on } x = \pm 1, \\ \theta_b^D &= 0, \text{ on } y = \pm 1, \end{cases} \qquad \begin{cases} \theta_b^R &= \frac{\pi}{2}, \text{ on } x = -1, \\ \theta_b^R &= -\frac{\pi}{2}, \text{ on } x = 1, \\ \theta_b^R &= 0, \text{ on } y = \pm 1. \end{cases}$$

Illustrations of the typical director profile in the D and R states are presented in Figure 2.2. In Figure 5.7, we plot a D and R solution with $L_2 = 3.5$ and $\bar{\lambda}^2 = 1000$. These configurations correspond to solutions of the Euler-Lagrange system (5.1.8)–(5.1.10). In these plots we show the order parameter and director pair, $(s^2, \mathbf{n})$, as well as the q_3-component of the solution. We see that q_3 is approximately constant on Ω, except for near the square vertices.

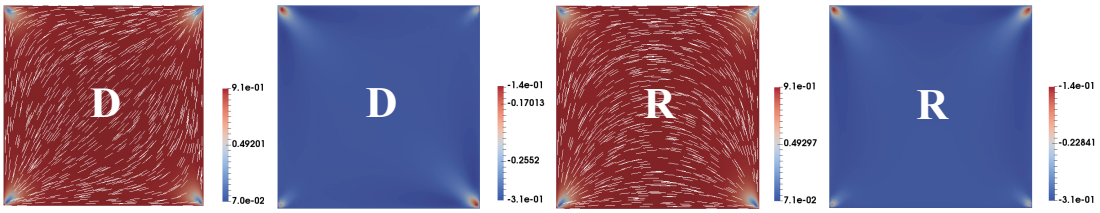

Figure 5.7: The D and R solutions with $L_2 = 3.5$ and $\bar{\lambda}^2 = 1000$.

In Figure 5.8, we study the effect of increasing L_2 on a D state, with $\bar{\lambda}^2 = 1000$. When $L_2 = 0$, we see that $q_1^2 + q_2^2 = \frac{s_+^2}{4}$, $q_3 = -\frac{s_+}{6}$, almost everywhere on Ω. In [74], the authors show that the limiting profiles, described in Proposition 5.4.4, are a good approximation to the solutions of (5.1.8)-(5.1.10), for large λ. The differences between the limiting profiles and the numerically computed D solutions concentrate around the vertices, for large λ. A square vertex is referred to as *splay*, or *bend*, according to whether the planar director rotates by $\frac{\pi}{2}$, or $-\frac{\pi}{2}$, radians along a circle centered at the vertex, oriented in an anticlockwise sense. As L_2 increases, q_3 deviates significantly from the limiting value $q_3^\infty = -\frac{s_+}{6}$, near the square vertices; the deviation being more significant near the bend vertices compared to the splay vertices. Notably, the value of q_3 near the vertices increases as L_2 increases and, from an optical perspective, we expect to observe larger defects near the square vertices for more anisotropic materials, with $L_2 \gg 1$, on large square domains.

5.4.4 The novel pWORS

For all $\lambda > 0$, and $L_2 = 0$, the WORS is a solution of (5.1.8)–(5.1.10) given by $(q, 0, -\frac{B}{6C})$, where q satisfies (5.4.1). In Section 5.4.1, we study the Euler-Lagrange equations, in the small λ and small L_2 limit, up to $\mathcal{O}(L_2)$; see (5.4.3)–(5.4.5). However, $g \equiv 0$ is a solution of (5.4.4) for all λ, and so we need to consider terms

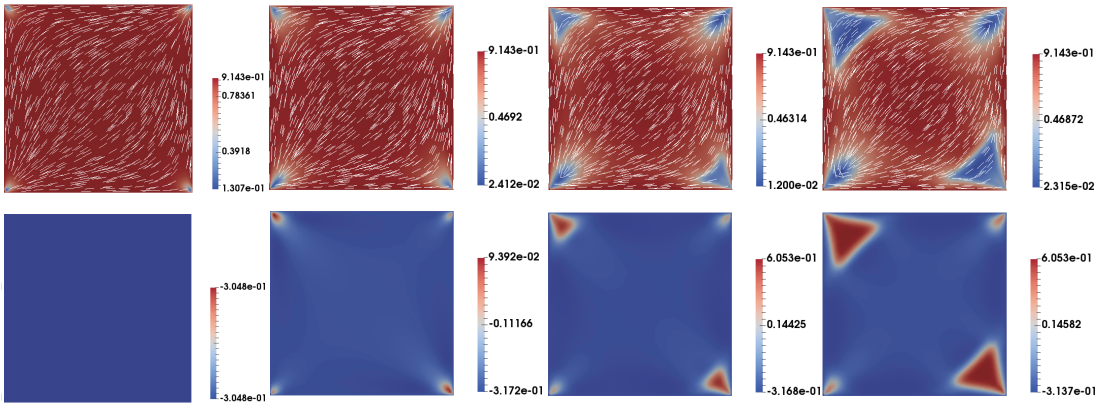

Figure 5.8: The D solution with $\bar{\lambda}^2 = 1000$, and $L_2 = 0, 10, 30,$ and 45, respectively.

of $\mathcal{O}(L_2^2)$ when dealing with the q_2 component. We assume that the solution, (q_1, q_2, q_3), of (5.1.8)-(5.1.10), can be expanded as follows:

$$\begin{aligned} q_1(x,y) &= q(x,y) + L_2 f(x,y) + L_2^2 \varphi(x,y) + \dots \\ q_2(x,y) &= 0 + L_2 g(x,y) + L_2^2 \gamma(x,y) + \dots \\ q_3(x,y) &= -\frac{B}{6C} + L_2 h(x,y) + L_2^2 \mu(x,y) + \dots \end{aligned}$$

Using the $\mathcal{O}(L_2)$ equations in (5.4.3)–(5.4.5), with respect to the quadruples (q, f, g, h), and rearranging, we can calculate the second order Euler-Lagrange system given by the corresponding partial differential equations for φ, γ, μ as shown below:

$$\begin{aligned} \Delta\varphi + \frac{1}{2}(h_{,yy} - h_{,xx}) =& \frac{2C\lambda^2}{L}\left\{q^2(2\varphi - f) + q(3f^2 + g^2 + 3h^2)\right. \\ & \left. -\frac{1}{4}(2f - q - 4\varphi)\left(q^2 - \frac{B^2}{4C^2}\right)\right\}, \end{aligned} \tag{5.4.19}$$

$$\Delta\gamma - h_{,xy} = \frac{2C\lambda^2}{L}\left\{2qfg + \left(\gamma - \frac{1}{2}g\right)\left(q^2 - \frac{B^2}{4C^2}\right)\right\}, \tag{5.4.20}$$

$$\Delta\mu + \frac{1}{6}(f_{,yy} - f_{,xx}) - \frac{1}{3}g_{,xy} = \frac{2C\lambda^2}{L}\left\{2h\left(qf - \frac{B}{C}h\right) + \left(\mu - \frac{1}{6}h\right)\left(q^2 + \frac{B^2}{4C^2}\right)\right\} + \frac{1}{36}(q_{,yy} - q_{,xx}), \tag{5.4.21}$$

where $\varphi = \gamma = \mu = 0$, on $\partial\Omega$. In Figure 5.9, we plot a branch of the γ solutions of (5.4.20). As λ increases, we observe an increasing number of zeroes on the square diagonals, where $\gamma = 0$.

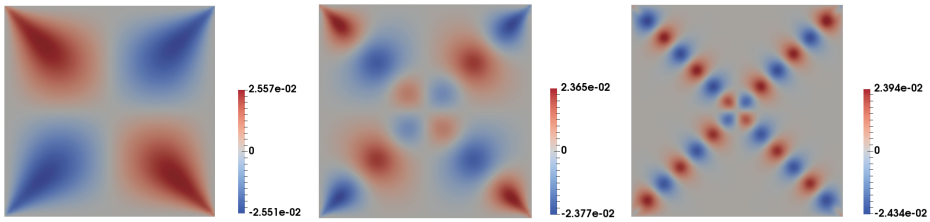

Figure 5.9: The $\mathcal{O}(L_2^2)$ contribution of q_2, γ, with $\bar{\lambda}^2 = 5$, 100 and 500, respectively.

For any $\lambda > 0$, we can use the initial condition $(q_1, q_2, q_3) = (q + L_2 f, L_2 g + L_2^2\gamma, -\frac{s_+}{6} + L_2 h)$ to numerically find a new branch of unstable solutions, referred to as *pWORS* configurations in Figure 5.10. f, g, h, γ are the solutions of (5.4.3), (5.4.4), (5.4.5), and (5.4.20), respectively. In the (q_1, q_2) plane, the pWORS has a constant set of eigenvectors away from the diagonals, and has multiple $\pm\frac{1}{2}$-point defects on the two diagonals, so that the pWORS is similar to the WORS, away from the square diagonals. As λ increases, the number of alternating $+\frac{1}{2}$ and $-\frac{1}{2}$ point defects on the square diagonals increases, for the numerically computed pWORS. This is mirrored by the function γ, in (5.4.20), that encodes the second order effect of L_2 on the WORS.

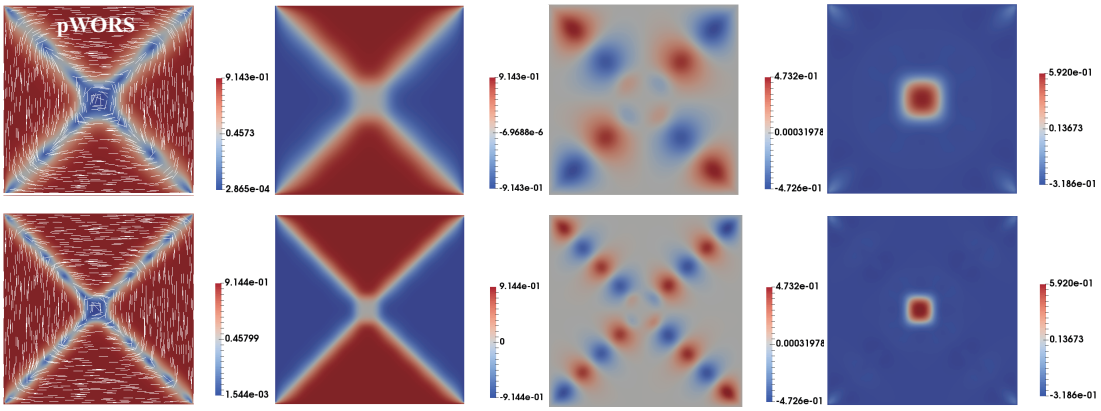

Figure 5.10: The pWORS with $L_2 = 3.5$ and $\bar{\lambda}^2 = 350, 1000$ (top and bottom, respectively). We plot (from left to right), s^2, q_1, q_2, and q_3, respectively.

5.5 Bifurcation diagrams

As explained in Section 5.2, we use the open-source package FEniCS [103] to perform all the finite-element simulations, numerical integration, and stability checks in this chapter [102], [103]. In what follows, we compute bifurcation diagrams for the solution landscapes, as a function of $\bar{\lambda}^2$, for five different values of L_2.

For λ small enough, say $\lambda < \lambda_0$, there is a unique solution for any value of L_2; see the results in Section 5.4. For $L_2 = 0$, the unique stable solution, for λ small enough, is the WORS. The unique solution deforms to the Ring$^+$, with a central $+1$-point defect, for $L_2 = 1$ and $L_2 = 2.6$. For $L_2 = 3$ and $L_2 = 10$, the unique solution is the Constant solution, on the grounds that this solution approaches the constant state, $(q_1, q_2, q_3) \to (0, 0, \frac{s_+}{3})$, in the square interior as $\lambda \to \infty$. In Figure 5.11, we plot the energies of the WORS, Ring$^+$, and Constant solutions for two distinct values of $\bar{\lambda}^2$, as a function of L_2. The energy is taken to be

$$J[q_1, q_2, q_3] - \int_\Omega \min f_b \, \mathrm{dA},$$

where $J[q_1, q_2, q_3]$ is as in (5.3.1), and $\min f_b = f_b(\pm\frac{s_+}{2}, 0, -\frac{s_+}{6})$, so that the energy is non-negative by definition. The WORS only exists for $L_2 = 0$. The Ring$^+$ solution branch only gains stability for L_2 large enough. The Constant solution branch exists if L_2 is large enough, and the Ring$^+$ and Constant solution branches coexist for some values of L_2 ($L_2 \in [2.7, 3.4]$ for $\bar{\lambda}^2 = 100$, $L_2 \in [2.85, 5.5]$ for $\bar{\lambda}^2 = 200$). When L_2 is large enough, the Constant solution has lower energy than the Ring$^+$ solution and, as L_2 further increases, the Ring$^+$ solution ceases to exist. When $\lambda < \lambda_0$, there is unique solution for any L_2 (see Proposition 5.3.4), which means the WORS, Ring$^+$, and Constant solution branches are connected.

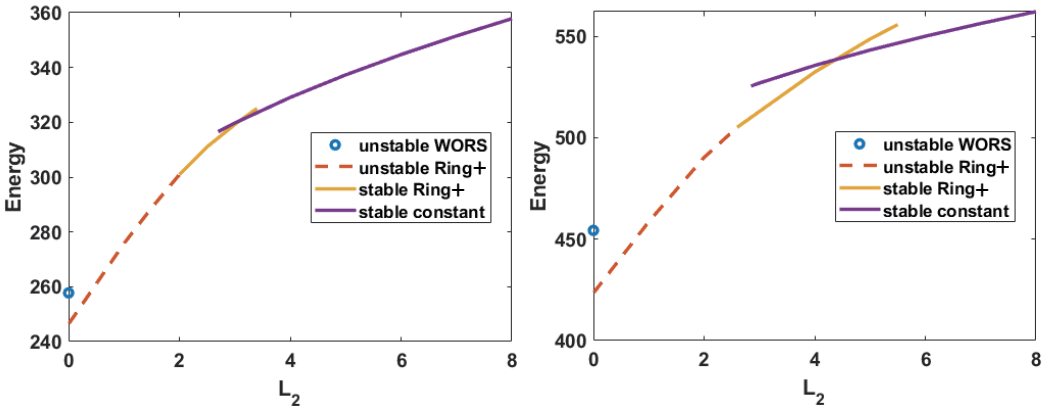

Figure 5.11: Energy of the WORS, Ring$^+$ and Constant solutions verses L_2 when $\bar{\lambda}^2 = 100$ and 200, respectively.

As mentioned in Section 5.2, we distinguish between the distinct solution branches by plotting the two measures $\int_\Omega q_1(1 + x + y)\mathrm{d}x\mathrm{d}y$, and $\int_\Omega q_2(1 + x + y)\mathrm{d}x\mathrm{d}y$. In addition to the WORS, Ring$^+$, and Constant solutions, there also exist the unstable Ring$^-$, and unstable pWORS solution branches with the same symmetries, which are indistinguishable by these measures. Hence, they appear on the same solution branch for all $L_2 > 0$ in our bifurcation diagrams. The difference between the Ring$^+$, Ring$^-$, WORS, Constant, and pWORS, can be spotted from the associated q_2-profiles. If $q_2 < 0$ on $x = y$ and $x > 0$, the corresponding solution is the

Ring$^+$ solution. If $q_2 > 0$ on $x = y$ and $x > 0$, the corresponding solution is the Ring$^-$ solution. The Ring$^+$ and Ring$^-$ solutions also exist for $L_2 = 0$. If $q_2 \equiv 0$, the solution is either the WORS, or the Constant solution. If q_2 has isolated zero points on the square diagonals, the corresponding solution is the pWORS.

We numerically solve the Euler-Lagrange equations (5.1.8)-(5.1.10), with $\bar{\lambda}^2 = 0.1$, by using Newton's method to obtain: the unique stable WORS with $L_2 = 0$; the Ring$^+$ solution, with $L_2 = 1$ and $L_2 = 2.6$ and; the Constant solution, with $L_2 = 3$ and $L_2 = 10$. The initial condition is not important here, since the solution is unique and the nonlinear term is small for $\bar{\lambda}^2 = 0.1$. We perform an increasing $\bar{\lambda}$ sweep for the WORS, Ring$^+$ and Constant solution branches, and a decreasing $\bar{\lambda}$ sweep for the diagonal D, and rotated R solution branches. The stable Ring$^+$ branch, with $L_2 = 3$, is obtained by taking the stable Ring$^+$ branch, with $L_2 = 2.6$, as the initial condition for our numerical procedure. The unstable WORS and Ring$^+$ solutions are tracked by continuing the stable WORS and stable Ring$^+$ solution branches. If the Ring$^+$ branch is given by (q_1, q_2, q_3) for a fixed $L_2 > 0$, then the initial condition for the unstable Ring$^-$ solution is given by the corresponding $(q_1, -q_2, q_3)$ solution, for any $\lambda > 0$. The initial condition for the unstable pWORS branch is given by $(q_1, q_2, q_3) = (q + L_2 f, L_2 g + L_2^2 \gamma, -\frac{s_+}{6} + L_2 h)$, where q, f, g, h, γ are the solutions of (5.4.3)–(5.4.5), and (5.4.20), respectively, for any $\lambda > 0$ (see Figure 5.10).

Consider the case $L_2 = 0$. For $\lambda < \lambda^*$, there is the unique WORS. For $\lambda = \lambda^*$, the stable WORS bifurcates into an unstable WORS, and two stable D solutions. When $\lambda = \lambda^{**} > \lambda^*$, the unstable WORS bifurcates into two unstable BD solution branches, which are featured by isotropic lines or defect lines, localised near a pair of opposite square edges. When $\lambda = \lambda^{***} > \lambda^{**}$, unstable Ring$^\pm$ solutions appear simultaneously. When $L_2 = 0$, the Ring$^+$ and Ring$^-$ solutions have the

same energy, and so they are indistinguishable in Figure 5.12. Each unstable BD solution branch further bifurcates into two unstable R solutions. As λ increases, the unstable R solutions gain stability. The WORS has the highest energy amongst the numerically computed solutions for $L_2 = 0$, for large λ.

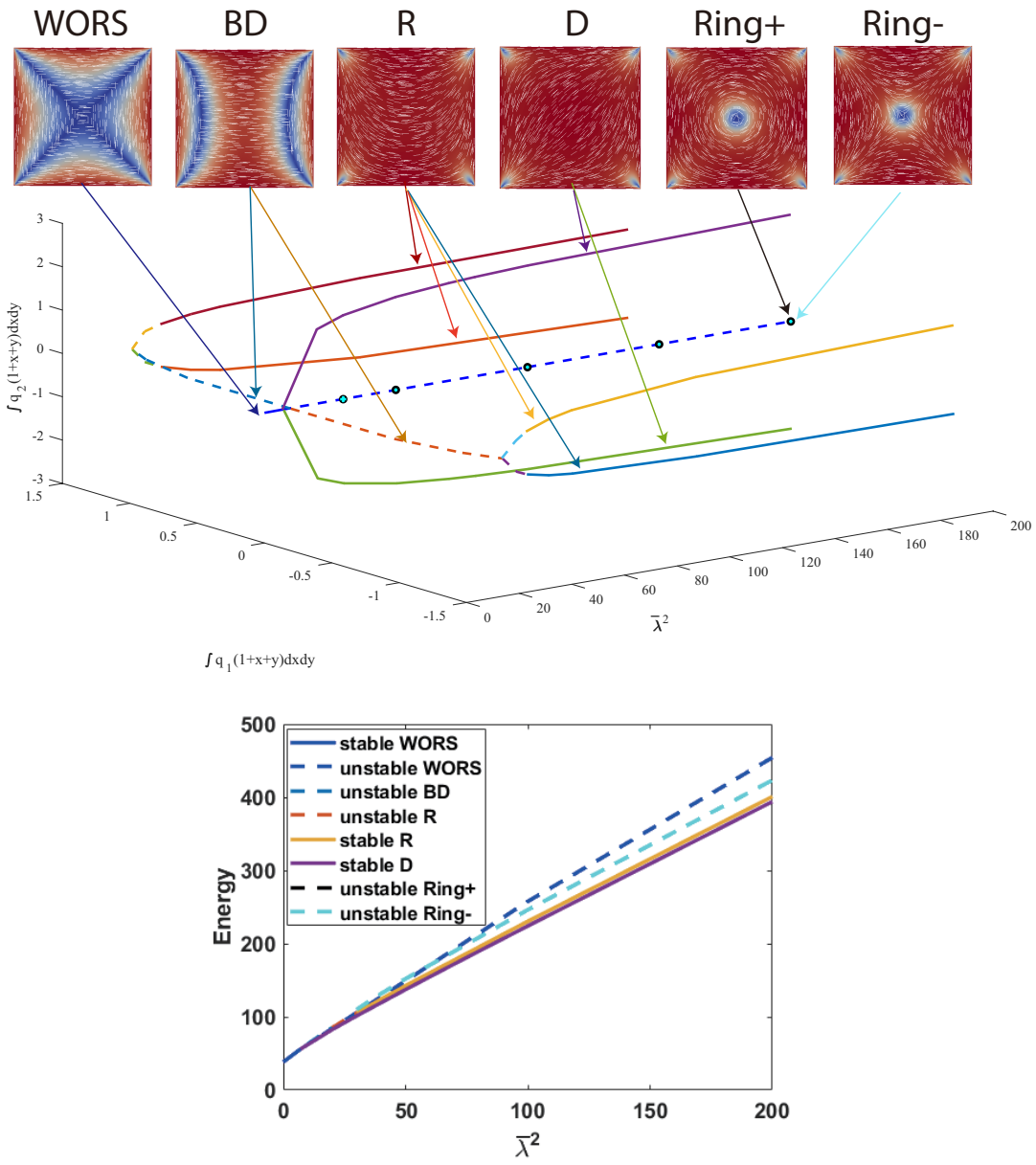

Figure 5.12: Bifurcation diagram as a function of $\bar{\lambda}^2$, and corresponding energy ($J - \int_\Omega \min f_b \, \mathrm{dA}$) plot, for the LdG model in square domain with $L_2 = 0$.

For $L_2 = 1$, the WORS ceases to exist and the unique solution, for λ small enough, is the stable Ring$^+$ solution. At the first bifurcation point, $\lambda = \lambda^*$, the Ring$^+$ solution bifurcates into an unstable Ring$^+$ and two stable D solutions. At the second bifurcation point, $\lambda = \lambda^{**} > \lambda^*$, the unstable Ring$^+$ bifurcates into two unstable BD solutions, and for $\lambda = \lambda^{***} > \lambda^{**}$, the unstable Ring$^-$ and unstable pWORS solution branches appear. The Ring$^-$ and pWORS are always unstable. When $L_2 \neq 0$, the Ring$^+$ solution has lower energy than the Ring$^-$ solution. The unstable pWORS has higher energy than the unstable Ring$^\pm$ solutions, when λ is large. The picture for large λ is qualitatively similar to the $L_2 = 0$ case, with the BD solution branches bifurcating into two unstable R solutions, which gain stability as λ increases.

The solution landscape for $L_2 = 1$, and $L_2 = 2.6$, are qualitatively similar but, for $L_2 = 2.6$, the unique Ring$^+$ solution, for small λ, is stable for $\bar{\lambda}^2 \leq 200$, and the unstable pWORS and Ring$^-$ appear for larger values of λ.

For $L_2 = 3$, the unique stable solution for small λ is the Constant solution, which is stable for $\bar{\lambda}^2 \leq 200$. We can clearly see that the Constant solution approaches $(q_1, q_2, q_3) \to (0, 0, \frac{s_+}{3})$ as λ gets large. The BD and D solution branches which,

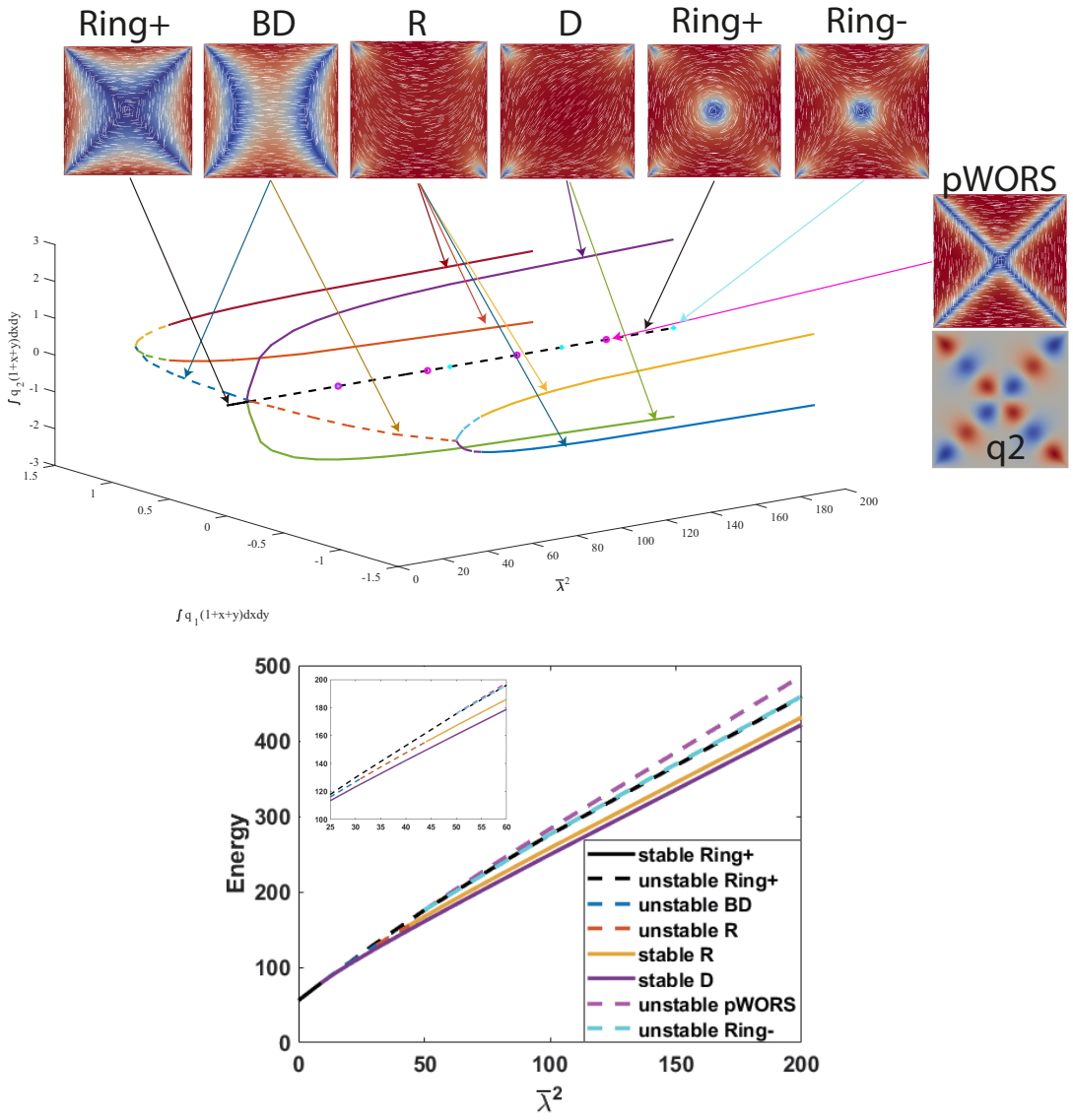

Figure 5.13: Bifurcation diagram and energy plot for $L_2 = 1$.

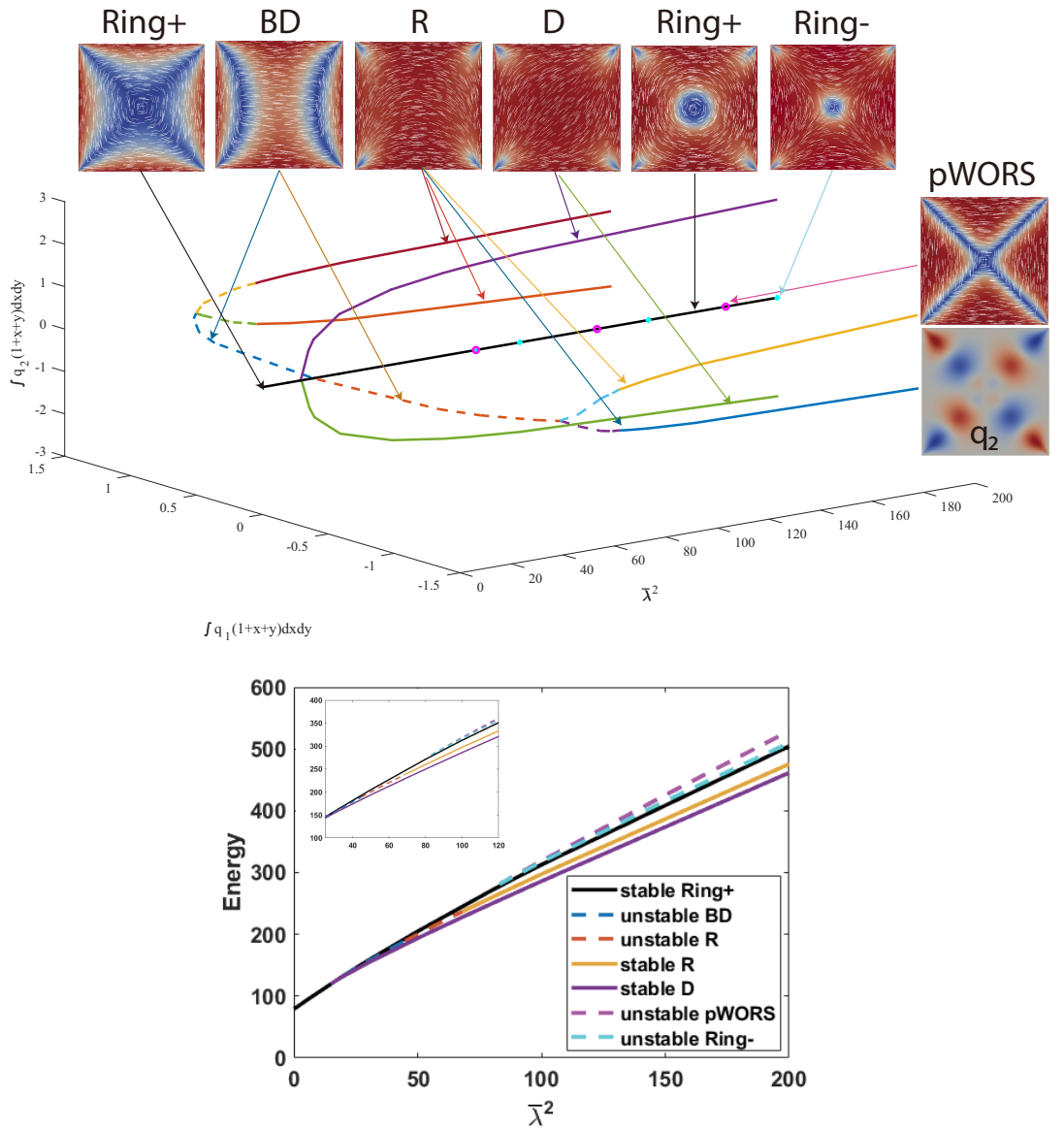

Figure 5.14: Bifurcation diagram and energy plot for $L_2 = 2.6$.

for smaller values of L_2 were connected to the unique solution branch for small λ, are now disconnected from the stable Constant solution branch. For $\lambda = \lambda^*$, the stable Ring$^+$ solution appears and, for $\lambda = \lambda^{**} > \lambda^*$, the unstable Ring$^-$ and pWORS appear. Similarly to the solution landscapes for smaller values of L_2, the unstable BD bifurcate into two unstable R solutions which then gain stability for larger λ.

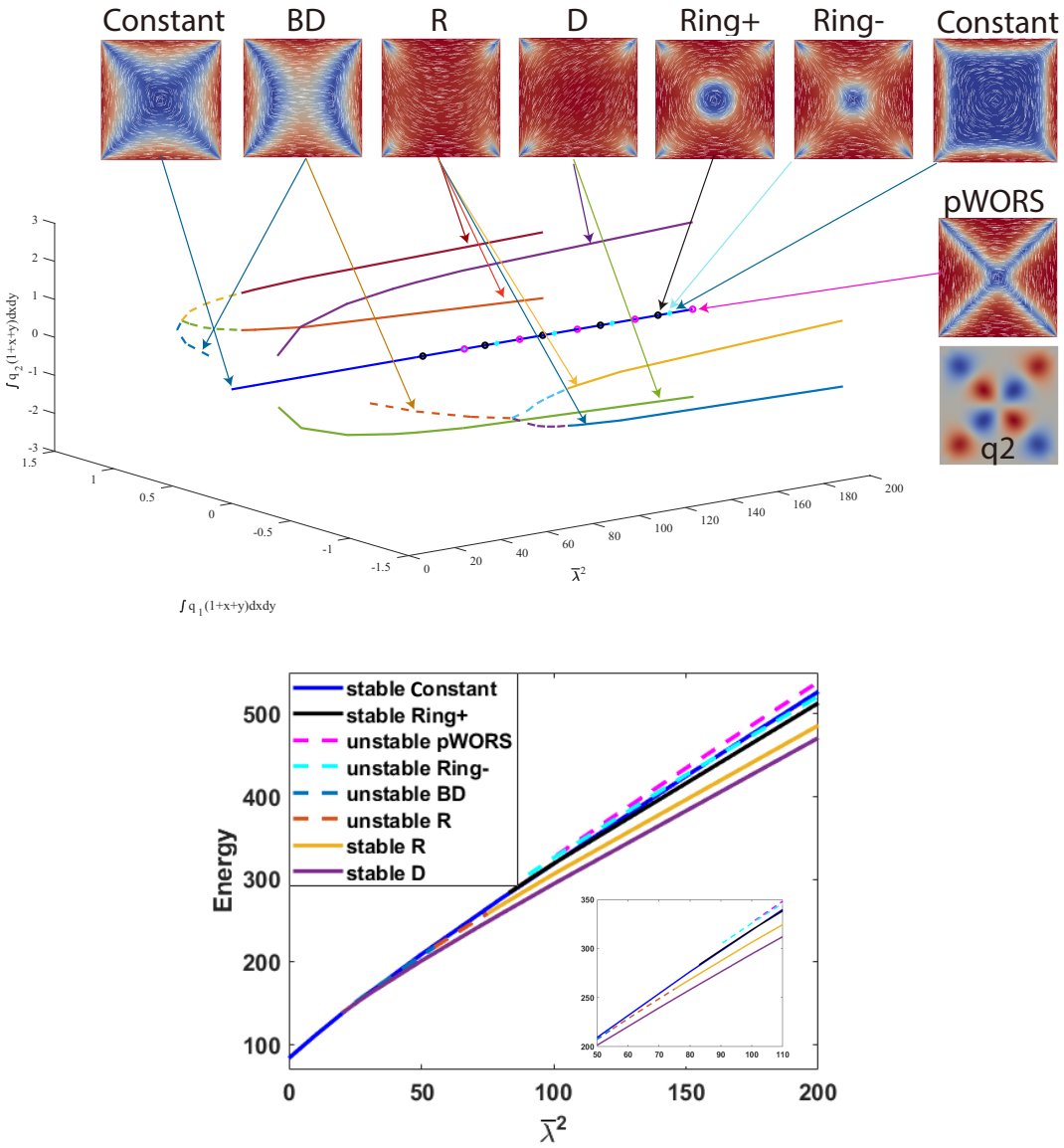

Figure 5.15: Bifurcation diagram and energy plot for $L_2 = 3$.

For $L_2 = 10$, the pWORS and Ring$^{\pm}$ states disappear, and the Constant solution does not bifurcate to any known states. The BD and D branches remain disconnected from the stable Constant branch. As λ increases, the BD branches bifurcate into two unstable R branches, which gain stability for λ large. As we perform a decreasing λ sweep for the D or BD solution branches, we cannot find a D or BD solution for $\lambda < \lambda_D$ or $\lambda < \lambda_{BD}$, for λ_D and λ_{BD} small enough. For L_2

large enough, the Constant solution has lower energy than the R and D solutions for large λ. For L_2 large enough, we only observe the Constant solution branch.

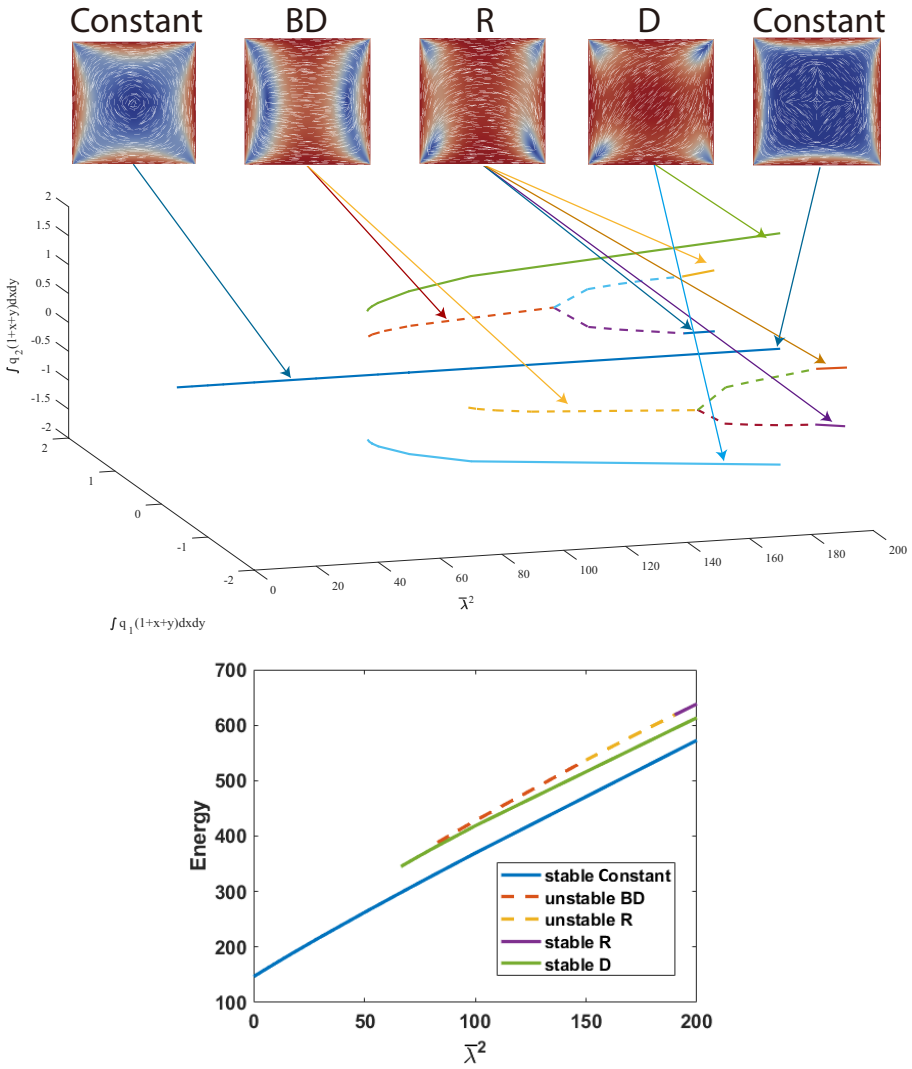

Figure 5.16: Bifurcation diagram and energy plot for $L_2 = 10$.

To summarise, the primary effect of the anisotropy parameter, L_2, is on the unique stable solution for small λ. The elastic anisotropy destroys the cross structure of the WORS, and also enhances the stability of the Ring$^+$ and Constant solutions. A further interesting feature for large L_2, is the disconnectedness of the D and R solution branches from the parent Constant solution branch. This indicates novel hidden solutions for large L_2, which may have different structural profiles to the discussed solution branches, and could be investigated in greater detail, in future work.

In the next proposition, we prove a stability result which gives partial insight into the stabilising effects of positive L_2. Let (q_1, q_2, q_3) be an arbitrary critical point of the energy functional (5.3.1). As is standard in the calculus of variations, we say that a critical point is locally stable if the associated second variation of the energy (5.3.1) is positive for all admissible perturbations, and is unstable if there exists an admissible perturbation for which the second variation is negative. To this end, we consider perturbations of the form $\mathbf{Q} + \epsilon\mathbf{V}$, where $\mathbf{V}$ vanishes at the boundary, $\partial\Omega$. In the following proposition, we prove the stability of these critical points with respect to two classes of admissible perturbations $\mathbf{V}$, for large L_2.

Proposition 5.5.1. *For $L_2 \geq \frac{\lambda^2}{L} c(A, B, C, \Omega)$, where c is some constant depending only on A, B, C and Ω, the critical points of the energy functional (5.3.1) in the restricted admissible space*

$$\mathcal{A}_* = \{(q_1, q_2, q_3) \in \mathcal{A}_0 : \int_\Omega |\nabla q_1|^2 \leq M_1, \int_\Omega |\nabla q_2|^2 \leq M_2, \int_\Omega |\nabla q_3|^2 \leq M_3\}$$

(where M_1, M_2, M_3 are constants depending only on A, B and C), are locally stable with respect to the perturbations

$$\mathbf{V}(x, y) = v_1(x, y)(\hat{\mathbf{x}} \otimes \hat{\mathbf{x}} - \hat{\mathbf{y}} \otimes \hat{\mathbf{y}}) + v_2(x, y)(\hat{\mathbf{x}} \otimes \hat{\mathbf{y}} + \hat{\mathbf{y}} \otimes \hat{\mathbf{x}}), \tag{5.5.1}$$

and

$$\mathbf{V}(x,y) = v_3(x,y)(2\hat{\mathbf{z}}\otimes\hat{\mathbf{z}} - \hat{\mathbf{x}}\otimes\hat{\mathbf{x}} - \hat{\mathbf{y}}\otimes\hat{\mathbf{y}}). \tag{5.5.2}$$

Proof. To begin, consider the admissible perturbation (5.5.2). The second variation of the LdG energy (5.3.1), with respect to this perturbation, is given by

$$\begin{aligned}\delta^2\mathcal{F}[v_3] = &\int_\Omega (6+L_2)|\nabla v_3|^2\,\mathrm{dA}\\ &+\frac{\lambda^2}{L}\int_\Omega v_3^2\left\{6A - 12Bq_3 + 72Cq_3^2 + 6C(2q_1^2+2q_2^2+6q_3^2)\right\}\mathrm{dA},\end{aligned}$$

where $v_3 \in W_0^{1,2}(\Omega)$. By an application of the Poincaré inequality, and use of the relevant embedding theorem as in Proposition 5.3.4, there exists some constant c_0, which depends on the domain Ω, such that

$$\begin{aligned}\int_\Omega (6+L_2)|\nabla v_3|^2\,\mathrm{dA} &= \frac{(6+L_2)}{1+K(\Omega)}\int_\Omega |\nabla v_3|^2\,\mathrm{dA} + \frac{(6+L_2)K(\Omega)}{1+K(\Omega)}\int_\Omega |\nabla v_3|^2\,\mathrm{dA}\\ &\geq \frac{(6+L_2)}{1+K(\Omega)}||v_3||^2_{W^{1,2}(\Omega)}\\ &\geq L_2 c_0(\Omega)||v_3||^2_{L^4(\Omega)}\end{aligned}$$

We will now restrict ourselves to studying critical points in the admissible space, $\mathcal{A}_*$, which respect the Dirichlet energy bounds for the scalar order parameters q_1, q_2, q_3. By applications of the Hölder inequality, and further applications of the embedding theorem and Poincaré inequality in $\mathcal{A}_*$, we have that there exists some constant c_1, depending only on A, B, C and Ω, such that

$$\begin{aligned}\delta^2\mathcal{F}[v_3] &\geq L_2 c_0||v_3||^2_{L^4(\Omega)} - \frac{\lambda^2}{L}c_1(A,B,C,\Omega)||v_3||^2_{L^4(\Omega)}\\ &= \left(L_2 c_0 - \frac{\lambda^2}{L}c_1\right)||v_3||^2_{L^4(\Omega)}\end{aligned} \tag{5.5.3}$$

The quantity (5.5.3) is positive if, and only if, $L_2 \geq \frac{\lambda^2}{L}c$, where $c := \frac{c_1}{c_0}$. Similarly, we may consider the admissible perturbation (5.5.1). The second variation of the

energy (5.3.1), with respect to this perturbation, is given by

$$\begin{aligned}\delta^2\mathcal{F}[v_1,v_2] = \int_\Omega (2+L_2)|\nabla v_1|^2 + (2+L_2)|\nabla v_2|^2 + 2L_2(v_{1,x}v_{2,y} - v_{1,y}v_{2,x})\,\mathrm{dA} \\ + \frac{\lambda^2}{L}\int_\Omega 2A + 4Bq_3 + 2C(2q_1^2 + 2q_2^2 + 6q_3^2)(v_1^2+v_2^2)\,\mathrm{dA} \\ + \frac{\lambda^2}{L}\int_\Omega 8C(q_1v_1 + q_2v_2)^2\,\mathrm{dA}\end{aligned}$$

Since $v_1, v_2 \in W_0^{1,2}(\Omega)$, the term

$$v_{1,x}v_{2,y} - v_{1,y}v_{2,x}$$

is a null Lagrangian and hence, applying the same reasoning as before, we have that there exist constants ξ_0, ξ, depending only on A, B, C and Ω, such that

$$\delta^2\mathcal{F}[v_1,v_2] \geq \left(L_2\xi_0 - \frac{\lambda^2}{L}\xi_1\right)(||v_1||^2_{L^4(\Omega)} + ||v_2||^2_{L^4(\Omega)}). \tag{5.5.4}$$

The right hand side of (5.5.4) is positive if, and only if, $L_2 \geq \frac{\lambda^2}{L}c$ where $c := \frac{\xi_1}{\xi_0}$, thus completing the proof. □

5.6 Summary

We study the effects of L_2 on stable nematic equilibria on a square domain, with tangent boundary conditions - primarily focusing on the interplay between the square edge length, λ, and the elastic anisotropy, L_2. We study LdG critical points with three degrees of freedom: q_1 and q_2, which measure the degree of nematic order in the plane of the square, and q_3, which measures the degree of out-of-plane order in terms of the eigenvalue about $\hat{\mathbf{z}}$. More specifically, $q_3 < 0$ indicates that the nematic molecules prefer to align in the plane of the square,

and $q_3 < 0$ indicates they prefer to align in the $\hat{\mathbf{z}}$-direction. We use symmetry arguments on an eighth of the square domain, to construct a LdG critical point for which q_1 vanishes on the square diagonals, and q_2 vanishes on the coordinate axes. The WORS is a special class of these critical points for $L_2 = 0$, with $q_2 \equiv 0$ on the square domain. In particular, q_2 cannot be identically zero for a reduced LdG critical point, for $L_2 \neq 0$. This symmetric critical point is the unique LdG energy minimizer for λ small enough, as follows from a uniqueness proof. There are different classes of these symmetric critical points for large λ. We perform asymptotic studies in the small λ, and large L_2, limits and provide good asymptotic approximations for the novel Ring$^+$ and Constant solutions, both of which are stable for small λ and relatively large values of L_2, when these solutions exist. We also provide asymptotic expansions for the novel unstable pWORS solution branches, featured by alternating zeroes of q_2 on the square diagonals. The WORS, Ring$^\pm$, Constant, and pWORS belong to the class of symmetric critical points constructed in Proposition 5.3.2. The large λ-picture, for $L_2 \neq 0$, is qualitatively similar to the $L_2 = 0$ case, with the stable diagonal D and rotated R solutions. The notable difference is the emergence of the competing stable Constant solution for large L_2, which is energetically preferable to the D and R solutions, for large L_2 and large λ. This suggests that for highly anisotropic materials with large L_2, the experimentally observable state is the Constant solution, with $q_1^2 + q_2^2 \approx 0$ in the square interior. In other words, the Constant state is almost perfectly uniaxial with uniaxial symmetry along the z-direction, and will offer highly contrasting optical properties compared to the D and R solutions. This offers novel prospects for multistability for highly anisotropic materials.

Another noteworthy feature is the stabilising effect of L_2, as discussed in Section 5.5. The Ring$^+$ solution has a central +1-point defect in the square interior,

and is unstable for $L_2 = 0$. However, it gains stability as L_2 increases, and ceases to exist for very large positive values of L_2. We note some similarity with the work on ferronematics in the next chapter, where the coupling between the nematic director and an induced spontaneous magnetisation stabilises interior nematic point defects, with $L_2 = 0$. It remains an open question as to whether elastic anisotropy, or coupling energies (perhaps with certain symmetry and invariance properties), can stabilise interior nematic defects, and help us tune the locations, dimensionality and multiplicity of defects for tailormade applications.

Chapter 6

Ferronematic equilibria on 2D polygons

The directional dependent properties of NLCs make them the preferred working material of choice for a plethora of electro-optic devices [29]. In recent years, there has been substantial interest in controlling nematic directors, and defects, by embedded inclusions e.g., dispersed colloidal nanoparticles, geometric frustration leading to complex self-assembled structures, new bio-materials, and topological materials etc. [28], [110]–[112]. In this chapter, we focus on dilute suspensions of magnetic nanoparticles (MNPs) in a nematic host. Here, the NLC-MNP interactions can lead to a spontaneous magnetization in addition to the nematic directors, in the absence of any external fields. The two effects: magnetization and nematic directors, are coupled by means of a nemato-magnetic mechanical coupling. This coupling is dictated by the surface treatment of the MNPs [75], [113]. In a purely NLC confined system, the sharp vertices of polygons play a key role in stabilising multiple optically contrasting states by the control of location, and multiplicity, of defects [74]. These 2D polygons thus have the potential to

become a new unit of liquid crystal display devices, and a full ferronematic system has yet to be fully studied in these geometries. In this chapter, we choose the square domain with right angle vertices, the hexagon with an even number of obtuse angle vertices, and the pentagon with an odd number of vertices, as generic examples of 2D polygons to systematically demonstrate how the confined nematic system responds to the inclusion of MNPs.

We present various new solutions for these nemato-magnetic systems, as will be described in the sections below, which are not reported for the pure nematic system in [74]. We show that, by tuning the model parameters, we can control the location of interior magnetic and nematic defects and the multiplicity of solutions, and we numerically observe stable solutions supporting magnetic domain walls.

6.1 Model formulation

We study partially ordered 2D systems on a square, pentagon and hexagon, with nematic orientational order and polar magnetic order, motivated by recent studies of dilute ferronematic suspensions [81]. As mentioned in Chapter 5, 2D polygons are an excellent approximation to shallow three-dimensional wells with a 2D polygon cross-section, such that the well height is much smaller than the polygon edge length. From a modelling perspective, it is reasonable to assume that the structural details are invariant across the well height, and it suffices to model the ferronematic profiles on the 2D polygonal cross-section; this reduced 2D approach can be rigorously justified (see [70], [63]). These 2D systems have two macroscopic order parameters: (i) the nematic order parameter, the Landau-de Gennes $\mathbf{Q}$-tensor order parameter, defined by (1.4.1); and (ii) a polar order parameter, described by the average spatial magnetization vector, $\mathbf{M} = (M_1, M_2)$,

of the suspended MNPs without external magnetic fields. In two dimensions, the reduced LdG **Q**-tensor order parameter can be written as [74]:

$$\mathbf{Q} = S(2\mathbf{n} \otimes \mathbf{n} - \mathbf{I}),$$

where the nematic director, $\mathbf{n} = (\cos\theta, \sin\theta)^T$, describes the preferred in-plane alignment of the nematic molecules, and S is the scalar order parameter which measures the degree of orientational order about the planar director. Therefore, **Q** has two independent components:

$$\mathbf{Q} = \begin{pmatrix} Q_{11} & Q_{12} \\ Q_{12} & -Q_{11} \end{pmatrix},$$

where $Q_{11} = S\cos 2\theta$, and $Q_{12} = S\sin 2\theta$. In this framework, we will not detect biaxial regions since $\mathrm{tr}\mathbf{Q}^3 = 0$, and we have $\mathrm{tr}\mathbf{Q}^2 = |\mathbf{Q}|^2 = 2Q_{11}^2 + 2Q_{12}^2$. We assume that **M** is the spontaneous magnetization induced by the MNPs with an internal magnetic moment, which interacts with **n** through surface anchoring conditions on the MNP surfaces. We also will assume **M** has variable magnitude, where magnetic vortices are defined by $|\mathbf{M}| = 0$, and defective regions are identified by reduced values of $|\mathbf{M}|$.

6.1.1 The effective ferronematic free energy

We model the experimentally observable profiles as minimizers of an appropriately defined energy, as in [80], [81], which in turn builds on the free energy descriptions in [79], [113], [114]. The proposed free energy has three essential contributions: a conventional nematic free energy that includes an elastic term to penalise spatial inhomogeneities, and a bulk term for temperature-dependent ordering transitions; a magnetic energy that coerces a preferred value of $|\mathbf{M}|$, as in [113]–[115], and

includes a Dirichlet energy density term to penalise arbitrary rotations between $\mathbf{M}$ and $-\mathbf{M}$; and crucially, a nemato-magnetic coupling energy parameterized by a coupling parameter. To this end, we define the generalized total free energy by:

$$\begin{aligned}\mathcal{F}[\mathbf{Q},\mathbf{M}] = &\int_\Omega \left\{ \frac{K}{2}|\nabla \mathbf{Q}|^2 - \frac{A}{2}\mathrm{tr}\mathbf{Q}^2 + \frac{C}{4}(\mathrm{tr}\mathbf{Q}^2)^2 \right\} \mathrm{dA} \\ &+ \int_\Omega \left\{ \frac{\kappa}{2}|\nabla \mathbf{M}|^2 - \frac{\alpha}{2}|\mathbf{M}|^2 + \frac{\beta}{4}|\mathbf{M}|^4 \right\} \mathrm{dA} \\ &- \int_\Omega \frac{\gamma\mu_0}{2}\mathbf{M}^T\mathbf{Q}\mathbf{M}\,\mathrm{dA},\end{aligned}$$

where Ω is our working domain, to be determined later. A is the same Landau temperature coefficient from the fourth order bulk potential (1.4.6), with $A = 0$ at some characteristic transition temperature for the NLC. Analogously, we take $\alpha = \alpha_0(T - T_c)$, where $\alpha_0 > 0$ is some constant, T is the absolute temperature in the system, and T_c is a critical temperature for the spontaneous magnetization. C and β are positive material-dependent constants, $K > 0$ is the nematic elastic constant, and $\kappa > 0$ is an elastic constant related to the magnetic stiffness. The Dirichlet energy density for $\mathbf{M}$ is, mathematically speaking, a regularisation term and does not introduce new physics into the problem for judicious parameter choices. Lastly, γ is the NLC-MNP coupling parameter, with $\mu_0 > 0$ representing some material-dependent constant related to the magnetic susceptibility of the composite material [76], [81], [116]. We note that from the form of the nemato-magnetic coupling energy density, $-\frac{\gamma\mu_0}{2}\mathbf{M}^T\mathbf{Q}\mathbf{M}$, positive γ favours $(\mathbf{n}\cdot\mathbf{M})^2 = 1$, so the nematic directors prefer to be parallel or anti-parallel to $\mathbf{M}$, whereas negative γ favours $\mathbf{n}\cdot\mathbf{M} = 0$, so the directors tend to be perpendicular to $\mathbf{M}$ (see [81]). From [82], both cases of positive and negative γ are physically relevant, and γ may be an experimentally tunable parameter. In the dilute limit, the nemato-magnetic coupling energy contribution is the *homogenized limit* of a Rapini-Papoular type of surface anchoring energy on the MNP surfaces [83]. Furthermore, in this limit we

do not see the individual MNPs, but rather account for the collective NLC-MNP interactions mediated by the surface anchoring energies in terms of this effective nemato-magnetic coupling energy. In principle, one could use homogenization methods to compute effective nemato-magnetic coupling energies, for arbitrary MNP shapes, and other types of MNP surface anchoring energies e.g., we expect the coupling energies to be different for platelet-shaped MNPs, but we adopt the simplest approach here.

We assume our domain to be a regular 2D polygon, with a physical edge length given by λ. We then define the rescaled 2D coordinates, $\bar{\mathbf{x}} := \frac{\mathbf{x}}{\lambda}$, as well as the rescaled nematic and polar magnetic order parameters, $\bar{\mathbf{Q}} := \sqrt{\frac{2C}{|A|}}\mathbf{Q}$, and $\bar{\mathbf{M}} := \sqrt{\frac{\beta}{|\alpha|}}\mathbf{M}$, respectively. We can thus define the following dimensionless ferronematic free energy for which we will minimize in the rest of this chapter:

$$\begin{aligned}\bar{\mathcal{F}}[\bar{\mathbf{Q}},\bar{\mathbf{M}}] :=& \frac{C}{A^2\lambda^2}\mathcal{F}[\mathbf{Q},\mathbf{M}] \\ =& \int_{\bar{\Omega}} \frac{1}{4}\left\{\ell_1|\bar{\nabla}\bar{\mathbf{Q}}|^2 + \frac{1}{4}|\bar{\mathbf{Q}}|^4 - |\bar{\mathbf{Q}}|^2\right\}\,\overline{\mathrm{dA}} \\ &+ \int_{\bar{\Omega}} \frac{\xi}{2}\left\{\ell_2|\bar{\nabla}\bar{\mathbf{M}}|^2 + \frac{1}{2}|\bar{\mathbf{M}}|^4 - |\bar{\mathbf{M}}|^2\right\}\,\overline{\mathrm{dA}} \\ &- \int_{\bar{\Omega}} \frac{c}{2}\bar{\mathbf{M}}^T\bar{\mathbf{Q}}\bar{\mathbf{M}}\,\overline{\mathrm{dA}},\end{aligned} \tag{6.1.1}$$

where $\bar{\Omega}$ is the rescaled domain, $\bar{\nabla}$ is the gradient with respect to the new rescaled spatial coordinates $\bar{\mathbf{x}}$, and $\overline{\mathrm{dA}}$ is the rescaled area element. We will drop the 'bars' in the rest of this chapter, for brevity, but all calculations should be thought of with respect to these rescaled coordinates and order parameters. There are four key dimensionless parameters above:

$$\ell_1 = \frac{K}{|A|\lambda^2}; \quad \ell_2 = \frac{\kappa}{|\alpha|\lambda^2}; \quad \xi = \frac{\alpha^2 C}{A^2\beta}; \quad c = \frac{\gamma\mu_0}{|A|}\sqrt{\frac{C}{2|A|}}\frac{|\alpha|}{\beta},$$

which represent the rescaled nematic elastic constant, the rescaled elastic constant associated with the magnetic stiffness, a magnetic coherence length, and the

rescaled nemato-magnetic coupling parameter, respectively. We work with low temperatures ($A, \alpha < 0$) so that the bulk favours an ordered nematic and magnetic phase, with $|\mathbf{Q}| \neq 0, |\mathbf{M}| \neq 0$. The total bulk potential is given by

$$\frac{1}{4}|\mathbf{Q}|^4 - |\mathbf{Q}|^2 + \xi|\mathbf{M}|^4 - 2\xi|\mathbf{M}|^2 - 2c\mathbf{M}^T\mathbf{Q}\mathbf{M};$$

for which the corresponding stationary points (in terms of c and ξ) are computed in [117].

As is standard in the calculus of variations, the physically observable equilibria are local or global minimizers of (6.1.1), subject to the boundary conditions. However, unstable critical points of (6.1.1) play a crucial role in transition pathways between distinct equilibria, see [118]. The critical points (stable or unstable) of (6.1.1) are solutions of the associated Euler-Lagrange equations:

$$\begin{aligned}
\ell_1\Delta Q_{11} &= \tilde{Q}Q_{11} - \frac{c}{2}(M_1^2 - M_2^2),\\
\ell_1\Delta Q_{12} &= \tilde{Q}Q_{12} - cM_1M_2,\\
\xi\ell_2\Delta M_1 &= \xi\tilde{M}M_1 - c(Q_{11}M_1 + Q_{12}M_2),\\
\xi\ell_2\Delta M_2 &= \xi\tilde{M}M_2 - c(Q_{12}M_1 - Q_{11}M_2),
\end{aligned} \tag{6.1.2}$$

where Δ is the two-dimensional Laplacian operator, and $\tilde{Q} = \left(\frac{1}{2}\text{tr}\mathbf{Q}^2 - 1\right)$ and $\tilde{M} = (|\mathbf{M}|^2 - 1)$. The phenomenological parameters, ℓ_1, ℓ_2, ξ and c, are typically estimated from experimentally measured quantities, in the presence of external magnetic fields [113], but the available data is limited. We investigate the sensitivity of the solution landscapes with respect to the rescaled elastic constants and c. The elastic constants depend on the temperature, material-dependent constants and the physical length λ of the domain, and hence, they are tunable parameters. The parameter c depends on the ratios of material-dependent constants, and the strength of the NLC-MNP interactions, so this could also be a tunable parameter.

The last parameter, ξ, is the ratio of NLC material constants and MNP-dependent constants, and again could be reasonably tuned in moderate regimes. For simplicity, we fix $\xi = 1$, and assume that the re-scaled nematic and magnetic elastic constants satisfy $\ell_1 = \ell_2 = \ell$, unless stated otherwise. These choices improve the efficiency of our numerical procedure, and allow us to capture the complex solution landscapes. For a dilute system, we expect ℓ_2 to be (much) smaller than ℓ_1, but the qualitative properties of the bifurcation diagrams remain unchanged compared to the $\ell_1 = \ell_2$ case, with shifted bifurcation points. It now remains to specify our choice of 2D domain, and boundary conditions for $\mathbf{Q}$ and $\mathbf{M}$.

6.1.2 The working domains and boundary conditions

We focus on NLC-MNP systems in a square, pentagon, and hexagon; these three examples are generic, and illustrate the role of geometry in defect-induced tailored multistability. More specifically, we define our working domain, Ω, to be a regular N-sided polygon, centered at the origin and, in our model problem, we take $N = 4, 5, 6$. We note that the physical edge length, λ, has been absorbed into the phenomenological parameters above. The polygon vertices are defined by

$$v_k = \left(\cos\left(\frac{2\pi(k-1)}{N}\right), \sin\left(\frac{2\pi(k-1)}{N}\right)\right) \tag{6.1.3}$$

for $k = 1, \ldots, N$. The polygon edges are labelled counterclockwise, as $C_1, \ldots, C_N$, such that C_1 connects v_1 to v_2, and so on.

Boundary conditions are a crucial consideration for confined systems. We impose fixed Dirichlet tangent boundary conditions for $\mathbf{Q}$ and $\mathbf{M}$, which requires both the nematic director, $\mathbf{n}$, and $\mathbf{M}$, to be tangent to the edges of Ω. Specifically, we specify the boundary conditions for $\mathbf{Q}$ and $\mathbf{M}$ on the edges, C_k, for $k = 1, \ldots, N$,

as follows:

$$(Q_{11b}, Q_{12b}) = \left(-\cos\left(\frac{2\pi(2k-1)}{N}\right), \sin\left(\frac{2\pi(1-2k)}{N}\right)\right), \tag{6.1.4}$$

and

$$(M_{1b}, M_{2b}) = \left(\sin\left(\frac{\pi(2k-1)}{N}\right), -\cos\left(\frac{\pi(2k-1)}{N}\right)\right). \tag{6.1.5}$$

These boundary conditions create a natural mismatch for the nematic director at the polygon vertices, v_k, making them natural candidates for defect sites [61], [74], [88]. As was explored in previous chapters of this thesis, tangent boundary conditions are well accepted for confined NLC systems, both experimentally and theoretically; see [60]. We impose a fixed topologically non-trivial tangent boundary condition for the spontaneous magnetization of the suspended MNPs. We assume that $\mathbf{M}$ rotates by 2π radians around $\partial\Omega$, which naturally leads to interior magnetic vortices, offering a wonderful playground for exploring exotic solution landscapes of these ferronematic systems. This is a purely theoretical choice for the time being. For a dilute system, it is reasonable to assume that the boundary conditions for the magnetization follow the tangent boundary conditions for the nematic director. From an experimental perspective, in [119], the authors argue that tangent boundary conditions for the spontaneous magnetization can arise from energetic considerations. We speculate that, the boundary conditions for the magnetization could be controlled, by applying an external magnetic field to fix the orientation, and position, of the MNPs on the boundaries, followed by the removal of the magnetic field, although this is largely open to the best of our knowledge. There are multiple choices of boundary conditions for the nematic director and the magnetization (including free boundary conditions for the magnetization, or weak anchoring effects), but our choice of Dirichlet tangent

boundary conditions offers rich possibilities, that could guide future experimental studies on these lines.

6.1.3 Numerical methods

We numerically compute the solutions of the system (6.1.2), subject to the tangent Dirichlet boundary conditions (6.1.4)–(6.1.5), which are necessarily critical points of (6.1.1). In our simulations, we define the square domain separately from the definition in (6.1.3). Here we set the square vertices at $(-0.5, \pm 0.5)$ and $(+0.5, \pm 0.5)$, such that

$$(Q_{11b}, Q_{12b}, M_{1b}, M_{2b}) = \begin{cases} (-1, 0, 0, -1), & \text{on } x = 0.5; \\ (-1, 0, 0, 1), & \text{on } x = -0.5; \\ (1, 0, 1, 0), & \text{on } y = 0.5; \\ (1, 0, -1, 0), & \text{on } y = -0.5. \end{cases} \tag{6.1.6}$$

This is purely for computational convenience, and to make comparisons with the numerical investigations in [81], and has no effect on the qualitative results. We employ the same numerical procedure to compute the local minimizers of (6.1.1) as in Chapter 5. For clarity, we use the DOLFIN library [101], from the popular open-source computing platform FEniCS [102], to solve the weak formulation of (6.1.2) (with $\ell = \ell_1 = \ell_2$ and $\xi = 1$), given by

$$\begin{aligned} 0 &= \int_\Omega \ell \nabla Q_{11} \cdot \nabla v_{11} + \left(\tilde{Q} Q_{11} - \frac{c}{2}(M_1^2 - M_2^2) \right) v_{11} \, \mathrm{dA}, \\ 0 &= \int_\Omega \ell \nabla Q_{12} \cdot \nabla v_{12} + \left(\tilde{Q} Q_{12} - c M_1 M_2 \right) v_{12} \, \mathrm{dA}, \\ 0 &= \int_\Omega \ell \nabla M_1 \cdot \nabla u_1 + \left(\tilde{M} M_1 - c(Q_{11} M_1 + Q_{12} M_2) \right) u_1 \, \mathrm{dA}, \\ 0 &= \int_\Omega \ell \nabla M_2 \cdot \nabla u_2 + \left(\tilde{M} M_2 - c(Q_{12} M_1 - Q_{11} M_2) \right) u_2 \, \mathrm{dA}, \end{aligned}$$

for arbitrary test functions v_{11}, v_{12}, u_1, u_2. This nonlinear system is solved using standard Finite Element Methods and Newton's method [103], with a linear LU solver for each iteration and with a tolerance set to $1e-13$. In our simulations, we use a fixed triangular mesh for the domain, with Lagrange elements of order 1, for the spacial discretization. Due to the high multiplicity of the solutions, convergence may be highly sensitive to the choice of initial condition. We will go into more detail on the choice of initial condition in the next sections. We also study the stability of the solutions by numerically calculating the smallest real eigenvalue, λ_1, of the Hessian of the reduced energy (6.1.1) with four degrees of freedom, Q_{11}, Q_{12}, M_1, and M_2, using the LOBPCG method, as summarized in Chapter 5 (also, see [106]). Essentially, $\lambda_1 > 0$ is a signature of local stability, and the numerical solution is unstable, if $\lambda_1 < 0$. In the figures of our numerical solutions, we regularly plot the scalar order parameter, $S = \sqrt{Q_{11}^2 + Q_{12}^2}$, labelled by the colour chart, and the nematic director, $\mathbf{n}$, shown by white lines, where $\mathbf{n}$ is given by

$$\mathbf{n} = (\cos\theta, \sin\theta), \qquad \theta = \frac{1}{2}\text{atan2}(Q_{12}, Q_{11}). \tag{6.1.7}$$

These measures capture the nematic order parameter for the system. We also plot the magnetization profile, with $|\mathbf{M}| = \sqrt{M_1^2 + M_2^2}$ labelled by the colour chart, and the accompanying white arrows describe the magnetic orientation, $(M_1, M_2)/|\mathbf{M}|$, for $|\mathbf{M}| \neq 0$. We also compute bifurcation diagrams as a function of ℓ, the rescaled parameter which is inversely proportional to λ^2. We plot solid lines to represent stable solution branches, and dashed lines correspond to unstable branches. The numerical computation of bifurcation diagrams requires continuation techniques, for which we first locate different stable solutions, for fixed c and ℓ. Depending on the solution branch, we perform a increasing/decreasing ℓ sweep

to produce these diagrams, and we plot two measures to distinguish between separate solution branches:

$$\int_\Omega Q_{11}\left(0.5+x+y\right)\,\mathrm{d}x\mathrm{d}y, \quad \text{and} \quad \int_\Omega Q_{12}\left(0.5+x+y\right)\,\mathrm{d}x\mathrm{d}y. \tag{6.1.8}$$

We will now present our numerical findings for the square, hexagon, and pentagon. We complement the investigation on a square with an asymptotic analysis of the minimizers of (6.1.1), in the $\ell \to 0$ and $\ell \to \infty$ limits, which correspond to large and small well-size limits, respectively.

6.2 Solution landscape on a square

We first recall the essential results for the purely nematic system ($c = 0$) in a square domain from [64], where the authors track the $\mathbf{Q}$-solutions of (6.1.2), subject to (6.1.6), as a function of the square edge-length, λ, at a fixed temperature. For large ℓ or small λ ($\ell > 0.1$ or $\lambda < 10^{-7}$m approximately), there is a unique WORS [52], distinguished by a pair of mutually orthogonal defect lines along the square diagonals (with $\mathbf{Q} \approx 0$). The WORS is a special case of the more general Ring solution for N-sided polygons, reported in [74], and exists for all $\ell > 0$ on a square domain, with tangent boundary conditions (6.1.6) for $\mathbf{Q}$. As ℓ decreases, the WORS loses stability, and bifurcates into two stable diagonal (D) solutions, for which $\mathbf{n}$ aligns along one of the square diagonals in the interior. As ℓ further decreases, there is a further bifurcation point, with two unstable BD solution branches bifurcating from the WORS branch. The BD solutions have two defect lines, parallel to a pair of opposite square edges, and the BD solutions further bifurcate into 4 unstable rotated (R) solutions, as ℓ decreases. The nematic director, $\mathbf{n}$, rotates by π radians between a pair of opposite square

edges for a R solution, and there are 4 rotationally equivalent R solutions, related by a $\frac{\pi}{2}$-rotation. The R solutions gain stability as ℓ decreases, and for ℓ small enough ($\ell < 10^{-3}$ or $\lambda > 10^{-6}$m approximately), there are six distinct stable nematic equilibria; 2 D solutions and 4 R solutions. We presented illustrations of the typical nematic director profile in D and R solutions, in Figure 2.2.

These "small ℓ" solutions can also be distinguished by the director orientation at the domain vertices and, for the purposes of this chapter, we introduce some terminology. The D solutions have two diagonally opposite *splay* vertices, such that the corresponding director, $\mathbf{n} = (\cos\theta, \sin\theta)$, has a splay pattern near the splay vertex. At a splay vertex, θ rotates by $\frac{2\pi}{N} - \pi$, where N is the number of polygon edges. In contrast to the D solutions, each R solution has a pair of splay vertices connected by a square edge. The director orientation on the remaining vertices displays a bend pattern, and so we refer to these as *bend* vertices. Here, θ rotates by $\frac{2\pi}{N}$. We include an illustration of a typical splay and bend vertex, in Figure 6.1.

Figure 6.1: Director orientation at a *splay* and *bend* vertex.

Our main results in this section include:

- The computation of solution landscapes for positive and negative coupling, c, as a function of ℓ, with multistability being strongly enhanced in the $c < 0$ regime, as ℓ decreases.

- The existence of solutions with a pair of $+\frac{1}{2}$ interior nematic point defects, for ℓ small enough, coerced by the interior magnetic vortex at the square center.

- Heuristic arguments for the multistability in "large" domains by considering the asymptotic of minimizers in the $\ell \to 0$ limit.

- The unique energy minimizer loses the cross structure of the WORS in the nematic profile, for ℓ large enough and $c \neq 0$, and minimizers in the $\ell \to \infty$ limit are shown to make good numerical approximations.

For the ferronematic configurations, $(\mathbf{Q}, \mathbf{M})$, we consider the $c > 0$, and $c < 0$, cases separately. For positive c, we observe the coexistence of stable $(\mathbf{Q}, \mathbf{M})$ profiles, with nematic defects pinned at the polygon vertices, and magnetic domain walls along polygonal diagonals, and polygon edges, that separate distinct domains of magnetization. These profiles maintain the typical D and R profiles for $\mathbf{Q}$, whilst $\mathbf{M}$ is coerced to align parallel to $\mathbf{n}$. We present the numerical solutions in Figure 6.2, for $\ell = 10^{-3}$ and $c = 0.25$. In this figure, and all subsequent figures, the nematic profiles are shown in the top row, and magnetization profiles in the bottom row. These configurations are in accordance with the numerical investigations of [81], and we find that solutions with magnetic domain walls become increasingly difficult to find, as c increases.

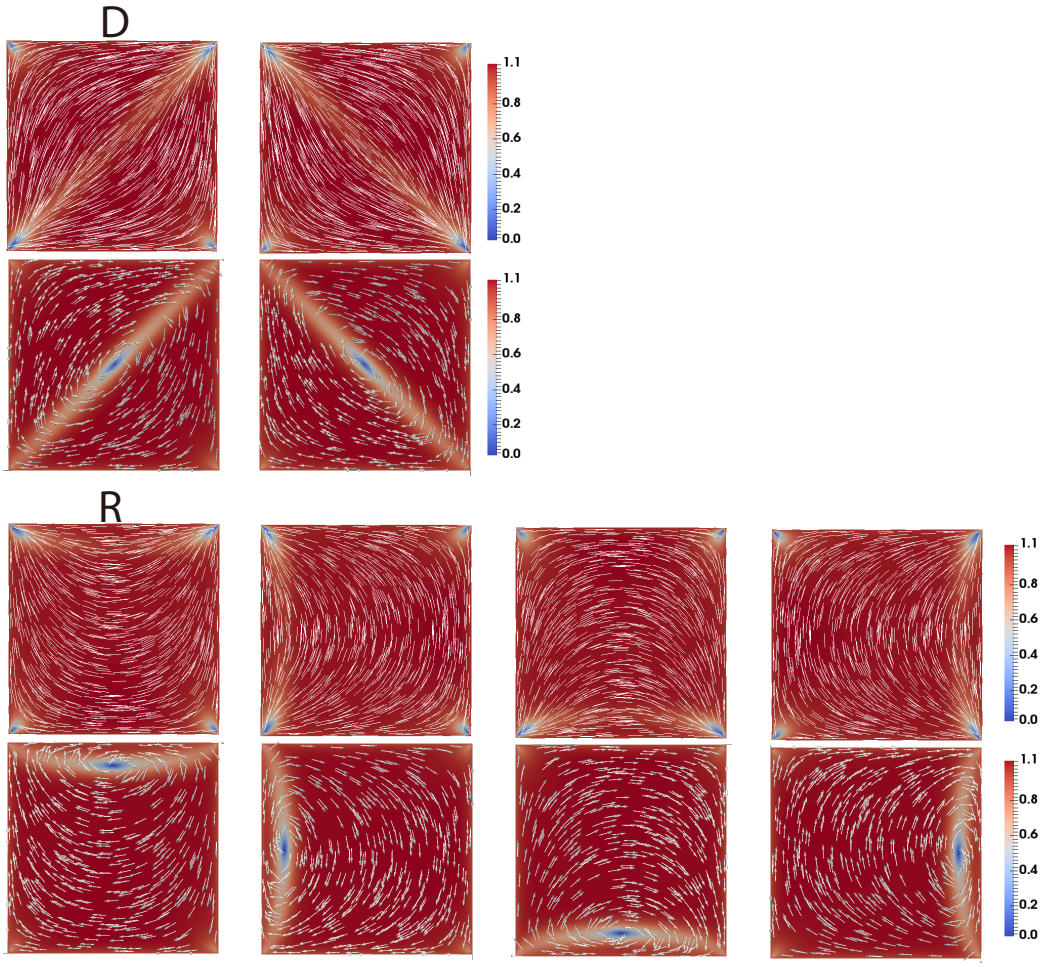

Figure 6.2: The plots of two D and four R solutions with $\ell = 10^{-3}$ and $c = 0.25$.

We observe a novel feature for $c > 0$ and ℓ small enough. By taking the D solution (for $c = 0$) as the initial condition in our numerical procedure, we find 2 solutions with a pair of $+\frac{1}{2}$ interior nematic point defects, along one of the square diagonals, and a corresponding magnetic vortex at the square center. We refer to this class of $(\mathbf{Q}, \mathbf{M})$-solutions as the *Peppa* solution. The Peppa solutions are stable for $c = 0.25$, and we speculate that they exist for all $c > 0$ but are unstable for $c = 0$. The corresponding $\mathbf{M}$-profiles have a smeared out vortex along the line connecting the nematic defect pair. We present the $(\mathbf{Q}, \mathbf{M})$-profiles for the two Peppa solutions in Figure 6.3, for $c = 0.25$ and $\ell = 10^{-3}$.

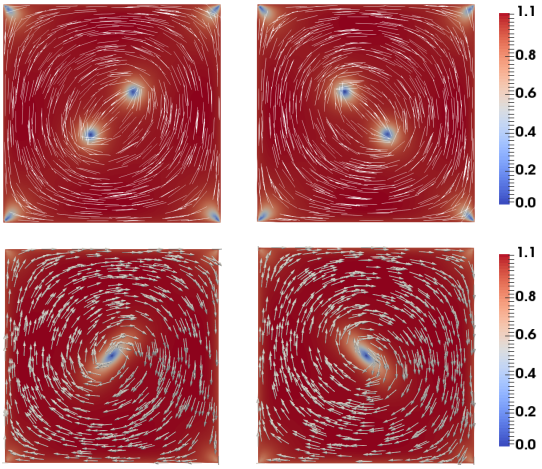

Figure 6.3: The two Peppa solutions with $\ell = 10^{-3}$ and $c = 0.25$.

Our numerical observations for $c > 0$ are an interesting example of how nemato-magnetic coupling stabilises domain walls in $\mathbf{M}$ (for the D and R solutions in Figure 6.2), and interior point defects in $\mathbf{Q}$ (for Peppa solutions in Figure 6.3). We present the bifurcation diagram as a function of ℓ, for $c = 0.25$, in Figure 6.5. In comparison with the bifurcation diagram for $c = 0$, the qualitative features are relatively unchanged for $c > 0$, apart from the addition of the Peppa solution branches. For $c = 0$ and ℓ large enough, the unique $\mathbf{Q}$-solution is the WORS reported in [52], and the unique $\mathbf{M}$-solution has a magnetic vortex of degree $+1$ (determined by the degree of the boundary conditions) at the square centre. For $c \neq 0$ and ℓ finite, the WORS loses its defect cross structure, and collapses into the unique *Ring* solution, with a circular nematic $+1$-degree point defect, analogous to the magnetic vortex, at the square centre. We refer to this solution branch, which is unique and globally stable for ℓ large enough, as the *Ring branch*. This solution branch exists for all $\ell > 0$, but loses stability as ℓ decreases. The Ring solution branch is distinguished by $Q_{11} = 0$ nodal lines along the square diagonals, and $Q_{12} = 0$ along the coordinate axes, $\{x = 0\} \cup \{y = 0\}$. We present the Ring solution for $c = 0.25$, and $\ell = 0.05$, in Figure 6.4. We include plots of $\mathbf{Q}$, and

the corresponding **M** profile, as well as the components Q_{11}, Q_{12}, M_1, and M_2. As ℓ decreases, the Ring branch loses stability, and bifurcates into two stable D

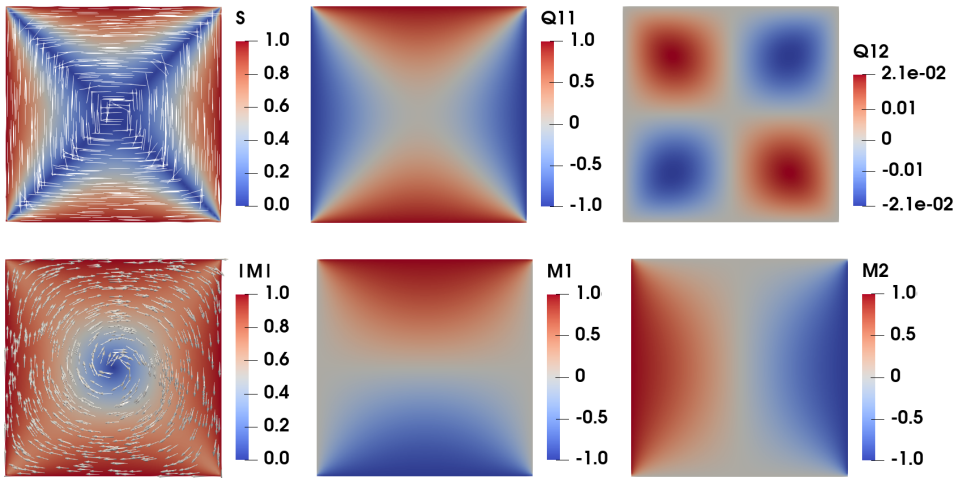

Figure 6.4: The Ring solution for $c = 0.25$ and $\ell = 0.05$.

solutions (with regards to the **Q**-solutions). The corresponding **M**-profiles have domain walls (with reduced $|\mathbf{M}|$) along the corresponding square diagonals. As we will explain below, these domain walls correspond to a π-rotation in the **M**-vector. As ℓ decreases further, the unstable Ring branch bifurcates into two unstable BD branches (with regards to the **Q**-solutions). Each BD solution bifurcates into two unstable R solutions, which gain stability when ℓ is small enough. The **M**-solutions, corresponding to the stable R solutions, exhibit a domain wall along the square edge with the two splay vertices. The stable D solutions bifurcate into two Peppa solution branches that have two $+\frac{1}{2}$-nematic defects along the square diagonal, for ℓ small enough. We also present orthogonal 2D projections of the bifurcation diagram, in Figure 6.5, which plot the two measures, (6.1.8), versus ℓ, respectively.

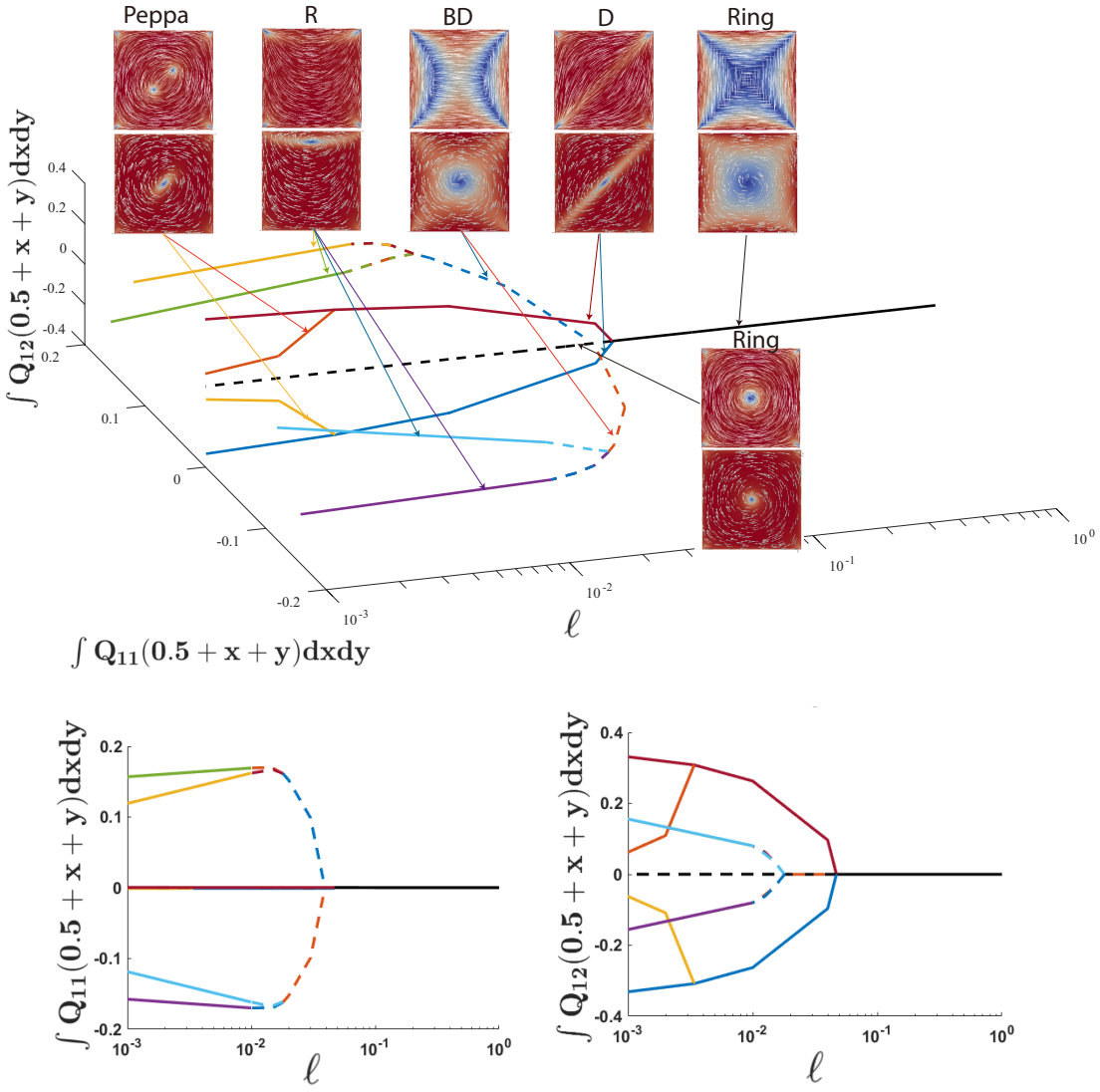

Figure 6.5: Bifurcation diagram for (6.1.1) as a function of ℓ on a square domain with $c = 0.25$.

The picture with negative c is more complex. In this regime, $\mathbf{n}$ and $\mathbf{M}$ tend to be perpendicular to each other in the polygon interior, and this naturally creates fascinating boundary layers near the polygon edges. We effectively double the number of stable states for small ℓ, compared to the results in [74], for $c = 0$. These stable states are distinguished by vertex defects for $\mathbf{Q}$, and vertex vortices for $\mathbf{M}$, and illustrate how $c < 0$ strongly enhances multistability in the square. Informally speaking, the symmetry between the splay vertices is broken in the nematic D solution, rendering 4 different D profiles for negative c. One splay vertex is more asymmetric than the other splay vertex, and the corresponding $\mathbf{M}$-profile orients perpendicular to the the nematic director (which follows a diagonal D profile), with the magnetic vortex localised near the asymmetric splay vertex. In the same vein, when ℓ is small enough, we find 8 stable R solution branches. The reasoning for observing twice the number of R solutions for the $\mathbf{Q}$-solution profile, for negative c, is the same as for the D solutions. The symmetry between the splay vertices is broken for the R solutions, with one splay vertex being more defective/asymmetric than the other splay vertex. The corresponding $\mathbf{M}$-profiles again orient perpendicular to the nematic director, and the magnetic vortex localises near the more asymmetric splay vertex. We plot the four D solutions, and eight R solutions, in Figure 6.6, for $c = -0.25$ and $\ell = 10^{-3}$.

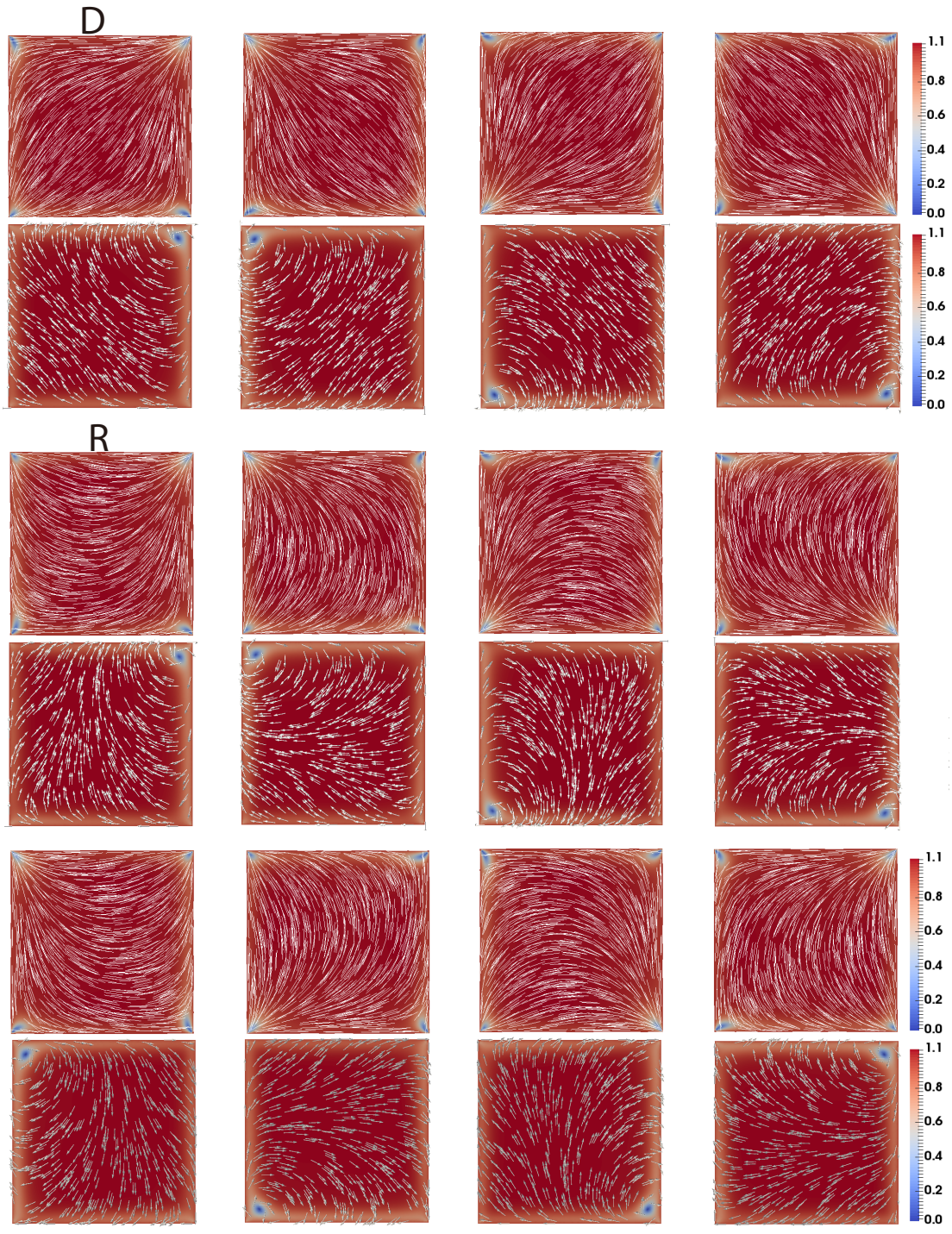

Figure 6.6: The plots of four D and eight R solutions with $\ell = 10^{-3}$ and $c = -0.25$.

Additionally, for small ℓ, we find twice as many Peppa solutions as were found for $c > 0$. These stable $(\mathbf{Q}, \mathbf{M})$-profiles are also distinguished by a pair of interior $+\frac{1}{2}$-nematic point defects along one of the square diagonals, accompanied by the interior magnetic vortex in the $\mathbf{M}$-profile. The novelty for $c < 0$ is that we find two separate classes of these configurations, referred to as $Peppa_{in}$ and $Peppa_{out}$ solutions, which have $\mathbf{M}$ pointing into, or out of, the interior magnetic vortex, respectively. We present plots of the $(\mathbf{Q}, \mathbf{M})$-profiles for the two Peppa$_{in}$, and two Peppa$_{out}$, solutions in Figure 6.7, for $c = -0.25$ and $\ell = 10^{-3}$. The new Peppa$_{in}$ and Peppa$_{out}$ solutions, for $c = -0.25$, are obtained by taking the profiles $(\mathbf{Q}, (M_2, -M_1))$ and $(\mathbf{Q}, (-M_2, M_1))$, respectively as initial conditions, where $(\mathbf{Q}, \mathbf{M} = (M_1, M_2))$ is the Peppa solution for $c = 0.25$.

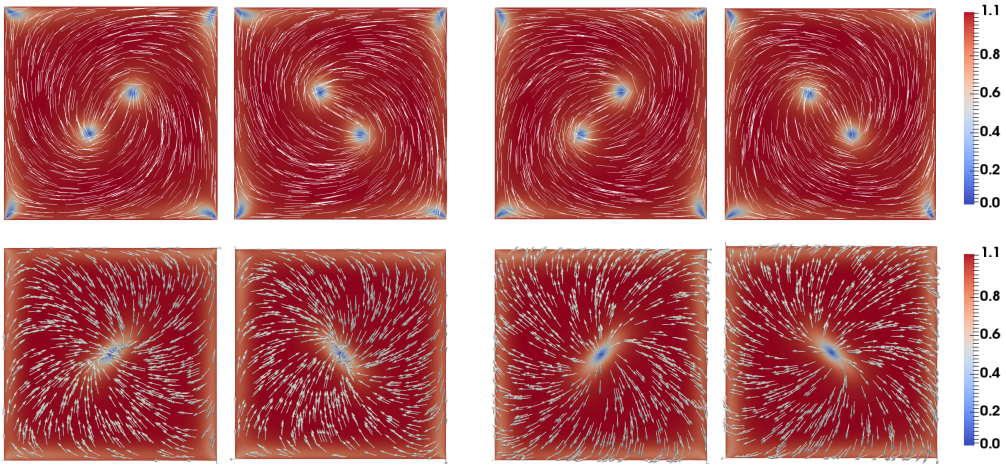

Figure 6.7: Plots of the two Peppa$_{in}$ and two Peppa$_{out}$ solutions with $\ell = 10^{-3}$ and $c = -0.25$.

The case of negative c illustrates how we can use nemato-magnetic coupling to break symmetry, increase the multiplicity of stable solutions (for small ℓ), and generate exotic permutations of defect profiles in $\mathbf{Q}$ and $\mathbf{M}$, all of which offer new prospects for engineered multistability. In Figure 6.9, we explore the solution landscape as a function of ℓ, for $c = -0.25$. There are striking novelties here.

For ℓ large, we observe the unique Ring branch, which is globally stable for large ℓ, and exists for all $\ell > 0$. The Ring branch loses stability as ℓ decreases. We note that the Ring profile for small ℓ, and $c = -0.25$, is different from its positive coupling counterpart at $c = 0.25$. This is essentially because $\mathbf{n}$ and $\mathbf{M}$ tend to be perpendicular in the square interior, since $c < 0$. In particular, the $\mathbf{Q}$-solution in the Ring branch adopts a hyperbolic-like central nematic defect structure, in sharp contrast to the vortex structure, for $c = 0.25$. The $\mathbf{M}$-profile has an interior magnetic vortex because of the topologically non-trivial Dirichlet conditions, as explained above. We present the $(\mathbf{Q}, \mathbf{M})$-profiles, and the corresponding Q_{11}, Q_{12}, M_1, and M_2 components, for the Ring solution with $c = -0.25$ and $\ell = 0.05$, in Figure 6.8. As ℓ decreases, the Ring branch bifurcates

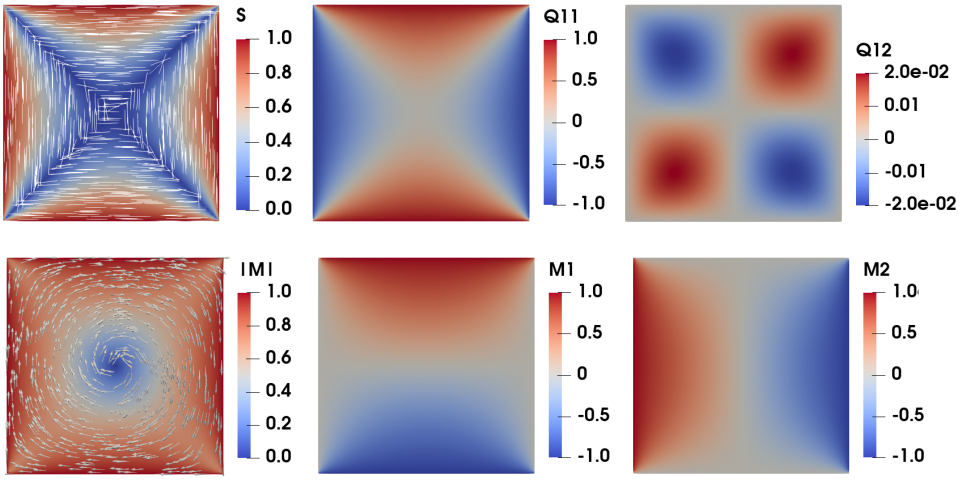

Figure 6.8: The Ring solution for $c = -0.25$ and $\ell = 0.05$.

into the 4 *stable D solutions*, presented in Figure 6.6. This is notably different from the $c \geq 0$ case. We no longer find unstable BD profiles for $c < 0$, and the 8 stable R configurations, and Peppa$_{in}$, Peppa$_{out}$ solution branches, are not connected in our numerical search. The bifurcation diagram in Figure 6.9 once again plots the measures (6.1.8) versus ℓ, and we also plot the 2D orthogonal projections below.

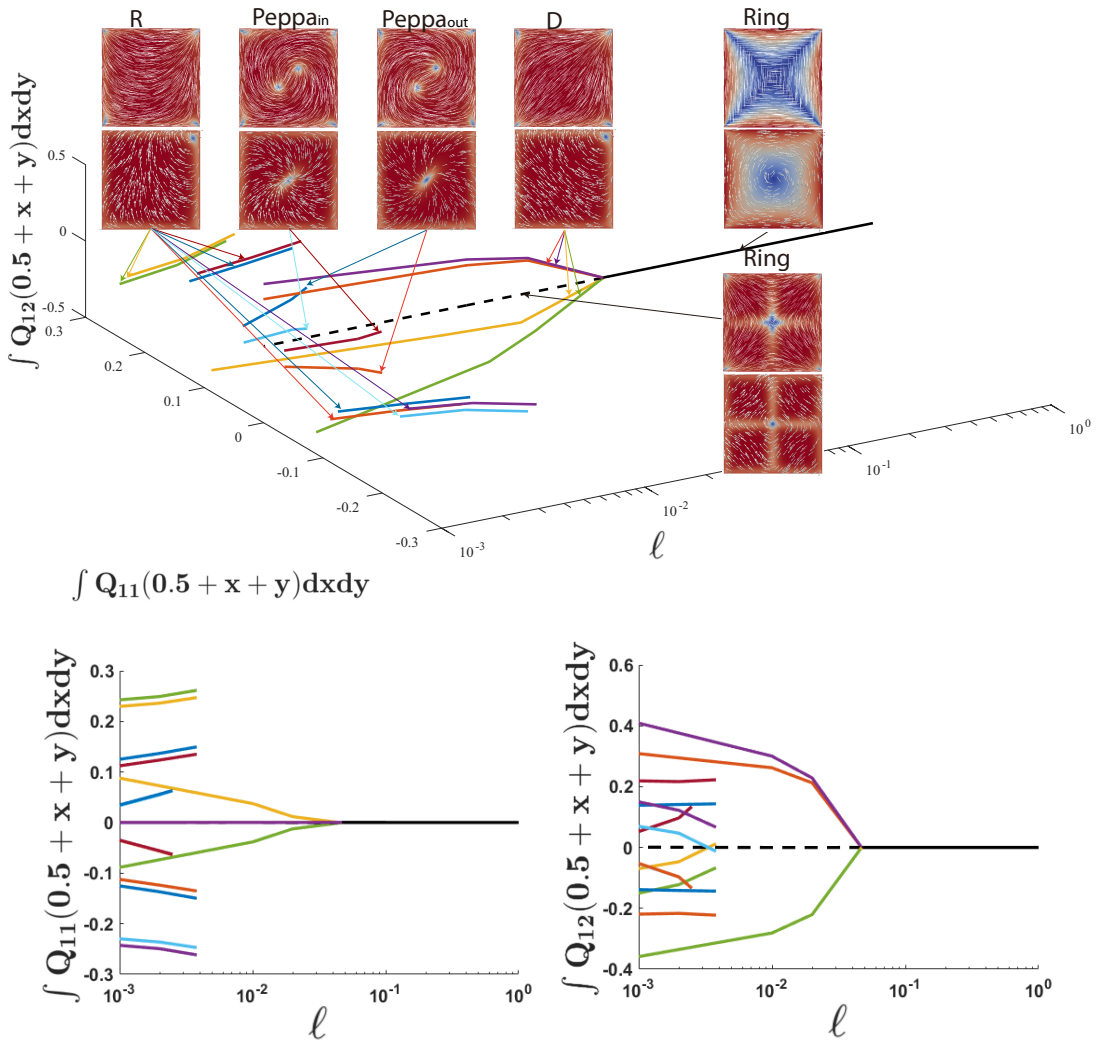

Figure 6.9: Bifurcation diagram for (6.1.1) as a function of ℓ on a square domain with $c = -0.25$.

6.2.1 The $\ell \to 0$ limit

In this section, we study the asymptotics of minimizers of (6.1.1), in the $\ell \to 0$ limit, which is relevant for macroscopic domains on the length scale of microns, or larger. We have seen that, as ℓ decreases, the multiplicity of stable $(\mathbf{Q}, \mathbf{M})$-solutions in the square increases, and the solution landscape becomes increasingly complicated. Recall that for $\ell_1 = \ell_2 = \ell$, $\xi = 1$, the dimensionless free energy of this NLC-MNP coupled system is given by:

$$\begin{aligned}\mathcal{F}[\mathbf{Q}, \mathbf{M}] = &\int_\Omega \frac{1}{4}\left\{\ell|\nabla \mathbf{Q}|^2 + \frac{1}{4}|\mathbf{Q}|^4 - |\mathbf{Q}|^2\right\} \mathrm{dA} \\ &+ \int_\Omega \frac{1}{2}\left\{\ell|\nabla \mathbf{M}|^2 + \frac{1}{2}|\mathbf{M}|^4 - |\mathbf{M}|^2\right\} \mathrm{dA} \\ &- \int_\Omega \frac{c}{2}\{Q_{11}(M_1^2 - M_2^2) + 2Q_{12}M_1M_2\}\,\mathrm{dA}.\end{aligned} \tag{6.2.1}$$

In a 2D framework, we can parameterize $\mathbf{Q}$ and $\mathbf{M}$ as:

$$Q_{11} = S\cos(2\theta), \quad Q_{12} = S\sin(2\theta), \quad M_1 = R\cos(\phi), \quad M_2 = R\sin(\phi),$$

where θ, ϕ, are orientation angles for $\mathbf{n}$, and $\mathbf{M}$, respectively. We note that $|\mathbf{Q}|^2 = 2S^2$, and $|\mathbf{M}| = R$. Substituting the parameterization above into (6.2.1), we obtain,

$$\begin{aligned}\frac{1}{\ell}\mathcal{F}[S, R, \theta, \phi] = &\int_\Omega \left\{\frac{1}{2}|\nabla S|^2 + 2S^2|\nabla\theta|^2\right\} \mathrm{dA} \\ &+ \int_\Omega \left\{\frac{1}{2}|\nabla R|^2 + \frac{1}{2}R^2|\nabla\phi|^2\right\} \mathrm{dA} \\ &+ \frac{1}{\ell}\int_\Omega \left\{\frac{1}{4}S^4 - \frac{1}{2}S^2 + \frac{1}{4}R^4 - \frac{1}{2}R^2\right\} \mathrm{dA} \\ &- \int_\Omega \frac{c}{2\ell}SR^2\cos(2(\theta - \phi))\,\mathrm{dA}.\end{aligned}$$

For $c > 0$ and small ℓ, we numerically solved for two D solutions and four R solutions, with nematic profiles similar to purely nematic solutions with zero coupling, as seen in Figure 6.2. The $\mathbf{M}$-profiles were less affected too, as they

retain the interior central magnetic vortex, with some distortion. The case of small ℓ and $c < 0$, where $\mathbf{n}$ prefers to align perpendicular to $\mathbf{M}$, is more complicated. The four D and eight R solutions we find in this regime, keep the nematic defect sites pinned to the vertices of the square well, but the magnetic vortex in the $\mathbf{M}$-profile is coerced to a square vertex - breaking a line of symmetry. These solutions were presented in Figure 6.6. Heuristically, the coupling energy density, $-\frac{c}{2\ell}SR^2\cos(2(\theta-\phi))$, determines the preferred relative orientation of $\mathbf{n}$ and $\mathbf{M}$. If $c > 0$, this term is minimized when

$$\theta = \phi + \pi k, \quad k \in \mathbb{Z} \tag{6.2.2}$$

i.e., when the director angle, θ, and the magnetization angle, ϕ, differ by a multiple of π, so that $(\mathbf{n}\cdot\mathbf{M}) = \pm 1$. In particular, the coupling energy does not distinguish between $\mathbf{M}$ and $-\mathbf{M}$, and the energetic term, $|\nabla\mathbf{M}|^2$, penalises such arbitrary rotations. If $c < 0$, the coupling energy is minimized when

$$\theta = \phi + \left(\frac{2k+1}{2}\right)\pi, \quad k \in \mathbb{Z} \tag{6.2.3}$$

i.e., when the director angle, θ, and the magnetization angle, ϕ, differ by an odd multiple of $\frac{\pi}{2}$, so that $\mathbf{n}\cdot\mathbf{M} = 0$.

In [117], the authors compute the minimizers, (S_c, R_c), of the bulk potential

$$f(S,R,\theta,\phi) = \left(\frac{1}{4}S^4 - \frac{1}{2}S^2\right) + \left(\frac{1}{4}R^4 - \frac{1}{2}R^2\right) - \frac{c}{2}SR^2\cos(2(\theta-\phi)).$$

They show that

$$S_c = \left(\frac{|c|}{4} + \sqrt{\frac{c^2}{16} - \frac{1}{27}\left(1+\frac{c^2}{2}\right)^3}\right)^{1/3} + \left(\frac{|c|}{4} - \sqrt{\frac{c^2}{16} - \frac{1}{27}\left(1+\frac{c^2}{2}\right)^3}\right)^{1/3};$$

$$R_c = \sqrt{|c|S_c + 1}.$$

As $\ell \to 0$, for a fixed c, minimizers of (6.2.1) converge to appropriately defined minimizers, $(\mathbf{Q}^*, \mathbf{M}^*)$, where $|\mathbf{Q}^*| = \sqrt{2}S_c$, $|\mathbf{M}^*| = R_c$, almost everywhere away from the polygon edges. This is in accordance with our numerical simulations for small ℓ and $c = \pm 0.25$, where the value of S, and R, approach 1.1 in the interior of the domain. We see that for $c = \pm 0.25$, $S_c \approx 1.07$ and $R_c \approx 1.12$. The corresponding orientation angles, θ^* and ϕ^*, are solutions of the Laplace equation ($\Delta\theta = 0$ and $\Delta\phi = 0$, respectively), and θ^* and ϕ^* are related by (6.2.2) for $c > 0$, and (6.2.3) for $c < 0$, respectively, away from the polygon edges.

We can illustrate these concepts by considering the diagonal solutions in Figure 6.2, and the corresponding **M**-profiles with domain walls along the square diagonals. For $c > 0$ and small ℓ, the preceding discussion suggests that θ and ϕ only differ by a multiple of π in the interior. Let $c = 0.25$, and consider one of the D solutions. The corresponding boundary conditions for θ are

$$\theta = \begin{cases} \frac{\pi}{2}, & x = \pm 0.5; \\ 0, & y = \pm 0.5. \end{cases}$$

However, this does not agree with the boundary conditions for ϕ, which are fixed by the boundary condition on **M**, given by the Dirichlet conditions (6.1.6) i.e.,

$$\phi = \begin{cases} 0, & y = 0.5; \\ \pi, & y = -0.5; \\ \frac{\pi}{2}, & x = -0.5; \\ \frac{3\pi}{2}, & x = 0.5. \end{cases}$$

Comparing the boundary conditions for θ, for this D solution, and ϕ above, along with the constraints imposed by (6.2.2), we deduce that $\theta \approx \phi$, for $y \geq x$, and $\phi \approx \theta + \pi$, for $y < x$. Hence, there is a π-wall in the corresponding **M**-profile along $x = y$ (see Figure 6.2). Analogous comments apply to the second D solution

(the second column in the first two rows of Figure 6.2), where we observe a π-wall in the **M**-profile, along $y = -x$, such that ϕ flips by π radians across the wall. $\mathbf{M} \neq 0$ on either side of the π-wall in these figures, so these domain walls separate ordered magnetic polydomains. We refer to such π-walls as *domain walls* for the remainder of this chapter. In Figure 6.2, there are also 4 stable R solutions, labelled by say, $R_1, \ldots, R_4$. These rotated states can be defined by their boundary conditions on the director angle e.g.,

$$\begin{aligned}
R_1: &\quad \theta(x, \pm 0.5) = 0;\ \theta(-0.5, y) = \frac{3\pi}{2};\ \theta(0.5, y) = \frac{\pi}{2},\\
R_2: &\quad \theta(\pm 0.5, y) = \frac{\pi}{2};\ \theta(x, -0.5) = 0;\ \theta(x, 0.5) = \pi,\\
R_3: &\quad \theta(x, \pm 0.5) = 0;\ \theta(-0.5, y) = \frac{\pi}{2};\ \theta(0.5, y) = \frac{3\pi}{2},\\
R_4: &\quad \theta(\pm 0.5, y) = \frac{\pi}{2};\ \theta(x, -0.5) = \pi;\ \theta(x, 0.5) = 0.
\end{aligned}$$

These boundary conditions are incompatible with the boundary conditions for ϕ in (6.1.6). In the $\ell \to 0$ limit, with fixed $c > 0$, we need θ and ϕ to differ by a multiple of π almost everywhere. Comparing (6.1.6) with the above, we deduce that the **M**-profile, corresponding to R_1, has a domain wall near the edge $y = 0.5$ i.e., ϕ rotates from $\phi = 0$, to $\phi = \pi$, across a domain wall parallel to $y = 0.5$, as can be clearly seen from the first column, of the fourth row, in Figure 6.2. In other words, $\theta \approx \phi$ for $y < 0.5$, and $\phi \approx \theta + \pi$ on $y = 0.5$. Analogous remarks apply to the **M**- profiles corresponding to $R_2, \ldots, R_4$, where we observe domain walls along one of the square edges, such that $\theta \approx \phi$ on one side of the wall, and $|\theta - \phi| = \pi$ on the other side that contains the square edge in question.

The Peppa solution branch for positive coupling, is an example of the nematic profile being tailored by the magnetization profile. The boundary conditions for ϕ are fixed in (6.1.6), but the boundary conditions for θ are not fixed by (6.1.6), except that 2θ is a multiple of 2π, on $y = \pm 0.5$, and that 2θ is an odd

multiple of π, on $x = \pm 0.5$. In other words, θ can also assume the topologically non-trivial boundary conditions satisfied by ϕ, and this is indeed observed in the Peppa solution branch, for which the corresponding nematic director rotates by 2π radians along the boundary. The 2π rotation around the square perimeter necessarily means that $\mathbf{n}$ must have interior topological defects, with a total charge of $+1$. For topological and energetic reasons, the $+1$-defect splits into two non-orientable $+\frac{1}{2}$-nematic defects in the interior, conserving the total topological charge. This is allowed in the reduced LdG framework, since the $\mathbf{Q}$-tensor includes non-orientable director fields, outside the scope of a vector field description. By contrast, the corresponding $\mathbf{M}$-profile has a single interior $+1$-vortex due to orientability constraints.

To summarize, for small ℓ and $c > 0$, the D and R solution branches illustrate that the nematic profile can generate domains walls in the $\mathbf{M}$-profile, and the Peppa solution branch demonstrates how the topologically non-trivial $\mathbf{M}$-profile can stabilise interior nematic point defects. The story with negative c is more complex and fascinating, as we describe below.

We consider the diagonal solutions in Figure 6.6, for $c = -0.25$. Consider D_1, such that the nematic director, $\mathbf{n}$, is aligned along the square diagonal $y = x$. The corresponding $\mathbf{M}$ vector tends to be perpendicular to $\mathbf{n}$ in the interior, so that $\phi \approx \frac{3\pi}{4}$, or $\phi \approx -\frac{\pi}{4}$, along $y = x$. Furthermore, the negative coupling breaks the symmetry between the two diagonally opposite splay vertices at $(0.5, 0.5)$, and $(-0.5, -0.5)$. In the first column of the first row, the splay vertex at $(0.5, 0.5)$ is "more defective" than the second splay vertex, in the sense that $|\mathbf{Q}|(0.5, 0.5) < |\mathbf{Q}|(-0.5, -0.5)$, and in the first column of the second row we see that $\phi \approx \frac{3\pi}{4}$ along $y = x$, for the corresponding $\mathbf{M}$-profile. Similarly, in the third column of the first and second rows, the splay vertex at $(-0.5, -0.5)$ of the D_1 solution is

more defective than the splay vertex at $(0.5, 0.5)$, and $\phi \approx -\frac{\pi}{4}$ along $y = x$, for the corresponding **M**-profile. Analogous remarks apply to the D_2 solution, with two splay vertices at $(-0.5, 0.5)$, and $(0.5, -0.5)$, respectively, with $\phi \approx \frac{\pi}{4}$, or $\phi \approx \frac{5\pi}{4}$, along $y = -x$. These can be seen in the second and fourth columns, of the first two rows, in Figure 6.6. The same reasoning applies to the 8 rotated solutions in the last four rows of Figure 6.6, for $c = -0.25$. Each of the rotated solutions for the **Q**-profile is distinguished by two splay defects along one of the square edges. For each rotated solution, we have $\theta \approx 0$, or $\theta \approx \frac{\pi}{2}$, at the square centre, which occurs when the two splay vertices are pinned to one of the edges, $y = \pm 0.5$ or $x = \pm 0.5$, respectively. Each possibility for the director angle generates two possibilities for the corresponding **M**-profiles, and the approximate value of ϕ, seen in the fourth and sixth rows of Figure 6.6. For example, $\phi \approx \frac{\pi}{2}$ or $\frac{3\pi}{2}$ if $\theta \approx 0$ at the square centre, for the **M**-profile, since negative c coerces θ and ϕ to differ by an odd multiple of $\frac{\pi}{2}$. For the same reason, $\phi \approx 0$ or π when $\theta \approx \frac{\pi}{2}$. The negative coupling further breaks the symmetry between the splay vertices, so that one vertex is "more asymmetric" than the other. This doubles the number of admissible rotated solutions. These heuristic arguments corroborate the existence of 8 rotated $(\mathbf{Q}, \mathbf{M})$-stable solution profiles for small ℓ, with $c = -0.25$.

Additionally, we find the Peppa solution branches with stable interior nematic defects, as with positive c. For $c < 0$, θ and ϕ tend to differ by an odd multiple of $\frac{\pi}{2}$ in the square interior, as $\ell \to 0$. In particular, this implies two choices for ϕ in the square interior, resulting in the Peppa$_{in}$ and Peppa$_{out}$ branches. There are two Peppa$_{in}$ solution branches, since the nematic defect pair can align along one of two square diagonals. Similarly, there are two Peppa$_{out}$ solution branches by the same reasoning. The case of negative coupling strongly enhances multistability for small ℓ, effectively doubling the number of admissible stable states compared to

positive coupling (compare Figures 6.5 and 6.9). We do not observe domain walls in $\mathbf{M}$ for negative coupling, rather we observe magnetic vortices at the square vertices, which are induced by the D and R nematic profiles. These corner defects may act as distinguished sites/binding sites for devices based on such NLC-MNP systems.

6.2.2 The $\ell \to \infty$ limit

The $\ell \to \infty$ limit is relevant for small nano-scale domains. Mathematically, this limit is much simpler than the $\ell \to 0$ limit, since we lose the nemato-magnetic coupling contribution, in this limit. Referring to [69], the leading order equations, in this limit, are:

$$\begin{aligned} \Delta \mathbf{Q} &= \mathbf{0}, \\ \Delta \mathbf{M} &= \mathbf{0}, \end{aligned} \tag{6.2.4}$$

subject to the Dirichlet conditions (6.1.6). The limiting solution is unique. It is straightforward to recover the WORS for the $\mathbf{Q}$-profile, and to show that there is a magnetic vortex of degree $+1$ at the square centre (with $\mathbf{M}(0,0) = 0$), for the $\mathbf{M}$-profile, in this limit. However, we see (at least numerically) that for $c \neq 0$, for sufficiently large but crucially, finite values of ℓ, we lose the cross structure of the WORS, and we have $|Q_{12}| \neq 0$ in the interior of the square. This is precisely the solution along the Ring branch for large ℓ, in the bifurcation diagrams in Figures 6.5 and 6.9, which is the unique energy minimizer in this limit. The Ring solution branch is distinguished by $Q_{11} = 0$ nodal lines, along the square diagonals, and $Q_{12} = 0$, along the coordinate axes, $\{x = 0\} \cup \{y = 0\}$, as shown in Figures 6.4 and 6.8.

Following the methods in [69], the limiting solution, $(\mathbf{Q}_\infty, \mathbf{M}_\infty)$, of (6.2.4) is an excellent approximation to the solutions, $(\mathbf{Q}_\ell, \mathbf{M}_\ell)$, of (6.1.2), for fixed c, subject to the same boundary conditions, for ℓ large enough i.e., $|(\mathbf{Q}_\ell, \mathbf{M}_\ell) - (\mathbf{Q}_\infty, \mathbf{M}_\infty)|^2 \sim \frac{1}{\ell^2}$. Hence, these solutions can be physically relevant for physically attainable, but large values of ℓ. The unique limiting solution, $(\mathbf{Q}_\infty, \mathbf{M}_\infty)$, remains an excellent approximation to the Ring solution, even for values of ℓ as small as unity. We demonstrate this by comparing two solutions along the Ring branch, for $\ell = 1$ and $\ell = 100$, denoted by $(\mathbf{Q}_1, \mathbf{M}_1)$ and $(\mathbf{Q}_{100}, \mathbf{M}_{100})$, respectively. The solution $(\mathbf{Q}_{100}, \mathbf{M}_{100})$ is effectively identical to the limiting solution, $(\mathbf{Q}_\infty, \mathbf{M}_\infty)$ described above, and serves as our *numerical* limiting solution. We define the components of $\mathbf{Q}_1, \mathbf{Q}_{100}, \mathbf{M}_1$, and $\mathbf{M}_{100}$, as:

$$
\begin{aligned}
(Q_{11}, Q_{12})|_{\ell=1} &= S_1(\cos 2\theta_1, \sin 2\theta_1), \\
(Q_{11}, Q_{12})|_{\ell=100} &= S_{100}(\cos 2\theta_{100}, \sin 2\theta_{100}), \\
(M_1, M_2)|_{\ell=1} &= R_1(\cos \phi_1, \sin \phi_1), \\
(M_1, M_2)|_{\ell=100} &= R_{100}(\cos \phi_{100}, \sin \phi_{100}).
\end{aligned}
$$

In Figure 6.10, we plot the $(\mathbf{Q}_1, \mathbf{M}_1)$ Ring solution profile, for $c = 0.25$, the constituent components Q_{11}, Q_{12}, M_1, M_2, and the differences between the director and magnetization orientation angles, given by $S_1 S_{100} \sin(2\theta_{100} - 2\theta_1)$ and $R_1 R_{100} \sin(\phi_{100} - \phi_1)$, respectively. We see that these differences are of the order of 10^{-4}, for both positive and negative values of c, from which we deduce that $(\mathbf{Q}_\infty, \mathbf{M}_\infty)$ is a reliable approximation to $(\mathbf{Q}_\ell, \mathbf{M}_\ell)$ along the Ring branch, for $\ell \geq 1$.

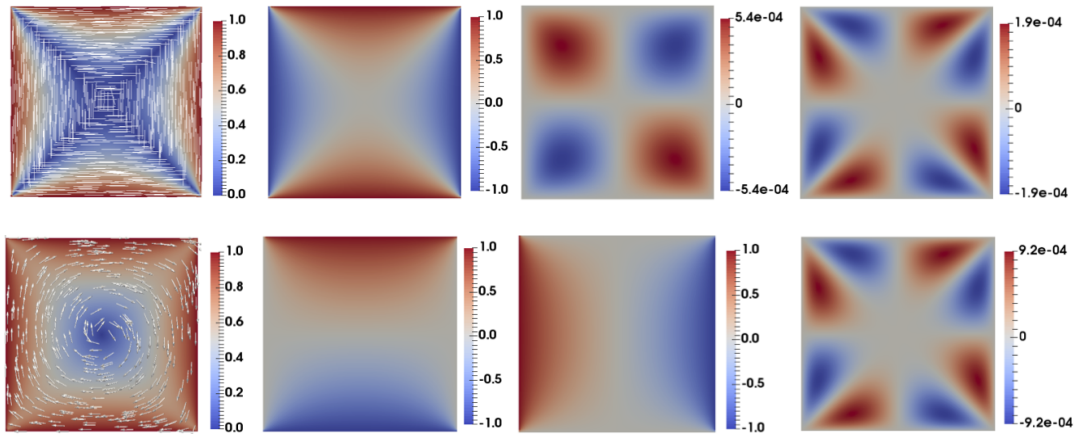

Figure 6.10: The Ring solution with $c = 0.25$. Plots in the first row from left to right are: $\mathbf{Q}_1$; the Q_{11} and Q_{12} components; and the difference $S_1 S_{100} \sin(2\theta_{100} - 2\theta_1)$. The second row from left to right shows: the corresponding $\mathbf{M_1}$; the M_1 and M_2 profile; and the difference $R_1 R_{100} \sin(\phi_{100} - \phi_1)$.

6.3 Ferronematics on 2D hexagons

Next, we consider a NLC-MNP suspension on a 2D regular hexagon, subject to the Dirichlet conditions for $\mathbf{Q}$ and $\mathbf{M}$ in (6.1.4) and (6.1.5), for $N = 6$ respectively. The purely nematic case, $c = 0$, has been well studied in [74]. For large $\ell_1 = \ell_2 = \ell$ and $c = 0$, there is a unique Ring solution on the hexagon, for which the corresponding $\mathbf{Q}$ and $\mathbf{M}$ profiles have a single +1-vortex at the centre of the well. This Ring solution branch loses stability as ℓ decreases. In the limit of small ℓ, with $c = 0$, there are at least 15 different stable states, with topologically trivial boundary conditions i.e.,

$$\deg(\mathbf{n}_b, \partial\Omega) = 0. \tag{6.3.1}$$

This represents the winding number, or *kink number* (referring to the terminology in [120]), of $\mathbf{n}_b$ considered as a map from $\partial\Omega$ into S^1, where $\mathbf{n}_b$ and $\mathbf{Q}_b$ are related

by the following:

$$\mathbf{Q}_b = \begin{pmatrix} Q_{11b} & Q_{12b} \\ Q_{12b} & -Q_{11b} \end{pmatrix} = (2\mathbf{n}_b \otimes \mathbf{n}_b - \mathbf{I})\,. \tag{6.3.2}$$

These 15 states are categorised by permutations of defects which are pinned to the hexagon vertices. There are 6 vertices, two of which have $+\frac{1}{3}$-charge (referred to as the *splay* vertices), and four of which have $-\frac{1}{6}$-charge (referred to as the *bend* vertices). We presented illustrations of the typical director orientation at the splay and bend vertices, in Figure 6.1. These 15 solutions are split into 3 rotationally invariant classes: (i) the 3 *Para* states, where the splay defects are opposite each other; (ii) the 6 *Meta* states, where the splay defects are separated by one vertex; and (iii) the 6 *Ortho* states, where the splay defects are connected by an edge. We give illustrations of the typical director orientation for a Para, Meta and Ortho state in a hexagon, in Figure 6.11.

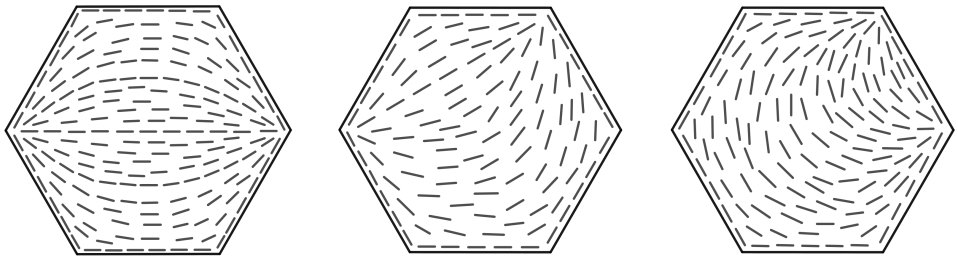

Figure 6.11: Nematic director orientation for the Para, Meta, and Ortho states in a hexagon.

In [74], the authors show that as ℓ decreases, the unique Ring solution bifurcates into either, the three stable Para states, or three unstable BD solution branches. The BD solutions in a hexagon, much like in a square, serve as transition states for the six Meta states, which gain stability, for ℓ small enough. As ℓ decreases further, they find the six stable Ortho states.

The main results of this section are as follows:

- Multistability is strongly enhanced in the negative coupling regime, as ℓ decreases, and the increase in the number of polygon vertices increases the number of potential defect sites.
- In the $c > 0$ regime, solutions with magnetic domain walls are hard to find for $\xi = 1$, and rely on a judicious interplay of ξ and c to be observed.

For a square domain, we observe diagonal (D) and rotated (R) solution branches for ℓ small enough, for $c = 0.25$, for which the corresponding $\mathbf{M}$-profile exhibits a domain wall either along a square diagonal, or along a square edge, respectively. These domain walls are characterized by a sharp drop in $|\mathbf{M}|$ compared to the surrounding values. It is evident that these domain wall $\mathbf{M}$-profiles are increasingly difficult to find in a hexagon for positive c, and in a pentagon as will be shown later. Therefore, in contrast to a square domain, we lose the Para, Meta, and Ortho solutions for $c > 0$. We will explore this in greater detail, but magnetic domain walls connecting pairs of diagonally opposite vertices for the Para-nematic state on a regular hexagon, have greater length than their corresponding counterparts on a square domain. Magnetic domain walls for Meta-nematic states have lesser symmetry. Heuristically, this may explain the absence of magnetic domain walls in stable $(\mathbf{Q}, \mathbf{M})$-profiles on a hexagon, with $c = 0.25$.

For positive c and ℓ small enough, we only recover three Peppa solution branches, featured by a pair of stable interior $+\frac{1}{2}$-nematic defects aligned along one of the hexagon diagonals, near the center of the hexagon. There are three hexagon diagonals, and hence there are three Peppa solution branches. The corresponding $\mathbf{M}$-profiles have a slightly smeared magnetic vortex along the line connecting the

nematic defect pair. We can find the three Para solutions, for very small values of c, but they quickly bifurcate into the Peppa solutions. To understand how the splay defects evolve in the Para solution branch for $c > 0$, we use the Para-nematic solution (for $c = 0$) as an initial condition, for small values of $c = 5, 6, 7 \times 10^{-3}$, $\ell = 10^{-4}$, to trace the Para branch using continuation methods. We present the **Q**-profile of the numerical solutions in Figure 6.12. As we move from left to right i.e., from $c = 5 \times 10^{-3}$ to $c = 7 \times 10^{-3}$, it is clear that the defects detach from the splay vertices as c increases, and migrate towards the hexagon interior, aligning on one of the hexagon diagonals. The interior nematic defects localise near the centre of the hexagon, yielding the Peppa solution branches. The Peppa solution branches are clear examples of nematic profiles being tailored by the magnetic profile. Namely, the central magnetic vortex coerces the creation of two $+\frac{1}{2}$-stable interior nematic defects, due to the positive nemato-magnetic coupling that favours co-alignment of **n** and **M**.

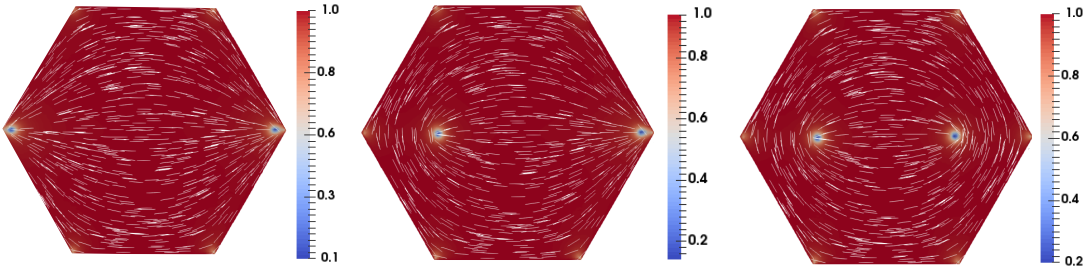

Figure 6.12: The nematic **Q**-profile for $\ell = 10^{-4}$ and (from left to right) $c = 5, 6, 7 \times 10^{-3}$, respectively.

In Figure 6.13, we track the different solution branches as a function of ℓ, with $c = 0.25$, using the Ring solution, the Para, Meta and Ortho states as initial conditions for the **Q**-solver. The Ring branch exists for all $\ell > 0$, is unique and globally stable for ℓ large enough, but loses stability as ℓ decreases, as expected by analogy with the $c = 0$ case. For ℓ small enough, we obtain the three stable Peppa

solution branches, but we find no other stable configuration in this parameter regime. Equally, our numerical methods are not exhaustive, and we may have omitted certain solution branches e.g., high energy Meta and Ortho solution branches. To visualize the different solution branches, we plot the two measures (6.1.8), versus ℓ.

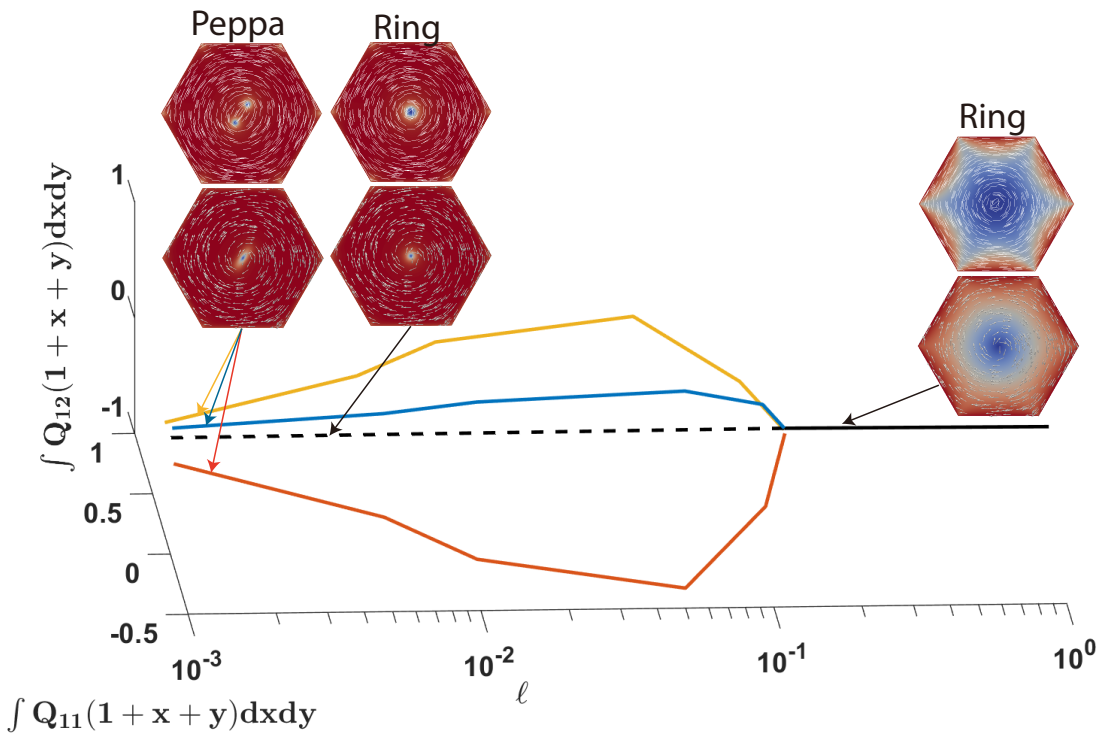

Figure 6.13: Bifurcation diagram for (6.1.1) as a function of ℓ on a hexagon domain with $c = 0.25$.

In the preceding simulations, we have assumed $\xi = 1$ in (6.1.1). We conjecture that smaller values of ξ will coerce the $\mathbf{Q}$-profile to tailor the $\mathbf{M}$-profile, for $c > 0$ i.e., the $\mathbf{M}$-texture will be determined by $\mathbf{n}$, leading to the creation of domain walls in $\mathbf{M}$. A smaller value of ξ suppresses the magnetic energy and hence, the nematic effects dominate in this regime. The domain walls are essentially a consequence of the topologically non-trivial boundary conditions for $\mathbf{M}$, so that $\mathbf{n}\cdot\mathbf{M} \approx 1$ on one side of the wall, and $\mathbf{n}\cdot\mathbf{M} \approx -1$ on the other side of the wall i.e.,

ϕ jumps by π radians across the domain wall. In Figure 6.14, we take $\xi = 0.01$, $\ell = 5\times10^{-4}$, and use the Para, Meta and Ortho-nematic solutions (for $c = 0$), and the **M**-solution with a central magnetic vortex (for $c = 0$), as initial conditions. We do indeed recover the Para solution for the **Q**-profile, with two defects pinned at a pair of diagonally opposite splay vertices, and the corresponding **M**-profile has a clear domain wall along the diagonal connecting the splay vertices, for $c \leq 0.02$. Analogous remarks apply to the Meta solutions, for which the **M**-profile has a distinct domain wall along the line connecting the two splay vertices. In other words, we can numerically find Meta solutions for which the **Q**-profile has two splay vertices (separated by a vertex), and **M** has an associated domain wall, for $0 < c \leq 0.02$. The Ortho solutions are easier to find for small ξ, with a short magnetic domain wall along the hexagon edge connecting the two adjacent splay vertices in the **Q**-solution. We find these Ortho solutions by continuation methods for $c \leq 1$. This domain wall is hard to see in our numerical simulations as the sharp reduction in $|\mathbf{M}|$ occurs extremely close to the edge of the domain. However, we can clearly see that (M_1, M_2) (presented by white arrows in the **M**-profile plot) does not satisfy the boundary conditions (6.1.5) along this edge, and a magnetic domain wall is required in order to remedy this constraint.

We also note that these small ℓ solutions (in Figure 6.14) converge to different values of S, and $|\mathbf{M}|$, in the hexagon interior away from domain walls. This is because, in the $\ell \to 0$ limit, minimizers of (6.1.1) with $\xi \neq 1$ converge to appropriately defined minimizers $(\mathbf{Q}^*, \mathbf{M}^*)$, with $|\mathbf{Q}^*| = \sqrt{2}S_c$, $|\mathbf{M}^*| = R_c$, where

$$S_c = \left(\frac{|c|}{4} + \sqrt{\frac{c^2}{16} - \frac{1}{27}\left(1 + \frac{c^2}{2\xi}\right)^3}\right)^{1/3} + \left(\frac{|c|}{4} - \sqrt{\frac{c^2}{16} - \frac{1}{27}\left(1 + \frac{c^2}{2\xi}\right)^3}\right)^{1/3};$$

$$R_c = \sqrt{\frac{|c|}{\xi}S_c + 1}.$$

Therefore, when $\xi = 0.01$ and $c = 0.02$, we have $S_c \approx 1.0$ and $R_c \approx 1.74$ (as seen in the plots of the Para and Meta solutions in Figure 6.14), and when $c = 1$, we have $S_c \approx 7.15$ and $R_c \approx 26.8$ (as seen in the Ortho solution in Figure 6.14). The reason S and $|\mathbf{M}|$ do not achieve their maximum colorbar value in the hexagon interior for the Ortho solution is due to numerical noise.

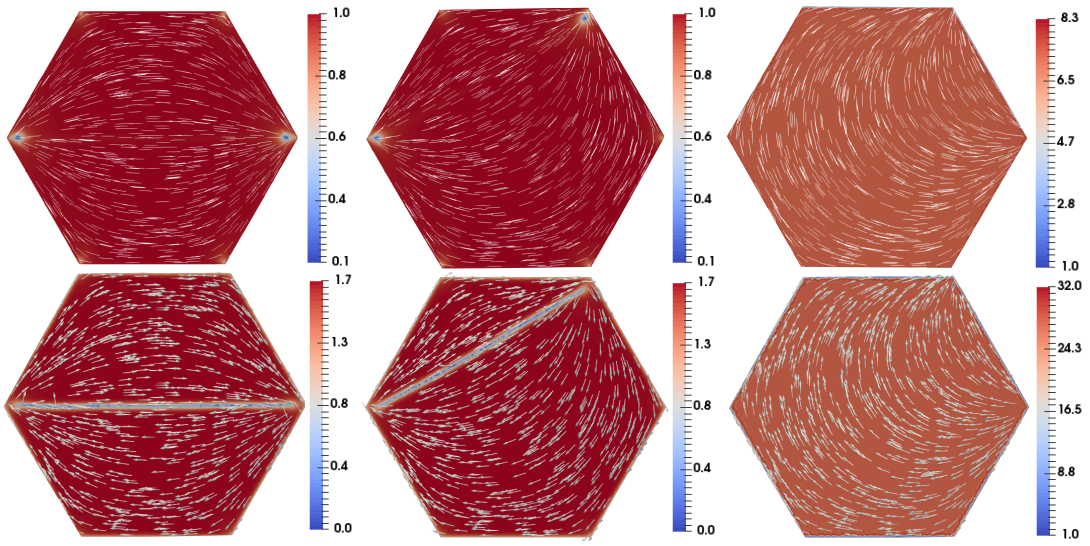

Figure 6.14: Para and Meta solution profiles for $c = 0.02$ and Ortho solution profile for $c = 1$, respectively with $\xi = 0.01$ and $\ell = 5 \times 10^{-4}$.

We now focus on the negative c regime in a hexagon. Here, as with a square domain, we effectively double the number of stable states, in the small ℓ limit, due to the broken symmetry between the splay vertices. We numerically observe six Para, twelve Meta, and twelve Ortho-nematic states. The corresponding $\mathbf{M}$-profiles are distinguished by the location of the magnetic vortex at one of the hexagon vertices (six possibilities) and the orientation of $\mathbf{M}$, since $\mathbf{M}$ is preferentially perpendicular to $\mathbf{n}$ in the hexagon interior, for $c < 0$. For example, there are six Para $(\mathbf{Q}, \mathbf{M})$-states, corresponding to six possibilities for the location of the, more asymmetric, splay vertex. For $c = 0$, there are six Meta stable states

for ℓ small enough, with two splay vertices separated by a vertex. When $c < 0$, the symmetry between the splay vertices is broken, and we obtain two stable Meta states for each admissible *splay vertex pair*, yielding a total of 12 Meta states. Analogous remarks apply to the Ortho solution branch.

We also observe three Peppa$_{in}$ and Peppa$_{out}$ solution branches, for ℓ small enough and $c < 0$, with pairs of stable interior $+\frac{1}{2}$-nematic defects along one of three hexagon diagonals. The *in*-branches refer to inwards-pointing $\mathbf{M}$-profiles, and *out*-branches refer to outward-pointing $\mathbf{M}$-profiles, from the central magnetic vortex. In Figure 6.15, we plot a Peppa$_{in}$ and Peppa$_{out}$ solution (the $(\mathbf{Q}, \mathbf{M})$ profiles), for $c = -0.1$, with $\xi = 1$ and $\ell = 5 \times 10^{-4}$.

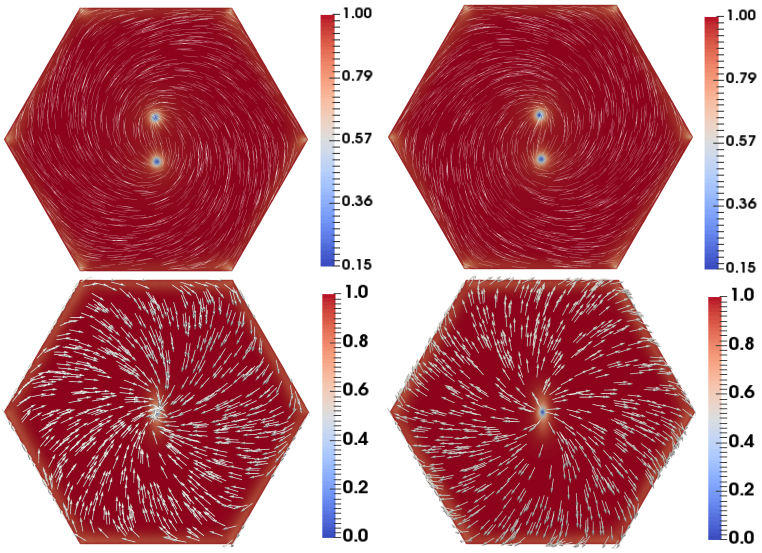

Figure 6.15: Peppa$_{in}$ and Peppa$_{out}$ solution profiles (from left to right) for $c = -0.1$, with $\xi = 1$, and $\ell = 5 \times 10^{-4}$.

In Figure 6.16, we plot the solution landscape on the re-scaled hexagon, as a function of ℓ, for $c = -0.25$. As before, we have a unique and globally stable Ring solution branch for large ℓ, which exists for all $\ell > 0$, and loses stability as ℓ decreases. As with a square domain, the Ring branch bifurcates into the six Para states, for ℓ small enough. Then as we decrease ℓ, we find the three Peppa$_{in}$ and three Peppa$_{out}$ solution branches, which are disconnected in our numerical simulation, which may possibly be a shortcoming of the numerical method which is not picking up on higher energy configurations, or transition states. For ℓ smaller, we find the 12 Meta solution branches which are again disconnected. For $\xi = 1$ and negative coupling, we can only find the stable Ortho solutions for very small values of ℓ. In order to find these states numerically, for $\ell \sim 10^{-4}$, we must reduce ξ, as in Figure 6.14 for the $c > 0$ case. We do not find the 12 Ortho states for $c = -0.25$ and $\ell > 10^{-4}$, and so they do not appear in our bifurcation diagram.

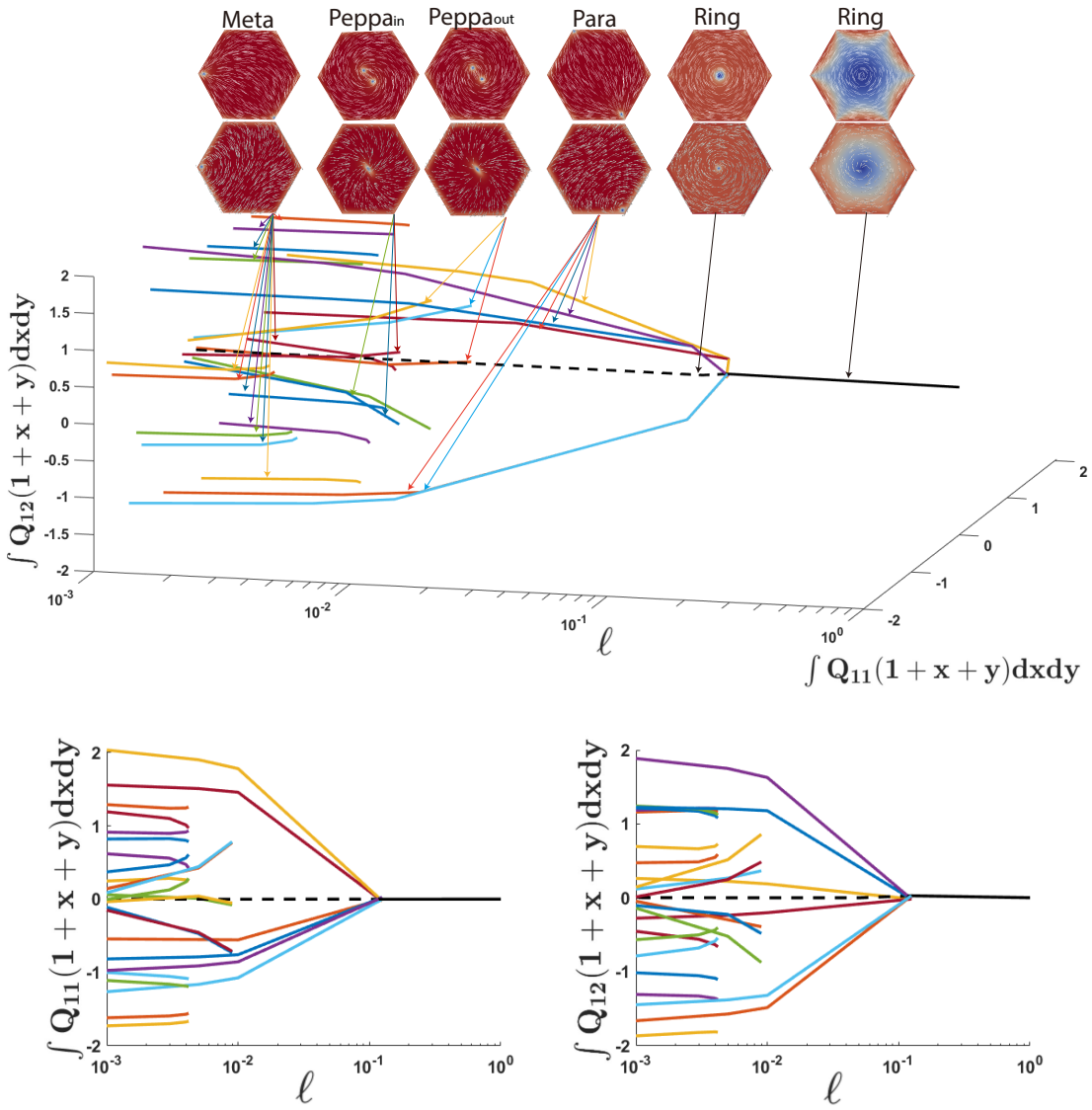

Figure 6.16: Bifurcation diagram for (6.1.1) on a hexagon domain as a function of ℓ with $c = -0.25$.

We deduce that we can stabilise either interior nematic point defects, or magnetic domain walls, depending on a judicious interplay of ξ and c, and this interplay depends on N - the number of sides of the regular polygon. We will now investigate the extent to which N can tailor the multistability of this ferronematic composite system. So far we have studied $N = 4, 6$, with high degrees of symmetry, and thus it is a natural extension to consider a domain with an odd number for N.

6.4 Ferronematics on 2D pentagons

We now consider a regular pentagon, with $N = 5$, and study the solution landscape as a function of ℓ, for positive c and negative c, respectively. The case of $c = 0$ has been well studied in [74]. For $c = 0$ and ℓ large enough, there is a unique Ring solution for the **Q**-solution (with a central +1-nematic defect), and a unique **M**-profile with a degree +1 central vortex. This Ring branch is globally stable for ℓ large enough, exists for all $\ell > 0$, and is unstable for ℓ small enough. For small ℓ, there are at least 10 different stable solutions (with $c = 0$) for the **Q**-solutions, for topologically trivial boundary conditions (6.3.1). As with the hexagon, the tangent boundary conditions, (6.1.4), naturally create a mismatch in $\mathbf{n}_b$ at the pentagon vertices, so that the vertices are natural candidates for nematic defects. The different vertices are classified as "splay" and "bend" vertices, as presented in Figure 6.1, and there are two splay, and three bend vertices for topologically trivial boundary conditions in a pentagon. The 10 solutions are classified into 2 rotationally invariant classes: (i) the 5 Meta states, where the splay vertices are separated by one vertex; and (ii) the 5 higher energy Ortho states, where the splay vertices are connected by an edge. In [74], the authors show that for ℓ small enough, the unique Ring solution bifurcates into either one of the five stable Meta states, or one of five unstable BD solutions. For ℓ even smaller, they find the five stable Ortho states. We give illustrations of the typical director orientation for a Meta and Ortho state in a pentagon, in Figure 6.17.

The main results of this section show that:

- Solutions with magnetic domain walls are easier to find in a pentagon than for a hexagon, indicating that they are observable for $\xi < \xi(N)$ and $0 < c < c(N)$, where N is the number of polygon edges.

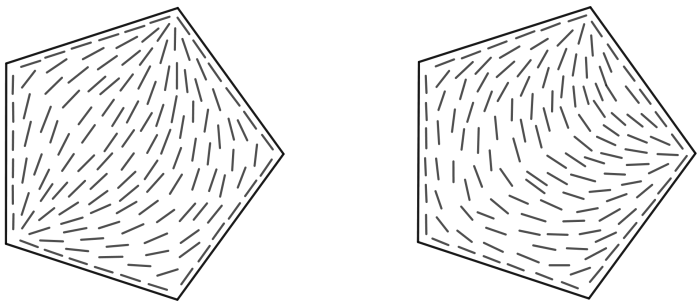

Figure 6.17: Nematic director orientation for the Meta, and Ortho states in a pentagon.

- There exist solutions with a pair of $+\frac{1}{2}$ interior nematic point defects, for ℓ small enough, coerced by the interior magnetic vortex at the center of the well, and these defects align parallel to a polygon edge due to the loss of symmetry for N odd.

For positive c in a hexagon, solutions which preserved the nematic profile, and exhibit magnetic domain walls (with reduced $|\mathbf{M}|$), were hard to find. We could only find solutions of this type for c, and ξ, small enough. Domain walls are easier to find in pentagons. In Figure 6.18, we recover the Meta and Ortho-nematic states in a pentagon, with $c = 0.05$ for $\xi = 1$, and ℓ small enough, which is not observed in a hexagon. For c small enough, the nematic profile is maintained, and the corresponding $\mathbf{M}$-profiles exhibit domain walls along straight lines connecting the splay vertices. We take the Meta and Ortho-nematic solutions on a pentagon for $c = 0$ as the initial guesses, and fix $\ell = 5 \times 10^{-4}$ and $\xi = 1$.

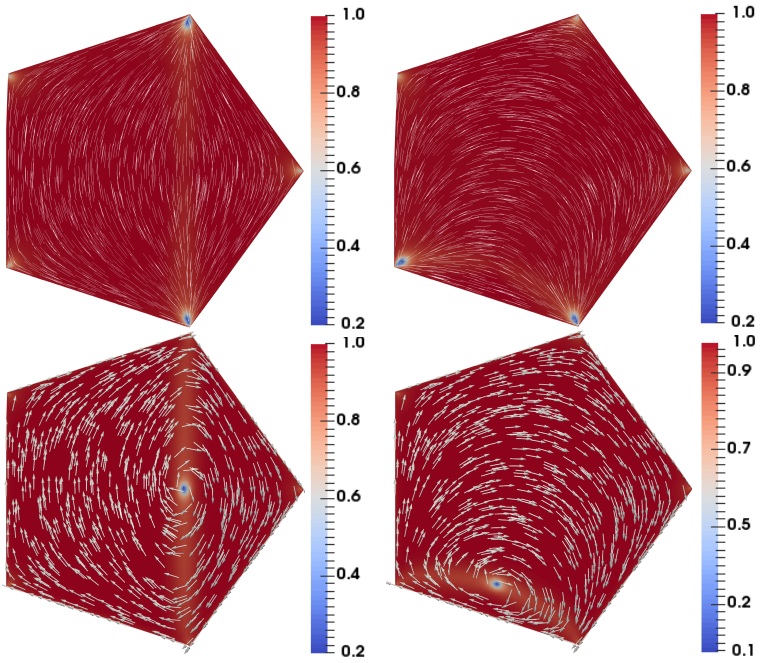

Figure 6.18: Meta and Ortho solutions in a pentagon for $c = 0.05$, $\ell = 5 \times 10^{-4}$.

As we increase c, the qualitative features are similar to those for a hexagon. We lose the Ortho and Meta states, and obtain stable Peppa solution branches for ℓ small enough, with two stable interior $+\frac{1}{2}$-nematic defects. For each Peppa branch, the nematic defect pair is localised near the centre of the pentagon, parallel to one of the pentagon edges. For this reason, we find five rotationally equivalent stable Peppa solutions, for $c > 0$. These solutions are similar to the Peppa solutions in a square and hexagon, as the magnetic profile retains the central vortex, and are examples of nematic profiles tailored by the magnetic profile. In Figure 6.19, we plot the bifurcation diagram for the $(\mathbf{Q}, \mathbf{M})$-solutions in a pentagon as a function of ℓ, for $c = 0.25$. For ℓ large enough, we find the unique globally minimizing Ring branch, which loses stability for ℓ small enough, as in a hexagon. For $c = 0.25$ and $\xi = 1$, the Ring solution branch bifurcates into the five Peppa solution branches, for ℓ large enough. We distinguish the solution branches by plotting the measures (6.1.8), versus ℓ.

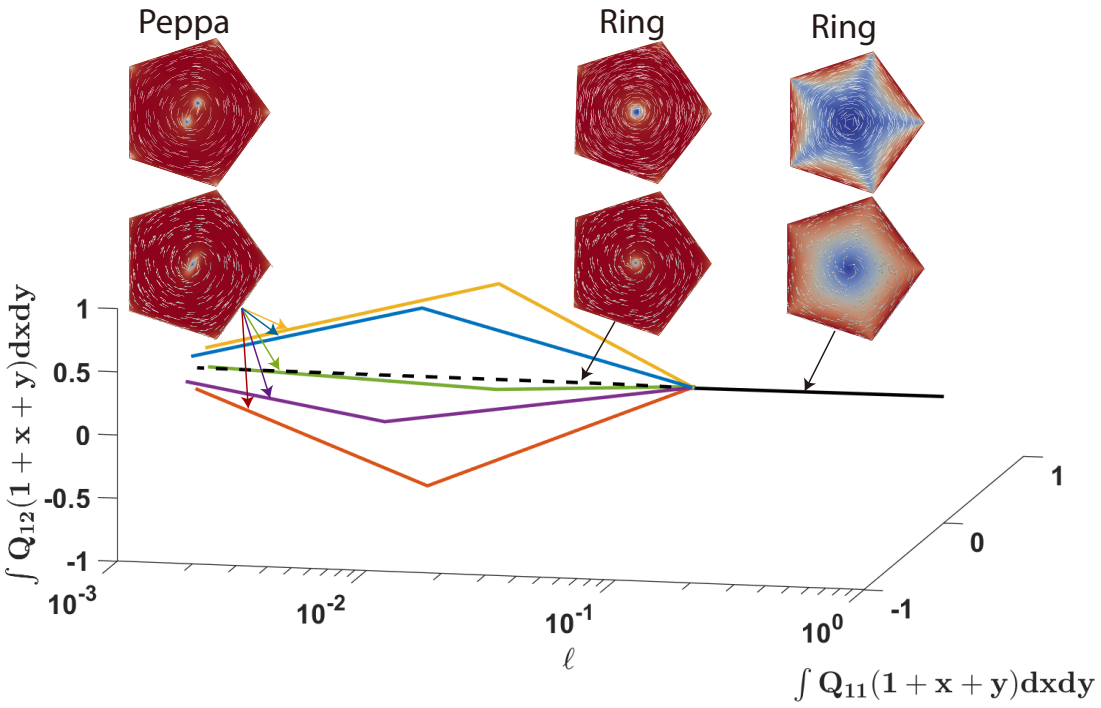

Figure 6.19: Bifurcation diagram for (6.1.1) as a function of ℓ on a pentagon domain with $c = 0.25$.

The case of negative c is similar to the square and hexagon. The preferential perpendicular co-alignment between $\mathbf{n}$, and $\mathbf{M}$, essentially doubles the number of admissible stable states for negative coupling, in the $\ell \to 0$ limit. This provides an ingenious mechanism for stabilising exotic point defects at polygon vertices and in the interior, which could offer novel optical and material responses for future applications. As described in Section 6.2.1 for the square, we lose the symmetry between the splay vertices, and for small ℓ. In Figure 6.20, we plot the bifurcation diagram for the $(\mathbf{Q}, \mathbf{M})$-solutions as a function of ℓ, for $c = -0.25$. For ℓ large enough, we have the unique Ring solution, and this solution loses its stability for ℓ small enough. The Ring solution branch bifurcates into the stable Meta solution branches and, for ℓ smaller, we find the Peppa$_{in}$, Peppa$_{out}$ and Ortho solution branches. The symmetry breaking of the splay vertices means we have 5

stable Peppa$_{in}$, 5 stable Peppa$_{out}$, 10 Meta and 10 Ortho stable solution branches. These classes of solutions are analogous to those in a hexagon, for $c < 0$.

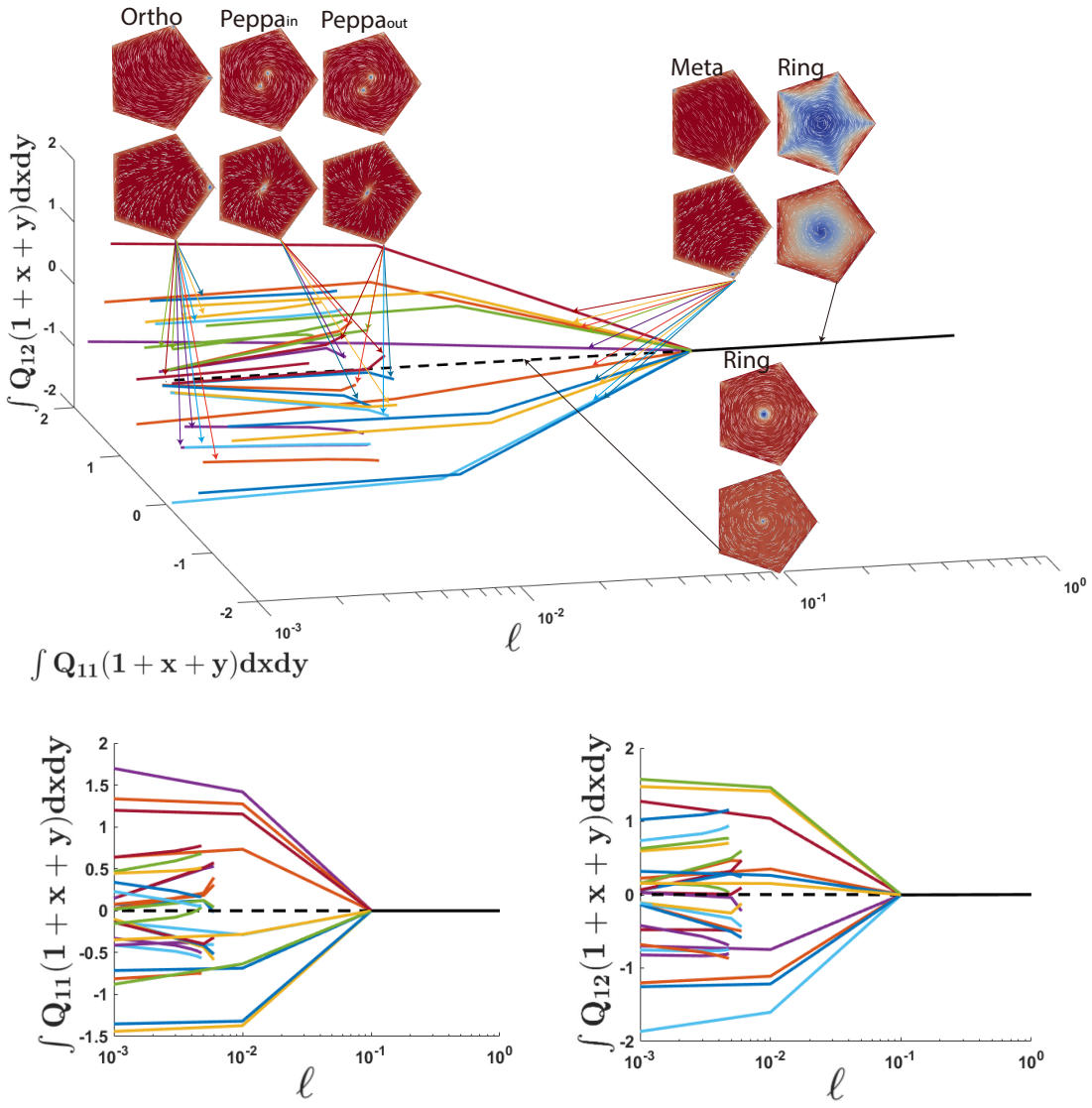

Figure 6.20: Bifurcation diagram (6.1.1) as a function of ℓ on a pentagon domain with $c = -0.25$.

6.5 Summary

In this chapter, we have studied 2D systems with nematic orientational order, and directional magnetic order, on regular 2D polygons, with Dirichlet conditions for $\mathbf{Q}$, and $\mathbf{M}$, on the polygon edges. The Dirichlet conditions are special in the sense that we impose a topologically non-trivial boundary condition on $\mathbf{M}$, which necessarily creates an interior magnetic $+1$-vortex for the $\mathbf{M}$-profiles. Our work is motivated by dilute ferronematic suspensions in 2D frameworks (see [80], [81], [83]), and we study observable, physically relevant states, in terms of local or global minimizers of an appropriately defined free energy. This approach may apply more widely to model systems with polar, and apolar, order parameters. The free energy has three contributions - a nematic energy, a magnetic energy, and a nemato-magnetic coupling energy. There are four phenomenological parameters in the free energy and, with some assumptions, we study the interplay between two parameters: a re-scaled elastic constant, ℓ, and a nemato-magnetic coupling parameter, c. We study the solution landscapes on a 2D square, hexagon, and pentagon, in terms of bifurcation diagrams for $c = 0.25$ and $c = -0.25$, as a function of ℓ. The asymptotics for large ℓ are well understood in terms of the Ring branch, since there is a unique critical point/global minimizer of the free energy, in the $\ell \to \infty$ limit. As ℓ decreases, the multiplicity of stable $(\mathbf{Q}, \mathbf{M})$-solutions increases, and the solution landscape becomes increasingly complicated. The multistability can be partially understood for small ℓ (which correspond to "large" domains on the micron scale or larger) in terms of boundary-value problems for ϕ, and relations between θ and ϕ, which define the nematic director and magnetization vector, respectively.

For $c = 0$ and ℓ small enough, the polygon vertices act as defect sites for stable **Q**-profiles and in fact, there are at least $\frac{N(N-1)}{2}$ stable **Q**-states, on a regular polygon with N sides. For positive c, that favours co-alignment between **n** and **M**, the number of stable states decreases as c increases, as $\ell \to 0$. In fact, we conjecture that there are only N stable states on a polygon with N sides, for odd N, and only $\frac{N}{2}$ stable states for a polygon with N sides, for N even, in the $\ell \to 0$ limit, and for large c. These stable states are featured by a pair of stable interior $+\frac{1}{2}$-nematic point defects in the polygon interior, aligned either parallel to a polygon edge (N odd), or along a polygon diagonal (N even). As $N \to \infty$ and $\ell \to 0$, we recover the solution landscape on a circle, with tangent boundary conditions for the **Q**-profiles: infinitely many stable states, with an interior nematic defect pair along one of the circle diagonals [121], for $c > 0$, and these states cannot be obtained for $c = 0$. The **M**-profiles are less affected in the regime of $c > 0$ and small ℓ, as they retain the interior central magnetic vortex, with some distortion. We refer to these novel solution branches, with interior nematic defect pairs, as Peppa solution branches for $c > 0$ and small ℓ. Informally speaking, positive c has the same effect as regularising the boundary, or rounding off the vertices, so that the nematic defects detach from the polygon vertices and localise near the polygon centre. Stable domain walls are observed in the **M**-profile, for very small positive values of c, or small values of ξ, whilst the corresponding **Q**-solutions retain their nematic profiles with defects pinned at the polygon vertices. We deduce that we can stabilise either interior nematic point defects, or magnetic domain walls, depending on a judicious interplay of ξ and c, and this interplay depends on N - the number of sides of the regular polygon. A reasonable conjecture is that magnetic domain walls are observable for $\xi < \xi(N)$, and $0 < c < c(N)$, for the boundary conditions in (6.1.4) and (6.1.5). We expect

that $\xi(N)$ and $c(N)$ are decreasing functions of N i.e., $\xi(N) \to 0$, $c(N) \to 0$ as $N \to \infty$, so that domain walls are increasingly difficult to find for coupled systems.

The case of $c < 0$, that favours $(\mathbf{n} \cdot \mathbf{M}) = 0$ in the polygon interior, is more complicated. The picture in the $\ell \to \infty$ limit (small nano-scale domains) is qualitatively unchanged in terms of the unique Ring solution branch, but $c < 0$ strongly enhances multistability in the $\ell \to 0$ limit. We obtain stable solution branches with interior defects for both $\mathbf{Q}$ and $\mathbf{M}$, and additionally, we also find stable solution branches with point defects at the polygon vertices in both the nematic and magnetic profiles. These solution branches with vertex defects, and interior defects, co-exist, and could offer exciting optical and electro-magnetic responses to light and external fields. Of course, the experimental tuning of c is expected to be hugely challenging and perhaps a material property, and we expect the case of positive c to be more common in applications than negative c. As mentioned in Section 6.1, one might expect $\ell_2 << \ell_1$ for a dilute ferronematic system. We have carried out preliminary numerical investigations by varying the ratio $\frac{\ell_2}{\ell_1}$, with $\ell_1 = 0.005$, $c = 0.25$, $\xi = 1$. As this ratio decreases from unity, the defects in the Peppa solution branch move towards the vertices, and we recover the Para-nematic solution branch on a hexagon, which is not attainable for $\ell_2 = \ell_1$ and $c = 0.25$. However, we recover the Peppa solution branch for $\ell_2 << \ell_1$, for large enough values of c. Hence, we argue that the solution branches for $\ell_1 = \ell_2$ survive for $\ell_2 << \ell_1$, for large values of c.

Our study is by no means exhaustive, but it does illustrate some generic features of positive and negative c, and the roles of ℓ and the geometry, in terms of N. We do not comment on physical relevance at this stage, but our methods have applications to generic systems, with multiple order parameters, of which dilute

ferronematics are an example [78], [82], [119]. Our numerical findings suggest that we will observe multistability in this regime, with co-existence of stable solutions supporting a variety of singular structures: magnetic domain walls, stable interior magnetic and nematic defects, and boundary vortices, all of which depend on a subtle interplay between N, c and ℓ. It may also be possible to stabilise multiple interior defect pairs, or interior and boundary vortices simultaneously, with a judicious interplay of the model parameters. Of course, we have neglected a number of crucial physical considerations e.g., elastic anisotropy, dipolar interactions, weak anchoring, mixed anchoring, the topology of the boundary conditions and flow effects, all of which offer new horizons for complex systems and tailor-made applications.

Chapter 7

The nematic-isotropic phase transition for a stochastic bulk potential

In this short chapter, we model the classic bifurcation analysis of the nematic-isotropic phase transition, as a function of temperature, within a stochastic modelling framework. Following the theory of stochastic elasticity, introduced in the papers by Mihai et al. [58], [59], we treat certain material-dependent terms as random variables following a non-Gaussian distribution. We then study the effects of stochasticity on the Landau-de Gennes order parameter, as a function of the temperature, and how this influences the well-studied deterministic nematic-isotropic phase transition in the Landau-de Gennes theory. In this preliminary research, we will show that within this stochastic framework, the nematic-isotropic transition, which occurs at some critical temperature in a deterministic setting, is modelled by a probability distribution which quantitatively describes the 'likelihood' of

observing an ordered nematic or isotropic fluid phase. This is believed to be of wider interest as the material-dependent parameters, for which the classic bifurcation analysis depends on, are difficult to measure in practice, and introduce an inherent degree of randomness to the system.

We consider uniaxial $\mathbf{Q}$-tensors of the form $\mathbf{Q} = s(\mathbf{n} \otimes \mathbf{n} - \frac{\mathbf{I}}{3})$, where $s \in \mathbb{R}$ is the scalar order parameter which measures the degree of orientational order about the director, $\mathbf{n} \in S^2$. We consider one of the simplest modelling scenarios in the Landau-de Gennes theory - the nematic-isotropic phase transition for the fourth order thermotropic bulk potential, $f_b(\mathbf{Q})$, given by (1.4.6). We recall the following results on minimizers of this bulk potential, from Section 1.4.2, in the deterministic setting: when $A > \frac{B^2}{24C}$, the isotropic fluid phase, characterized by $s = 0$, is the unique global minimizer of f_b; for $0 < A < \frac{B^2}{24C}$, f_b is minimized by either the isotropic state or a continuum of uniaxial nematic states with $s = s_+$ and; for $A < 0$, the isotropic state loses its stability.

7.1 Stochastic problem formation

We next consider a stochastic version of this minimization problem. Consider a large number of NLC samples. Following the approach of [58], [59], we assume that the material-dependent constants, B (which are experimentally measured material-dependent quantities, [9]), are distributed according to a known probability function which appropriately models inherent uncertainties of this parameter using only the available information of the mean value, and the variance, of the measurements. For mathematical simplicity, we do not consider a liquid crystalline system with spatially inhomogeneous terms, such as the inclusion of an elastic energy density term. Furthermore, we do not wish to introduce any thermal

fluctuations by treating the temperature-dependent parameter A as a random variable in this framework. As a simplest proof of concept study, we consider this unbounded modelling problem for liquid crystals where either parameter, $B > 0$ or $C > 0$, could be redefined in this way. We assume for any given temperature, the parameter B is a second-order random variable, with finite mean value and finite variance. To this end, we assume that

$$\mathbb{E}[B] = \bar{B} > 0, \quad \mathbb{E}[\log B] = \nu, \quad \text{such that} \quad |\nu| < +\infty. \tag{7.1.1}$$

We do not believe there to be any physical relevance of the quantity ν, but simply we restrict the variance of the data for measured values of B to be finite. Following the approach in [87], and the related papers in [58], [59], we base our stochastic model on the notion of entropy of discrete probability distributions initially introduced by [122], and employ the maximum entropy principle for a discrete probability distribution, introduced by [86] i.e., of all the choices of probability distribution that encode prior data, the best choice is the one with largest entropy. Under the above constraints, we have that the material-dependent parameter, B, follows a Gamma probability distribution with hyperparameters $\rho_1, \rho_2 > 0$, satisfying

$$\bar{B} = \rho_1 \rho_2, \quad \text{Var}(B) = \rho_1 \rho_2^2.$$

The corresponding probability density function takes the form [84]

$$g(B; \rho_1, \rho_2) = \frac{B^{\rho_1 - 1} e^{-B/\rho_2}}{\rho_2^{\rho_1} \Gamma(\rho_1)}, \quad \text{for} \quad B > 0, \tag{7.1.2}$$

where $\Gamma : \mathbb{R}_+^* \to \mathbb{R}$ is the complete Gamma function:

$$\Gamma(z) = \int_0^{+\infty} t^{z-1} e^{-t} \, \mathrm{d}t.$$

We consider only the nematic-isotropic transition problem for uniaxial **Q**-tensors, but other phase transitions can be studied in this way. Assuming $A > 0$ that is, temperatures above the nematic super-cooling temperature, and that the material-dependent parameter, B, follows the Gamma distribution defined by (7.1.2), with hyperparameters $\rho_1, \rho_2 > 0$, then the probability of observing the isotropic state only, at a given temperature A, is given by

$$P_1(A) = \int_0^{\sqrt{24AC}} g(B; \rho_1, \rho_2)\, \mathrm{d}B, \tag{7.1.3}$$

since it is the unique stable state in the range $A > \frac{B^2}{24C}$ i.e., $0 < B < \sqrt{24AC}$. Since both the ordered nematic state, and isotropic state, are stable in the lower temperature range $0 < A < \frac{B^2}{24C}$ i.e., $\sqrt{24AC} < B < \infty$, the probability of observing two states, at a given temperature A, corresponds to

$$P_2(A) = 1 - P_1(A). \tag{7.1.4}$$

From our understanding of the deterministic model, we would expect a high probability of observing just one solution (the isotropic fluid state) for higher temperatures, and we expect a high probability of observing two solutions (either the isotropic or ordered nematic states) for temperatures near the nematic super-cooling temperature. At temperatures below the nematic super-cooling temperature ($A < 0$), the isotropic state loses its stability, however the ordered nematic state corresponding to $s = s_-$ is metastable in this temperature range. Therefore, the probability of observing two possible NLC states, for $A < 0$, approaches unity, which is what we see as we extend our results for $A > 0$ to the negative A region ($P_2(0) = 1$).

7.2 Numerical results

For a given temperature A, we simulate the nematic-isotropic transition. In our simulations, we have $\rho_2 = \frac{\bar{B}}{\rho_1}$, and use fixed values for $\bar{B}$ and $\rho_1 > 0$. These values would, in practice, be determined by the data obtained but, for now, we fix $\rho_1 = 40$, and $\bar{B} = 0.64 \times 10^4$ [1]. We sample a number of Gamma distributed values for B to simulate and plot a cumulative distribution function of the two possible configurations. Again, in practice, the number of samples would be given by the number of experimental observations. In our cumulative distribution plot, we take the number of samples to be 100. We also include a tally of the number of randomly generated samples that observe one (or two) solutions, as a function of the temperature. This is calculated by the percentage of samples with A above (or below) $\frac{B^2}{24C}$, where B is Gamma distributed. As a direct comparison with these simulated results, we plot the probabilities (7.1.3) and (7.1.4). What we see is a clear competition between states across the nematic-isotropic transition temperature. This competition is so far just for illustrative purposes, as the probability distribution is heavily dependent on the variance of the data. In Figure 7.1, we plot the analytical and simulated probabilities of observing either one, or two, NLC states, as a function of the temperature, $A > 0$. We take $C = 0.35 \times 10^4$ and so the deterministic phase transition occurs at $A = \frac{\bar{B}^2}{24C} \approx 490$.

In the deterministic case, the possible equilibria of the thermotropic bulk potential are well understood. However, if we are to assume that B follows the Gamma distribution given by (7.1.2), then the bifurcation diagram is far from complete. In our numerical simulations, we produce a stochastic bifurcation diagram as a probability distribution, for the various nematic states, as a function of temper-

[1] $\bar{B}$ and ρ_1 would be determined by experimental data and our choices are simply for numerical fitting.

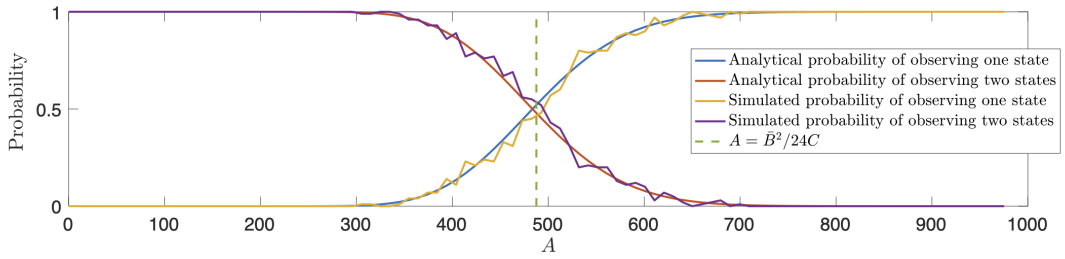

Figure 7.1: Probability distributions (7.1.3) and (7.1.4) given by the blue and red solid lines, respectively. Simulated data is given by the yellow and purple lines. The vertical dashed line represents the (deterministic) nematic super-heating temperature, $A = \frac{\bar{B}^2}{24C}$.

ature, which is presented in Figure 7.2. The probability of observing either the isotropic or nematic phase is also dictated by the relative energy well depths of the thermotropic bulk potential. In the deterministic model, between the super-heating temperature and the super-cooling temperature ($0 < A < \frac{B^2}{24C}$), there is a competition between the isotropic state and the ordered nematic state. In our stochastic model, we assume that the probability of finding an ordered nematic state, over the isotropic state, is

$$\mathbb{P} = \frac{f_b(s_+) - f_b(s_-)}{f_b(s_+) + f_b(0) - 2f_b(s_-)} \times 100\%, \tag{7.2.1}$$

where B follows the Gamma distribution (7.1.2). This represents the depth of the ordered nematic state critical point as a percentage of the total depths of the two possible states. Therefore, when $A = \frac{B^2}{27C}$ and the two states have equal energies, the probability is 50%. As expected, we see that $s = 0$ is for large values of A, but as we approach $A = \frac{\bar{B}^2}{24C}$, there is a competition between the possible states. As A decreases, the probability of observing the isotropic state decreases and, for A small enough, we only observe the ordered nematic state. Since the order parameter of the nematic state depends on the material-dependent

parameter B, the probability distribution is more spread out in this diagram. As in Figure 7.1, we assume a number of experimental values and assume the variance of data. In practice, this would be determined by actual findings. We take 1000 samples and assume that $\rho_1 = 40$, purely for illustrative purposes. We again take $\bar{B} = 0.64 \times 10^4$ and $C = 0.35 \times 10^4$, and B is generated from Gamma distribution functions. For each value of the temperature, we plot the relative probabilities of the order parameter s, given by stationary points of the bulk energy potential, $f_b(s)$. As was indicated by the probability distributions shown in Figure 7.1, we see a competition of states around the nematic super-heating temperature, $A = \frac{\bar{B}^2}{24C}$, where there is a small probability of observing the ordered nematic state, for temperatures above this deterministic value.

In summary, we assume inherent variation, and material uncertainty, in a spatially homogeneous liquid crystalline system. For mathematical simplicity, we consider a system without an elastic energy density as a first step. Following the approach of Mihai et al. [58], [59], we treat the parameter B, in the thermotropic bulk potential, as a random variable following a non-Gaussian distribution which can be derived from the maximum entropy principle in [87]. There is no obvious reason why this distribution cannot apply to B, however it may be an interesting research problem to consider random elastic or thermal effects. In contrast to the deterministic nematic-isotropic phase transition, where a deterministic critical temperature strictly separates the cases where either the isotropic fluid phase or a stable ordered nematic phase occurs, for the stochastic problem, there are probabilistic temperature intervals, where there is a quantifiable chance for both the isotropic and nematic phases to be observed. We have numerically shown, assuming B is Gamma distributed, that there is a probability, depending on the variance of the data, that ordered nematic phases can be observed above the deterministic

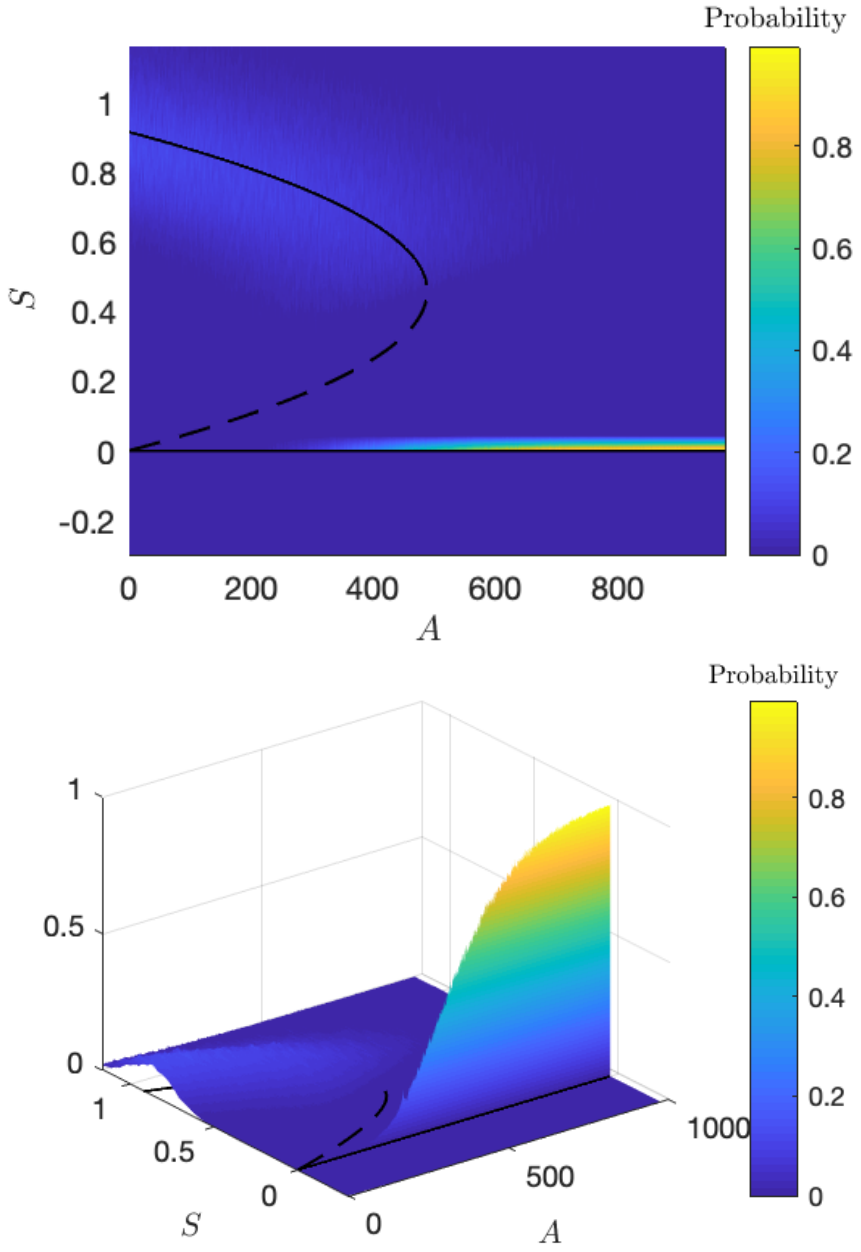

Figure 7.2: Completed probability distribution of the order parameter, s, as a function of temperature, A, when B follows the Gamma distribution (7.1.2) with $\rho_1 = 40$, $\bar{B} = 0.64 \times 10^4$. $C = 0.35 \times 10^4$. The deterministic values are shown by the black lines (stable is solid and unstable is dashed). We also include a 3D surface plot of the same diagram.

phase transition temperature, and that the scalar order parameter of the nematic state varies due its dependence on this random parameter. These preliminary findings present a new framework for studying liquid crystal phenomena, which shows that it is possible to quantify, and study, the influence of inherent variation in measured parameters and stochastic behaviour, not previously captured by deterministic approaches.

Chapter 8

Conclusions and future work

The aim of this thesis has been to analyse, and present, the exotic defect structures of nematic liquid crystalline systems in confinement, with different geometrical and material properties. These systems are modelled using the Landau-de Gennes continuum theory, and long-time behaviour is described by complex boundary-value problems for systems of coupled elliptic nonlinear partial differential equations. We have been able to manipulate the location of defects and tailor the multiplicity of equilibrium profiles by altering geometrical, material, and anchoring properties, and present delicate bifurcation analyses using sophisticated numerical tools for tracking solution branches. We now summarize each chapter, and discuss the open problems and future avenues of research generated from this work.

In Chapter 3, we consider three-dimensional square wells with both tangent Dirichlet boundary conditions, and physically relevant surface energies, in the Landau-de Gennes theory. We have shown that for sufficiently small cross-sectional edge length, λ, the WORS constructed in [52] for the 2D problem is the global LdG minimizer in the full 3D scenario. A natural extension of this work would include

an analytical study of three-dimensional solutions that are not z-invariant, and whether these solutions can be constructed by, or related to, the plethora of two-dimensional LdG critical points on a square domain, reported in previous work. In particular, we could include an isotropic inclusion, as in [63], for truly three-dimensional confining geometries, or consider the exotic zoo of unstable equilibria in two-dimensional domains in [64] as transitional cross-sections of a stable three-dimensional configuration. Another possible avenue for future research is to consider how homeotropic boundary conditions on the lateral surfaces of a 3D square well changes the solution landscape, which would be of both mathematical and applications-oriented interest.

Chapter 4 of this thesis continues on from Chapter 3, by computing three-dimensional nematic equilibria in confinement, using an energy minimization-based numerical approach. We presented 3D solutions with diagonal or rotated profiles in the plane of the well cross-section, for λ large enough, and the 3D WORS for λ small enough, for arbitrary well height, ϵ, corroborating our analysis in Chapter 3. We also numerically demonstrate the existence of stable mixed 3D solutions, which interpolate between two distinct diagonal profiles on the top and bottom well surfaces, for wells with sufficiently large ϵ and λ. We also extend this numerical study for domains with a rectangular cross-section to address the effects of geometrical anisotropy on confined NLC systems. In our numerical scheme, we employed a one-dimensional optimal shrinking dimer method from [66] to assess stability. This essentially determines the smallest eigenvalue of the Hessian, associated with the numerical solution. In the future, one could utilize the multi-dimensional approach of this work to discover new LdG critical points, and determine the degree of instability (or amount of unstable directions), of each configuration, such as the work in [121]. This would be of great interest

for switching device applications, as it would give insight into possible transition states between LdG minimizers, in three-dimensional scenarios. With regard to the numerical search itself, an extension of this work would be to employ different boundary conditions on the lateral surfaces of the computational domain, such as homeotropic anchoring or mixed boundary conditions.

Chapter 5 focuses on a reduced two-dimensional study of nematic equilibria, but with the addition of an anisotropic elastic energy term in the LdG free energy. We study the interplay between the square edge length, λ, and the elastic anisotropy, L_2, considering LdG critical points with three degrees of freedom, which measure the degree of nematic order in the plane of the square, and the degree of out-of-plane order. We prove that for $L_2 \neq 0$, we effectively lose the defect cross structure of the WORS, and show the stabilising effect of large L_2 on solutions with almost constant uniaxial alignment out of the plane. Our results for highly anisotropic materials (in the $L_2 \to \infty$ limit) are so far based on heuristic arguments with respect to the choice of boundary conditions. An open problem for the future would be to rigorously determine the true nature of the Constant solution in this regime. As we have shown, the leading order approximations of solutions, in this physically relevant limit, solve a non-elliptic system, and so this a great mathematical challenge which we were unfortunately unable to solve. Furthermore, our bifurcation diagrams in this chapter distinguish between the different solution branches by taking two measures, as in [74], however for large L_2, and large λ, we cannot distinguish between the Constant solution, the Ring$^{\pm}$ solutions, or the pWORS, and so other choices of measure could be considered to give more insight into the nature of these distinctive profiles. In our stability analysis we proved that, for L_2 larger than some constant that depends on λ, the critical points of the LdG free energy are locally stable with respect to two special

classes of admissible perturbations. In future work, it would be interesting to prove similar results with respect to more general perturbations, as our numerical investigations would suggest.

In Chapter 6, we consider a dilute suspension of magnetic nanoparticles in a nematic liquid crystal host. We study the equilibrium configurations of an appropriately defined ferronematic free energy in a two-dimensional square, hexagon, and pentagon. We have shown that we can stabilise either interior nematic point defects, or magnetic domain walls, depending on a judicious interplay of the rescaled elastic constant, ℓ, the magnetic coherence, ξ, and the nemato-magnetic coupling parameter, c, and this interplay depends on N - the number of sides of the regular polygon. This work offers up several potential directions for studying ferronematic equilibria with boundary defects. As in Chapter 5, one possibility is to compute high-index saddle points, with the numerical approach in [66], to determine transition pathways for the different equilibrium configurations. Another option would be to analyse the critical points on regular polygons, as in [74], and prove stability results with respect to the domain edge length, and other local parameters. Furthermore, we briefly consider solutions with a small ξ, and a more rigorous study of this physically relevant parameter regime would be of wider interest.

Finally in Chapter 7, we introduce a new methodology for studying nematic equilibria by assuming certain material-dependent parameters, in the fourth-order thermotropic bulk potential, follow a non-Gaussian probability distribution. This preliminary research is based on the assumption that uncertainties in the measurement of these parameters may alter the critical behaviour of the nematic-isotropic phase transition in a deterministic framework. We argue that instead of a phase transition occurring at some critical temperature, determined by concrete

parameter choices, we observe a competition of liquid crystal states in a range of temperature values, and this range is dependent on the mean value, and variance, of experimental data. Our findings do not suggest any unexpected phenomena for this simple problem but it does pave the way for future research in the wider liquid crystal community. One potential approach would be to study the stochastic Allen-Cahn equation with some added Gaussian space-time white noise term, as in [123], to model the two-dimensional system in [62], in a stochastic setting. Another approach is to employ similar modelling assumptions, following the work of [58], to study the more complicated nematic-isotropic phase transition problem for a sixth-order thermotropic bulk potential, which allows for biaxial nematic configurations.

Bibliography

[1] G. Canevari, J. Harris, A. Majumdar and Y. Wang, 'The well order reconstruction solution for three-dimensional wells, in the Landau–de Gennes theory,' *International Journal of Non-Linear Mechanics*, vol. 119, p. 103 342, 2020.

[2] Y. Han, J. Harris, L. Zhang and A. Majumdar, 'Elastic anisotropy of nematic liquid crystals in the two-dimensional Landau-de Gennes model,' 2021,
arXiv:2105.10253 [math.AP].

[3] Y. Han, J. Harris, J. Walton and A. Majumdar, 'Tailored nematic and magnetization profiles on two-dimensional polygons,' *Physical Review E*, vol. 103, no. 5, p. 052 702, 2021.

[4] E. Van den Pol, D. Thies–Weesie, A. Petukhov, D. Byelov and G. Vroege, 'Uniaxial and biaxial liquid crystal phases in colloidal dispersions of board-like particles,' *Liquid Crystals*, vol. 37, no. 6-7, pp. 641–651, 2010.

[5] S. Chandrasekhar, *Liquid Crystals*, 2nd Edition. Cambridge University Press, Cambridge, 1992.

[6] E. G. Virga, *Variational theories for liquid crystals*. Chapman & Hall, London, 1994.

[7] S. Elston and R. Sambles, *The optics of thermotropic liquid crystals*. Taylor & Francis, 1998.

[8] E. Priestley, P. J. Wojtowicz and P. Sheng, *Introduction to Liquid Crystals*. Plenum Press, New York, 1975.

[9] P. G. de Gennes and J. Prost, *The physics of liquid crystals*, 2nd Edition. Clarendon Press, Oxford, 1993.

[10] F. Reinitzer, 'Beiträge zur kenntniss des cholesterins,' *Monatshefte für Chemie*, vol. 9, pp. 421–441, 1888.

[11] H. Kelker, 'History of liquid crystals,' *Molecular Crystals and Liquid Crystals*, vol. 21, no. 1-2, pp. 1–48, 1973.

[12] G. Friedel, 'Les états mésomorphes de la matière,' *Annales de Physique*, vol. 18, pp. 273–474, 1922.

[13] I. W. Stewart, *The static and dynamic continuum theory of liquid crystals: a mathematical introduction*. Taylor & Francis, 2004.

[14] S. Chandrasekhar, B. Sadashiva and K. Suresh, 'Liquid crystals of disc-like molecules,' *Pramana*, vol. 9, no. 5, pp. 471–480, 1977.

[15] P. J. Collings and M. Hird, *Introduction to Liquid Crystals: Chemistry and Physics*. Taylor and Francis, London, 1997.

[16] M. J. Stephen and J. P. Straley, 'Physics of liquid crystals,' *Reviews of Modern Physics*, vol. 46, no. 4, p. 617, 1974.

[17] P. S. Pershan, *Structure of liquid crystal phases*. World Scientific, 1988, vol. 23.

[18] A. Spicer, 'Front propagation for nematic liquid crystals,' Ph.D. dissertation, University of Bath, 2016.

[19] N. J. Mottram and C. J. Newton, 'Introduction to Q-tensor theory,' *arXiv preprint arXiv:1409.3542*, 2014.

[20] C. Bahr and H.-S. Kitzerow, *Chirality in liquid crystals*. Springer, 2001.

[21] D. Dunmur and T. Sluckin, *Soap, science, and flat-screen TVs: a history of liquid crystals*. Oxford University Press, 2014.

[22] H. Kawamoto, 'The history of liquid-crystal displays,' *Proceedings of the IEEE*, vol. 90, no. 4, pp. 460–500, 2002.

[23] J. C. Jones, 'The fiftieth anniversary of the liquid crystal display,' *Liquid Crystals Today*, vol. 27, no. 3, pp. 44–70, 2018.

[24] G. W. Gray and S. M. Kelly, 'Liquid crystals for twisted nematic display devices,' *Journal of Materials Chemistry*, vol. 9, no. 9, pp. 2037–2050, 1999.

[25] M. Oh-e and K. Kondo, 'Electro-optical characteristics and switching behavior of the in-plane switching mode,' *Applied Physics Letters*, vol. 67, no. 26, pp. 3895–3897, 1995.

[26] A. Raisch and A. Majumdar, 'Order reconstruction phenomena and temperature-driven dynamics in a 3D zenithally bistable device,' *EPL (Europhysics Letters)*, vol. 107, no. 1, p. 16 002, 2014.

[27] T. Spencer, C. Care, R. Amos and J. Jones, 'Zenithal bistable device: Comparison of modeling and experiment,' *Physical Review E*, vol. 82, no. 2, p. 021 702, 2010.

[28] H. K. Bisoyi and S. Kumar, 'Liquid-crystal nanoscience: An emerging avenue of soft self-assembly,' *Chemical Society Reviews*, vol. 40, no. 1, pp. 306–319, 2011.

[29] J. P. Lagerwall and G. Scalia, 'A new era for liquid crystal research: Applications of liquid crystals in soft matter nano-, bio- and microtechnology,' *Current Applied Physics*, vol. 12, no. 6, pp. 1387–1412, 2012.

[30] H. Stark, 'Director field configurations around a spherical particle in a nematic liquid crystal,' *The European Physical Journal. B*, vol. 10, pp. 311–321, 1999.

[31] M. Čopič, A. Mertelj, O. Buchnev and Y. Reznikov, 'Coupled director and polarization fluctuations in suspensions of ferroelectric nanoparticles in nematic liquid crystals,' *Physical Review. E*, vol. 76, p. 011 702, 2007.

[32] I. Muševič, M. Škarabot, U. Tkalec, M. Ravnik and S. Žumer, 'Two-dimensional nematic colloidal crystals self-assembled by topological defects,' *Science*, vol. 313, no. 5789, pp. 954–958, 2006.

[33] F. Brochard and P. G. De Gennes, 'Theory of magnetic suspensions in liquid crystals,' *Journal de Physique*, vol. 31, no. 7, pp. 691–708, 1970.

[34] Q. Liu, Y. Cui, D. Gardner, X. Li, S. He and I. I. Smalyukh, 'Self-alignment of plasmonic gold nanorods in reconfigurable anisotropic fluids for tunable bulk metamaterial applications,' *Nano Letters*, vol. 10, pp. 1347–1353, 2010.

[35] P. Palffy-Muhoray, W. Cao, M. Moreira, B. Taheri and A. Munoz, 'Photonics and lasing in liquid crystal materials,' *Philosophical Transactions of the Royal Society of London. Series A: Mathematical, physical, and engineering sciences*, vol. 364, pp. 2747–2761, 2006.

[36] C.-H. Chen and K.-L. Yang, 'Detection and quantification of DNA adsorbed on solid surfaces by using liquid crystals,' *Langmuir*, vol. 26, no. 3, pp. 1427–1430, 2010.

[37] C. Zannoni, 'Molecular design and computer simulations of novel mesophases,' *Journal of Materials Chemistry*, vol. 11, pp. 2637–2646, 2001.

[38] G. R. Luckhurst and P. S. J. Simmonds, 'Computer simulation studies of anisotropic systems,' *Molecular Physics*, vol. 80, no. 2, pp. 233–252, 1993.

[39] E. de Miguel, E. Martín del Rio, J. T. Brown and M. P. Allen, 'Effect of the attractive interactions on the phase behavior of the Gay–Berne liquid crystal model,' *The Journal of Chemical Physics*, vol. 105, no. 10, pp. 4234–4249, 1996.

[40] S. Mkaddem and E. Gartland Jr, 'Fine structure of defects in radial nematic droplets,' *Physical Review E*, vol. 62, no. 5, p. 6694, 2000.

[41] G. Di Fratta, J. Robbins, V. Slastikov and A. Zarnescu, 'Half-integer point defects in the Q-tensor theory of nematic liquid crystals,' *Journal of Nonlinear Science*, vol. 26, no. 1, pp. 121–140, 2016.

[42] N. D. Mermin, 'The topological theory of defects in ordered media,' *Reviews of Modern Physics*, vol. 51, no. 3, p. 591, 1979.

[43] A. Majumdar, J. Robbins and M. Zyskin, 'Energies of S^2-valued harmonic maps on polyhedra with tangent boundary conditions,' in *Annales de l'IHP Analyse non linéaire*, vol. 25, 2008, pp. 77–103.

[44] C. Oseen, 'The theory of liquid crystals,' *Transactions of the Faraday Society*, vol. 29, no. 140, pp. 883–899, 1933.

[45] F. C. Frank, 'I. Liquid crystals. on the theory of liquid crystals,' *Discussions of the Faraday Society*, vol. 25, pp. 19–28, 1958.

[46] A. Lewis, 'Defects in liquid crystals: Mathematical and experimental studies,' Ph.D. dissertation, University of Oxford, 2015.

[47] J. L. Ericksen, 'Liquid crystals with variable degree of orientation,' *Archive for Rational Mechanics and Analysis*, vol. 113, pp. 97–120, 1991.

[48] A. M. Sonnet and E. G. Virga, *Dissipative Ordered Fluids: Theories for Liquid Crystals*. Springer, New York, 2010.

[49] J. M. Ball, 'Mathematics and liquid crystals,' *Molecular Crystals and Liquid Crystals*, vol. 647, no. 1, pp. 1–27, 2017.

[50] A. Majumdar, 'Equilibrium order parameters of nematic liquid crystals in the Landau-de Gennes theory,' *European Journal of Applied Mathematics*, vol. 21, no. 2, pp. 181–203, 2010.

[51] A. Rapini and M. Papoular, 'Distorsion d'une lamelle nématique sous champ magnétique conditions d'ancrage aux parois,' *Le Journal de Physique Colloques*, vol. 30, no. 4, p. 54, 1969.

[52] S. Kralj and A. Majumdar, 'Order reconstruction patterns in nematic liquid crystal wells,' *Proceedings of the Royal Society A: Mathematical, Physical and Engineering Sciences*, vol. 470, no. 2169, p. 20 140 276, 2014.

[53] H. Mori, E. C. Gartland Jr., J. R. Kelly and P. J. Bos, 'Multidimensional director modelling using the Q-tensor representation in a liquid crystal cell and its application to the π cell with patterned electrodes,' *Japanese Journal of Applied Physics*, vol. 38, p. 135, 1999.

[54] D. W. Berreman and S. Meiboom, 'Tensor representation of Oseen-Frank strain energy in uniaxial cholesterics,' *Physical Review A*, vol. 30, p. 1955, 1984.

[55] S. Kralj, E. G. Virga and S. Žumer, 'Biaxial torus around nematic point defects,' *Physical Review E*, vol. 60, no. 2, p. 1858, 1999.

[56] A. Majumdar and A. Zarnescu, 'Landau–de Gennes theory of nematic liquid crystals: The Oseen–Frank limit and beyond,' *Archive for Rational Mechanics and Analysis*, vol. 196, no. 1, pp. 227–280, 2010.

[57] L. C. Evans, *Partial differential equations*. American Mathematical Society, 1998.

[58] L. A. Mihai, T. E. Woolley and A. Goriely, 'Likely equilibria of the stochastic Rivlin cube,' *Philosophical Transactions of the Royal Society A*, vol. 377, no. 2144, p. 20 180 068, 2019.

[59] L. A. Mihai, D. Fitt, T. E. Woolley and A. Goriely, 'Likely cavitation in stochastic elasticity,' *Journal of Elasticity*, vol. 137, no. 1, pp. 27–42, 2019.

[60] C. Tsakonas, A. Davidson, C. Brown and N. Mottram, 'Multistable alignment states in nematic liquid crystal filled wells,' *Applied Physics Letters*, vol. 90, no. 11, p. 111 913, 2007.

[61] C. Luo, A. Majumdar and R. Erban, 'Multistability in planar liquid crystal wells,' *Physical Review E*, vol. 85, no. 6, p. 061 702, 2012.

[62] G. Canevari, A. Majumdar and A. Spicer, 'Order reconstruction for nematics on squares and hexagons: A Landau–de Gennes study,' *SIAM Journal on Applied Mathematics*, vol. 77, no. 1, pp. 267–293, 2017.

[63] Y. Wang, G. Canevari and A. Majumdar, 'Order reconstruction for nematics on squares with isotropic inclusions: A Landau–de Gennes study,' *SIAM Journal on Applied Mathematics*, vol. 79, no. 4, pp. 1314–1340, 2019.

[64] M. Robinson, C. Luo, P. E. Farrell, R. Erban and A. Majumdar, 'From molecular to continuum modelling of bistable liquid crystal devices,' *Liquid Crystals*, vol. 44, no. 14-15, pp. 2267–2284, 2017.

[65] Y. Wang, P. Zhang and J. Z. Chen, 'Topological defects in an unconfined nematic fluid induced by single and double spherical colloidal particles,' *Physical Review E*, vol. 96, no. 4, p. 042 702, 2017.

[66] J. Yin, L. Zhang and P. Zhang, 'High-index optimization-based shrinking dimer method for finding high-index saddle points,' *SIAM Journal on Scientific Computing*, vol. 41, no. 6, A3576–A3595, 2019.

[67] J. Yin, Y. Wang, J. Z. Chen, P. Zhang and L. Zhang, 'Construction of a pathway map on a complicated energy landscape,' *Physical Review Letters*, vol. 124, no. 9, p. 090 601, 2020.

[68] A. H. Lewis, I. Garlea, J. Alvarado, O. J. Dammone, P. D. Howell, A. Majumdar, B. M. Mulder, M. Lettinga, G. H. Koenderink and D. G. Aarts, 'Colloidal liquid crystals in rectangular confinement: Theory and experiment,' *Soft Matter*, vol. 10, no. 39, pp. 7865–7873, 2014.

[69] L. Fang, A. Majumdar and L. Zhang, 'Surface, size and topological effects for some nematic equilibria on rectangular domains,' eng, *Mathematics and Mechanics of Solids*, vol. 25, no. 5, pp. 1101–1123, 2020.

[70] D. Golovaty, J. A. Montero and P. Sternberg, 'Dimension reduction for the Landau-de Gennes model in planar nematic thin films,' *Journal of Nonlinear Science*, vol. 25, no. 6, pp. 1431–1451, 2015.

[71] P. Bauman, J. Park and D. Phillips, 'Analysis of nematic liquid crystals with disclination lines,' *Archive for Rational Mechanics and Analysis*, vol. 205, no. 3, pp. 795–826, 2012.

[72] D. Golovaty, M. Novack, P. Sternberg and R. Venkatraman, 'A model problem for nematic-isotropic transitions with highly disparate elastic constants,' *Archive for Rational Mechanics and Analysis*, vol. 236, no. 3, pp. 1739–1805, 2020.

[73] D. Golovaty, P. Sternberg and R. Venkatraman, 'A Ginzburg–Landau-type problem for highly anisotropic nematic liquid crystals,' *SIAM Journal on Mathematical Analysis*, vol. 51, no. 1, pp. 276–320, 2019.

[74] Y. Han, A. Majumdar and L. Zhang, 'A reduced study for nematic equilibria on two-dimensional polygons,' *SIAM Journal on Applied Mathematics*, vol. 80, no. 4, pp. 1678–1703, 2020.

[75] V. Zadorozhnii, T. J. Sluckin, V. Y. Reshetnyak and K. Thomas, 'The Frederiks effect and related phenomena in ferronematic materials,' *SIAM Journal on Applied Mathematics*, vol. 68, no. 6, pp. 1688–1716, 2008.

[76] S. V. Burylov and Y. L. Raikher, 'Ferronematics: Enhanced magneto-optical response of a liquid crystalline system,' *Materials Science and Engineering: C*, vol. 2, no. 4, pp. 235–241, 1995.

[77] J. Rault, P. Cladis and J. Burger, 'Ferronematics,' *Physics Letters A*, vol. 32, no. 3, pp. 199–200, 1970.

[78] A. Mertelj, D. Lisjak, M. Drofenik and M. Čopič, 'Ferromagnetism in suspensions of magnetic platelets in liquid crystal,' *Nature*, vol. 504, no. 7479, pp. 237–241, 2013.

[79] A. Mertelj and D. Lisjak, 'Ferromagnetic nematic liquid crystals,' *Liquid Crystals Reviews*, vol. 5, no. 1, pp. 1–33, 2017.

[80] K. Bisht, V. Banerjee, P. Milewski and A. Majumdar, 'Magnetic nanoparticles in a nematic channel: A one-dimensional study,' eng, *Physical Review. E*, vol. 100, no. 1, pp. 012 703–012 703, 2019.

[81] K. Bisht, Y. Wang, V. Banerjee and A. Majumdar, 'Tailored morphologies in 2D ferronematic wells,' *Physical Review E*, vol. 101, no. 2, p. 022 706, 2020.

[82] M.-C. Calderer, A. DeSimone, D. Golovaty and A. Panchenko, 'An effective model for nematic liquid crystal composites with ferromagnetic inclusions,' *SIAM Journal on Applied Mathematics*, vol. 74, no. 2, pp. 237–262, 2014.

[83] G. Canevari and A. Zarnescu, 'Design of effective bulk potentials for nematic liquid crystals via colloidal homogenisation,' *Mathematical Models and Methods in Applied Sciences*, vol. 30, no. 02, pp. 309–342, 2020.

[84] B. Staber and J. Guilleminot, 'Stochastic modeling of a class of stored energy functions for incompressible hyperelastic materials with uncertainties,' *Comptes Rendus Mécanique*, 2015.

[85] L. Mihai, D. Fitt, T. Woolley and A. Goriely, 'Likely equilibria of stochastic hyperelastic spherical shells and tubes,' *Mathematics and Mechanics of Solids*, vol. 24, pp. 2066–2082, 2018.

[86] E. Jaynes, 'Information theory and statistical mechanics II,' *Physical Review*, vol. 106(4), pp. 620–630, 1957.

[87] C. Soize, 'A nonparametric model of random uncertainties for reduced matrix models in structural dynamics,' *Probabilistic Engineering Mechanics*, vol. 15, no. 3, pp. 277–294, 2000.

[88] J. Walton, N. Mottram and G. McKay, 'Nematic liquid crystal director structures in rectangular regions,' *Physical Review E*, vol. 97, no. 2, p. 022 702, 2018.

[89] F. Bethuel, H. Brezis, B. Coleman and F. Hélein, 'Bifurcation analysis of minimizing harmonic maps describing the equilibrium of nematic phases between cylinders,' *Archive for Rational Mechanics and Analysis*, vol. 118, no. 2, pp. 149–168, 1992.

[90] H. Dang, P. C. Fife and L. Peletier, 'Saddle solutions of the bistable diffusion equation,' *Zeitschrift für angewandte Mathematik und Physik ZAMP*, vol. 43, no. 6, pp. 984–998, 1992.

[91] X. Lamy, 'Bifurcation analysis in a frustrated nematic cell,' *Journal of Nonlinear Science*, vol. 24, no. 6, pp. 1197–1230, 2014.

[92] R. Ignat, L. Nguyen, V. Slastikov and A. Zarnescu, 'Instability of point defects in a two-dimensional nematic liquid crystal model,' in *Annales de l'Institut Henri Poincaré C, Analyse non linéaire*, Elsevier, vol. 33, 2016, pp. 1131–1152.

[93] M. Osipov and S. Hess, 'Density functional approach to the theory of interfacial properties of nematic liquid crystals,' *The Journal of Chemical Physics*, vol. 99, no. 5, pp. 4181–4190, 1993.

[94] A. Sen and D. Sullivan, 'Landau–de Gennes theory of wetting and orientational transitions at a nematic-liquid–substrate interface,' *Physical Review A*, vol. 35, no. 3, p. 1391, 1987.

[95] T. A. Davis and E. C. Gartland Jr, 'Finite element analysis of the Landau–de Gennes minimization problem for liquid crystals,' *SIAM Journal on Numerical Analysis*, vol. 35, no. 1, pp. 336–362, 1998.

[96] M. Ravnik and S. Žumer, 'Landau–de Gennes modelling of nematic liquid crystal colloids,' *Liquid Crystals*, vol. 36, no. 10-11, pp. 1201–1214, 2009.

[97] P. Wolfe, 'Convergence conditions for ascent methods,' *SIAM Review*, vol. 11, no. 2, pp. 226–235, 1969.

[98] S. Wright and J. Nocedal, *Numerical optimization*. volume 35. Springer, 1999.

[99] M. A. Peletier, 'Variational modelling: Energies, gradient flows, and large deviations,' *arXiv preprint arXiv:1402.1990*, 2014.

[100] S. Kralj and S. Žumer, 'The stability diagram of a nematic liquid crystal confined to a cylindrical cavity,' *Liquid Crystals*, vol. 15, no. 4, pp. 521–527, 1993.

[101] A. Logg and G. N. Wells, 'DOLFIN: Automated finite element computing,' *ACM Transactions on Mathematical Software*, vol. 37, no. 2, 2010,
doi:10.1145/1731022.1731030.

[102] M. S. Alnæs, J. Blechta, J. Hake, A. Johansson, B. Kehlet, A. Logg, C. Richardson, J. Ring, M. E. Rognes and G. N. Wells, 'The FEniCS project version 1.5,' *Archive of Numerical Software*, vol. 3, no. 100, 2015,
doi:10.11588/ans.2015.100.20553.

[103] A. Logg, K.-A. Mardal and G. Wells, *Automated solution of differential equations by the finite element method: The FEniCS book*. Springer Science & Business Media, 2012, vol. 84.

[104] R. R. Maity, A. Majumdar and N. Nataraj, 'A priori and a posteriori error analysis for the Nitsche's method of a reduced Landau-de Gennes problem,' *Accepted for publication in Computational Methods in Applied Mathematics*, 2021.

[105] ——, 'Discontinuous Galerkin finite element methods for the Landau–de Gennes minimization problem of liquid crystals,' *IMA Journal of Numerical Analysis*, vol. 41, no. 2, pp. 1130–1163, 2021.

[106] A. V. Knyazev, 'Toward the optimal preconditioned eigensolver: Locally optimal block preconditioned conjugate gradient method,' eng, *SIAM Journal on Scientific Computing*, vol. 23, no. 2, pp. 517–541, 2001.

[107] H. Brezis, *Functional analysis, Sobolev spaces and partial differential equations*. Springer Science & Business Media, 2010.

[108] Y. Han, J. Yin, P. Zhang, A. Majumdar and L. Zhang, 'Solution landscape of a reduced Landau–de Gennes model on a hexagon,' *Nonlinearity*, vol. 34, no. 4, p. 2048, 2021.

[109] C. Gu, X. Ding and C. Yang, *Partial Differential Equations in China*. Springer Science+Business Media, 1994, doi:10.1007/9789401111980.

[110] I. Muševič, M. Škarabot, U. Tkalec, M. Ravnik and S. Žumer, 'Two-dimensional nematic colloidal crystals self-assembled by topological defects,' *Science*, vol. 313, no. 5789, pp. 954–958, 2006.

[111] P. J. Ackerman and I. I. Smalyukh, 'Static three-dimensional topological solitons in fluid chiral ferromagnets and colloids,' *Nature Materials*, vol. 16, no. 4, pp. 426–432, 2017.

[112] M. Mur, J. A. Sofi, I. Kvasić, A. Mertelj, D. Lisjak, V. Niranjan, I. Muševič and S. Dhara, 'Magnetic-field tuning of whispering gallery mode lasing from ferromagnetic nematic liquid crystal microdroplets,' *Optics Express*, vol. 25, no. 2, pp. 1073–1083, 2017.

[113] T. Potisk, D. Svenšek, H. R. Brand, H. Pleiner, D. Lisjak, N. Osterman and A. Mertelj, 'Dynamic magneto-optic coupling in a ferromagnetic nematic liquid crystal,' *Physical Review Letters*, vol. 119, no. 9, p. 097 802, 2017.

[114] T. Potisk, A. Mertelj, N. Sebastián, N. Osterman, D. Lisjak, H. R. Brand, H. Pleiner and D. Svenšek, 'Magneto-optic dynamics in a ferromagnetic nematic liquid crystal,' *Physical Review E*, vol. 97, no. 1, p. 012 701, 2018.

[115] S. Burylov and A. Zakhlevnykh, 'Magnetically induced bistable behavior of ferronematic liquid crystals,' *Physical Review E*, vol. 88, no. 5, p. 052 503, 2013.

[116] H. Pleiner, E. Jarkova, H. Muler and H. Brand, 'Landau description of ferrofluid to ferronematic phase transition,' *Magnetohydrodynamics*, vol. 37, no. 254, p. 146, 2001.

[117] J. Dalby, P. E. Farrell and A. M. J. Xia, 'One-dimensional ferronematics in a channel: Order reconstruction, bifurcations and multistability,' *arXiv preprint arXiv:2102.06347*, 2021.

[118] H. Kusumaatmaja and A. Majumdar, 'Free energy pathways of a multistable liquid crystal device,' *Soft Matter*, vol. 11, no. 24, pp. 4809–4817, 2015.

[119] M. Shuai, A. Klittnick, Y. Shen *et al.*, 'Spontaneous liquid crystal and ferromagnetic ordering of colloidal magnetic nanoplates,' eng, *Nature Communications*, vol. 7, no. 1, pp. 10 394–10 394, 2016.

[120] J. Robbins and M. Zyskin, 'Classification of unit-vector fields in convex polyhedra with tangent boundary conditions,' *Journal of Physics A: Mathematical and General*, vol. 37, no. 44, p. 10 609, 2004.

[121] Y. Han, Y. Hu, P. Zhang and L. Zhang, 'Transition pathways between defect patterns in confined nematic liquid crystals,' *Journal of Computational Physics*, vol. 396, pp. 1–11, 2019.

[122] C. E. Shannon, 'A mathematical theory of communication,' *The Bell System Technical Journal*, vol. 27, no. 3, pp. 379–423, 1948.

[123] T. Funaki, *Lectures on random interfaces*. Springer, 2016.